Directive antennas
based on
two-dimensional dielectric EBG crystals

Claudio Biancotto

Submitted for the degree of Doctor of Philosophy

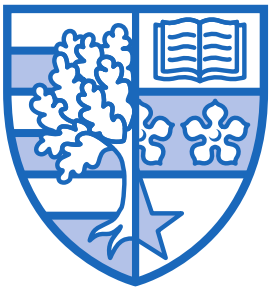

HERIOT-WATT UNIVERSITY

School of Engineering and Physical Sciences

January 2012

Abstract

The aim of this work is the design and analysis of novel antennas realised with electromagnetic bandgap (EBG) structures based on simple two-dimensional cylindrical, triangular and square lattices of dielectric rods.

In particular, we focused our attention on designing antennas with high directivity and front-to-back-ratio (FTBR) on the azimuthal plane. Several EBG structures have been investigated, divided in two main categories: multilayer EBG structures with an angular defect window and EBG corner reflectors. The former are based on a feeding source excited within a cavity: fields at badgap frequencies are trapped inside the cavity and opening an angular defect window allows propagation in that privileged directions leading to directive radiation patterns. The latter are based on a source placed in front of an EBG corner reflector: at bandgap frequencies, the excited fields are reflected toward the corner aperture (in a similar fashion to metallic corners of analogous dimensions) enhancing radiation patterns' directivity.

The analysed structures have been also modified to host multiple sources to create multiple-feed antenna structures with the ability of rotating the radiation patterns on the azimuthal plane.

Antennas have been modelled using an in-house developed Finite-Difference Time-Domain solver and the commercial Finite Element Method solver Ansoft HFSS, focusing on structures designed to operate in the X-band frequency region (8.2GHz-12.4GHz) in order to take advantage of the available equipment and facilities at Heriot-Watt University for prototypes testing. The proposed structures can be nevertheless scaled up or down in size in order to respectively scale down or up of the same factor the frequency of operation.

The main achievements of the analysed multilayer EBG structures and corner EBG reflectors are the large impedance bandwidth (greater than 30%) with stable radiation patterns within, high gain ($>$12dBi) and high FTBR (greater than 25dB) accomplished using EBG structures made with a small number (10-20) of low-loss ceramic rods arranged in very simple two-dimensional crystals. EBG corner reflectors have been also found basically equivalent (at badgap frequencies) to metal reflectors in terms of achieved gain and radiation patterns, suggesting them as possible substitutes for high frequencies applications where dielectric losses would be smaller than metal losses.

to Kinga

Acknowledgements

I would like to say thank you to everyone who helped me throughout my PhD studies. Firstly my supervisor, Paul Record, whose encouragement, supervision and support enabled me to develop this project.

The Doctoral Training Award program of the School of Engineering and Physical Sciences at Heriot-Watt University deserves my gratitude for the financial support, it wouldn't have been possible for me to pursue my research without it.

I would like to thank all my colleagues at Heriot-Watt University, as well as all the colleagues from different institutions I met in many different occasions, for the interesting, fruitful and sometimes even enlightening discussions we had.

A big thank you goes to my family members for supporting me in a so far lifelong student career, their encouragement has been always very important to me.

Thanks to all my friends back home and in Edinburgh for the moral support I received in all these years of academic studies.

Finally, but most importantly, I want to express my gratitude to my future wife Kinga, for her constant encouragement, devotion and unconditional love: thank you for being always on my side no matter where and what I'm doing.

*La filosofia è scritta in questo grandissimo libro che continuamente ci sta aperto innanzi a gli occhi (io dico l'universo), ma non si può intendere se prima non s'impara a intender la lingua, e conoscer i caratteri, ne' quali è scritto. Egli è scritto in lingua matematica, e i caratteri son triangoli, cerchi, ed altre figure geometriche, senza i quali mezi è impossibile a intenderne umanamente parola; senza questi è un aggirarsi vanamente per un oscuro laberinto.**

Galileo Galilei

** Philosophy is written in this grand book which constantly lies open in front of our eyes (I say the universe), but it cannot be understood until one has learned to understand its language, and recognize the characters, in which it is written. It is written in mathematical language, and the characters are triangles, circles and other geometrical figures, without the aid of which it is impossible to understand any human word; without these characters it is like aimlessly wandering around a dark labyrinth.*

ACADEMIC REGISTRY
Research Thesis Submission

Name*:*	Claudio Biancotto		
School/PGI:	Engineering and Physical Sciences		
Version: *(i.e. First, Resubmission, Final)*	Final	Degree Sought (Award **and** Subject area)	PhD, Electrical Engineering

Declaration

In accordance with the appropriate regulations I hereby submit my thesis and I declare that:

1) the thesis embodies the results of my own work and has been composed by myself
2) where appropriate, I have made acknowledgement of the work of others and have made reference to work carried out in collaboration with other persons
3) the thesis is the correct version of the thesis for submission and is the same version as any electronic versions submitted*.
4) my thesis for the award referred to, deposited in the Heriot-Watt University Library, should be made available for loan or photocopying and be available via the Institutional Repository, subject to such conditions as the Librarian may require
5) I understand that as a student of the University I am required to abide by the Regulations of the University and to conform to its discipline.

* *Please note that it is the responsibility of the candidate to ensure that the correct version of the thesis is submitted.*

Signature of Candidate*:*		Date:	

Submission

Submitted By *(name in capitals):*	
Signature of Individual Submitting:	
Date Submitted:	

For Completion in the Student Service Centre (SSC)

Received in the SSC by *(name in capitals):*			
Method of Submission *(Handed in to SSC; posted through internal/external mail):*			
*E-thesis Submitted (**mandatory for final theses**)*			
Signature:		Date:	

Please note this form should bound into the submitted thesis.

Updated February 2008, November 2008, February 2009, January 2011

Contents

Publications

Journal Publications

C. Biancotto and P. Record, "Dielectric EBG Corner Reflector Antenna," *Journal of ElectroMagnetic Waves and Applications*, Vol. 24, no. 14/15, pp. 2107-2118, 2010.
C. Biancotto and P. Record, "Design of a beam forming dielectric cylindrical EBG antenna," *Progress In Electromagnetics Research B*, Vol. 18, 327-346, 2009.
C. Biancotto and P. Record, "Triangular Lattice Dielectric EBG Antenna," *IEEE Antennas and Wireless Propagation Letters*, Vol. 9, pp. 95-98, 2010.
C. Biancotto and P. Record, "Conical steerable dielectric resonator antenna," *Electronics Letters*, vol. 44, 2008, pp. 1107-1109.

Conference Papers

C. Biancotto and P. Record, "Multifeed Triangular Lattice Dielectric EBG Antennas," in *Microwave Conference Proceedings (APMC)*, 2010, pp. 881-884.
C. Biancotto and P. Record, "Beam Forming Dielectric Cylindrical EBG Antenna," *Antennas and Propagation Conference, 2009*, LAPC 2009. Loughborough, pp. 425-428.

Chapter 1 – Introduction

Electromagnetic BandGap (EBG) structures [1, 2] (also called Photonic BandGap - PBG) and their characteristics have found numerous applications in antenna design. An EBG structure can be realized arranging metallic and/or dielectric elements in an organized lattice in which a unit cell is periodically repeated along one or more directions. EBG structures can be therefore classified according to the number of directions in which the lattice presents a periodicity, ie one-dimensional, two-dimensional and three-dimensional crystals, as depicted in figure 1.1. The lattice geometry influences the presence, position and extension of frequency bands in which electromagnetic propagation is forbidden, ie bandgaps. Breaking the lattice periodicity allows propagation through the defect and it is a common approach to create cavites, waveguides, etc. within an EBG structure.

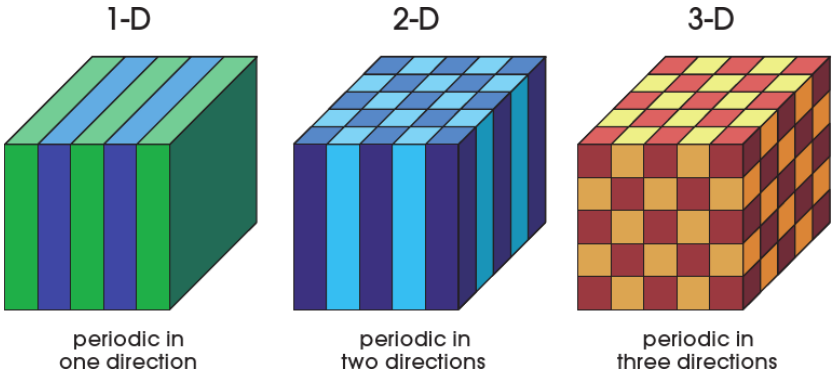

Figure 1.1: *One-, two and three-dimensional EBG crystals [2].*

Electromagnetic energy propagation is usually forbidden along the periodicity directions, therefore to create a complete bandgap, ie a frequency range in which propagation is forbidden for any given direction and polarization, a 3-D lattice is usually required. 3-D crystals are obviously more complex to analyse and manufacture, figure 1.2, but there are many applications in which EM energy direction of propagation and polarization are known a-priori and therefore 1-D or 2-D crystals may suffice.

A typical example of 1-D EBG crystal is a multilayer film, figure 1.2a, which is created by alternating layers of materials (of infinite extension in the x and y directions) with different dielectric permittivities. Two simple 2-D EBG crystals are shown in figure 1.2b-c: in the first case a square lattice of dielectric rods (of infinite extension in the z direction) is embedded in a background dielectric; in the second case a triangular lattice of circular holes (of infinite extension in the z direction) is drilled in a background dielectric. Structures as the one shown in figure 1.2b, typically present well defined TM[1] bandgaps; conversely, structures as the one shown in figure 1.2c usually present well

[1] In this work we follow the convention of photonic-crystal literature: with reference to figure 1.2b, the electromagnetic field components of propagating modes for transverse-magnetic (TM) and transverse-electric (TE) modes are respectively (E_z, H_x, H_y) and (H_z, E_x, E_y). The direction of propagation is on the xy plane with no variation along the z direction.

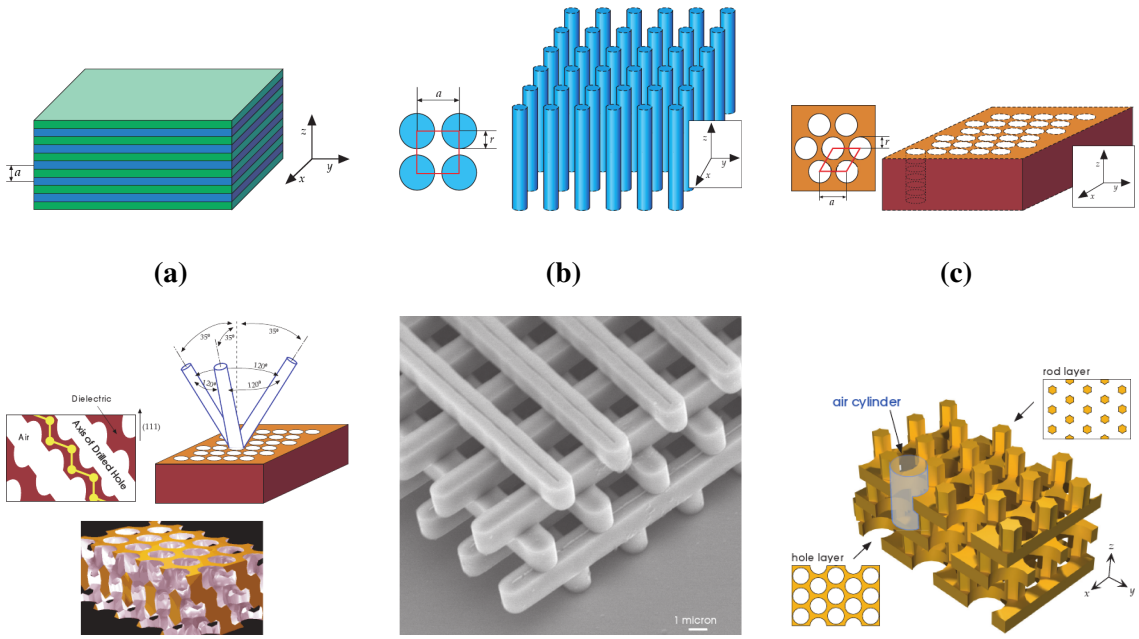

Figure 1.2: *EBG crystals [2]: a) 1-D crystal, multilayer film; b) 2-D crystal, square lattice of dielectric rods; c) 2-D crystal, triangular lattice of air columns in a background dielectric; d) 3-D crystal, Yablonovite; e) 3-D crystal, woodpile; f) 3-D crystal, alternating layers of dielectric rods in air and holes in dielectric.*

defined TE bandgaps. Three 3-D crystals are shown in figure 1.2d-f: Yablonovite, a "woodpile" and a structure created by alternating layers of dielectric rods in air and holes in dielectric; these crystals may present a complete bandgap for any given polarization and direction of propagation. Dielectric EBG crystals are analysed in more details in Appendix B.

Planar metallo-dielectric 2-D EBG crystals can be easily realised in printed technology and they are usually refered as Frequency Selective Surfaces (FSS) or High-Impedance Surfaces (HIS) [3]. They are composed by an array of conducting patches or aperture elements on a dielectric substrates, figure 1.3a; patches can be connected to a ground plane using vias creating "mushroom" elements [4, 5], figure 1.3b. These planar structures present two very interesting properties: a frequency bandgap for incident surface waves and a frequency dependant reflection phase for incident planar waves.

1.1 Antenna applications of EBG structures

Several applications of dielectric and/or metallic EBG structures have been presented in antenna design literature. The deployed EBG structure is generally used either as a partially reflective surface (PRS) or to guide/reflect the excited fields toward a particular direction. In the first case, a feeding source is usually placed between a ground plane and the EBG structure: fields at bandgap frequencies are partially trapped within the cavity;

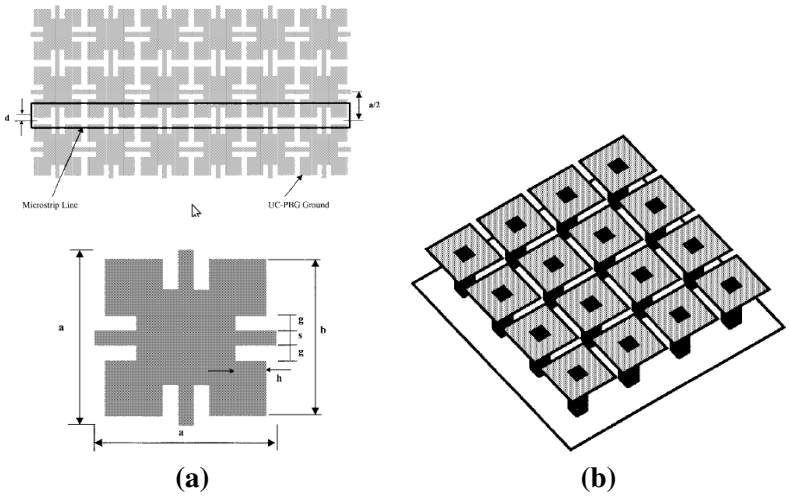

Figure 1.3: *a) Uniplanar Frequency Selective Surface [6]; b) "mushrooms" Frequency Selective Surface [4].*

the resulting standing-wave distribution synthesizes a larger radiating aperture, therefore enhancing the directivity of the enclosed source. In the second case, a feeding source is usually embedded in an EBG structure in which defects may have been introduced in order to shape or guide the excited fields, enhancing the radiated fields toward a specific direction.

1.1.1 EBG resonator antennas

Dielectric planar multilayer [7–11], woodpile [12–17, 10, 18, 19] and based on more complicated geometries [8, 10] superstrates placed over a ground plane and a feeding source, figure 1.4, have been used to create resonator antennas which directivity is proportional to the area of the EBG superstrate [13, 12], figure 1.5a. In [17], the superstrate directivity sidelobes have been also reduced by tapering the EBG structure periodicity along the edges, figure 1.5b-c. Given a frequency of operation f_0, the EBG superstrate is usually placed at a distance d satisfying the resonance condition

$$f_0 = \frac{c}{2d} \cdot \left(\frac{\phi_{EBG} + \pi}{2\pi} \right) \tag{1.1}$$

where ϕ_{EBG} is the phase reflection coefficient introduced by the EBG superstrate and c is the speed of light. The high realized gain achieved in the normal direction can be attributed to the electric field distribution between EBG superstrate and ground plane: at bandgap frequencies, the excited fields are reflected back and the standing wave type distribution synthesizes an aperture larger than the enclosed antenna, figure 1.5b.

FSSs have been also used as EBG superstrates to create resonant cavities [20–25]. The FSS is designed to be used at frequencies close to the resonance condition to take advantage of the partially reflective behaviour. Given the resonating nature of these

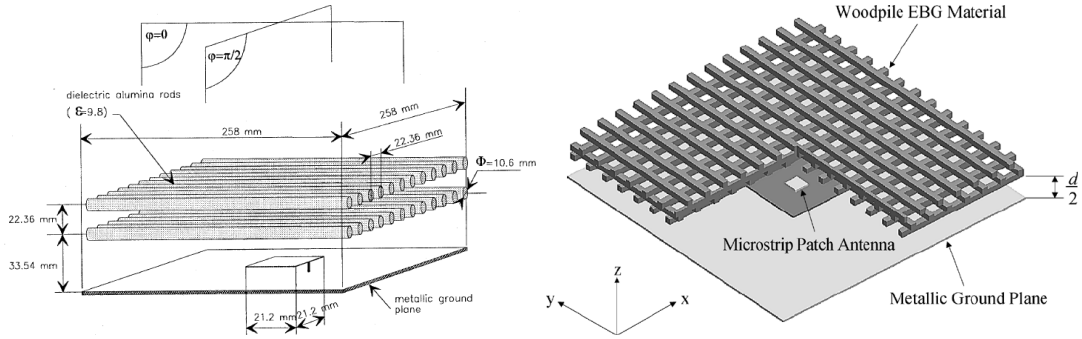

(a) **(b)**

Figure 1.4: *a) Planar multilayer EBG antenna [9]; b) Planar woodpile EBG antenna [13].*

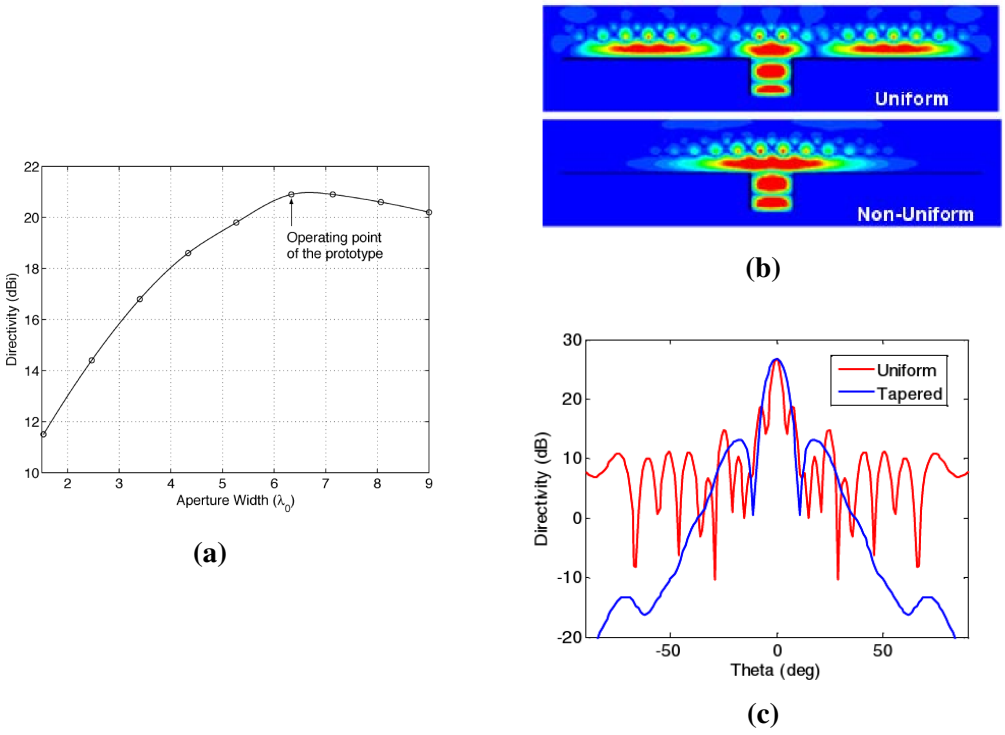

(a) **(b)** **(c)**

Figure 1.5: *a: Directivity as a function of EBG superstrate dimensions [13]; b) Electric field distribution between EBG superstrate and ground plane [17]; c) Uniform and tapered EBG superstrates directivity pattern [17].*

structures, directivity patterns deteriorate quickly at frequencies distant from resonance. Radiation bandwidth can be improved at the expenses of the realized gain by reducing the quality factor of the resonator [23] or by using multi-layer FSS [26, 27, 24] or multiple feeds [24].

Cylindrical EBG (CEBG) structures have been also used in antenna design. CEBG structures made with metallic patches surrounding a dipole antenna [28, 29], figure 1.7a, or a cylindrical patch antenna [30, 31], figure 1.8a, have been studied by Palikiras et al. These structures act as partially reflective surfaces creating a resonating field distribution within the CEBG structure: the E-plane directivity pattern of the enclosed antenna is

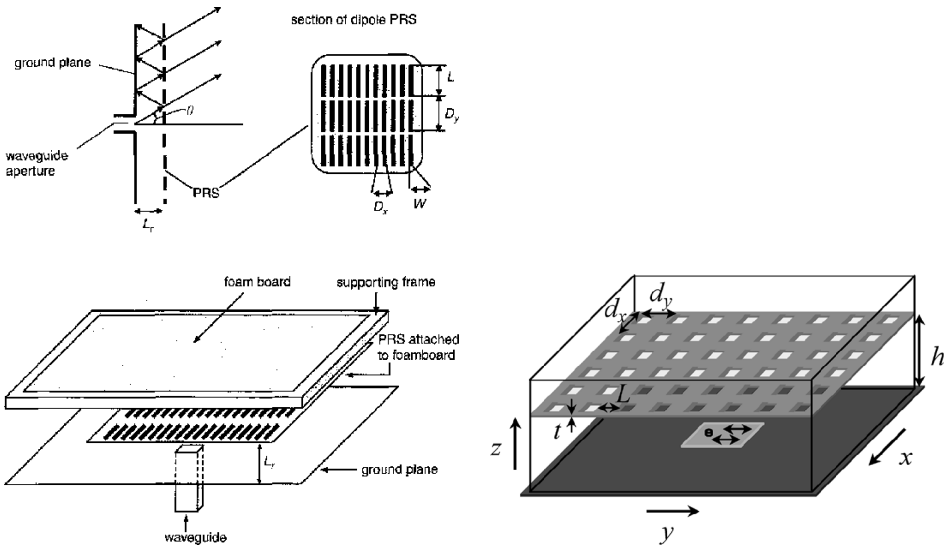

Figure 1.6: *a) PRS superstrate made by printed dipoles on a substrate [20]; b) PRS superstrate made by a grid of crossed copper strips [22].*

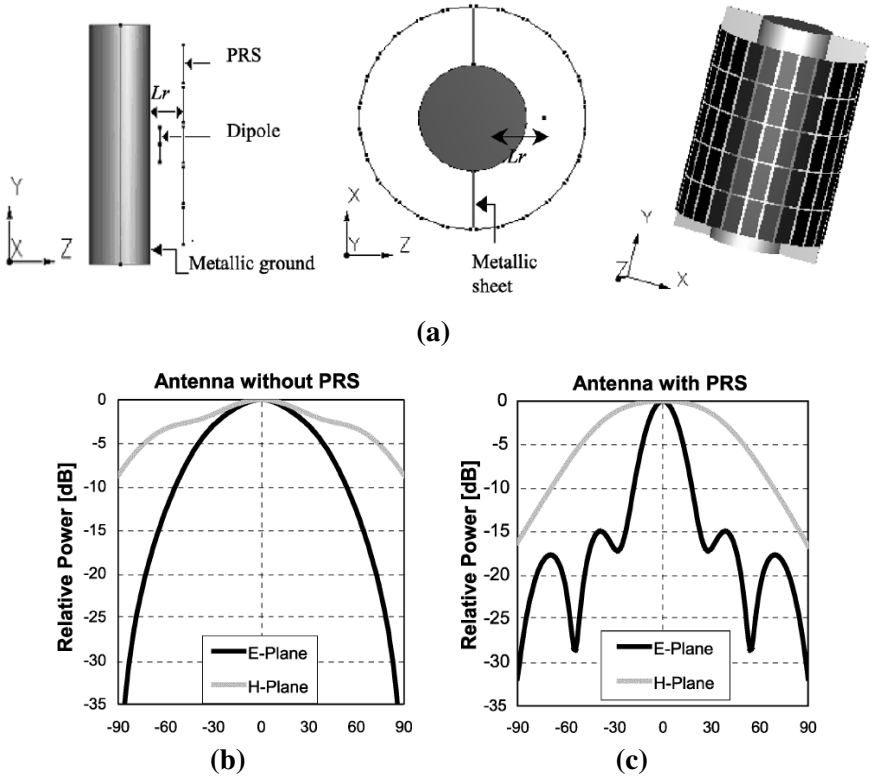

Figure 1.7: *Metallic patches Cylindrical EBG antennas feed by a dipole[28]: a) antenna structure ; b) normalized radiation patterns on principal planes without the EBG structures; c) normalized radiation patterns on principal planes with the EBG structures.*

enhanced while presenting an omnidurectional pattern on the azimuthal plane, figure 1.7c and figure 1.8c.

Metallic rods have been used by Chreim et al to design CEBG antenna structures

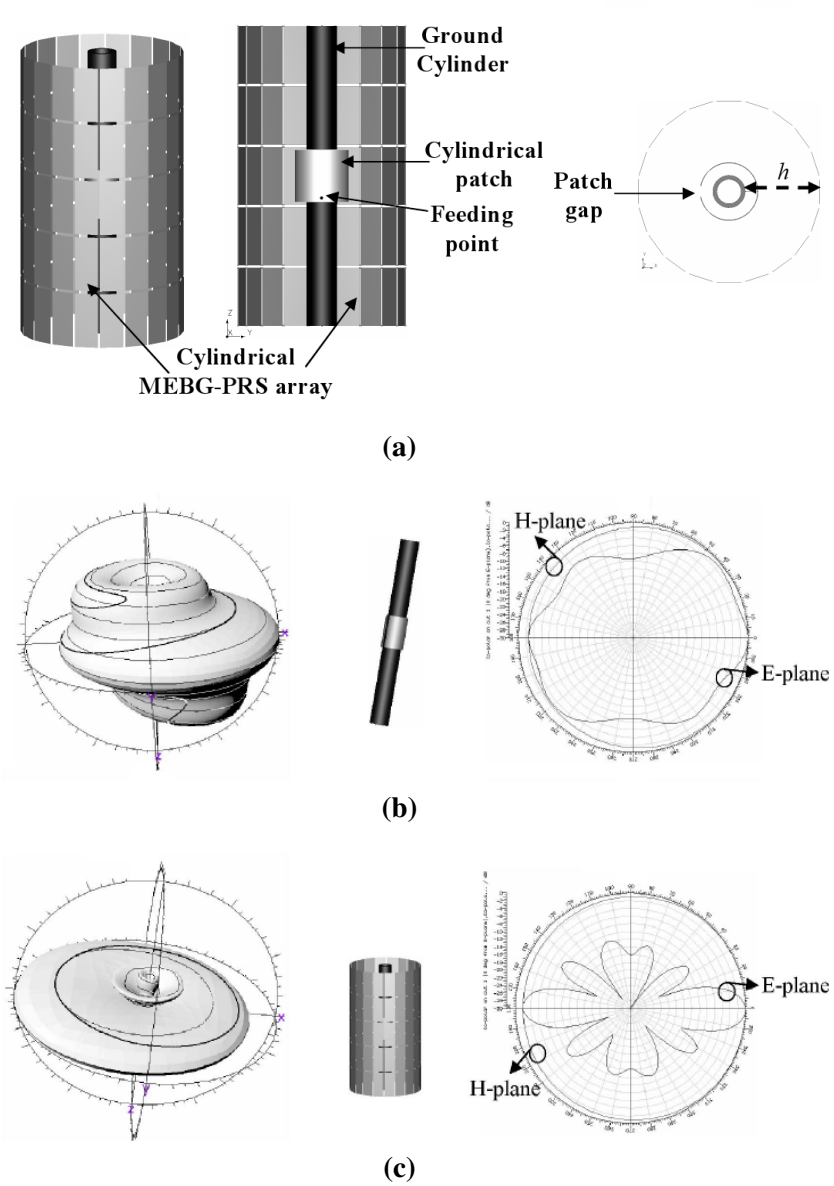

Figure 1.8: *Metallic patches Cylindrical EBG antennas feed by a cylindrical patch[30]: a) antenna structure ; b) normalized radiation patterns on principal planes without the EBG structures; c) normalized radiation patterns on principal planes with the EBG structures.*

presenting omnidirectional radiation patterns on the azimuthal plane [32] with a vertical polarization, figure 1.9: as in the previous case, E-plane directivity is improved by the resonating field within the CEBG structure, figure 1.9b. The concept has been extended in [33] to design dual-polarized EBG antennas, figure 1.10: an EBG structure made with metallic rings is superimposed to the metallic wires EBG structure. The metallic rings EBG structure presents a horizontal polarized omnidirectional pattern on the azimuthal plane and the superimposed structure presents dual polarization capabilities.

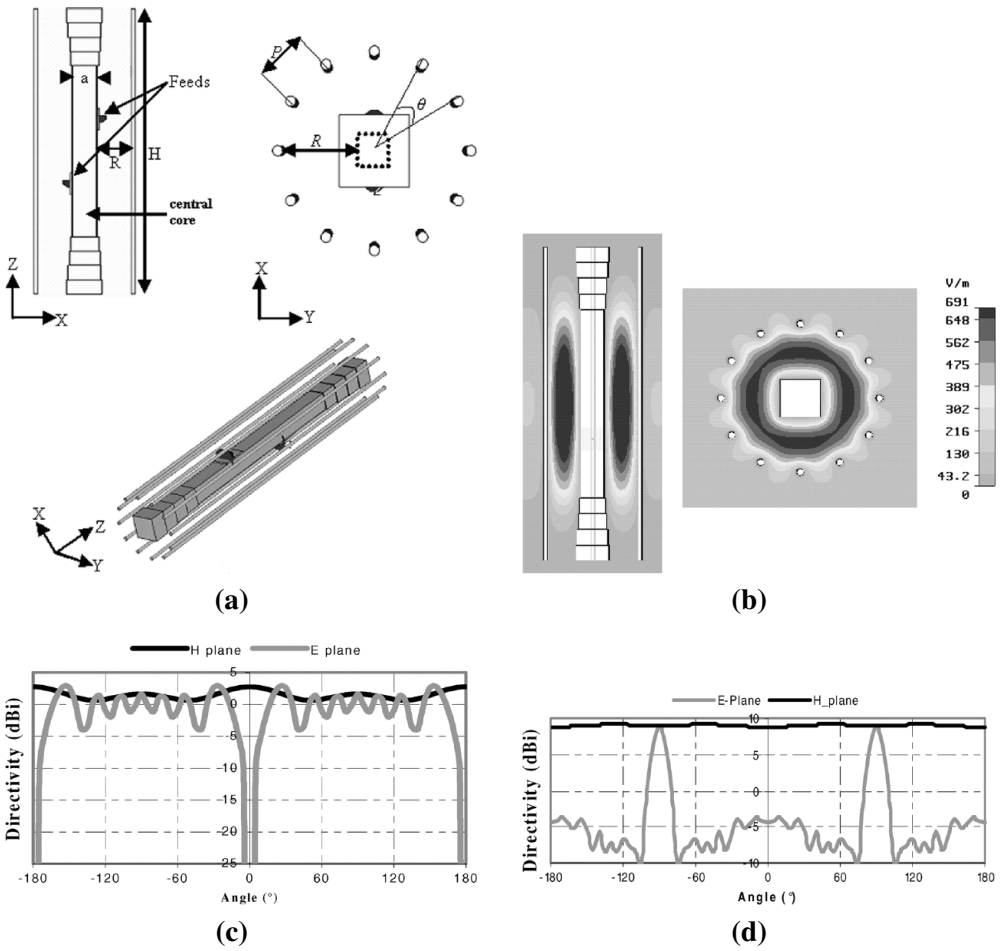

Figure 1.9: *Metallic wires Cylindrical EBG antenna [32]: a) antenna structure; b) electric field distribution; c) radiation patterns without the EBG structure; d) radiation patterns with the EBG structure.*

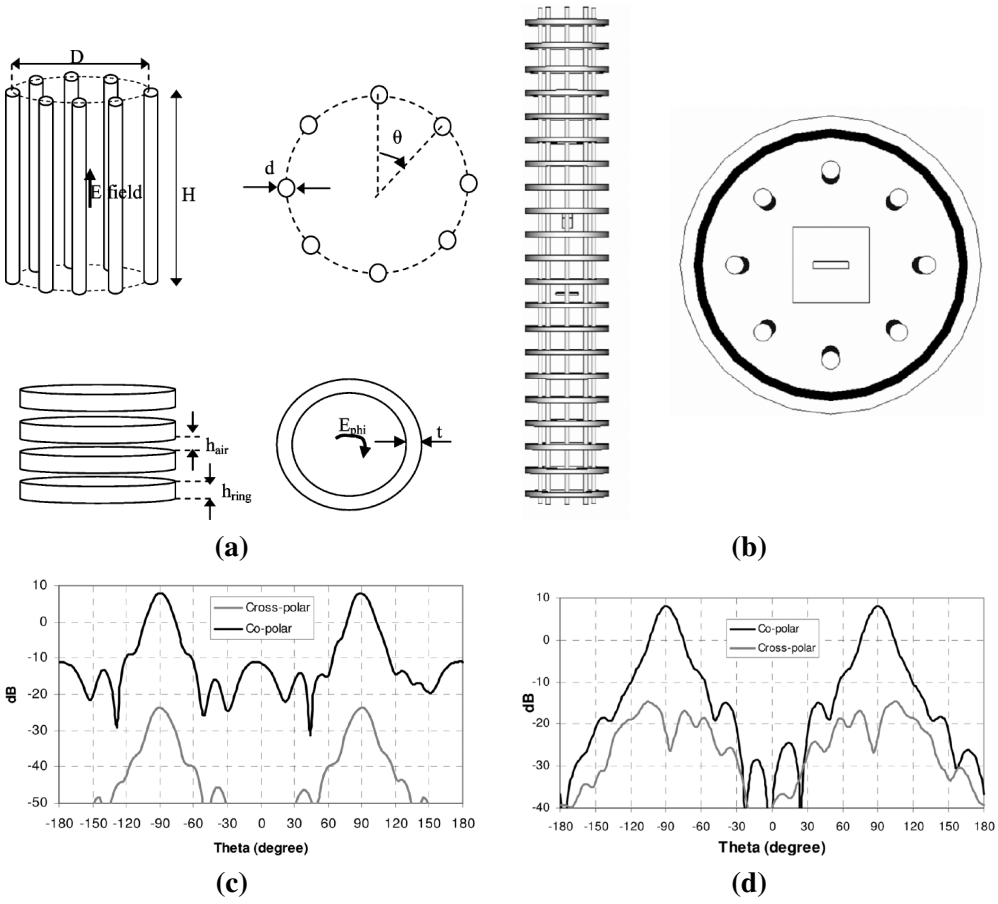

Figure 1.10: *Dual polarized metallic Cylindrical EBG antenna [33]: a) metallic wires and metallic rings EBG structures; b) superimposed structure; c) vertical polarization radiation patterns; d) horizontal polarization radiation patterns.*

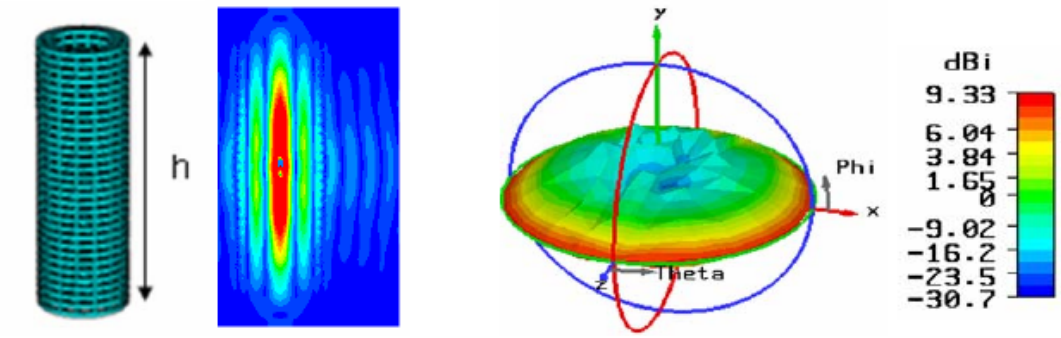

Figure 1.11: *Electric field distribution and 3-D radiation pattern of a dielectric woodpile CEBG structure excited in the middle[17].*

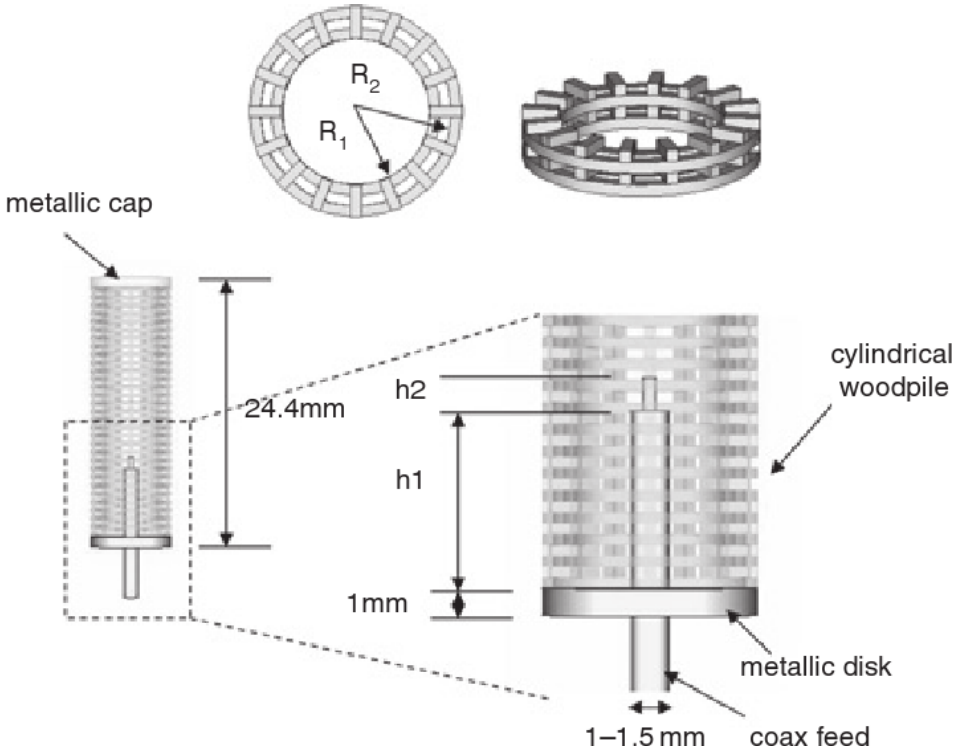

Figure 1.12: *Dielectric woodpile CEBG antenna[34].*

Dielectric cylindrical woodpile CEBG structures have been investigated by Lee et al [17, 34–36] and it has been found that the resonant frequencies of the cylindrical woodpile cavity are similar to those of conventional metallic cavities and, as for metallic CEBG, a narrow beam along the elevation plane is created by the resonating fields within the cavity, figure 1.11. A prototype realized with a monopole antenna enclosed in a dielectric woodpile CEBG structure, figure 1.12, achieved a directive pattern on the E-plane and omnidirectional on the azimuthal plane with 5dBi gain at 94.2GHz [34].

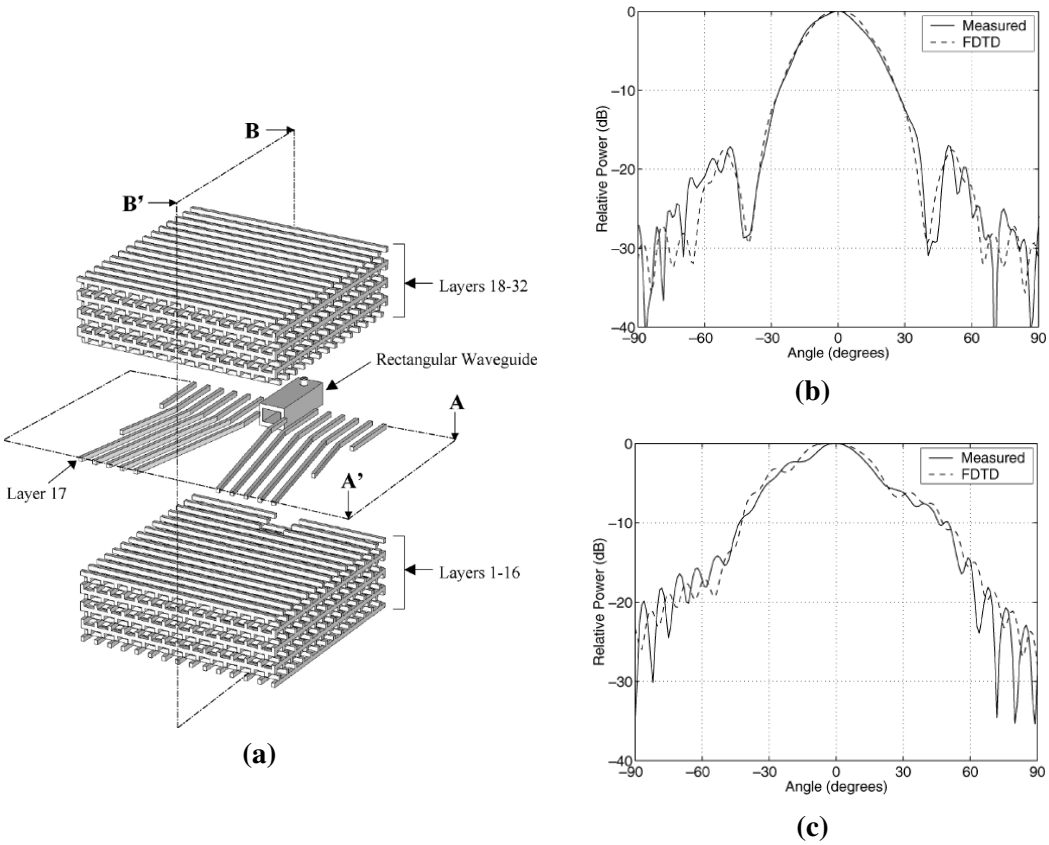

Figure 1.13: *Dielectric woodpile EBG horn antenna [39]: a) antenna structure; b) H-plane radiation pattern at 13GHz; b) E-plane radiation pattern at 13GHz.*

1.1.2 EBG antennas with defects

Defects in the EBG structure can be used to direct the flow of electromagnetic energy [37–40] or to create resonating structures at frequencies within the bandgap [41, 37]. In [38] a sectoral horn antenna based on the electromagnetic confinement mechanism of a woodpile dielectric structure has been presented. The horn antenna side walls are created by flaring apart the rods of one specific layer and it is fed by a defect waveguide created by removing a single rod from the woodpile structure, figure 1.13; the achieved bandwidth is within the structure bandgap frequencies with the typical sectorial horn radiation patterns. Khromova et al [42] extended the concept to create a pyramidal horn antenna with symmetrical radiation patterns on both H-plane and E-plane achieving a 16.35dBi gain and 10% impedance bandwidth in the frequency region of 107GHz, figure 1.14.

Temelkuran et al. [41, 37] presented a monopole antenna surrounded by planar woodpile structure in which a planar defect was formed by separating two layers of the structure to create an asymmetric structure with a planar cavity. The planar defect and the asymmetric positioning of the enclosed monopole achieved a very directional beam in both planes. Similar results were achieved in [40] where a monopole antenna was placed inside a cavity created by removing one dielectric rod from a woodpile EBG structure,

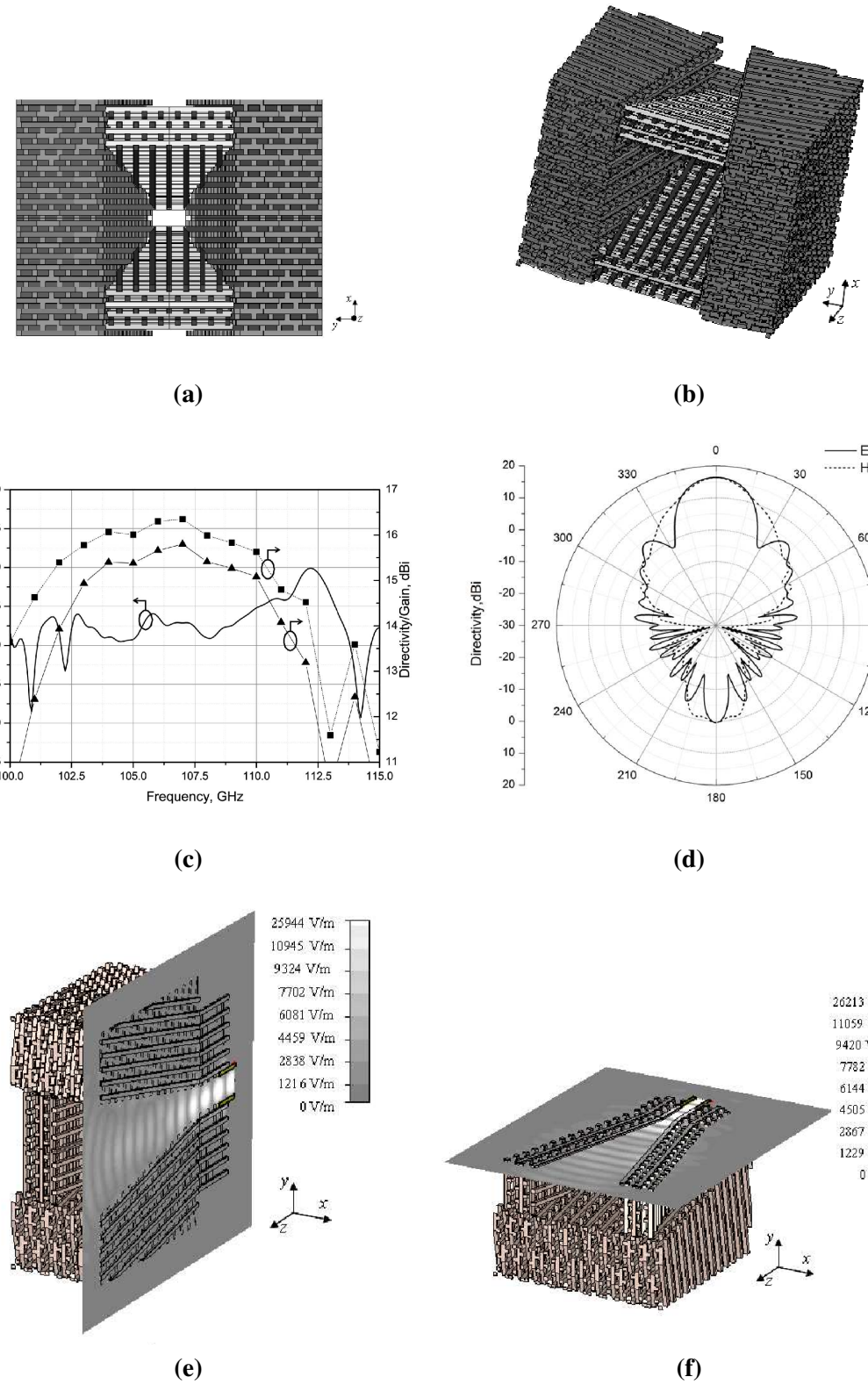

Figure 1.14: *Dielectric woodpile pyramidal EBG horn antenna [42]: a) front view; b) 3-D view; c) input reflection coefficient (black solid curve), peak directivity value (dashed curve with black squares) and peak gain (solid curve with black triangles); d) radiation pattern at 107 GHz; e) electric field magnitude in H-plane cross-sections at 107GHz; f) electric field magnitude in E-plane cross-sections at 107GHz.*

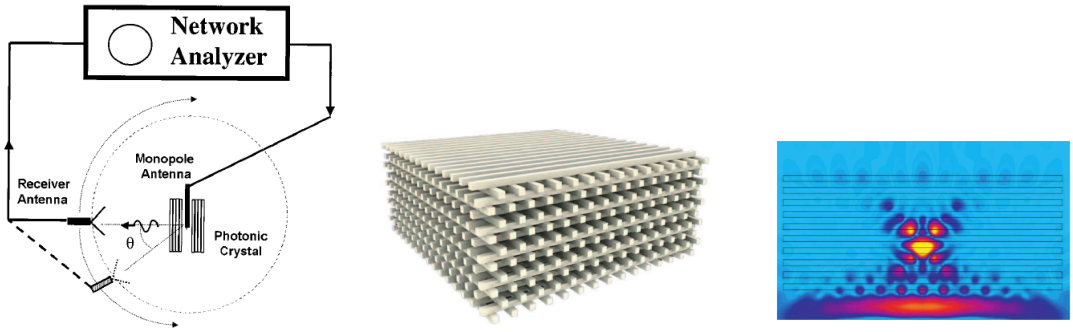

(a) **(b)** **(c)**

Figure 1.15: *a) Dielectric woodpile EBG antenna with planar asymmetric defect [41]; b) dielectric woodpile EBG structure; c) field distribution escited by a monopole buried within a cavity created by removing one rod.*

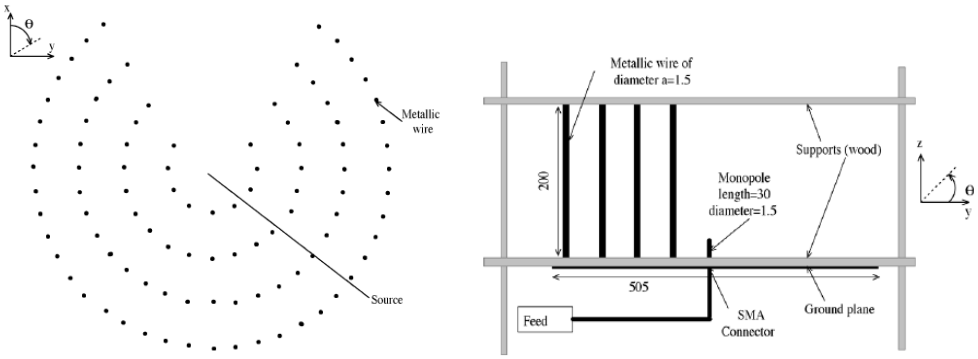

(a) **(b)**

Figure 1.16: *a) Metallic rods cylindrical EBG structure with angular defect [45]; b) Metallic rods cylindrical EBG antenna with angular defect window [45].*

figure 1.15.

Boutayeb et al [43–45] presented antennas in which metallic rods elliptical and cylindrical EBG structures with an angular defect window improved the directivity of the enclosed feed, figure 1.16. The excited fields in the open cavity are redirected toward the angular defect window creating a directive radiation pattern in that privileged direction, figure 1.17

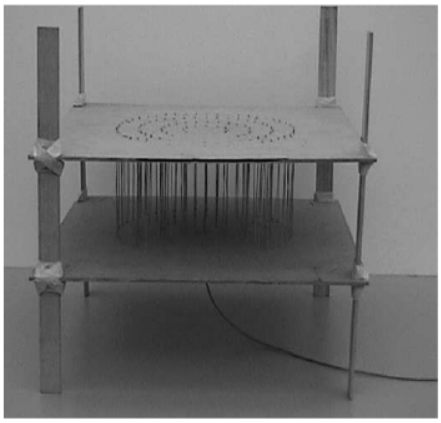

(a)

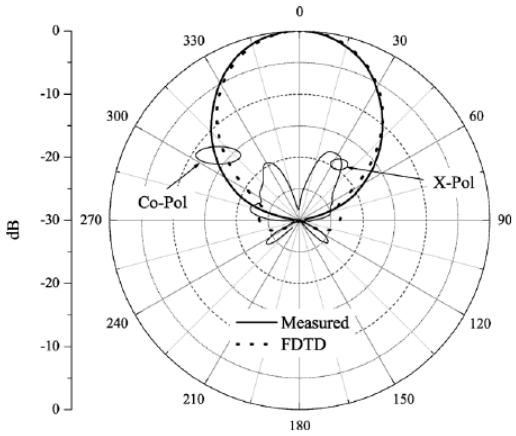

(b)

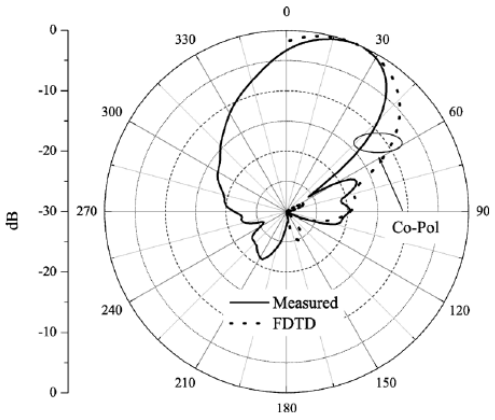

(c)

Figure 1.17: *Metallic rods cylindrical EBG antennawith angular defect window [45]: a) prototype; b) H-plane directivity pattern; c) E-plane directivity pattern.*

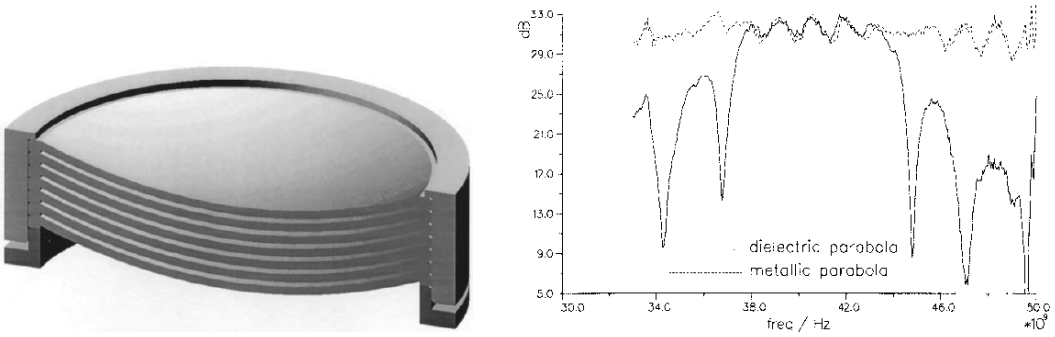

(a) **(b)**

Figure 1.18: *EBG parabolic reflector a) prototype; b) measured gain.*

1.1.3 EBG reflectors antennas

Two-dimensional and three-dimensional EBG materials have been used as all-dielectric reflector for a dipole antenna [46, 47]; at frequency within the bandgap, the structures were found equivalent to an effective reflection plane buried within the material. A parabolic reflector [8] built with seven dielectric dishes separated by a slab of air was found as good as a classic metallic reflector at frequency within the bandgap, figure 1.18.

The frequency dependent reflection phase of FSSs have also found several applications [4, 21, 48–53]. Figure 1.19a,b shows the reflection phase of a double-layer mushroom FSS [4] and of a uni-planar FSS based on square patches [21]: in both cases, it is clearly visible a frequency point at which the phase reflection is 0° and the FSS therefore mimics the behaviour of a magnetic conductor, ie synthesizing an artificial magnetic conductor (AMC). The 0° reflection phase of AMCs can be used to reduce antennas profile: if we replace a PEC ground plane with a PMC ground plane (synthesised by an AMC), a parallel dipole could be placed right on top of the PMC rather than at the usual $\lambda/4$ distance, figure 1.19c; a PRS, usually placed at a distance $h = \lambda/2$, could be placed at half the distance, ie $h = \lambda/4$ [21], figure 1.19d.

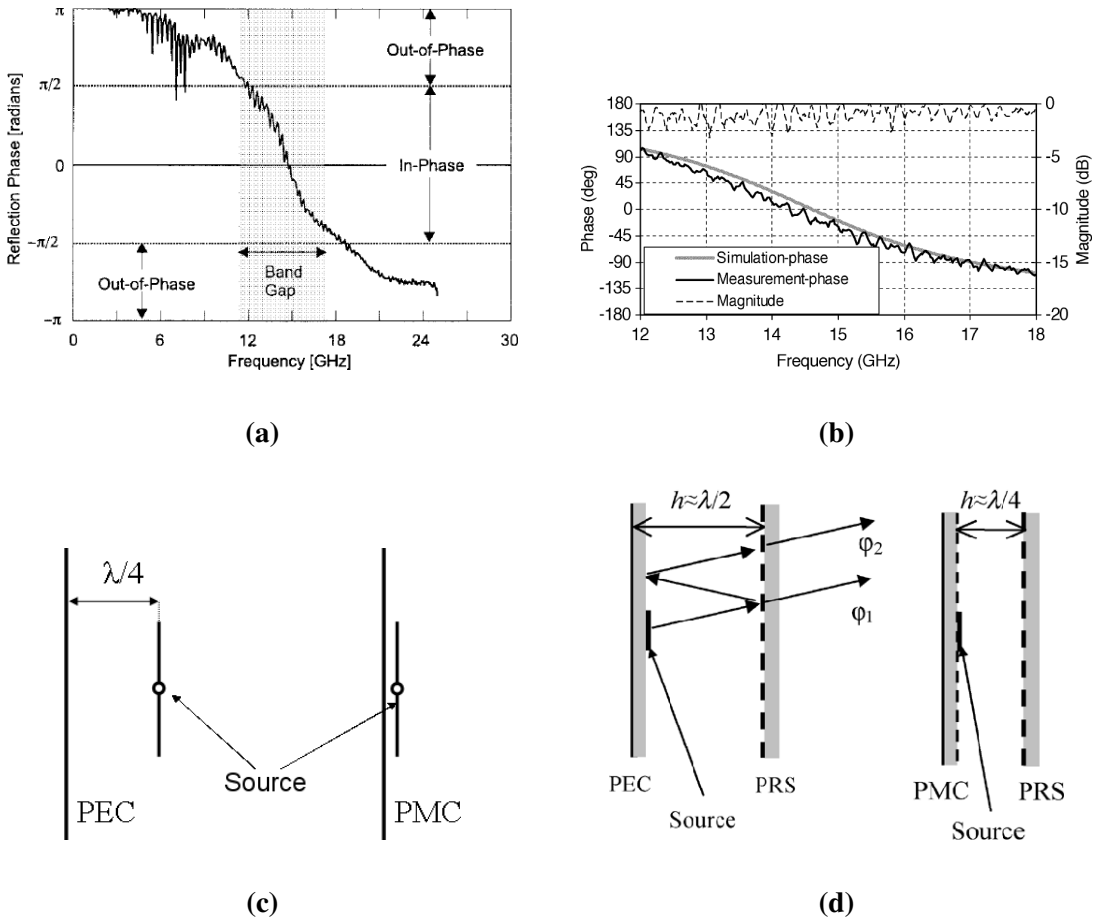

Figure 1.19: *a) Reflection phase of a double-layer mushroom FSS [4]; b) Reflection phase of a uni-planar FSS based on square patches [21]; c) Parallel dipole placed on top of a PEC or PMC ground plane; d) PRS placed at a reduced distance from the PMC ground plane [21].*

1.1.4 Various applications of EBG structures

The bandgap behaviour of uni-planar, "mushroom" and different EBG crystals geometries has been also used to improve antennas performances. A source antenna is usually surrounded by an EBG structure [54–62], figure 1.20a-b, or placed on top of an EBG ground plane [63, 64], figure 1.20c-d, in order to block the propagation of surface waves as well as to modify the configuration of the excited near fields to increase the bandwidth, the realized gain and to reduce radiation patterns side lobes level, figure 1.21. Similar results were obtained using EBG substrates made by drilling holes in a high dielectric constant material [65–68].

EBG structures with multiple sources have been also investigated. Weily et al analyzed fixed beam and scanning beam linear arrays of woodpile EBG sectoral horn antennas [39] as an extension of the structure presented in [38]. In [69–71] a cylindrical array of EBG sectoral antennas separated by metallic walls was presented, achieving high decoupling between adjacent sectors and multibeam capabilities by feeding one sector at a time, figure 1.22. A multifed sectoral EBG antenna was presented in [72, 73], where four patches antennas enclosed in a metallic EBG structure based on Babinet's principle[2], achieved a very narrow 3-dB aperture angle in the E-plane.

Planar EBG stuctures can be used to reduce the mutual coupling in arrays and multiple-feed antennas [75–80]. The EBG structure is usually placed between feeding sources increasing the decoupling between close-spaced sources, figure 1.23.

[2]Babinet's priciple in optics states that *when the field behind a screen with an opening is added to the field of a complementary structure, the sum is equal to the field when there is no screen* [74].

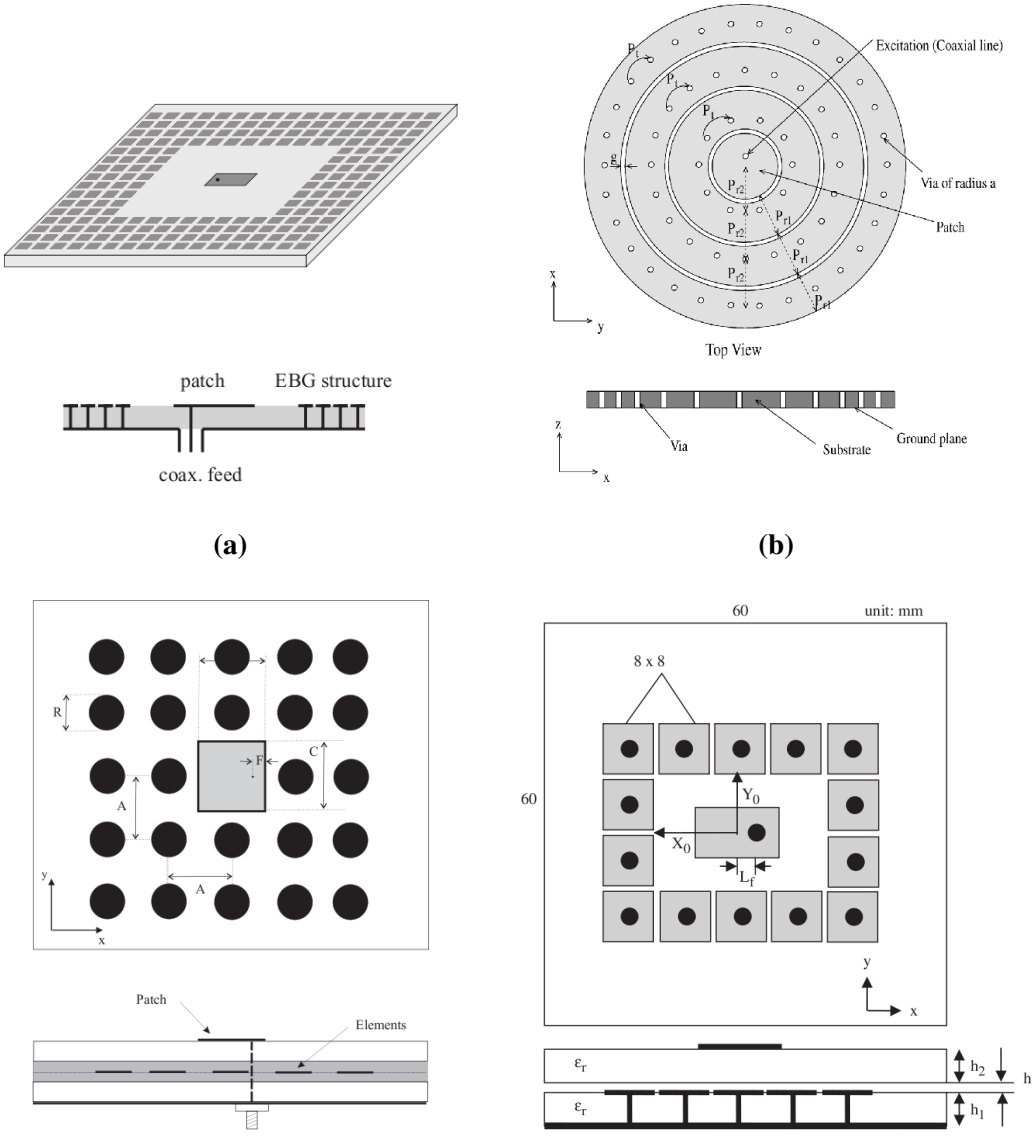

Figure 1.20: *a) Patch antenna surrounded by a mushroom-like EBG structure [55]; b) circular patch antenna with cylindrical musroom-like EBG crystal composed of metal rings and vertical vias [61]; c) Multilayer microstrip patch antenna surrounded by EBG circular elements [64]; d) dual-layer patch antenna with mushroom-like EBG ground plane [63].*

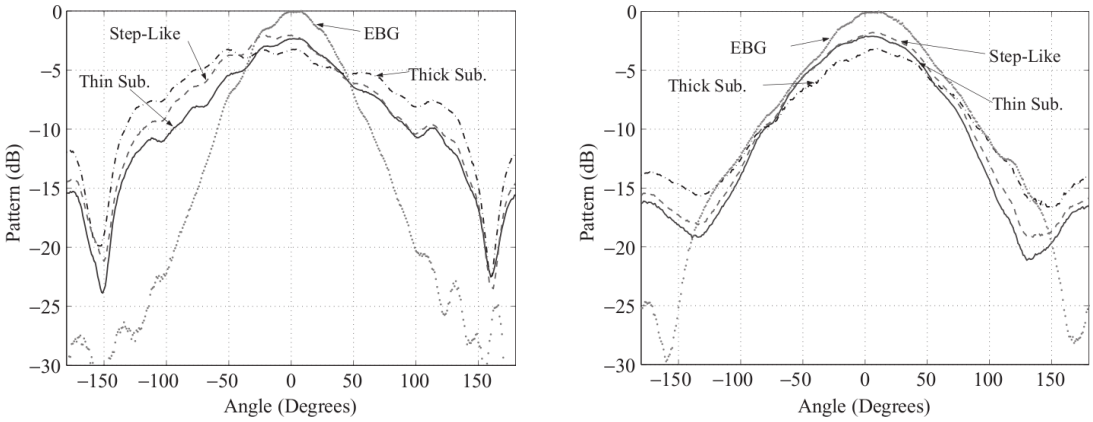

(a) **(b)**

Figure 1.21: *Patch antenna surrounded by a mushroom-like EBG structure radiation patterns [55]: a) E-plane; b) H-plane.*

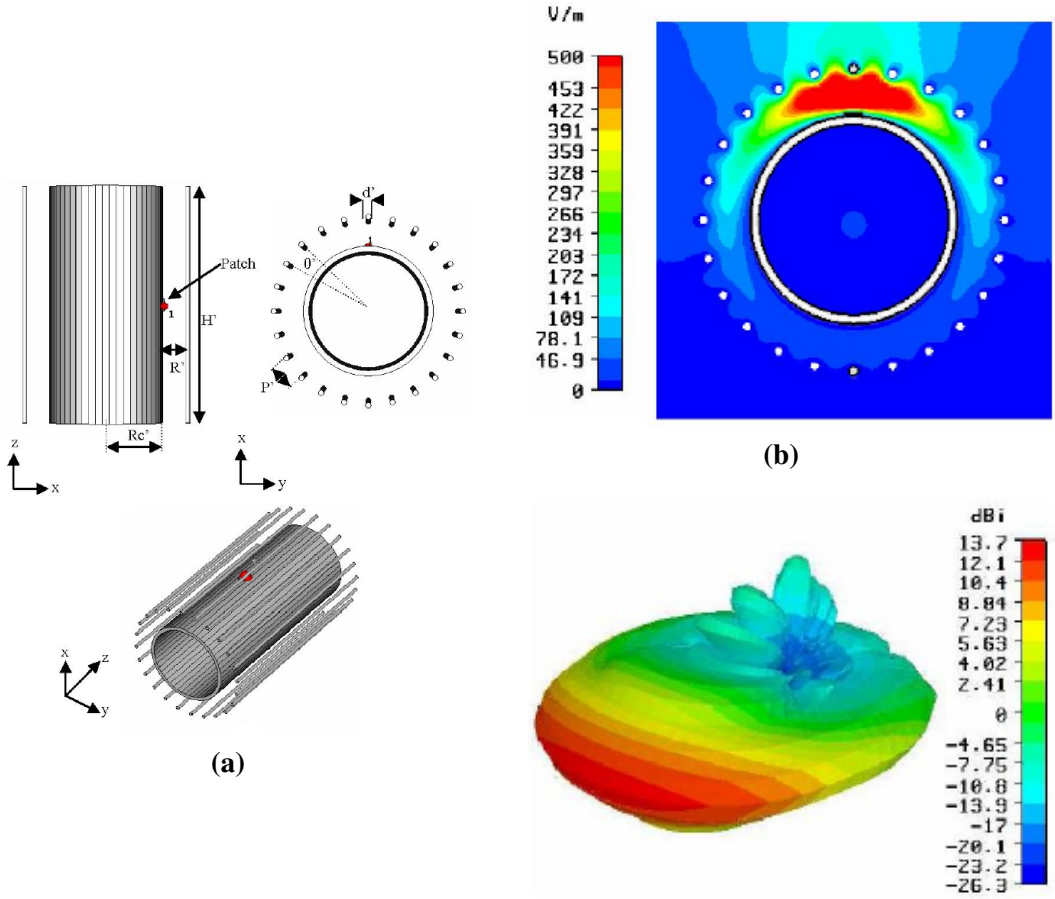

(a)

(b)

(c)

Figure 1.22: *Multibeam EBG antenna [69]: a) prototype; b) electric field distribution; c) radiation pattern.*

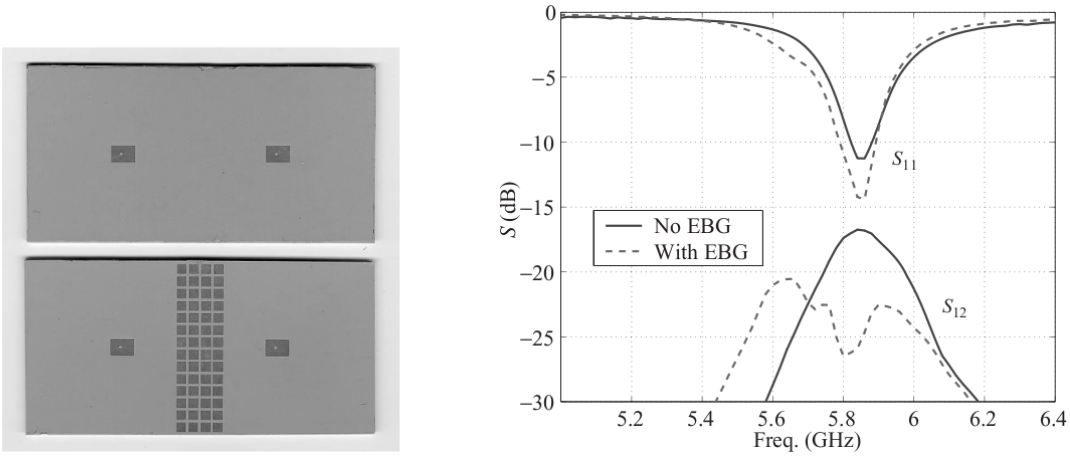

(a)

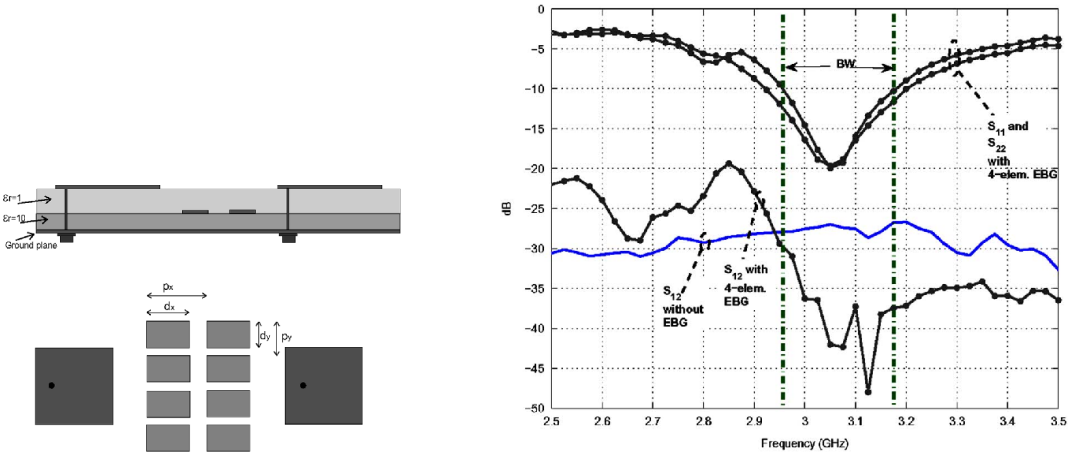

(b)

Figure 1.23: *a) Microstrip antennas with and without the EBG mushroom-like structure: geometries (left) and measured results (right) [75]; b) Array of two patches in a multilayer dielectric substrate including a planar EBG structure: geometry (left) and measured results (right) [79].*

1.2 Scope of this work

Most of the applications of three-dimensional EBG structures for enhancing antennas directivity mainly rely on resonating structures [7–10, 12–18, 28–34, 36] or embedded sources [41, 37]. These structures can usually achieve high gain at their resonant frequency, but performance usually decays quite rapidly when moving away from the resonant condition; therefore the operational bandwidth is usually limited to circa 6%.

There are just a few examples in literature of three-dimensional EBG structures realised with defects [37–40, 42], open cavities [43–45] or to act as reflectors[46, 47, 8]. Since these are non-resonating structures, they present a lower gain but a wider frequency range of operation, theoretically up to the bandgap frequency range of the deployed EBG crystal.

The scope of this work is to investigate novel dielectric three-dimensional EBG antenna structures realised with multilayer structures presenting an angular defect window or realised with corner reflectors. Design process main goals are the realization of:

- simple EBG structures based on 2-D crystals;
- high gain and high front-to-back-ratio on a privileged direction on the azimuthal plane;
- a wide impedance bandwidth with stable radiation patterns within.

In this work, the front-to-back-ratio (FTBR) is defined as the ratio, expressed in dB, between the gain realised in the defect window or corner aperture axis direction and the gain realised in the opposite direction.

To the author's knowledge, multilayer with an angular defect window and corner reflector dielectric EBG structures have not been studied before. Other than investigating novel EBG antenna structures, the author wanted to demonstrate that the presented structures can achieve competitive performance to those achieved by more complex structures.

In this dissertation the design steps, simulations and measurements results of single feed and multiple feed EBG antennas based on the above requirements are presented.

Single-feed antennas were realized by placing a monopole feed either inside an open cavity presenting an angular defect window or in front of a corner reflector; both open cavity and reflector were assembled using dielectric rods of circular section arranged in a 2-D crystal placed above a ground plane. Multi-feed antennas were realized by modifying single feed structures in order to host multiple feeds while preserving a functional EBG structure.

The *monopole feed with an EBG structure placed above a ground plane* configuration was chosen for the following reasons:

- monopole feeds are easy to realize and interface with a feeding coaxial cable;
- ground plane offers mechanical support to the EBG structure;
- dipole feed configurations, although may present a larger number of applications, are more difficult to realize; however, their radiative properties can be easily extrapoleted by monopole feed configuration counterparts.

2-D crystals based on dielectric rods were chosen to build the EBG structures especially for:

- easy of realization;
- cost effective: ceramic materials can be expensive and complicated "made to order" 3-D structures could be very expensive;
- monopole (as well as dipole) feeds excite an electromagnetic field configuration with a dominant electric field axial component, hence a 2-D crystal EBG structure may suffice;
- 2-D crystals realized with dielectric rods (immersed in a dielectric background) may present large TM bandgaps [2] and therefore are very appropriate for this particular application.
- dielectric rods can be manufactured using low loss ceramic materials: for high frequency applications ($\geq$100GHz) this would be an advantage compared to metallic structures which could present prohibitive loss and/or very low efficiency;
- an EBG crystal based on dielectric rods could be micromachined and integrated using for example LTCC (Low Temperature Co-fired Ceramic) technologies.

The investigated single-feed and multiple-feed dielectric EBG antennas were realized with dielectric rods arranged in cylindrical, triangular and square lattices. The first set of simulations and measurements was focused to extend the approach of Boutayeb et al [43–45] on metallic CEBG structures to dielectric CEBG structures. The analyzed cylindrical lattice was created by periodically arranging dielectric rods along the radial and the transverse directions of a multilayer cylindrical lattice. Dielecric CEBG antennas were created by introducing an angular defect window in the EBG structure.

Similar structures based on a multilayer triangular lattice were then analyzed and compared to CEBG structures and found able to achieve better performance. Multiple-feed structures were also investigated demonstrating the ability to rotate the radiation patterns of discrete angular steps.

90° dielectric corner EBG antennas based on a square lattice were designed and analyzed along with a cross-shaped multiple-feed antenna. 60° and 120° dielectric corner

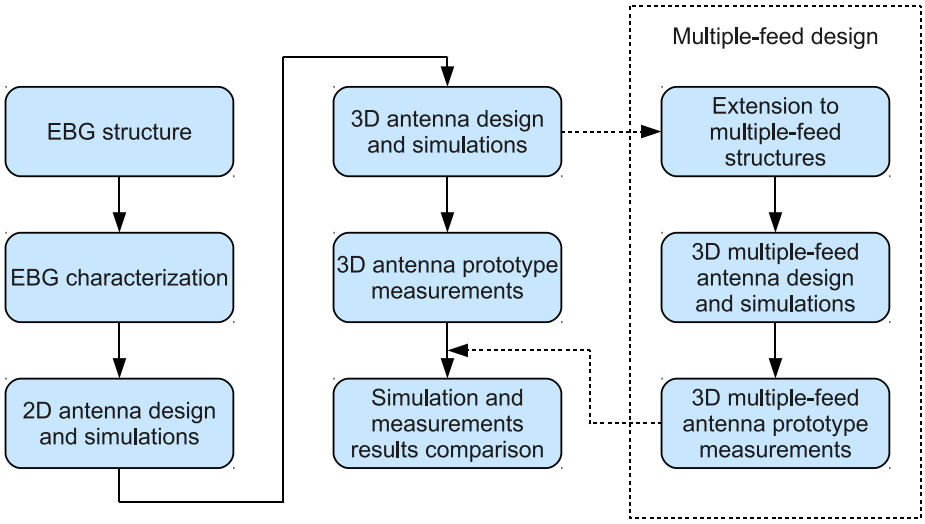

Figure 1.24: *Methodological approach.*

EBG antennas (based on a triangular lattice) were then investigated and compared to the 90° dielectric corner EBG antenna.

Antennas have been designed to operate in the X-band frequency range, 8.2GHz-12.4GHz, to take advantage of the in-house available equipment, Appendix C. The design concepts though, can be easily extended to higher or lower frequencies simply by respectively scaling down or up the geometrical dimensions (with the exception of the water CEBG antennas, Section 2.2, where the dispersive nature of water must be taken into account).

1.3 Methodological approach

The methodological approach of this work is summarised in figure 1.24, in particular:

EBG structure: whether a multilayer with an angular defect window or a corner reflector EBG structure along with a cylindrical, triangular or square lattice.

EBG characterization: the EBG lattice was characterized through simulations using either a Finite-Difference Time-Domain (FDTD) solver, Appendix A, or a plane-wave eigensolver, Appendix B, according to the lattice geometry. Simulation results were then collected and analyzed to identify the most promising sets of geometrical parameters and rods dielectric permittivity in terms of bandgaps position and extension.

2-D antenna design and simulations: 2-D antennas were simulated using the sets identified in the previous step. Simulation results would give a first insight on the radiative performance of the selected combinations of geometrical and material parameters, identifying in turn the best candidates to design 3-D antennas.

3-D antenna design and simulations: using the output of the previous steps, 3-D antennas would be designed and simulated. The general assumption is that the 3-D structures made with finite length dielectric rods and the fields excited by the monopole feed are a good approximation of the ideal 2-D case, where rods and the feeding current line source have infinite extension. 3-D antennas were simulated using the FDTD solver, extracting S_{11} response, input impedance, near-field distribution, far-fields radiation patterns, etc.

3-D antenna prototype measurements: A set of geometrical and material properties would be then selected to build a prototype in order to validate the design process and assumptions. As already mentioned, prototypes were build by arranging dielectric rods on top of a ground plane. Measurements were made using the available in-house facilities, Appendix C.

Simulation and measurements results comparison: finally, simulations and measurements results would be compared and analyzed.

Multiple-feed design: triangular and square lattices present a high degree of symmetry and the structures analyzed in the previous steps could be modified to host multiple feeds and, at the same time, still be functional for each feed. The main way to achieve the aforementioned requirements is to copy and rotate, along the lattice vectors, the base structure and remove dieletric rods whenever superimposed to a monopole feed. Once suitable multi-feed structures were found, similar design steps used for single-feed antennas design and characterization would be followed. Ansoft HFSS was used to simulate multiple-feed structures: the Finite-Element-Method (FEM) used by HFSS can solve multiple port structures in one run, while the in-house developed FDTD solver would need multiple runs. The FDTD solver was prefered to HFSS for characterizing single-feed structures mainly for two reasons:

1. the first set of simulations and measurements were made using water as dielectric material to build the EBG structures. The in-house available version of HFSS could not handle the dispersive properties of water whilst the FDTD solver could easily do it.
2. the FDTD solver can produce wideband results in one run; HFSS would require a much longer computational time to produce wideband not-interpolated results.

1.4 Chapter contents

The content of the following chapters can be summarised as follows:

Chapter 2 - Multilayer cylindrical lattice EBG antennas - Multilayer dielectric CEBG antennas are presented and analysed. FDTD simulations and measurements results are then compared and discussed.

Chapter 3 - Multilayer triangular lattice EBG antennas - Multilayer dielectric TEBG antennas are presented and analysed following the approach used in the previous chapter. In addition to FDTD simulations, a plane-wave eigensolver is also used to characterize the EBG structure. Multiple feed structures are also presented and analysed.

Chapter 4 - Dielectric EBG corner reflector antennas - In this chapter, corner antennas realized with dielectric EBG structures are introduced. A 90° corner realized using a square lattice of dielectric rods is presented and analysed. A multiple feed structure is also presented and analyzed. Finally, 60° and 120° EBG corner antennas based on a triangular lattice are analyzed and compared to the 90° EBG corner antenna.

Chapter 5 - Discussion and Conclusion - The main results presented in this work are summarised, analysed and discussed.

Appendix A - The Finite-Difference Time-Domain algorithm - The FDTD algorithm and its main capabilities are briefly introduced. Most of the simulation results presented in this work have been produced by an FDTD solver realized with Matlab. The solver has been developed for maximum freedom in handling the simulated dielectric properties of the material such as the lossy and dispersive materials reported in Chapter 2.

Appendix B - The Plane-Wave Eigensolver - A plane-wave eigensolver has been developed in Matlab to calculate the electromagnenetic bandgap structures of 2-D lattices based on triangular or square geometries. Althought we focused our attention on dielectric rods embedded in air, the plain-wave eigensolver can handle any unit cell dielectric distribution.

Appendix C - Antenna measurements setup - The in-house equipment and facilities are presented along with the experiments setup used to measure the scattering parameters, gain and radiation patterns of the prototypes.

Chapter 2 – Multilayer cylindrical lattice EBG antennas

2.1 Introduction

Boutayeb et al [43–45] presented and analyzed antennas in which a metallic rods cylindrical EBG (CEBG) structure with an angular defect window is used to improve the directivity of the enclosed monopole feed. The antenna is designed to operate at frequencies for which the CEBG structure presents a bandgap in order to achieve a directive radiation pattern in the angular window direction, Section 1.1.

We extended this concept to CEBG antennas made with dielectric rods. At first water was used as dielectric rods material in order to facilitate prototype creation and modification. Dispersive and lossy electrical properties of water have been taken into account in the simulations. Water, for obvious reason, is not the best material for building antennas, but its high dielectric permittivity at 10GHz allowed us to create cylindrical structures with frequency bandgaps. Water prototypes also allowed us to validate our design with little expense.

Once simulations and measurements validated our approach, we ordered a set of ceramic rods from Morgan Electroceramics [81] to build and test prototypes made with more conventional materials, ie low loss ceramics designed for high frequency applications.

The methodological approach used to design and characterize multilayer CEBG antennas has been described in Section 1.3; it can be summarised as follow:

- a 4 layers two-dimensional CEBG structure is parametrically studied as a function of geometrical parameters;
- the results are collected in gapmaps to easily visualize the dependancy of bangaps position and extension on the geometrical parameters;
- suitable combinations of geometrical parameters are used to design and parametrically study three-dimensional CEBG antennas;
- prototypes are then built using the results of the previous steps;
- measurements and simulations are finally compared to validate the design approach.

In the next sections the design steps, simulation and measurements results of multilayer CEBG antennas made with water and then ceramic materials will be presented, analysed and discussed.

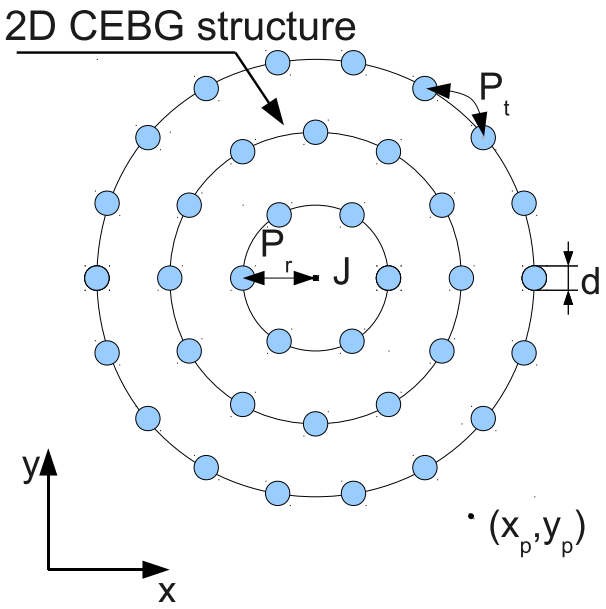

Figure 2.1: *2D Cylindrical EBG structure.*

2.1.1 Cylindrical EBG Structure

The 2D CEBG structure, figure 2.1, is composed by infinite long dielectric rods arranged in a simple multilayer cylindrical geometry. Layers are periodically spaced by P_r, the radial period, whilst dielectric rods are periodically spaced on each layer by P_t, the transverse period. The n-th layer radius and number of rods are respectively equal to $n \cdot P_r$ and $n \cdot N_1$, where N_1 is the first layer number of rods. Transverse period P_t, radial period P_r and first layer number of rods N_1 are related by:

$$P_t = \frac{2\pi n P_r}{n N_1} = \frac{2\pi P_r}{N_1} \tag{2.1}$$

where n represents the n-th layer. The structure is fed by an infinite long current line source (J) placed in the axis which excites a TM cylindrical wave.

The characterization of this structure is based on the transmission coefficient T, extracted by normalizing the transverse electric field $E(x_p, y_p)|_{CEBG}$ recorded when the CEBG structure is present with the transverse electric field $E(x_p, y_p)|_0$ recorded when the CEBG structure is not present:

$$T = \frac{E(x_p, y_p)|_{CEBG}}{E(x_p, y_p)|_0} \tag{2.2}$$

Bandgap position and extension are functions of the above mentioned geometrical parameters, rods permittivity ε_r and radius r.

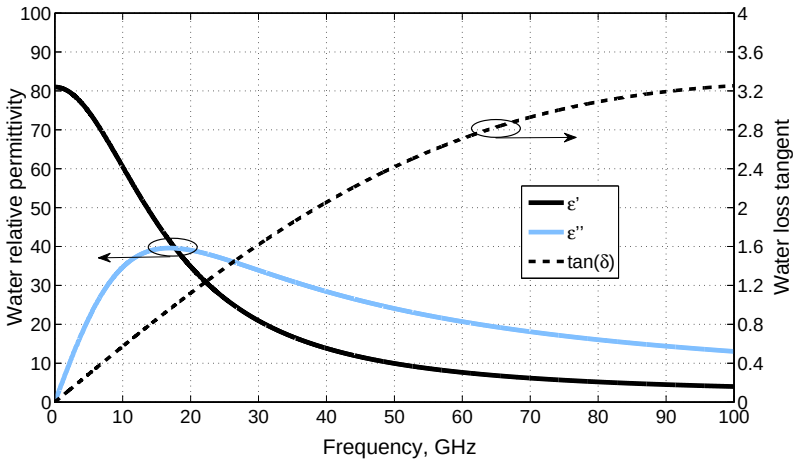

Figure 2.2: *Water relative permittivity and loss tangent as a function of frequency.*

2.2 CEBG antenna realized with water

2.2.1 Dielectric properties of water

As already mentioned, water is not the most attractive material to build dielectric structures for antennas for many reasons, including its lossy and dispersive characteristics. The relative dielectric permittivity of water is a complex function of frequency and can be expressed using the Debye equation:

$$\varepsilon(\omega) = \varepsilon' - j\varepsilon'' = \varepsilon_\infty + \frac{\varepsilon_S - \varepsilon_\infty}{1 + j\omega t_0} \tag{2.3}$$

$$tan(\delta) = \frac{\varepsilon''}{\varepsilon'} \tag{2.4}$$

where ε_∞ is the infinity frequency permittivity, ε_S is the zero frequency permittivity, t_0 is the relaxation time and $tan(\delta)$ is the dielectric loss tangent. Typical values of these parameters are $\varepsilon_\infty = 81$, $\varepsilon_S = 1.8$ and $t_0 = 9.4 \times 10^{-12} s$ [82]. Water complex permittivity and dielectric loss tangent as a function of frequency are shown in figure 2.2.

2.2.2 CEBG design

A 4 layers structure was parametrically studied as a function of radial period P_r, first layer number of rods N_1 and rods radius r, setting the separation between stopband and passband by T=-20dB. Water dispersive and lossy characteristics were included in the FDTD simulations. Results are shown in figure 2.3-2.5, where T is depicted in several gapmaps to show how the bandgap is influenced by the above-mentioned parameters. For each parameter 2 series of gapmaps are shown; in each series a second parameter is kept constant whilst the third one is varied; X-band limits have been superimposed on the gapmaps as reference.

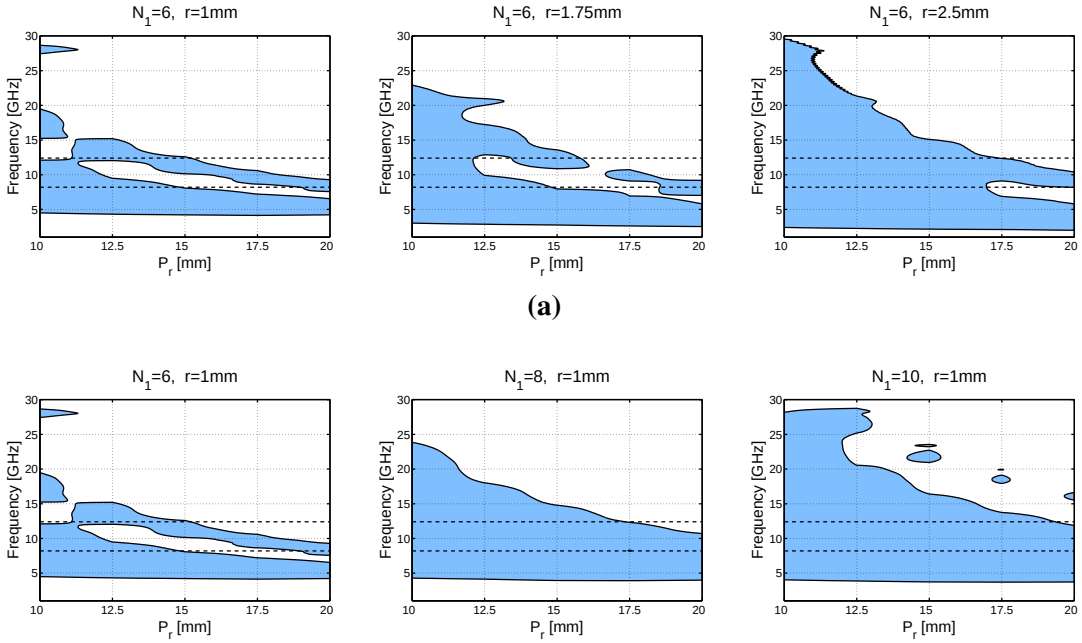

Figure 2.3: *Gapmaps - in blue is where the simulated transmission coefficient is lower than -20dB, dashed lines represent the X-band limits: a) as a function of P_r and r; b) as a function of P_r and N_1.*

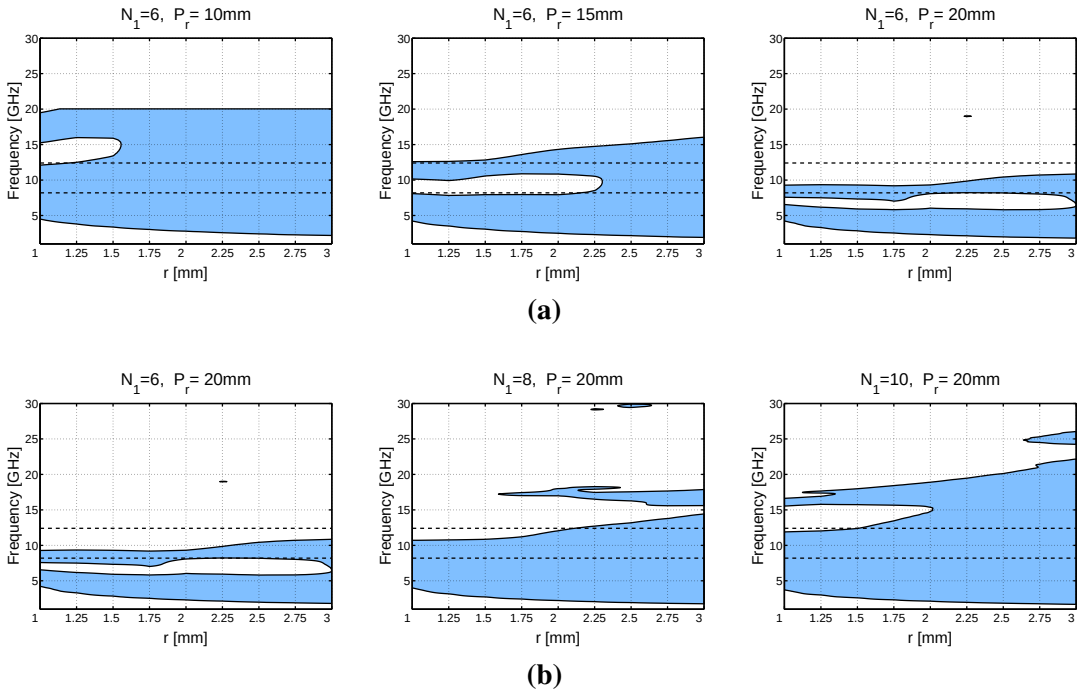

Figure 2.4: *Gapmaps - in blue is where the simulated transmission coefficient is lower than -20dB: a) as a function of P_r and r; b) as a function of P_r and N_1.*

In figure 2.3 the radial period is kept constant and the influence of r and N_1 are shown respectively in figure 2.3a and figure 2.3b; both show that increasing r or N_1 generally enlarges the bandgap, and with higher N_1 new bandgaps appear at high frequencies. Bandgap position generally decreases as P_r increases.

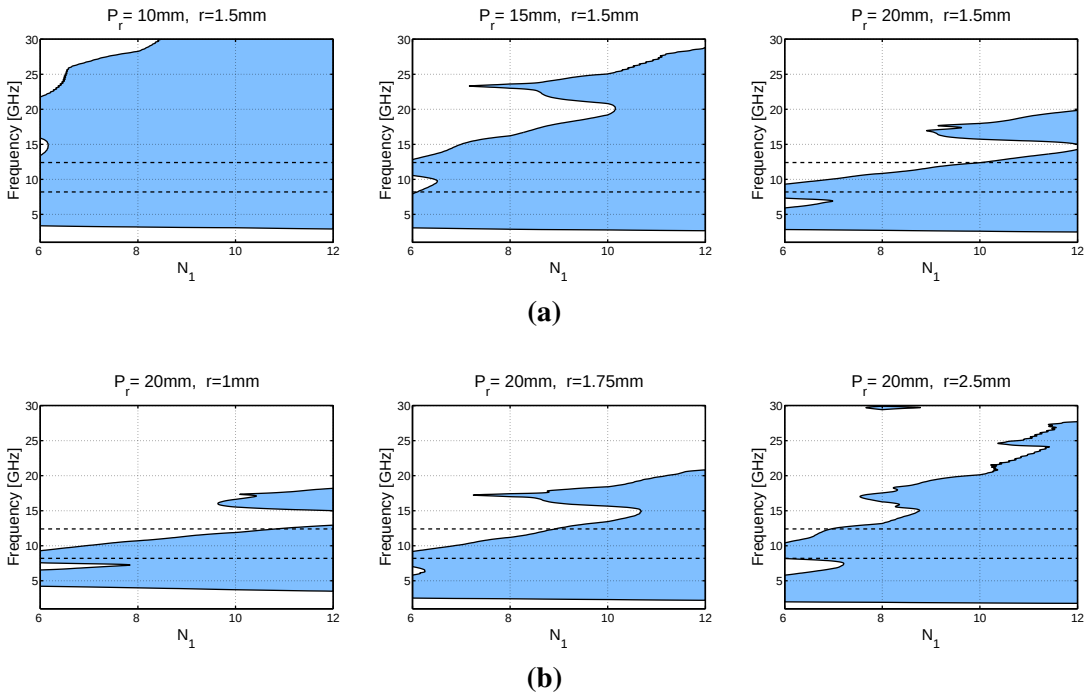

Figure 2.5: *Gapmaps - in blue is where the simulated transmission coefficient is lower than -20dB: a) as a function of N_1 and P_r ; b) as a function of N_1 and r.*

In figure 2.4 the rods radius is kept constant and the influence of P_r and N_1 are shown respectively in figure 2.4a and figure 2.4b. Increasing P_r narrows the bandgap and shifts it down in frequency; increasing N_1 widens the bandgap and creates new ones at higher frequencies. Bandgaps width also increases with larger r.

Finally, in figure 2.5 the first layer number of rods N_1 is kept constant and the influence of P_r and r are shown respectively in figure 2.5a and figure 2.5b. Increasing P_r narrows the bandgap and shifts it down in frequency; increasing r widen the bandgap and creates new ones at higher frequencies. Number of bandgaps and their width increase with N.

In summary, bandgap extension is directly proportional to r, N and inversely proportional to P_r; bandgap central frequency is inversely proportional to P_r and not much influenced by the other two parameters; the number of bandgaps is increased as N and r increase.

The transmission coefficient T as a function of the number of layers for a 2D CEBG structure realised with rods made of water with geometrical parameters N_1=6, P_r=15mm and r=2.5mm is reported in figure 2.6; as expected, T is generally decreasing as the number of layers increases.

It could be argued that the bandgap is given by the lossy characteristics of water; for this reason in figure 2.6a two more curves have been reported. The first curve is the loss tangent of water. The second curve shows the transmission coefficient T of a 2D CEBG structure made with the same geometrical parameters using a lossless and dispersionless

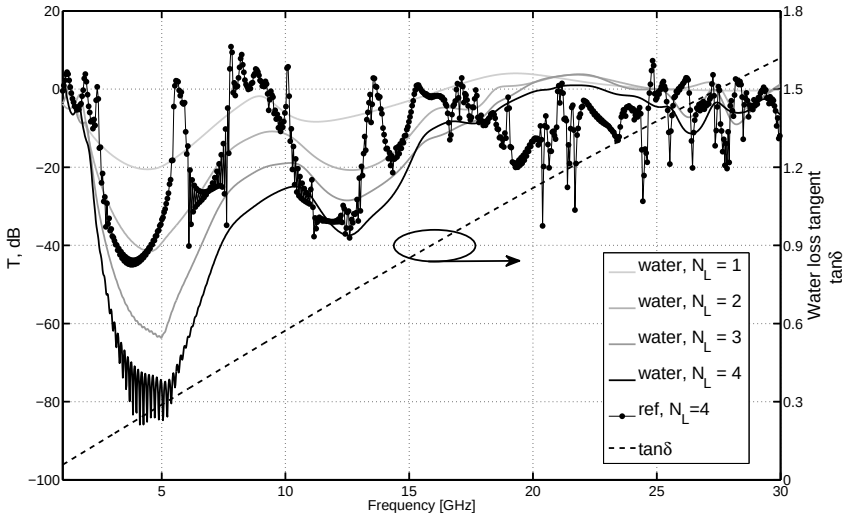

(a)

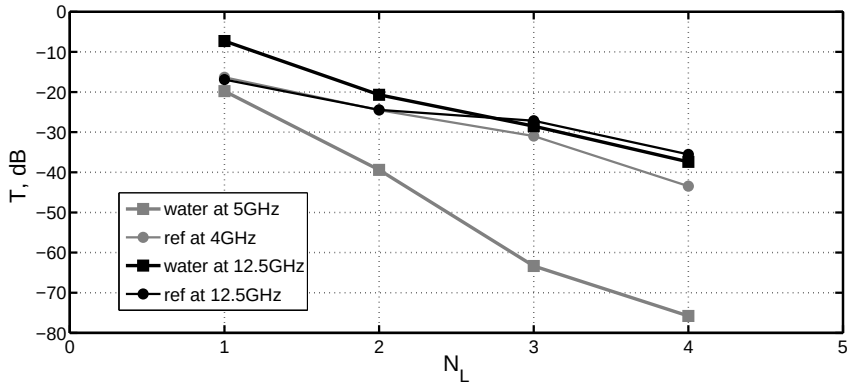

(b)

Figure 2.6: *2D CEBG structure, simulated transmission coefficient: a) as a function of frequency; b) as a function of layers at bandgaps centre frequency.*

material which dielectric permittivity has been set to the average value of water ε' in the frequency range 0-20GHz, ie ε_r=60, N_1=6, N_L=4, P_r=15mm and r=2.5mm. This structure presents three bandgaps in the frequency range 0-20GHz: first bandgap at 2.55-5.4GHz, second bandgap at 6.15-7.6GHz and third bandgap at 10.4-13.1GHz; the bandgap of the water structure goes from 2GHz to 15GHz, it is created by the superposition of two bandgaps respectively centered at 5GHz and 12.5GHz. As shown in figure 2.6a, the transmission coefficient of the water structure is minimum where water loss tangent is actually lower, and not minimum where water loss tangent is maximum as it would be expected if T was influenced mainly by losses. Figure 2.6b shows both structures transmission coefficient T measured in the bandgaps centre frequency. T decreases linearly with the number of layers as expected; regarding the water structure, T is decreasing at a faster rate in the first bandgap where dielectric losses are lower ($tan\delta$=0.3) than in the second bandgap ($tan\delta$=0.7). Losses characteristics of water are certainly playing a role in the establishment of bandgaps position, extension and introduced attenuation, but they

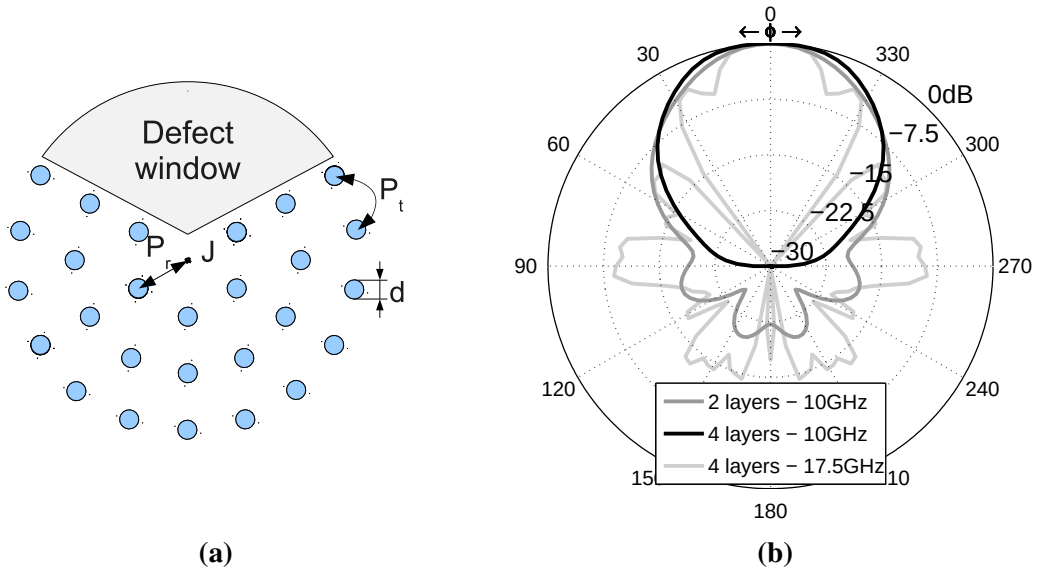

(a) **(b)**

Figure 2.7: *2D water CEBG antenna: a) structure; b) simulated normalized radiation patterns: N_1=6, P_r=15mm, r=2.5mm (the gapmap for this geometrical parameters is shown in figure 2.4a).*

are not the main cause.

2.2.3 2D Antenna configuration and design

In figure 2.7a is depicted the 2D CEBG antenna structure, which is realized by opening an angular defect window in the CEBG structure. The defect window is created by removing 1 rod from first layer, 3 rods from second layer and so on. High directivity patterns are expected within the bandgap: the angular defect window allows radiation in that particular direction whilst the CEBG prevents radiation in the other directions. This is clearly shown in figure 2.7b where the normalized radiation patterns of a 2D CEBG antenna made with N_1=6, P_r=15mm, r=2.5mm is shown (the gapmap for this geometrical parameters is shown in figure 2.4a). At 10GHz, inside the bandgap, the antenna is very directive and 2 layers are enough to achieve very directive patterns; at 17.5 GHz, outside the bandgap, antenna radiation pattern has lost directivity.

Best results for X-band implementation in terms of bandgap frequencies, 2D CEBG antenna directivity pattern, geometrical dimension and complexity were achieved with N_1 equals to 6, 8 and 10; N_L=2, P_r=15mm, r=2.5mm; therefore we used these optimum parameters as a starting point for studying 3D CEBG antenna structures.

2.2.4 3D Antenna configuration and design

The 3D dielectric CEBG antenna structure is depicted in figure 2.8: the antenna is composed by dielectric rods of height h and radius r arranged with transversal period P_t and radial period P_r around a monopole feeding probe placed in the axis.

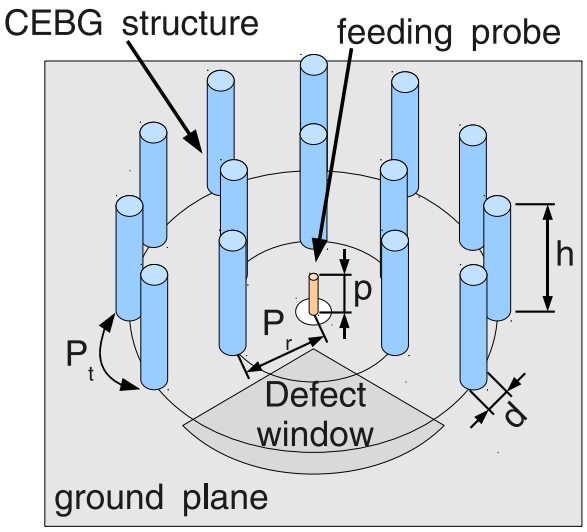

Figure 2.8: *3D water CEBG antenna structure, N_1=6, N_L=2.*

The 3D CEBG structure is a finite approximation of an infinite long structure as the ones analysed in the previous sections. For low elevation angles, the excited fields have a strong radially propagating component which is expected to be attenuated by the structure bandgap; for greater angles, although the structure is not expected to attenuate the propagating fields, low radiation is expected given the intrinsic configuration of fields excited by the monopole feed. Thus, as for the 2D case, gain is expected in the same angular direction of the defect window whilst in the opposite direction, where the structure is intact, the radiation is attenuated. This is shown in figure 2.9 where the normalized field distribution on the azimuthal plane for a 3D CEBG antenna realized with geometrical parameters N_1=6, N_L=2, P_r=15mm, r=2.5mm is reported for several frequencies. At frequencies within the 2D structure bandgap 5GHz-15GHz, the field distribution in the defect window has much higher magnitude than outside the 3D CEBG structure, high directive radiation patterns are achieved; at frequencies outside the 2D structure bandgap, 17.5-30GHz, fields distribution outside the 3D CEBG structure and in the defect window have similar magnitude leading to radiation patterns with low directivity and multiple sidelobes.

The optimal parameters found in the previous step have been used as starting point for the design of 3D structures. A parametric study has been carried out, studying the 3D CEBG antenna as a function of N_L, N_1 and h. Antennas were simulated on an infinite ground plane and two prototypes were built and tested to confirm the simulated results. Dielectric rods were realized with PVC drinking straws glued to a 200mm x 150mm copper ground plane and filled with distilled water, arranged in a 3D CEBG structure with P_r=15mm, r=5mm and N_1 equals to 6 in prototype *I* and N_1 equals to 8 in prototype *II*. Excitation is given through a monopole feed (p=7.2mm in prototype I and p=6.8mm in prototype *II*).

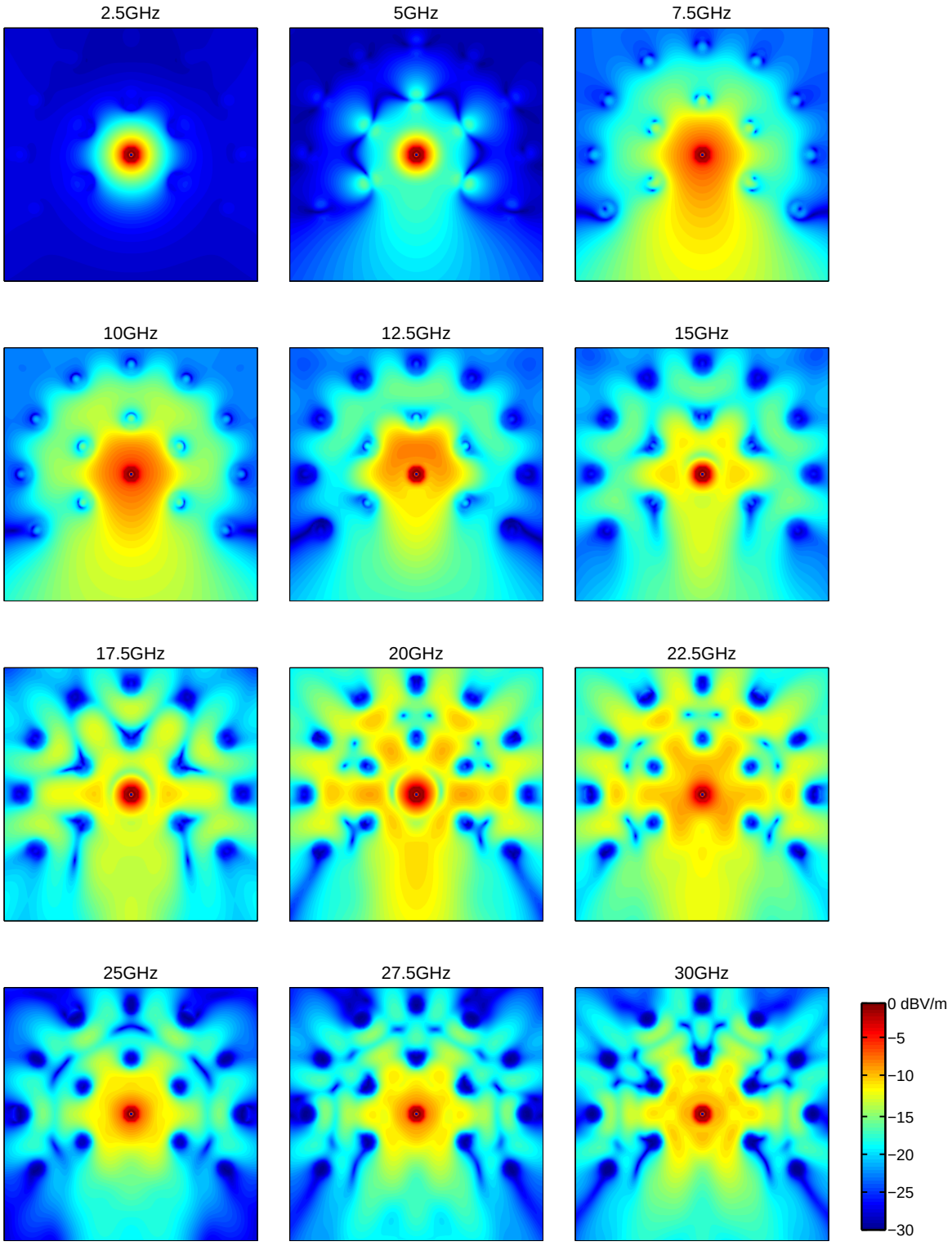

Figure 2.9: *3D water CEBG antenna, simulated normalized electric field distribution on the azimuthal plane, N_1=6, N_L=2, P_r=15mm, r=2.5mm, h=24mm.*

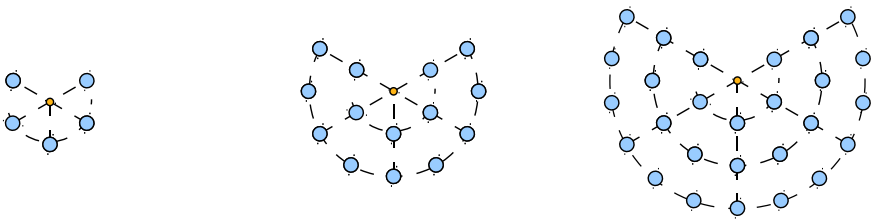

(a) **(b)** **(d)**

Figure 2.10: *3D water CEBG antenna as a function of layers geometries: a) N_L=1; b) N_L=2; c) N_L=3.*

2.2.4.1 Number of layers - N_L

Figure 2.11 (measurement results for N_L=3 are not available) shows that the number of layers has a marginal influence on the S_{11} response of the antenna (almost identical for simulated configurations with 2 and 3 layers), measurements show a better matching within the impedance bandwidth but resonances and bandwidth positions are well predicted. The -10dB impedance bandwidth goes from 6.8GHz to 11.5 GHz, 50% fractional bandwidth.

Far fields radiation patterns, figure 2.12, show a very directive pattern in the defect window direction, confirming the design assumptions. Gain and front to back ratio increase as the number of layer increases in first approximation, even tough, according to the simulations, the differences between 2 and 3 layers configurations are very small. Due to finite ground plane edge effect, the maximum gain falls on the E-plane with an elevation angle $\neq 0$, see Section 2.2.4.4. Without considering the finite ground plane edge effect, simulations and measurement results are in good agreement.

Table 2.1 summarises the maximum and average gain and FTBR for this parametric study. Comparing S_{11} response and radiative properties of 2 and 3 layers configurations shows that 2 layers are a good compromise in terms of antenna dimensions and overall performances, achieving 50% fractional bandwidth, 9.6dBi maximum gain and an average FTBR of 18.1dB.

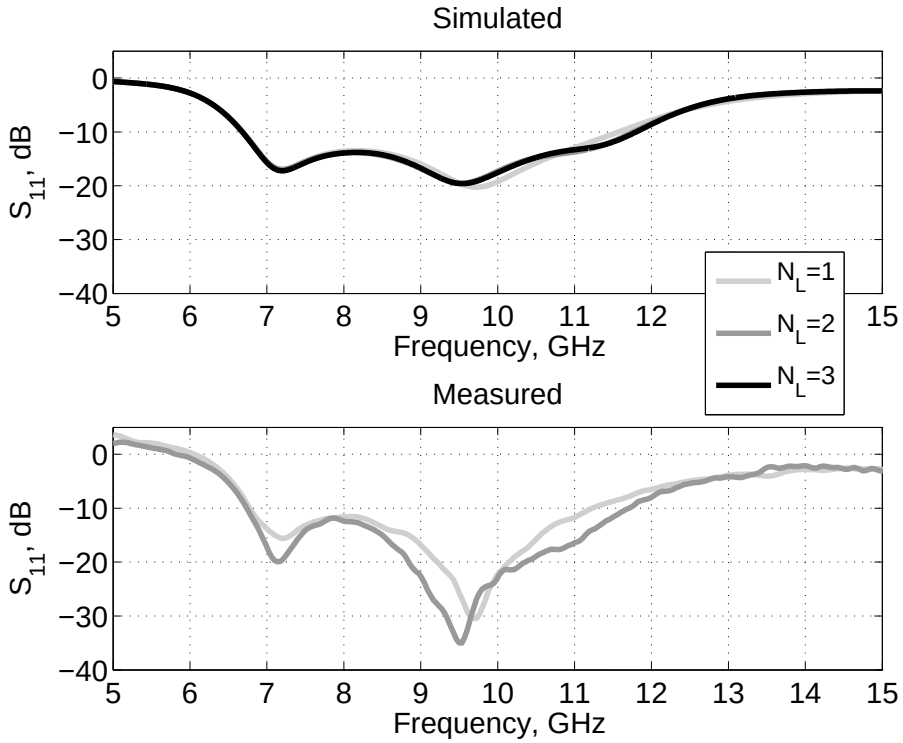

Figure 2.11: *3D water CEBG antenna, simulated and measured S_{11} as a function of number of layers N_L, N_1=6, P_r=15mm, r=2.5mm, h=24mm.*

N_L	Gain, dBi	FTBR, dB	Bandwidth	N_{rods}	Max dim.
1	7.9 (6.0)	34.8 (14.4)	53.5% 6.7-11.6GHz	5	$2 \cdot P_r$
2	9.6 (8.2)	24.4 (18.0)	55.1% 6.7-11.8GHz	14	$4 \cdot P_r$
3	N/A	N/A	N/A	27	$6 \cdot P_r$

Table 2.1: *3D water CEBG antenna, simulated gain and FTBR performance as a funcion of number of layers N_L, N_1=6 P_r=15mm, r=2.5mm, h=24mm (in brackets are reported the average values within the impedance bandwidth).*

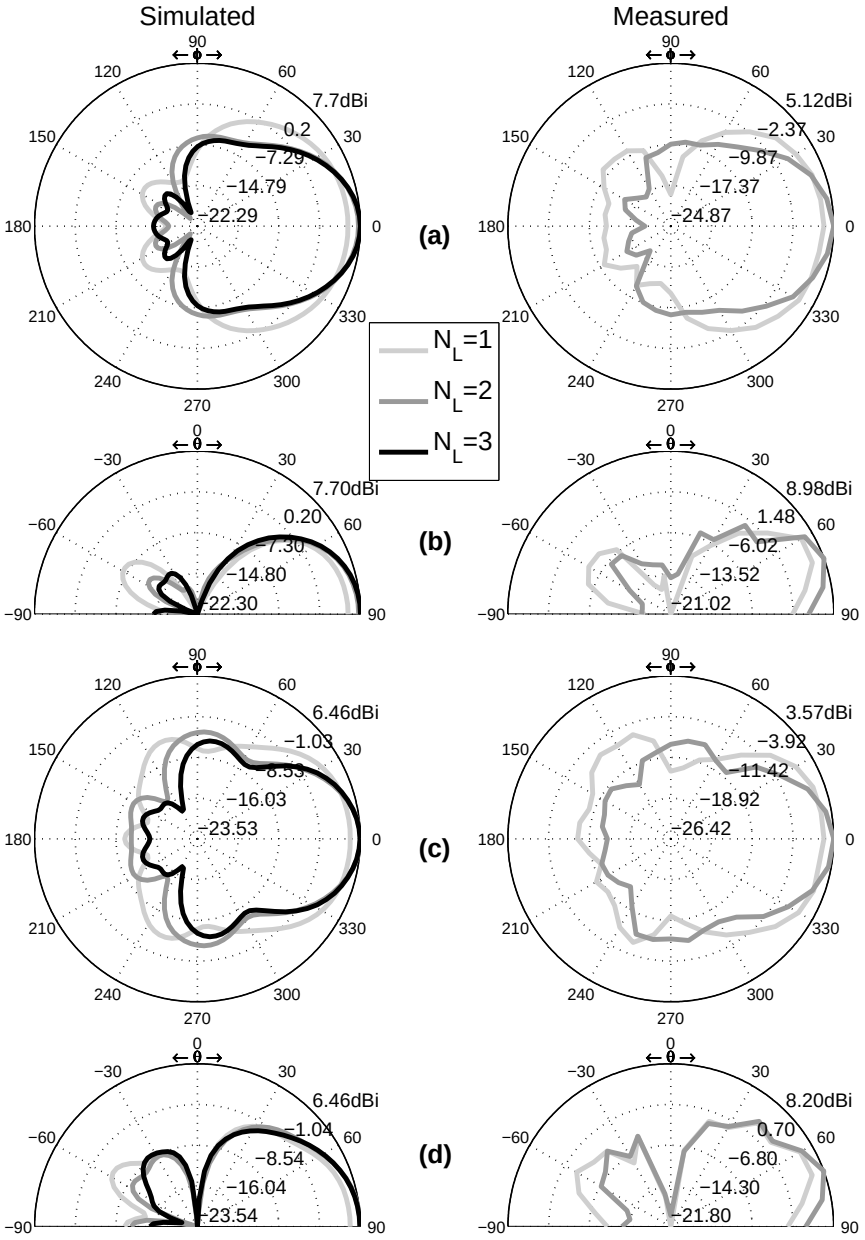

Figure 2.12: *3D water CEBG antenna, H-plane and E-plane simulated and measured radiation patterns as a function of number of layers N_L, N_1=6 P_r=15mm, r=2.5mm, h=24mm: a) 8.5GHz; b) 10GHz.*

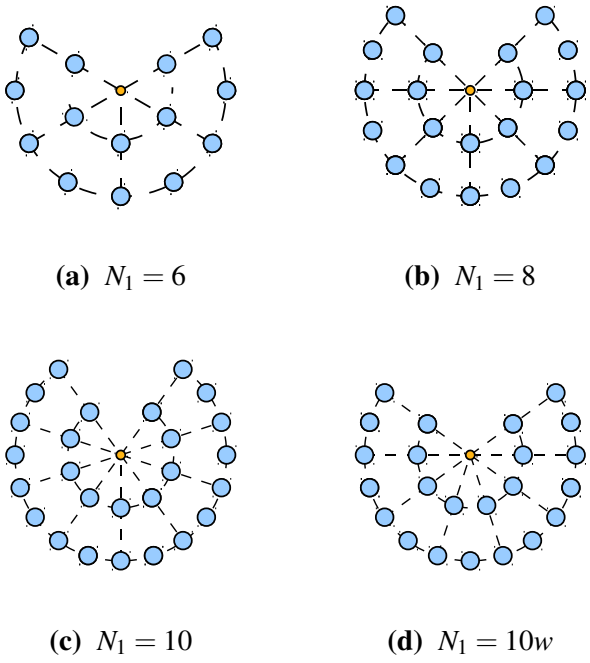

(a) $N_1 = 6$ **(b)** $N_1 = 8$

(c) $N_1 = 10$ **(d)** $N_1 = 10w$

Figure 2.13: *CEBG structures geometries.*

2.2.4.2 Number of rods in the first layer - N_1

In figure 2.14-2.15 are reported the S_{11} response and far field radiation patterns as a function of N_1; two configurations with N_1 equals to 10 were simulated but not measured: in the first one the angular defect window was created as shown in figure 2.13c, in the second version a wider defect window was created by removing 2 rods from the first layer and 5 rods from the second layer, figure 2.13d.

Prototype *II* measured impedance bandwidth ($N_1 = 8$), without considering a small mismatch at 8.5GHz, goes from 7.4GHz to 12.7GHz, 52.8% fractional bandwidth. Compared to measurement results, simulations show better matching; bandwidth extension and peak positions are well predicted.

The simulated -10 dB impedance bandwidth for N_1 = 10w goes from 7.2GHz to 12.5GHz, 54% fractional bandwidth, whilst the configuration with N_1 = 10 has a narrower bandwidth, 9.6GHz to 12.4GHz, 25.9% fractional bandwidth. Radiation patterns are also influenced by the extension of the angular defect window: configurations with N_1 equals to 6 and 10w, defect window respectively equals to 120° and 108°, have very similar simulated radiative properties and achieved the best overall performances; configurations with N_1 equals to 10 and 10w, defect window respectively equals to 72° and 108°, although having the same geometrical parameters, clearly show very different radiative properties.

Simulations and measurements, the results are summarised in table 2.2, therefore shown that N_1 has a big influence on the behaviour of the antenna; the best results in terms of overall performances and required number of rods were achieved with N_1=6.

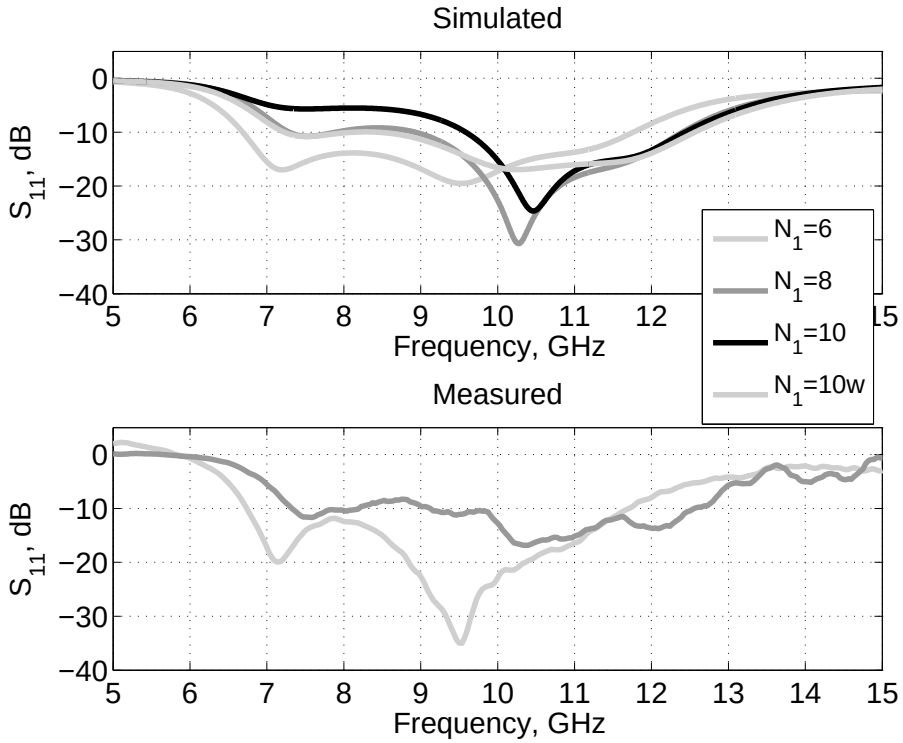

Figure 2.14: *3D water CEBG antenna, simulated and measured S_{11} as a function of number of rods in the first layer N_1, N_L=2, P_r=15mm, r=2.5mm, h=24mm.*

N_1	Gain, dBi	FTBR, dB	Bandwidth	N_{rods}	window
6	9.6 (8.2)	26 (18.1)	53.4% 6.8-11.8GHz	14	120°
8	6.5 (5.8)	24.3 (16.6)	52.8% 7.4-12.7GHz	20	90°
10*	9.4 (6.4)	14.0 (9.9)	25.9% 9.6-12.4GHz	26	72°
10w*	10.5 (9.4)	26.0 (20.8)	53.3% 7.2-12.5GHz	23	108°

Table 2.2: *3D water CEBG antenna, measured gain and FTBR performance as a funcion of number rods in the first layer N_1, N_L=2, P_r=15mm, r=2.5mm, h=24mm (in brackets are reported the average values within the impedance bandwidth). *simulations*

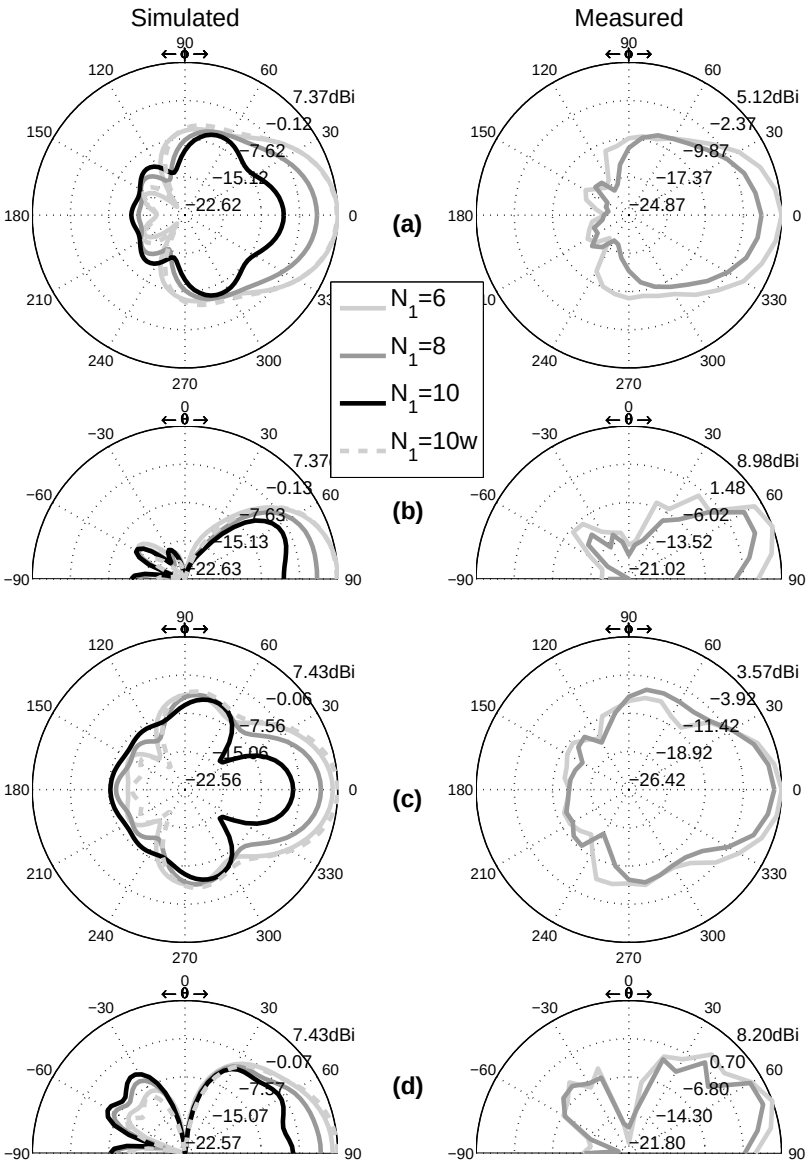

Figure 2.15: *3D water CEBG antenna, H-plane and E-plane simulated and measured radiation patterns as a function of number rods in the first layer N_1, N_L=2, P_r=15mm, r=2.5mm, h=24mm: a) 8.5GHz; b) 10GHz.*

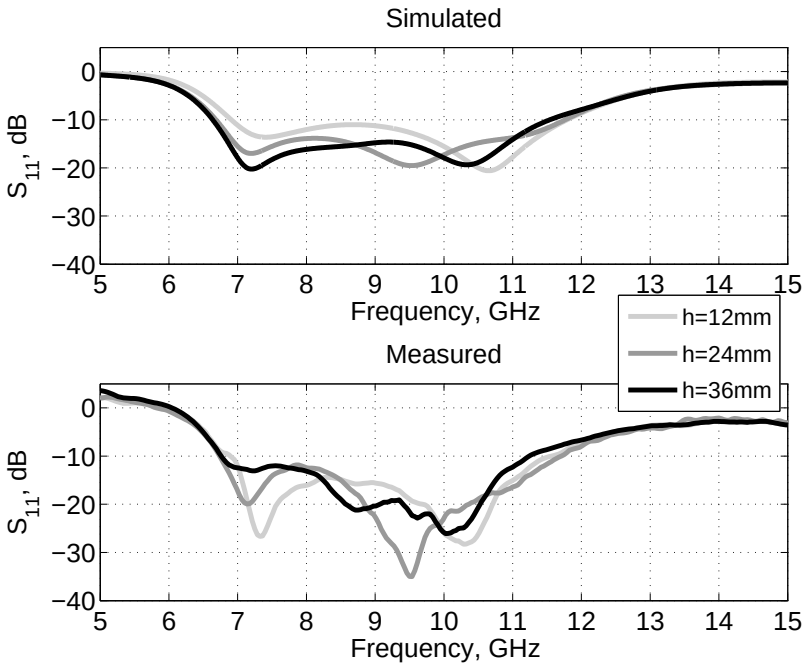

Figure 2.16: *3D water CEBG antenna, simulated and measured S_{11} as a function of rods height h, N_1=6, N_L=2, P_r=15mm, r=2.5mm.*

2.2.4.3 Rods height - *h*

A CEBG antenna with geometrical parameters N_1=6, N_L=2, P_r=15mm, r=2.5mm, figure 2.8 was parametrically studied as a function of rods heigth h. The S_{11} response of the antenna is moderately influenced by the rods height: figure 2.16 shows that resonance frequencies are modified by rods height whilst bandwidth extension is almost unaffected.

Gain generally improves as the height is increased, figure 2.17,even tough the difference between configurations with h equals to 24mm and 36mm is really small. The FTBR is maximum for the configuration with h=24mm, and in contrast with simulation results where it did not significantly change, it is decreasing for higher rods.

Measurement results are summarised in table 2.3.

h, mm	Gain, dBi	FTBR, dB	Bandwidth
12	8.7 (8.2)	15.6 (13.2)	48.5 % 7-11.5GHz
24	9.6 (8.2)	26 (18.1)	53.4% 6.8-11.8GHz
36	9.7 (9)	17.7 (12.2)	49.7% 6.8-11.3GHz

Table 2.3: *3D water CEBG antenna, measured gain and FTBR performance as a funcion of rods height h, N_1=6, N_L=2, P_r=15mm, r=2.5mm (in brackets are reported the average values within the impedance bandwidth).*

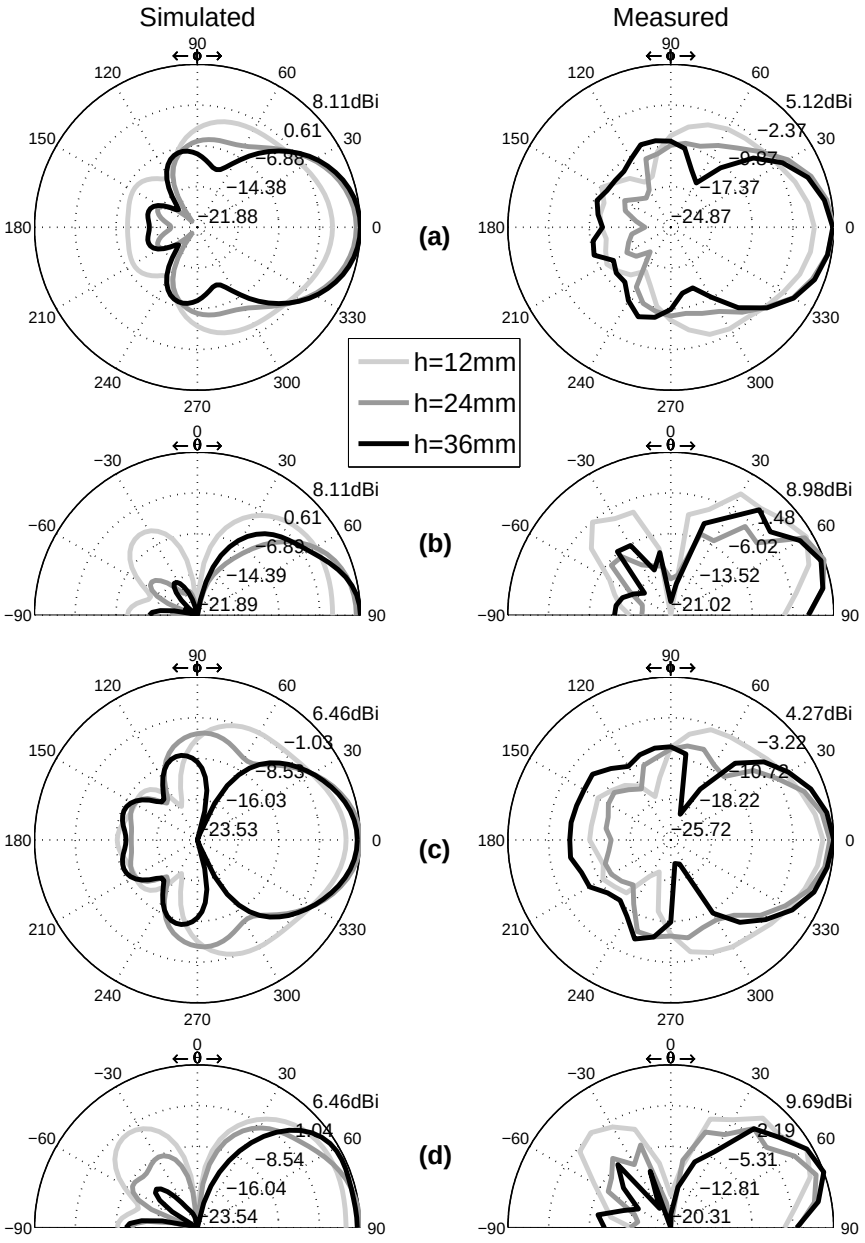

Figure 2.17: *3D water CEBG antenna, H-plane and E-plane simulated and measured radiation patterns as a function of Rods height h, N_1=6, N_L=2, P_r=15mm, r=2.5mm: a) 8.5GHz; b) 10GHz.*

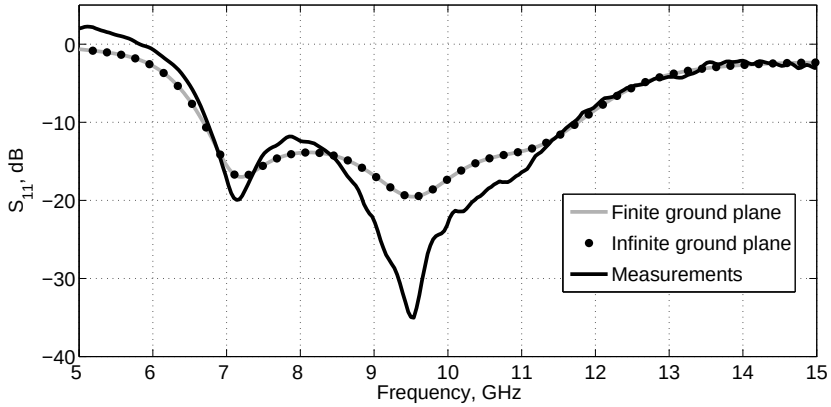

Figure 2.18: *3D water CEBG antenna S_{11} comparison between measurements and simulations as a function of ground plane size, N_1=6, N_L=2.*

2.2.4.4 Ground plane size influence on simulation results.

The influence of ground plane dimensions on simulations results is analysed in figure 2.18 and figure 2.19.

The simulated S_{11} responses are almost identical, only radiation patterns present differences. Simulated H-plane radiation patterns, figure 2.19a-b, are quite similar in terms of shape and sidelobes relative level although finite ground plane radiation patterns are circa 5dBi lower in terms of maximum gain. This difference is caused by the finite ground plane size, resulting in radiation patterns ”skewed” away from the azimuthal plane (ie H-plane); the direction of maximum radiation is therefore changed to an angle elevated from the H-plane.

There is a better agreement between simulations and measurements when a finite ground plane is modeled, figure 2.19b-c: the maximum gain elevation angle on the E-plane is well predicted as well as the H-plane radiation patterns absolute magnitude. Computational effort and memory requirements are very demanding though; therefore, as a good compromise in terms of predicted antenna performances and computational time/effort, all simulations were run modelling an infinite ground plane.

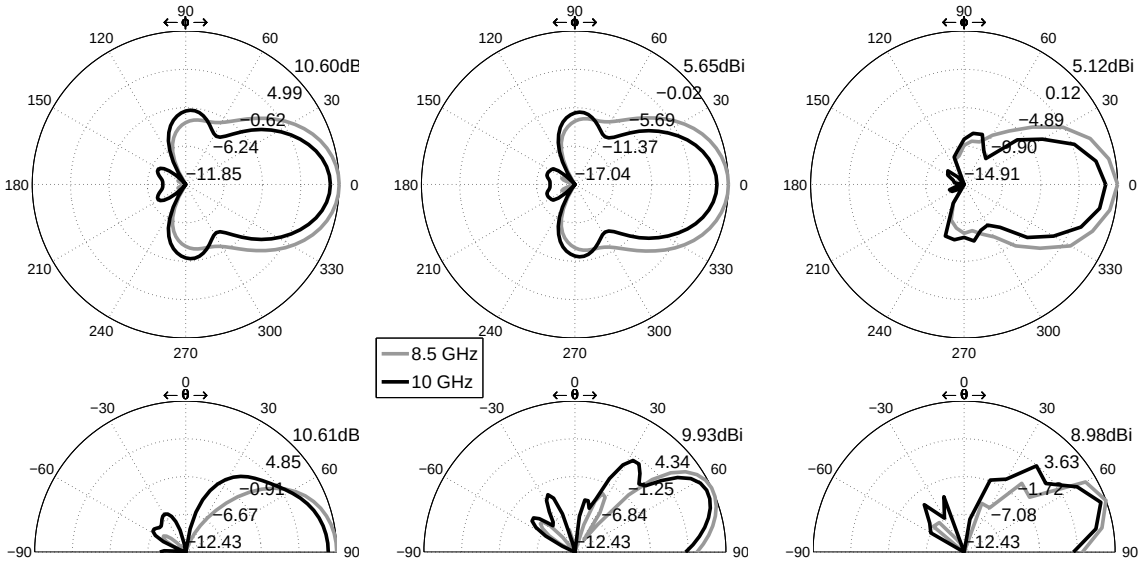

(a) Infinite ground plane **(b)** Finite ground plane **(c)** Measurements

Figure 2.19: *3D water CEBG antenna, H-plane and E-plane radiation patterns comparison between measurements and simulations as a function of ground plane size, N_1=6, N_L=2: a) simulations with an infinite ground plane; b) simulations with a finite ground plane of the same size as used in the measurements; c) measurements.*

2.2.5 Summary

The parametric study shown that the best compromise in terms of impedance matching, far field behaviour and also considering antenna overall dimensions and number of rods, is obtained with h=24mm, r=5mm, P_r=15mm, N_1 equals to 6.

Increasing the number of layers N_L has a little impact on the S_{11} frequency response of the antenna but improves gain and FTBR, although the improvement is minimal when more than 2 layers are used.

The rods heigth h has a bigger influence on the antennas S_{11} in terms of resonance frequencies but little on the bandwidth extension. Gain and FTBR are also influenced by h which can be tuned to achieve optimal performance.

2.3 Ceramic EBG

The water CEBG antenna analyzed in the previous section allowed us to demonstrate the concepts and the design approach of dielectric CEBG antennas. As already mentioned, water is not a practical material for the realization of antennas, therefore the next step has been the design and analysis of CEBG antenna made with ceramic materials. The dielectric permittivity of the chosen material is an additional degree of freedom to consider in the design process. We focused our attention on the ceramic materials available from Morgan Electroceramics [81] in order to use dielectric permittivity values of materials available on the market.

The design approach is the one described in Section 2.1; in particular 2D CEBG structures have been characterized in terms of transmission coefficient and bandgap frequencies focusing on:

- first layer number of rods $N_1 = 6$;
- radial period $P_r = 10 - 20$mm ;
- rods radius $r = 1 - 3$mm;
- rods dielectric permittivity $\varepsilon_r = 9.8,\ 20,\ 30,\ 37,\ 43,\ 76.5,\ 88$.

Several simulations were run to characterize a 4 layers CEBG structure realized with all possible combinations of the above parameters; the results were then collected and visualised in gapmaps as shown in figure 2.20-2.22 (stopband is set at T=-20dB). Ceramics were simulated using the dielectric permittivity and loss tangent values supplied by Morgan Electroceramics.

Once a suitable (ie whether the bandgap would cover, even partially, the X-band frequency range) combination of the above parameters was found, the whole design process would start. Four main geometrical and electrical parameters combinations were identified as possible candidates for the design process, they are reported in table 2.4. Figure 2.23 shows the gapmaps as a function of dielectric permittivity for the chosen combinations of geometrical properties (A and C have the same geometrical properties).

Figure 2.24 shows the simulated radiation patterns (within the bandgap) of two layers 2D CEBG antennas built according to table 2.4; models B, C and D present directive direction patterns within the bandgap, whilst model A performance is very poor and therefore this model was discarded. 3D CEBG antennas were then designed, simulated and compared using model B, C and D geometrical properties and dielectric permittivity. Figure 2.25 and figure 2.26 respectively show the S_{11} and the radiation patterns at bandgap frequencies of 3D CEBG antennas designed according to table 2.4: even though the probe length was in each case adjusted to optimize matching at bandgap frequencies, model C matching is always very poor, whilst model B and D could achieve 2GHz

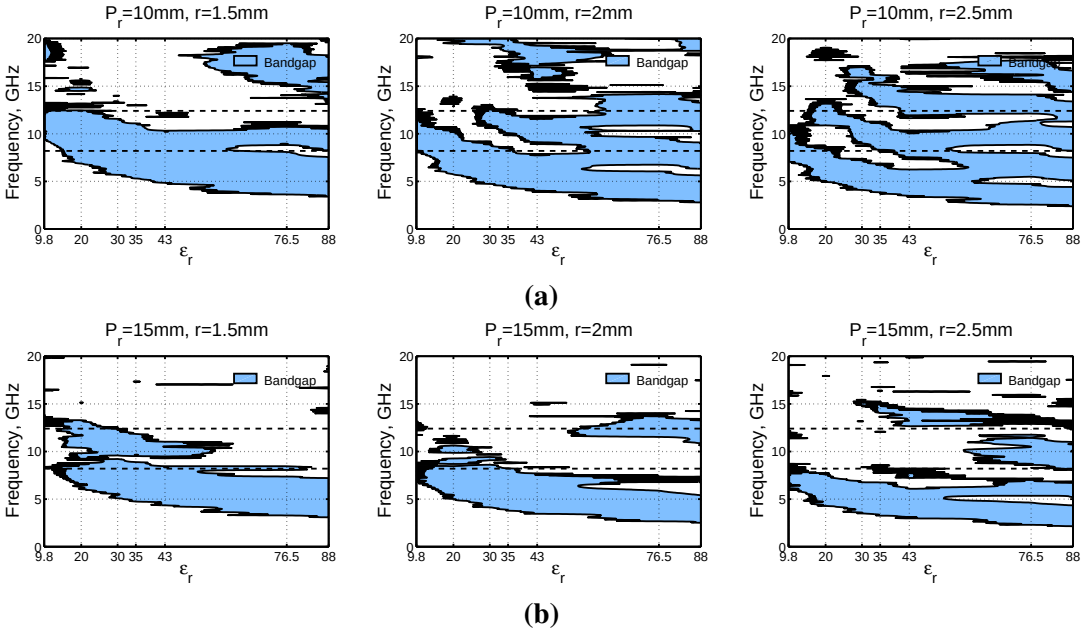

Figure 2.20: *Gapmaps as a function of ε_r, in blue is where the simulated transmission coefficient is lower than -20dB: a) P_r=10mm, r=1.5-2.5mm; b) P_r=15mm, r=1.5-2.5mm.*

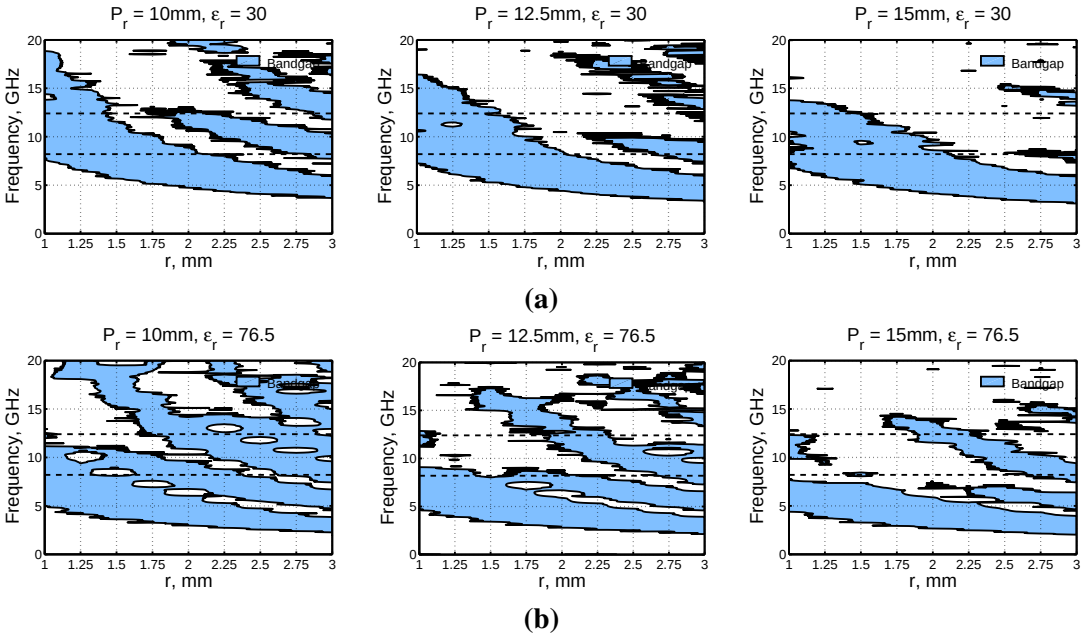

Figure 2.21: *Gapmaps as a function of r, in blue is where the simulated transmission coefficient is lower than -20dB: a) ε_r=30, P_r=10-15mm; b) ε_r=76.5, P_r=10-15mm.*

(18%) and 1.7GHz (17%) -10dB impedance bandwith respectively (impedance bandwidth could be tuned or improved by using a different feed rather than the standard coaxial transition used for all prototypes and modeled in the simulations, see Section 3.3.3). Model *C* was therefore discarded and of the two remaining candidates, after checking material availability with the ceramic rods supplier, model *D* was chosen for design and prototyping.

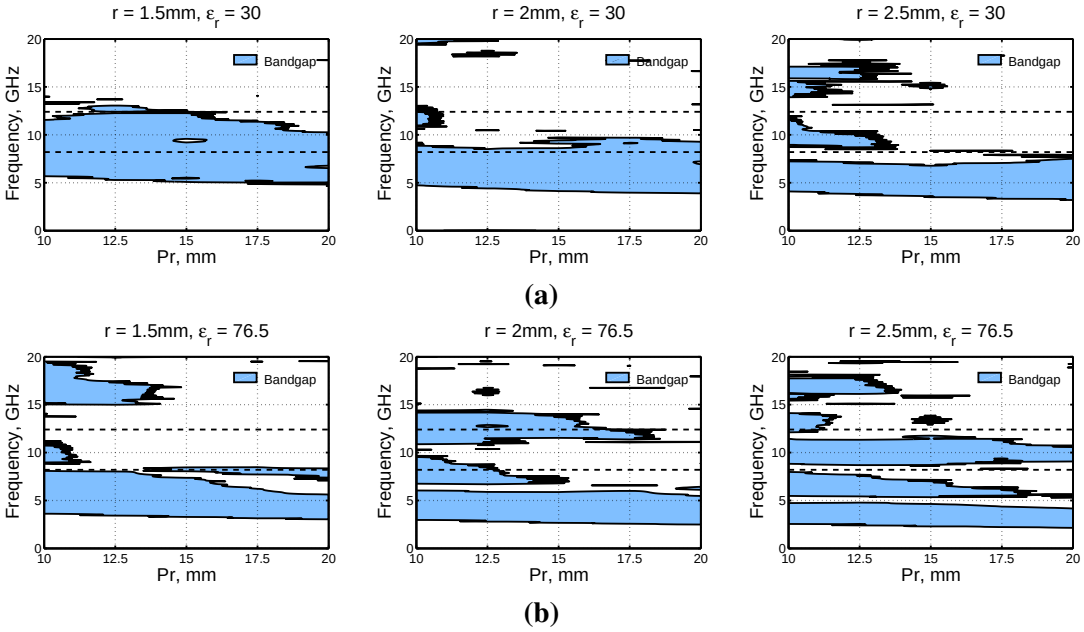

Figure 2.22: *Gapmaps as a function of P_r, in blue is where the simulated transmission coefficient is lower than -20dB: a) ε_r=30, r=1.5-2.5mm;; b) ε_r=76.5, r=1.5-2.5mm;.*

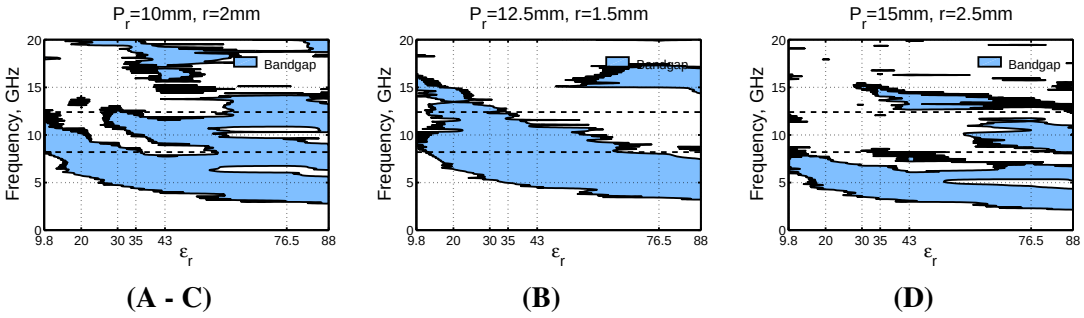

Figure 2.23: *Simulated gapmaps of the selected candidates:*
A - P_r=10mm, r=2mm and ε_r=9.8;
B - P_r=12.5mm, r=1.5mm and ε_r=30;
C - P_r=10mm, r=2mm and ε_r=43;
D - P_r=15mm, r=2.5mm and ε_r=76.5.

Name	P_r, mm	r, mm	ε_r	$tan\delta$	Bandgap, GHz
A	10	2	9.8	$10 \cdot 10^{-3}$	8.24-11.6
B	12.5	1.5	30	$0.1 \cdot 10^{-3}$	5.3-12.25
C	10	2	43	$0.23 \cdot 10^{-3}$	9.1-11.7
D	15	2.5	76.5	$0.95 \cdot 10^{-3}$	8.7-11.75

Table 2.4: *CEBG antenna with N_L=2, selected candidates geometrical properties and dielectric permittivity.*

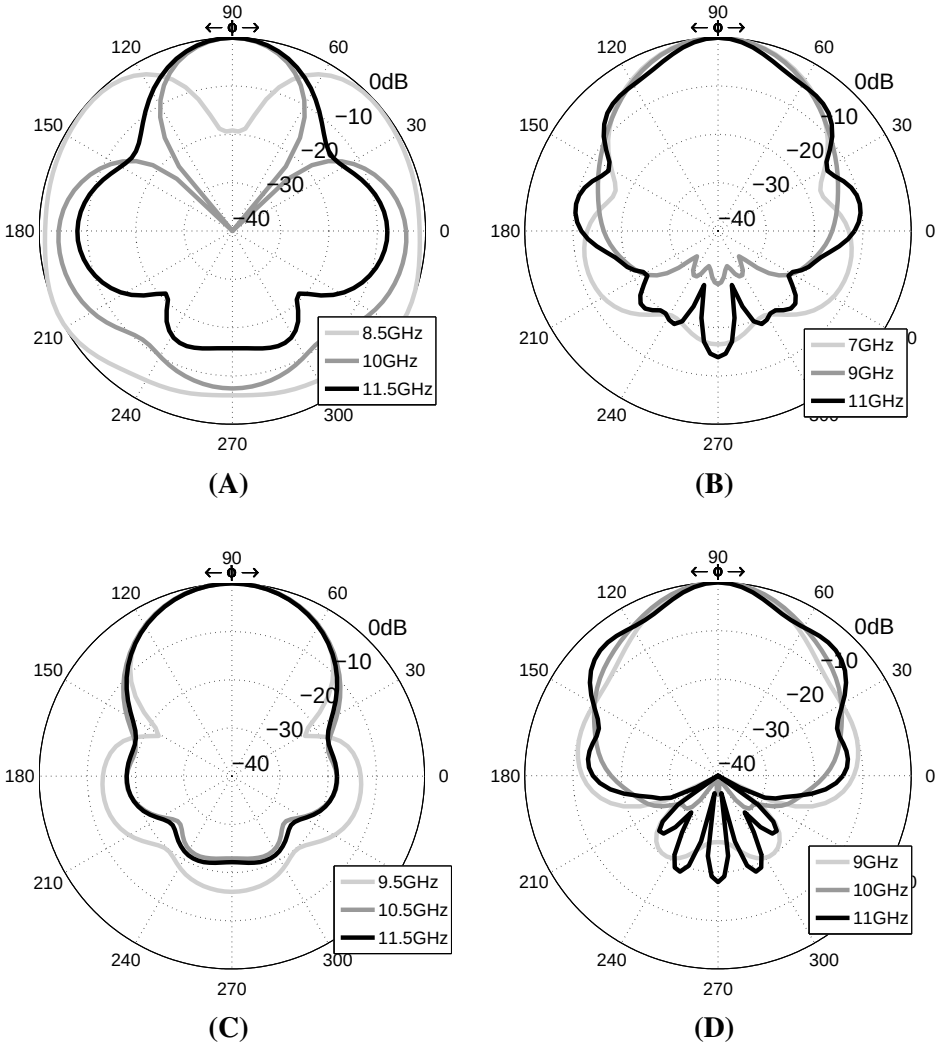

Figure 2.24: *2-D CEBG antenna with N_L=2, simulated radiation patterns (within the bandgap) of the selected models:*
A - P_r=10mm, r=2mm and ε_r=9.8;
B - P_r=12.5mm, r=1.5mm and ε_r=30;
C - P_r=10mm, r=2mm and ε_r=43;
D - P_r=15mm, r=2.5mm and ε_r=76.5.

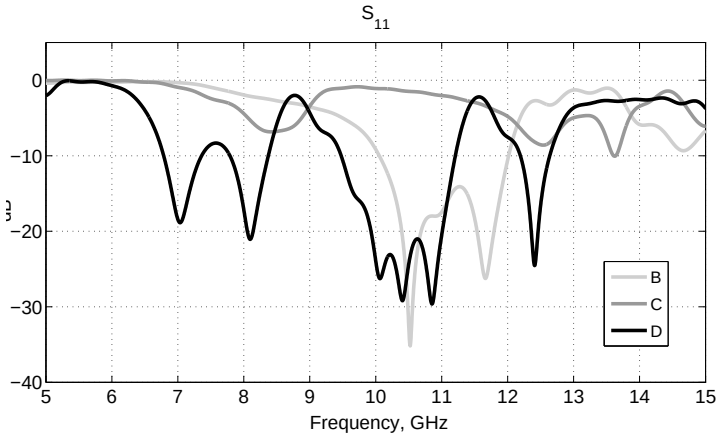

Figure 2.25: *3-D CEBG antenna with N_L=2 and h=20mm, simulated S_{11} of the selected models (feeding probe length was adjusted in each case for optimal matching):*
B - P_r=12.5mm, r=1.5mm and ε_r=30;
C - P_r=10mm, r=2mm and ε_r=43;
D - P_r=15mm, r=2.5mm and ε_r=76.5.

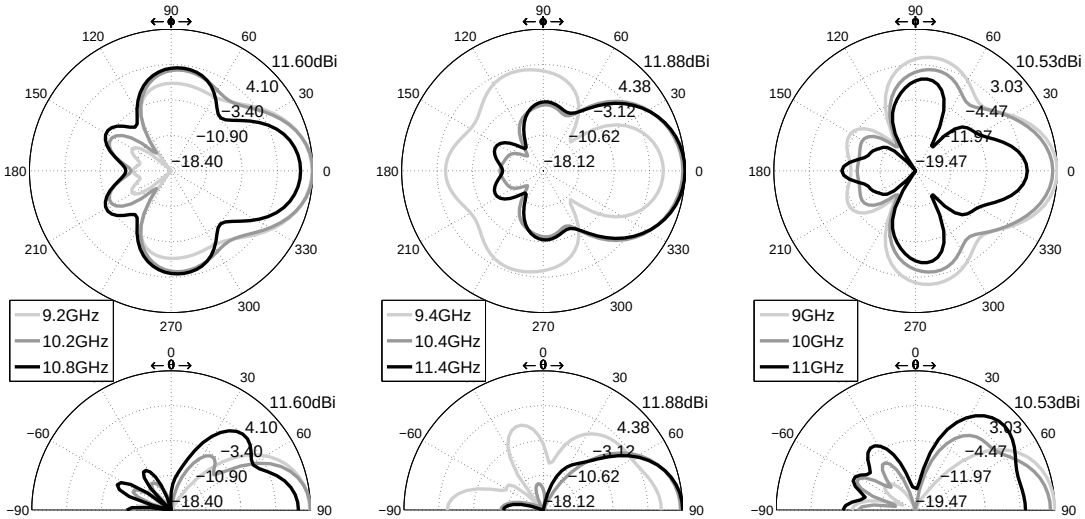

Figure 2.26: *3-D CEBG antenna with N_L=2 and h=20mm, simulated radiation patterns (within the bandgap) of the selected models:*
B - P_r=12.5mm, r=1.5mm and ε_r=30;
C - P_r=10mm, r=2mm and ε_r=43;
D - P_r=15mm, r=2.5mm and ε_r=76.5.

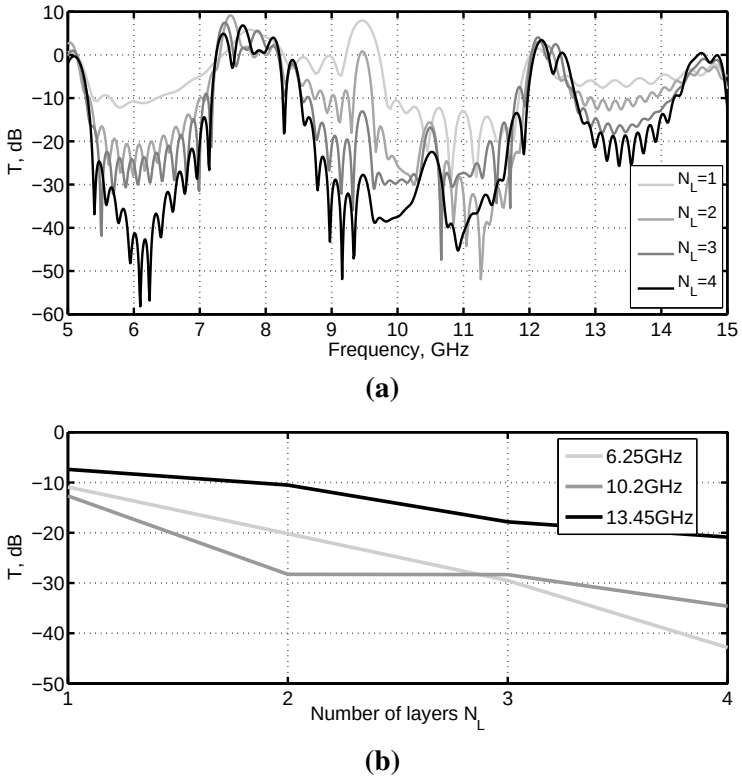

Figure 2.27: *Simulated transmission coefficient T of a CEBG structure with P_r=15mm, r=2.5mm and ε_r=76.5: a) as a function of frequency; b) as a function of number of layers N_L.*

2.3.1 Two-dimensional CEBG structure characterization

Figure 2.27a shows the transmission coefficient T as a function of frequency and number of layers for a 2D CEBG structure with the chosen geometrical properties, ie P_r=15mm, r=2.5mm and ε_r=76.5; there are 3 bandgaps in this structure in the shown frequency range: 5.3-7.2GHz, 8.5-11.9GHz and 12.7-14.2GHz[1]. As shown in figure 2.27b T, expressed in dB, decreases almost linearly inside the bandgaps as a function of number of layers. This suggests that, within the bandgaps, the electric field is evanescent and decaying exponentially while propagating through the CEBG structure as expected [2].

The normalized radiation patterns as a function on number of layers N_L of a 2D CEBG antenna are shown in figure 2.28a: two layers were found sufficient to achieve high directivity. In figure 2.28b radiation patterns are shown as a function of frequency for a 2D CEBG antenna with N_L=2: antenna is very directive at 6GHz and 10GHz, inside the second and third bandgap; at frequencies outside the bandgaps, 8GHz and 12GHz, the antenna is not directive any more. At 13.5GHz (fourth bandgap) directivity is very poor but as shown in figure 2.27, two layers do not introduce enough attenuation in that frequency region.

Figure 2.29 shows the normalized electric field distribution as a function of fre-

[1] In the 0-20GHz frequency range, actually there are 4 bandgaps: 2.3-4.6GHz, 5.3-7.2GHz, 8.5-11.9GHz and 12.7-14.2GHz. The first one is outside figure 2.27a limits.

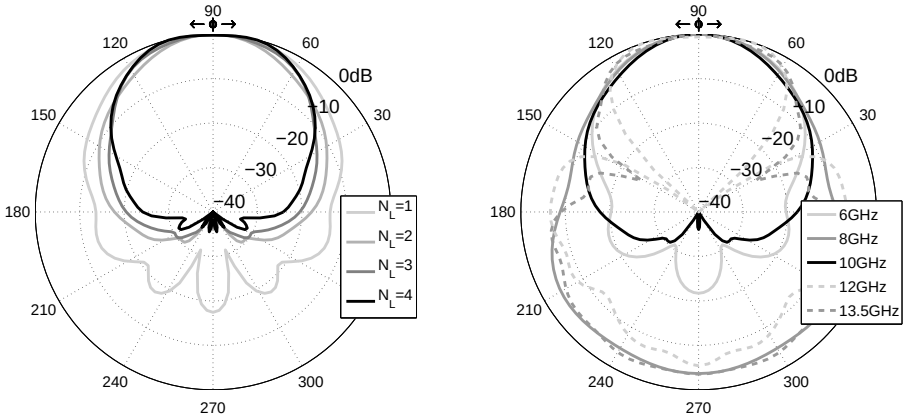

(a) **(b)**

Figure 2.28: *2D CEBG antenna, simulated radiation patterns, P_r=15mm, r=2.5mm and ε_r=76.5: a) 10GHz as a function of layers; b) N_L=2, as a function of frequency.*

quency. At frequency within the first 3 bandgaps, ie 4GHz, 6GHz, 7GHz, 9GHz, 10GHz and 11GHz, the electric field is confined within the CEBG structure and re-directed toward the angular defect window: the 2D CEBG antenna is therefore very directive at these frequencies. At 13 GHz and 14GHz the 4th bandgap is not very efficient: the excited fields can propagate through the CEBG structure with scarce attenuation leading to not directive radiation patterns, as shown in figure 2.28b.

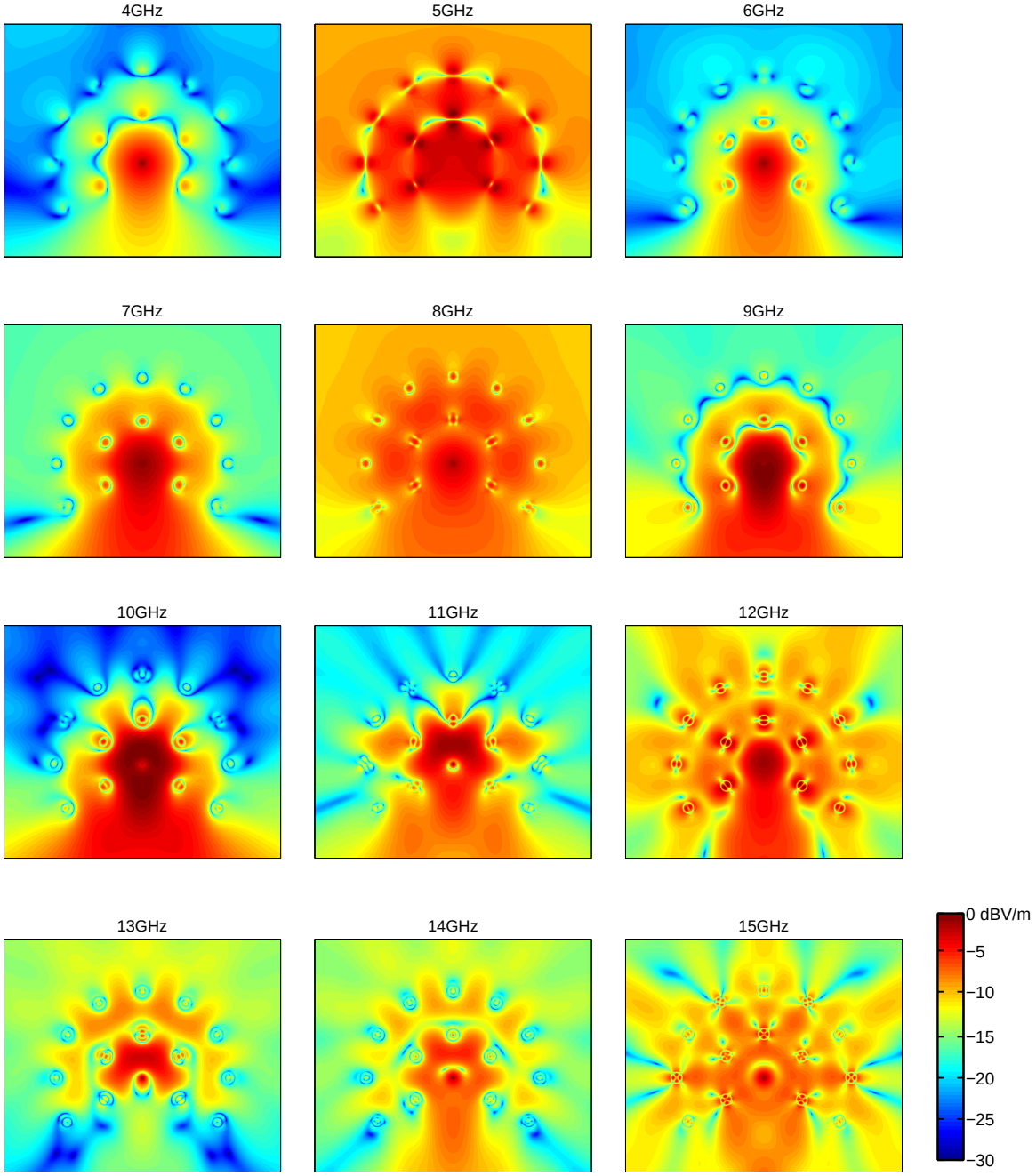

Figure 2.29: *2D CEBG antenna, simulated normalised electric field distribution, P_r=15mm, r=2.5mm and ε_r=76.5.*

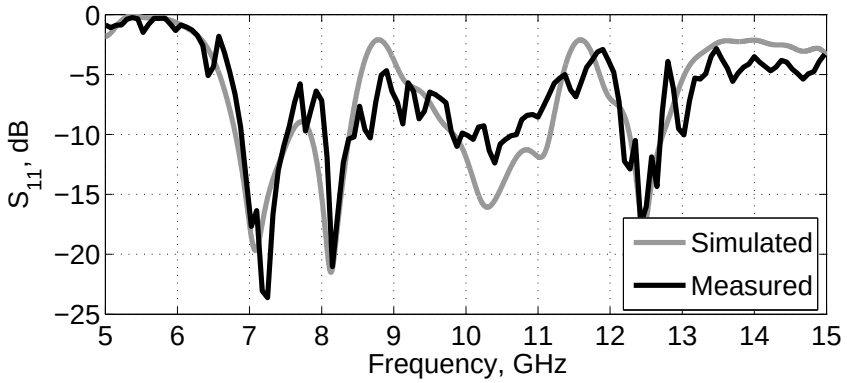

Figure 2.30: *2 layers 3D CEBG antenna simulated and measured S_{11}; P_r=15mm, r=2.5mm, ε_r=76.5 and h=20mm.*

2.3.2 3D CEBG Antenna

Using the information gathered from the previous steps, a 3D CEBG antenna prototype was simulated, built and tested using cylindrical ceramic rods (D77 modified barium titanate ε_r=76.5$\pm$2 [81]) placed on a 150mm $\times$ 150mm ground plane, arranged in a 2 layers 3D CEBG structure with P_r=15mm and r=2.5mm and h=20mm. The antenna is fed through a monopole feed of length p=7.2mm. In all simulations the antenna structure is placed above an infinite ground plane.

In figure 2.30-2.32 simulations and measurements are compared showing a very good agreement; -10dB bandwidth goes from 9.7GHz to 10.8GHz, 11% fractional bandwidth, average gain and front-to-back-ratio of 9.5dBi and 13dB respectively within the bandwidth. Best performance are achieved at 9.7GHz with gain and FTBR equal to 11.5dBi and 22dB respectively, figure 2.32. The gain decreasing in the measurements for low elevation angle, figure 2.31, is again caused by the finite ground plane used for measurements compared to the infinite ground plane modeled in the simulations, Section 2.2.4.4. Discrepancies between simulations and measurements can be also attributed to tolerances in rods dimensions and position.

Figure 2.33 shows the electric field distribution on the azimuthal plane at several frequencies. If we compare this figure with figure 2.27a it is clear that at bandgap frequencies (plots at 6GHz and 7GHz are within the second bandgap, plots at 9GHz, 10GHz and 11GHz are within the third bandgap) the electric field is strongly attenuated by the the CEBG structure; an exception is made at frequencies within the fourth bandagp, ie 13GHz where, as for the 2-D structure, the introduced attenuation is low. At frequencies outside the bandgap (plots at 4GHz, 8GHz, 12GHz, 14GHz and 15GHz) the electric field is less attenuated by the CEBG structure. This confirms the design assumptions that at low elevation angles the 3D CEBG structure is a good approximation of the 2D CEBG structure. For greater elevation angles the 3D CEBG structure is less effective but it is balanced by the intrinsic nature of the mode excited by the monopole feed (the electric field magnitude is decreasing as the elevation angle increases) as shown in figure 2.34.

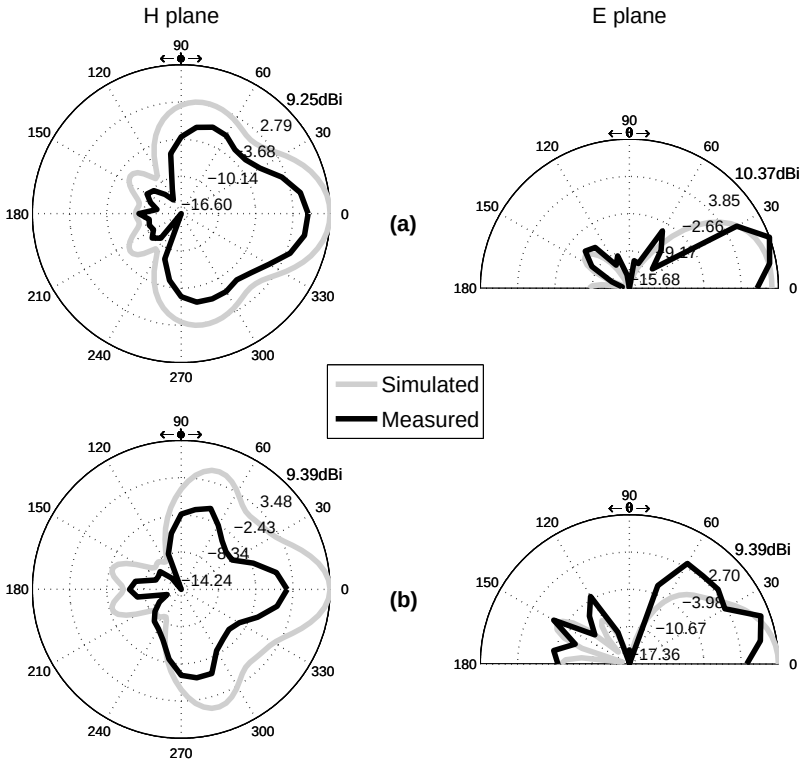

Figure 2.31: *3D CEBG antenna simulated and measured radiation patterns, P_r=15mm, r=2.5mm, ε_r=76.5 and h=20mm: a) 9.8GHz; b) 10.6GHz.*

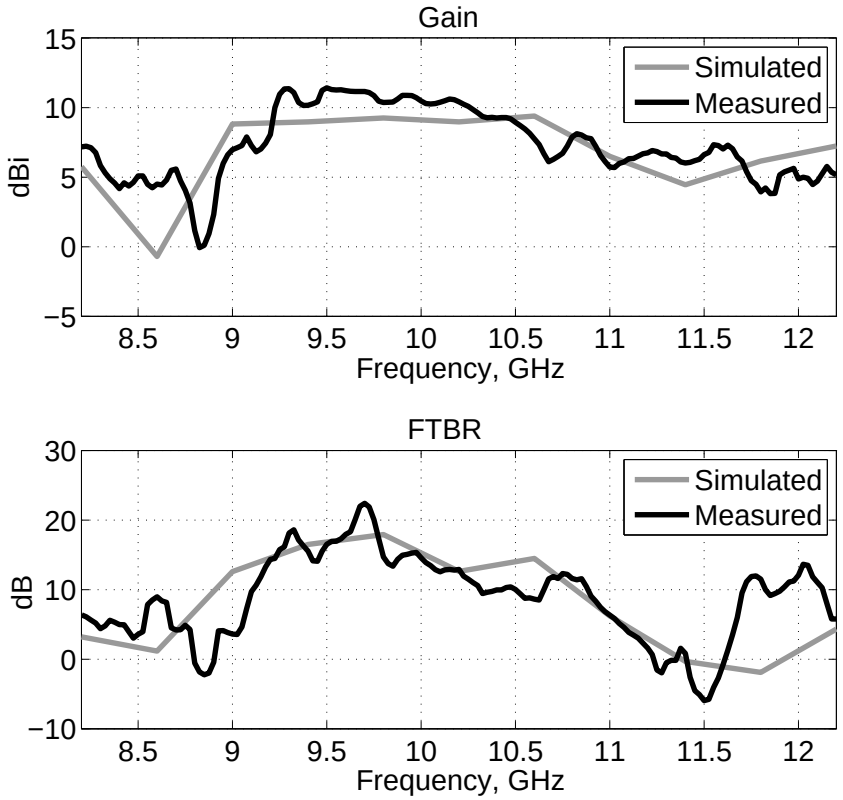

Figure 2.32: *2 layers 3D CEBG antenna simulated and measured gain (above) and front-to-back-ratio (below); P_r=15mm, r=2.5mm, ε_r=76.5 and h=20mm.*

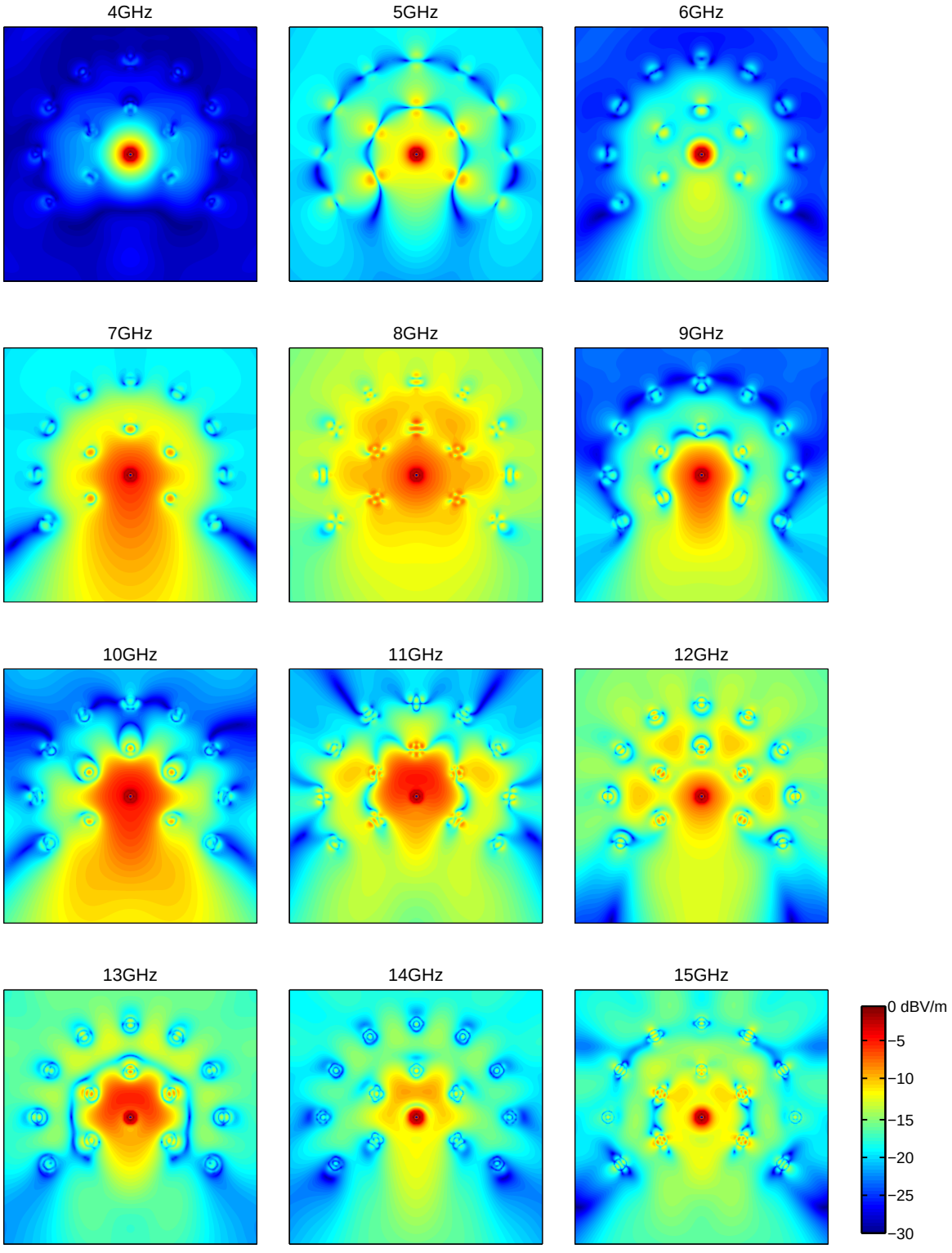

Figure 2.33: *3D CEBG antenna, simulated electric field distribution on the azimuthal plane, P_r=15mm, r=2.5mm, ε_r=76.5 and h=20mm.*

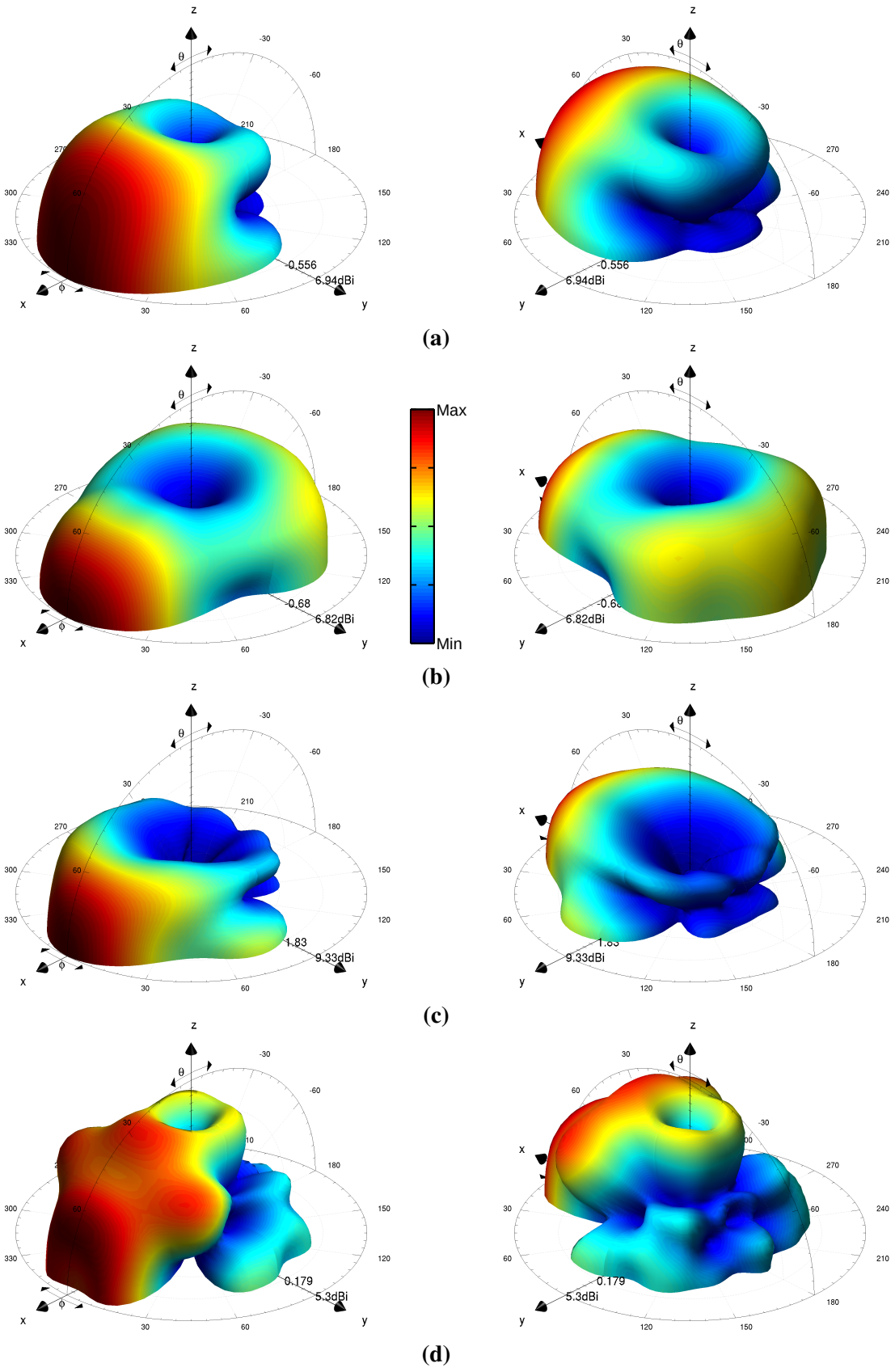

Figure 2.34: *3D CEBG antenna simulated 3D radiation patterns, P_r=15mm, r=2.5mm, ε_r=76.5 and h=20mm: a) 6.5GHz, b) 8GHz, c) 10GHz, d) 12.5GHz.*

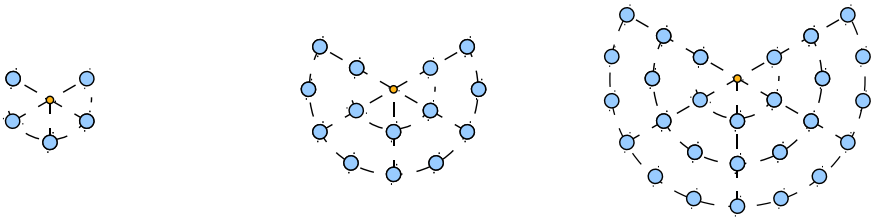

(a) **(b)** **(c)**

Figure 2.35: *CEBG antenna geometry as a function of layers: a) N_L=1; b) N_L=2; c) N_L=3.*

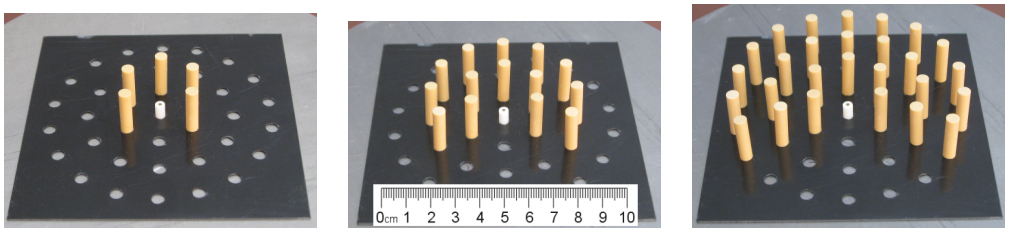

(a) **(b)** **(c)**

Figure 2.36: *CEBG antenna photo as a function of layers: a) N_L=1; b) N_L=2; c) N_L=3.*

2.3.3 Parametric study

As already mentioned in the previous sections, the geometrical parameters N_1, P_r and d along with ε_r are responsible for bandgaps position and extension, these parameters would be therefore chosen accordingly to antenna frequencies of operation. The remaining two geometrical parameters, h and N_L, have been parametrically studied to analyse their influence on the performance of the antenna; the probe length p has been kept constant in this parametric study.

2.3.3.1 Number of layers - N_L

Figure 2.37 shows the antenna S_{11} as a function of N_L (h=20mm). Increasing the number of layers improves the matching within the impedance bandwidth but the overall differences are very small. The S_{11} response also presents several resonances at higher and lower frequencies; it is interesting to note that the for N_L=1 the lower frequency resonances merge to form a second band between 6.8 and 8.5GHz. Radiation pattern is also influenced by the number of layers; as shown in figure 2.38-2.40 and summarised in table 2.5, increasing the number of layers improves antenna gain and directivity patterns. Gain and FTBR are considerably improved when the number of layers N_L is increased from 1 to 2 but differences are minimal when increased from 2 to 3.

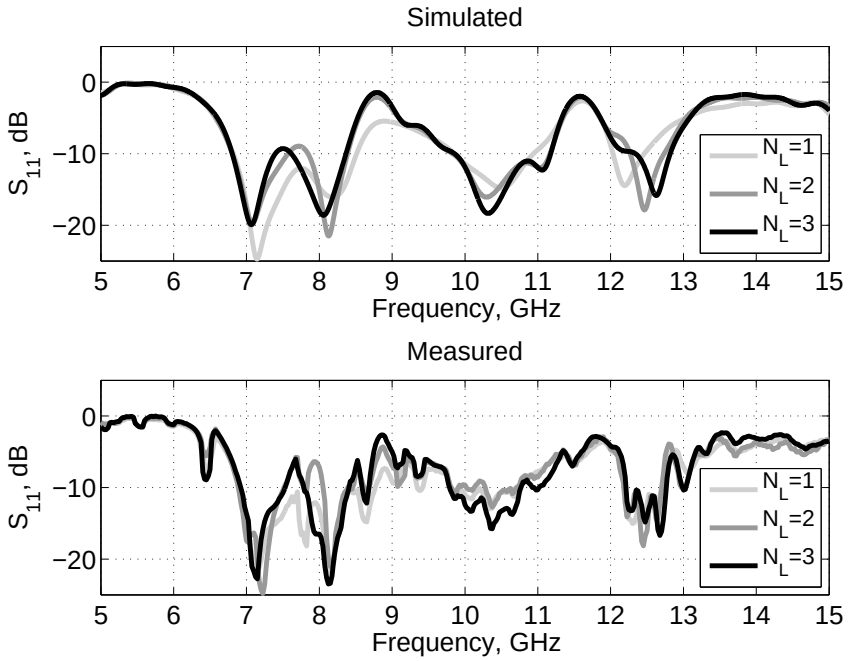

Figure 2.37: *3D CEBG antenna simulated and measured S_{11} as a function of number of layers N_L; P_r=15mm, r=2.5mm, ε_r=76.5 and h=20mm.*

N_L	Gain, dBi	FTBR, dB	Bandwidth	N_{rods}	Max dim.
1	9.6 (8.7)	10.2 (7.8)	9.8% 9.8-10.8GHz	5	$2 \cdot P_r$
2	11.4 (9.5)	22.4 (11.8)	8.8% 9.8-10.7GHz	14	$4 \cdot P_r$
3	11.4 (8.9)	25.1 (14.7)	11.5% 9.8-11.0GHz	27	$6 \cdot P_r$

Table 2.5: *3D CEBG antenna measured performance as a function of number of layers N_L; P_r=15mm, r=2.5mm, ε_r=76.5 and h=20mm (in brackets are reported the average values within the impedance bandwidth).*

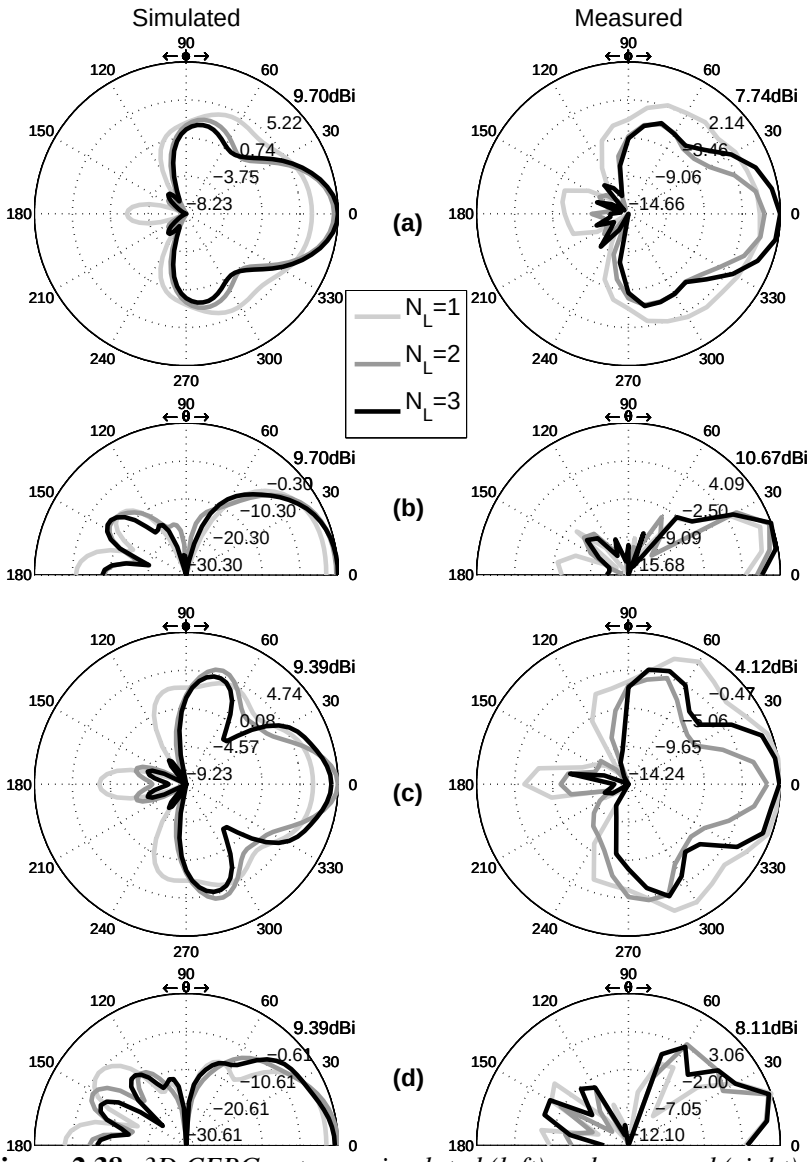

Figure 2.38: *3D CEBG antenna simulated (left) and measured (right) radiation patterns as a function of number of layers N_L; P_r=15mm, r=2.5mm, ε_r=76.5 and h=20mm: a) H-plane at 9.8GHz; b) E-plane at 9.8GHz; c) H-plane at 10.6GHz; d) E-plane at 10.6GHz.*

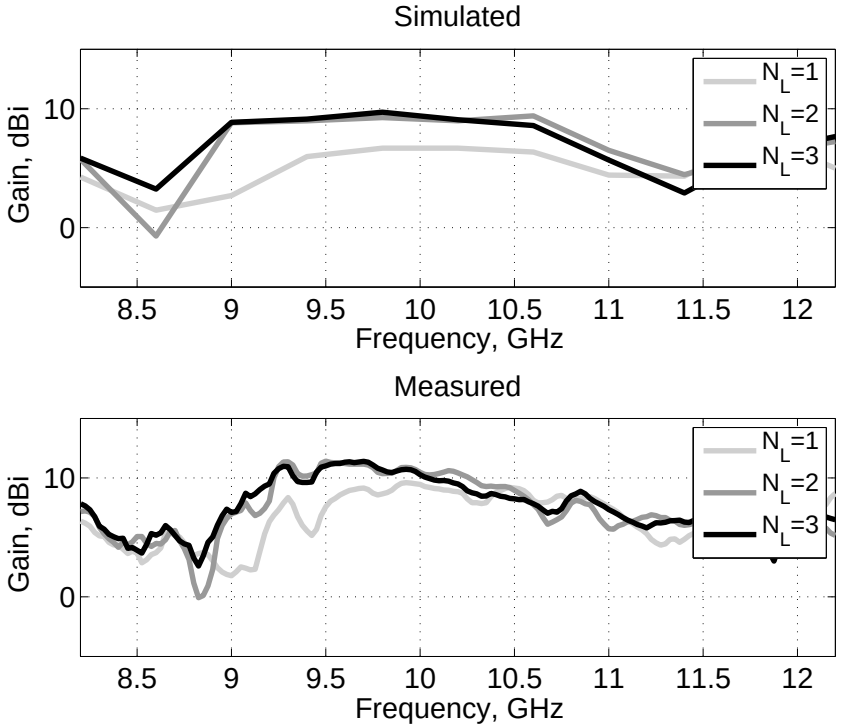

Figure 2.39: *3D CEBG antenna simulated and measured gain as a function of number of layers N_L; P_r=15mm, r=2.5mm, ε_r=76.5 and h=20mm.*

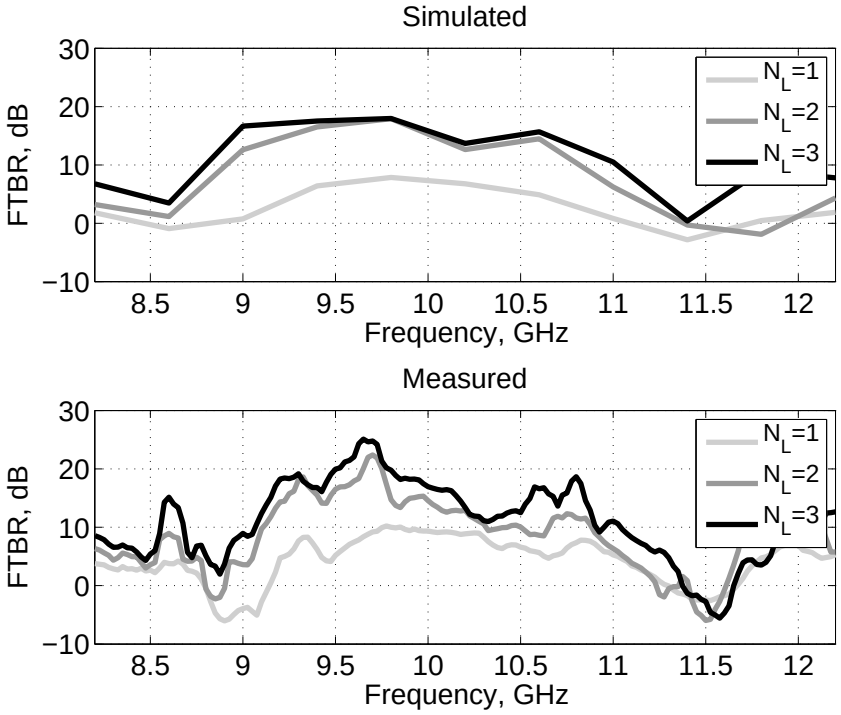

Figure 2.40: *3D CEBG antenna simulated and measured front-to-back-ratio (FTBR) as a function of number of layers N_L; P_r=15mm, r=2.5mm, ε_r=76.5 and h=20mm.*

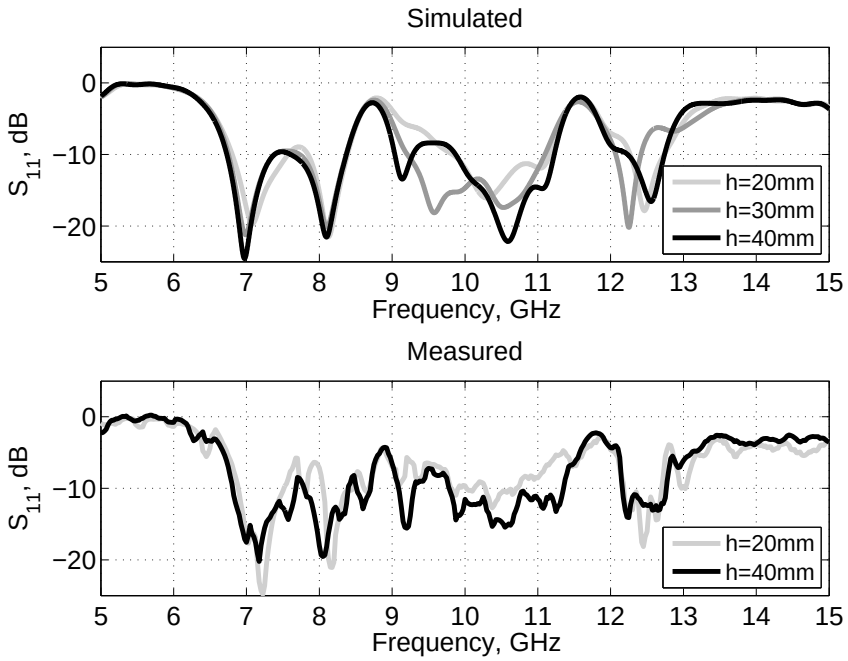

Figure 2.41: *3D CEBG antenna simulated and measured S_{11} as a function of rods length h; P_r=15mm, r=2.5mm, ε_r=76.5 and N_L=2.*

2.3.3.2 Rods length - *h*

The S_{11} of a 2 layer structure as a function of rods length *h* is show in figure 2.41. Rods length can significantly influence the frequency response of the antenna and as in the previous case a second band can appear between 6.8 and 8.5GHz. Simulations and measurements shown that increasing *h* generally improves directivity patterns, gain and FTBR, figure 2.42-2.44 and summarised in table 2.6. Impedance bandwidth can also be improved by tuning rods height *h*: simulations shown that with *h*=30mm bandwidth is 40% wider compared to *h*=20mm, figure 2.41; measurements were taken with *h*=20mm and 40mm, showing almost a 70% bandwidth increase in the latter case, figure 2.41.

h, mm	Gain, dBi	FTBR, dB	Bandwidth
20	11.4 (9.5)	22.4 (11.8)	8.8 % 9.8-10.7GHz
40	12.0 (10.2)	27.0 (16.0)	14.9% 9.8-11.4GHz

Table 2.6: *3D CEBG antenna measured performance as a function of rods length h; P_r=15mm, r=2.5mm, ε_r=76.5 and N_L=2 (in brackets are reported the average values within the impedance bandwidth).*

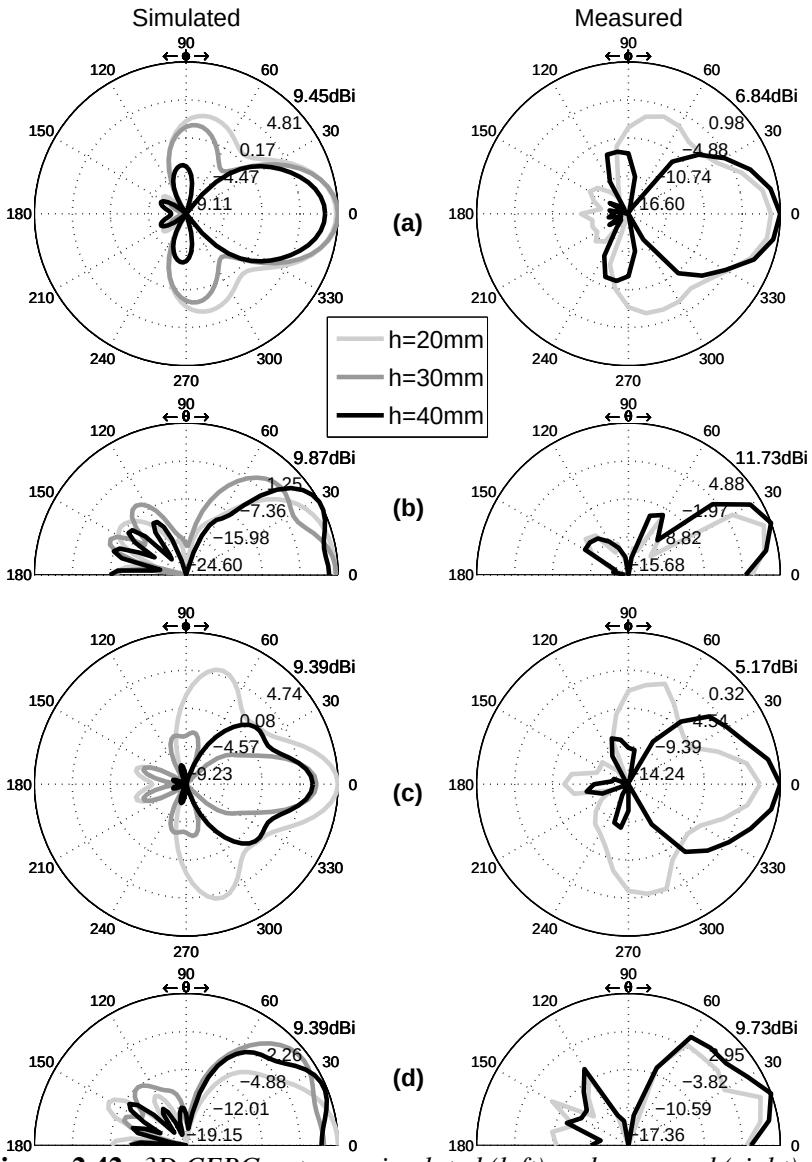

Figure 2.42: *3D CEBG antenna simulated (left) and measured (right) radiation patterns as a function of rods length h; P_r=15mm, r=2.5mm, ε_r=76.5 and N_L=2: a) H-plane at 9.8GHz; b) E-plane at 9.8GHz; c) H-plane at 10.6GHz; d) E-plane at 10.6GHz.*

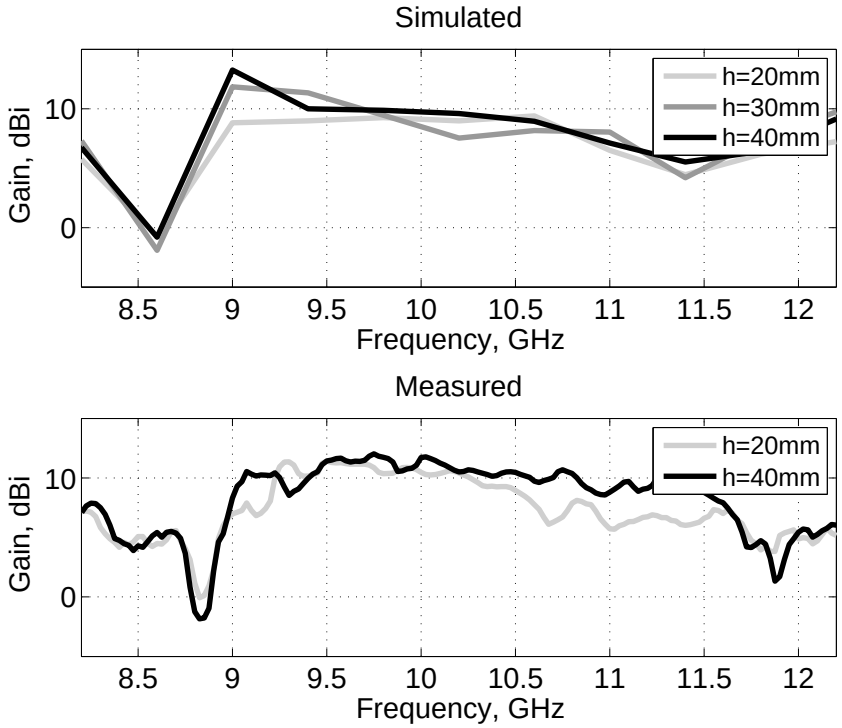

Figure 2.43: *3D CEBG antenna simulated and measured gain as a function of rods length h; P_r=15mm, r=2.5mm, ε_r=76.5 and N_L=2.*

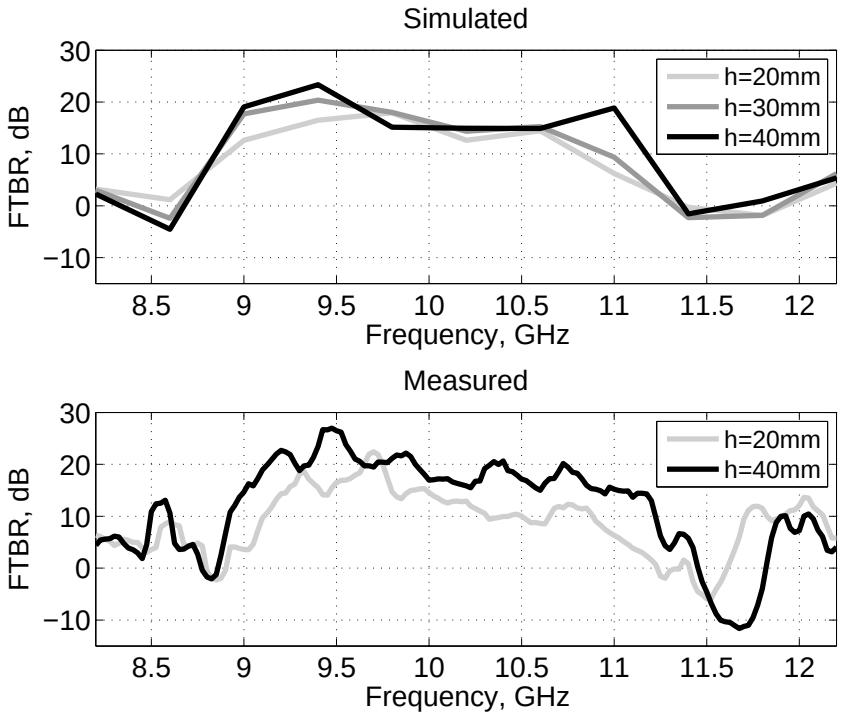

Figure 2.44: *3D CEBG antenna simulated and measured front-to-back-ratio (FTBR) as a function of rods length h; P_r=15mm, r=2.5mm, ε_r=76.5 and N_L=2.*

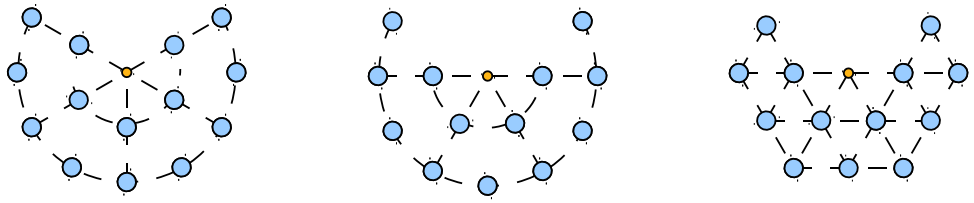

(a) *CEBG1* **(b)** *CEBG2* **(c)** *TEBG*

Figure 2.45: *Alternative geometries.*

2.3.4 Summary and Discussion

The proposed dielectric CEBG (DCEBG) antenna is based on a cylindrical geometry similar to the 4 layers metallic CEBG (MCEBG) antenna presented and analysed by Boutayeb et al in [43–45].

The MCEBG antenna achieved a higher peak gain and a wider fractional impedance bandwidth, respectively 15.8dBi and 28%, compared to the presented DCEBG antenna, 11.4dBi peak gain and 11% bandwidth. However, the DCEBG antenna has smaller relative dimensions: 20% narrower diameter (2λ against 2.4λ) and 50% lower profile (0.67λ against 1.33λ). Moreover the required number of rod elements is much lower, 14 dielectric rods are used for the DCEBG antenna and 96 metallic rods for the MCEBG antenna.

The parametric study shown that increasing the number of layers N_L slightly influences the bandwidth of the antenna but improves radiation patterns and maximum gain, as reported in [45], though the differences between 2 or 3 layers are minimal. This suggests that 2 layers are a good compromise in terms of antenna performances and dimensions for the presented DCEBG antenna.

Rods length h also influence matching and radiation patterns and it can be set in order to optimize gain and bandwidth extension: 2 layers configuration with h=40mm achieved 15% fractional bandwidth (70% wider compared to h=20mm), and higher peak gain and front-to-back-ratio, respectively 12dBi and 27dB.

2.4 Alternative geometries

The defect window used in the presented CEBG antenna has been create by removing $2n-1$ rods from the n-th layer; alternative defect windows and geometries can be also used to create multilayers EBG structures. Figure 2.45 shows the used geometry, *CEBG1*, along with an alternative defect window configuration, *CEBG2*, and an alternative multilayer structure based on a triangular lattice, *TEBG*. Configurations *CEBG2* and *TEBG*

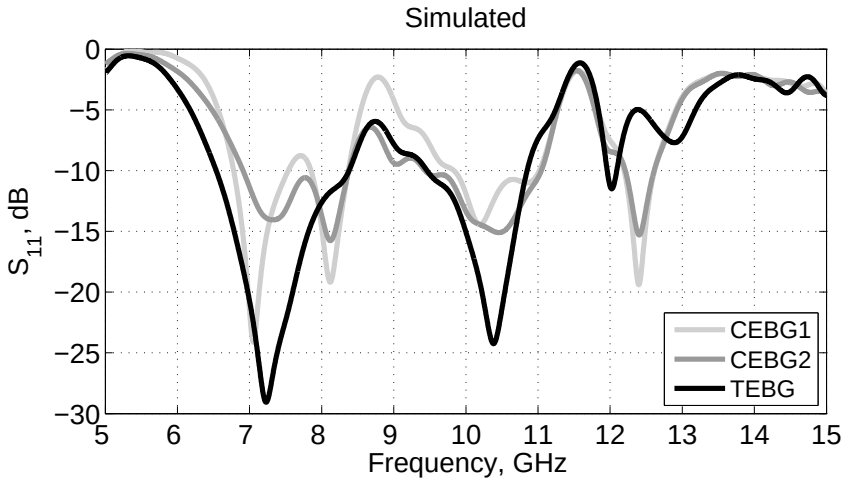

Figure 2.46: *Alternative geometries, simulated* S_{11}

are created by removing $n+1$ rods from the n-th layer and they are quite similar to each other, although structures with 3 or more layers would show more discrepancies in terms of rods positioning as the number of layers increases.

The simulated S_{11} response of these three configurations is compared in figure 2.46, showing that configuration *TEBG* can achieve a better impedance matching and, along with configuration *CEBG2*, a second band between 6.6GHz and 8.2GHz. Simulated gain and FTBR are shown in figure 2.47: *CEBG2* and *TEBG* present a very similar gain but *TEBG* achieved a higher FTBR between 8GHz and 11GHz. The radiation patterns shown in figure 2.48 basically confirm that *TEBG* and *CEBG2* can achieve similar results in terms of maximum gain but the former presents a higher FTBR and lower sidelobes up to 11GHz raising the maximum frequency of operation. Figure 2.47-2.48 also show that both *CEBG2* and *TEBG* configurations present directive radiation patterns between 5.5GHz and 7.5GHz and therefore these configurations could be used for dual band applications.

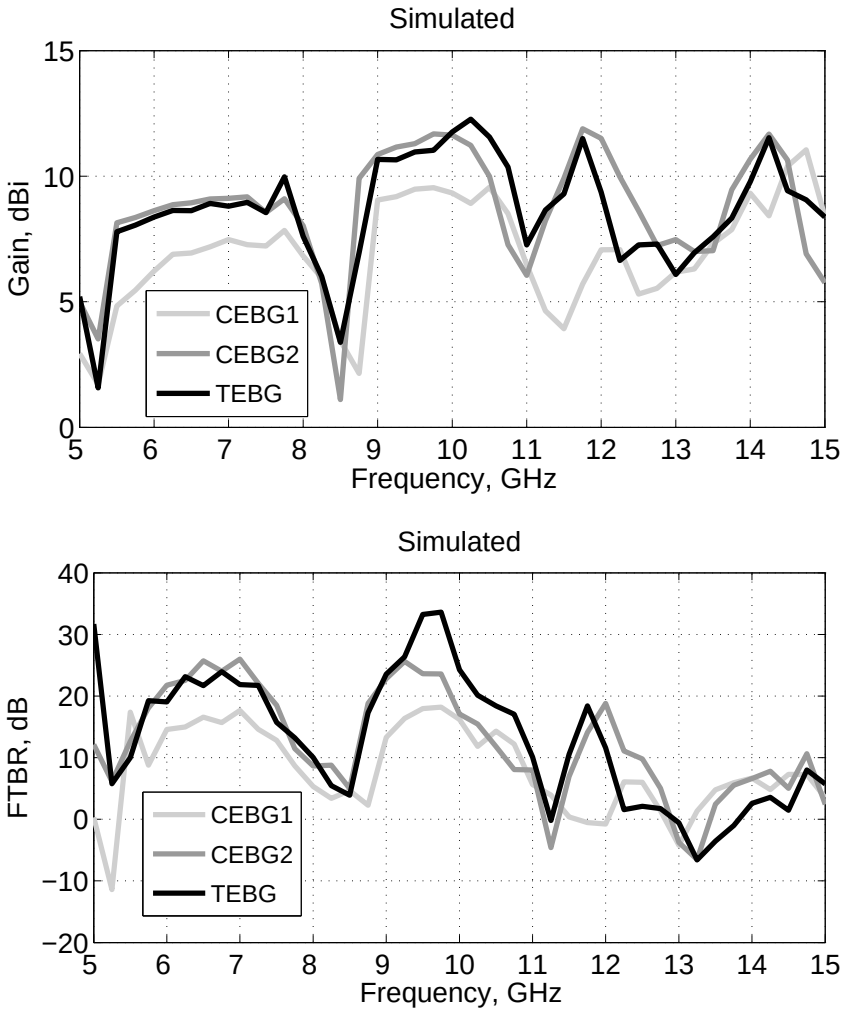

Figure 2.47: *Alternative geometries, simulated gain and FTBR comparison.*

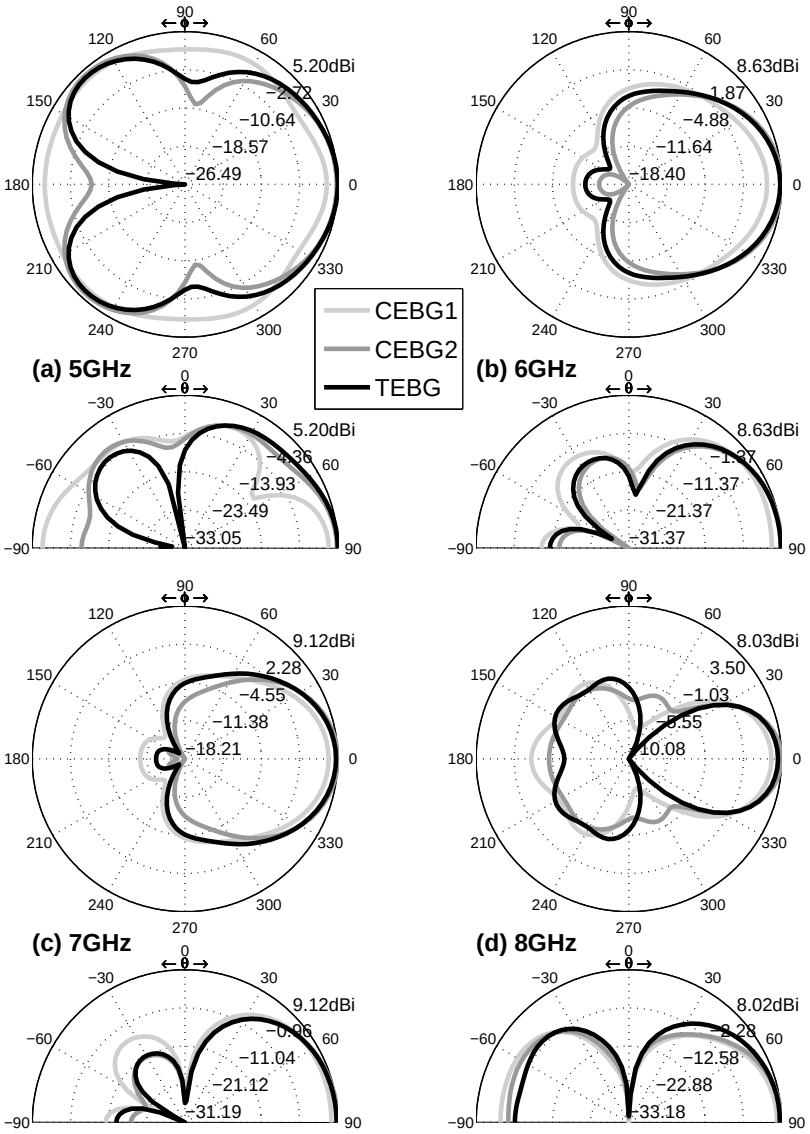

Figure 2.48: *Alternative geometries, simulated radiation patterns comparison.*

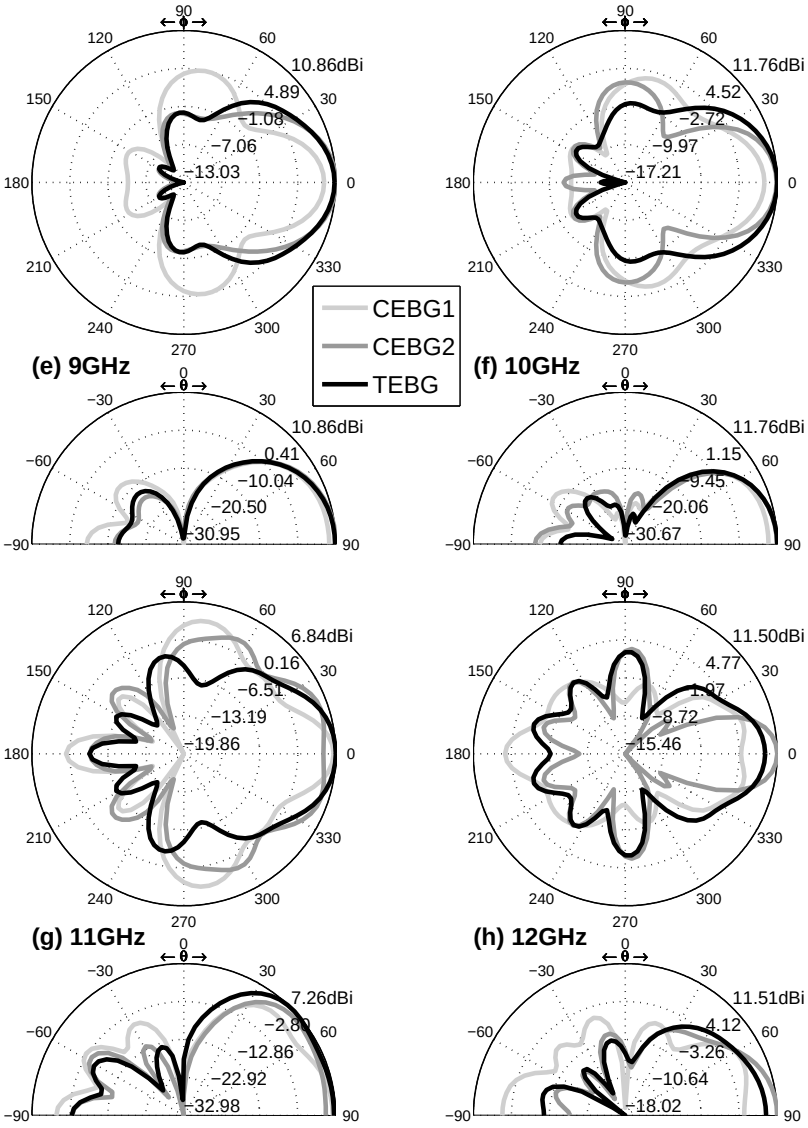

Figure 2.48: *Alternative geometries, simulated radiation patterns comparison.*

2.5 Conclusions

The design steps of a dielectric CEBG antenna have been presented and confirmed by the good agreement between simulations and experimental parametric studies. Several prototypes were realized using dispersive and lossy dielectric materials, i.e. water, as well as ceramic materials, modified barium titanate ε_r=76.5$\pm$2 [81].

Water prototypes achieved a 50% fractional bandwidth and high directivity patterns on the H-plane within the impedance bandwidth, average gain of 8.2dBi with 18.7dB average front-to-back-ratio. Ceramic prototypes achieved a higher gain, 9.5dBi but a narrower bandwidth, 11% and a lower front-to-back-ratio, 13dB. As discussed in Section 2.3, ceramic rods dielectric permittivity is an additional degree of freedom to consider in the design process and can be set, among with geometrical parameters, to optimize bandgap position and extension according to the frequency of operation.

Antennas were designed to operate at 10GHz in order to take advantage of our lab facilities; scaling down or up the geometrical parameters will respectively scale up or down of the same factor the frequency characteristics of the antenna.

A parametric study based on FDTD simulations and prototypes measurements have been also presented. The aim of this study was to investigate the relationship between antenna geometrical parameters and performances, focusing on the parameters which are not bound during the design process by bandgap position and frequency of operation, i.e. rods height h and number of layers N_L.

Performances can be improved by using different defect window geometries as well as different EBG structure geometries: a brief comparative study of the presented CEBG antenna with an antenna based on a triangular lattice shown that the latter, along with a different defect window geometry, could achieve better impedance matching and higher gain and FTBR as well as dual band capabilities.

Chapter 3 – Multilayer triangular lattice EBG antennas

3.1 Introduction

The multilayer CEBG structure presented in the previous chapter was shown to be able to achieve directive radiation patterns on the azimuthal plane. The cylindrical lattice though, does not present a high level of symmetry: the crystal is built around a privileged axis and although radial and transverse period are kept constant, as the number of layers increases, the distance between neighbouring rods is not constant and varies between two limit cases, as shown in figure 3.1a-b. The first case resemble a triangular geometries in which the lattice vectors $\mathbf{a}_1$ and $\mathbf{b}_1$ are:

$$\begin{aligned}
\mathbf{a}_1 &= P_t \cdot \hat{\mathbf{y}} = \frac{2\pi P_r}{N_1} \cdot \hat{\mathbf{y}} = \frac{\pi P_r}{3} \cdot \hat{\mathbf{y}} \simeq 1.045 P_r \cdot \hat{\mathbf{y}} \\
&|\mathbf{a}_1| \simeq 1.045 P_r \\
\mathbf{b}_1 &= P_r \cdot \hat{\mathbf{x}} + \frac{P_t}{2} \cdot \hat{\mathbf{y}} \\
&|\mathbf{b}_1| = \sqrt{P_r^2 + \left(\frac{P_t}{2}\right)^2} = P_r \sqrt{1 + \left(\frac{2\pi}{2N_1}\right)^2} = P_r \sqrt{1 + \left(\frac{\pi}{6}\right)^2} \simeq 1.274 P_r
\end{aligned} \tag{3.1}$$

with $\hat{\mathbf{x}}$ and $\hat{\mathbf{y}}$ being the cartesian unit vectors and N_1 the number of dielectric rods in the first layer. The second case resemble a rectangular geometry with lattice vectors $\mathbf{a}_2$ and $\mathbf{b}_2$ equal to:

$$\begin{aligned}
\mathbf{a}_2 &= P_t \cdot \hat{\mathbf{y}} \simeq 1.045 P_r \cdot \hat{\mathbf{y}} \\
&|\mathbf{a}_2| \simeq 1.045 P_r \\
\mathbf{b}_2 &= P_r \cdot \hat{\mathbf{x}} \\
&|\mathbf{b}_2| = P_r
\end{aligned} \tag{3.2}$$

In Section 2.4 a triangular lattice EBG (TEBG) structure was found more effective than a CEBG structure of similar dimensions. The triangular lattice, compared to the CEBG lattice, presents a higher level of symmetry where both lattice vectors $\mathbf{a}_T$ and $\mathbf{b}_T$

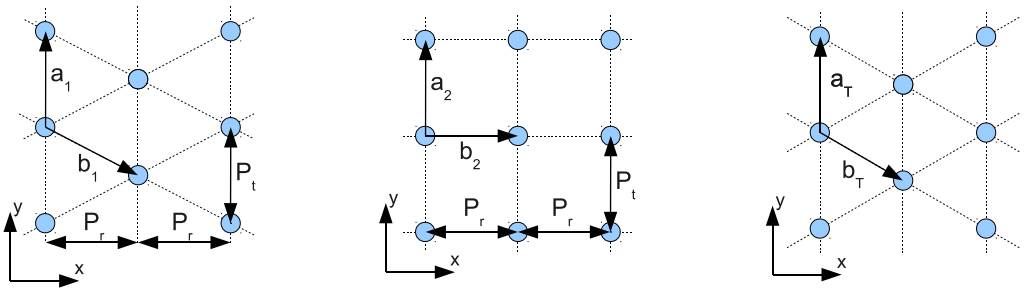

(a) **(b)** **(c)**

Figure 3.1: *Lattice vectors.*

have the same magnitude equals to the lattice constant a, figure 3.1c:

$$\begin{aligned}
\mathbf{a}_T &= a \cdot \hat{\mathbf{y}} \\
|\mathbf{a}_T| &= a \\
\mathbf{b}_T &= \frac{a}{2}\left(\hat{\mathbf{x}}\sqrt{3} + \hat{\mathbf{y}}\right) \\
|\mathbf{b}_T| &= \frac{a}{2}\sqrt{\sqrt{3}^2 + 1} = \frac{a}{2}2 = a
\end{aligned} \tag{3.3}$$

Moreover, the intrinsic symmetry of the lattice can be exploited to create structures with multiple feeds.

In the next sections the design steps, simulations and measurements results of single feed and multiple feed multilayer EBG antennas based on a triangular lattice of dielectric rods are presented.

3.2 EBG Structure Characterization

The 2D triangular EBG structure is realized arranging dielectric rods of radius r in a simple triangular geometry according to the lattice constant a, figure 3.2.

2D TEBG antennas are created in a similar fashion to 2D CEBG antennas: if we excite a TM mode in a cavity created by removing a dielectric rod from the lattice, figure 3.2a, energy at frequencies outside the bandgap will be free to propagate through the structure whilst energy at frequencies within the bandgap will be trapped in the cavity; trapped energy can be directed toward a specific direction by creating an angular defect in the structure. Figure 3.2b shows a 2D TEBG antenna realized with dielectric rods arranged in a multilayer triangular lattice around an infinite long axial current line source (J) placed in the axis. An angular defect windows has been created in the TEBG structure by removing $n+1$ rods from the n-th layer.

Two methods have been used to characterize the EBG structure:

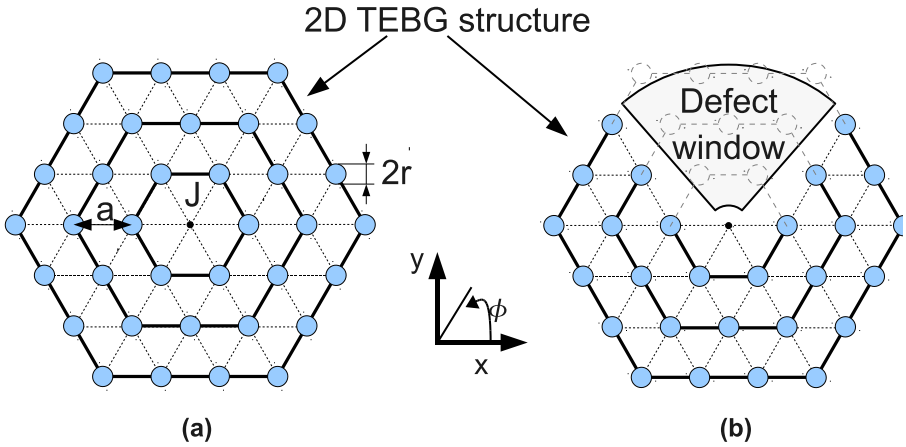

Figure 3.2: *a) 2D TEBG structure; b) 2D TEBG antenna.*

- the electromagnetic band structure of a 2D structure of infinite extension was computed using a planewave eigensolver in order to identify bandgaps position and extension;
- the transmission coefficient of a multilayer 2D structure with a finite number of layers was then computed, using the FDTD solver, in order to assess the stopband behaviour of a structure of finite dimensions.

3.2.1 Electromagnetic Band Structure

The triangular lattice EBG (TEBG) structure may present a complete bandgap for TM polarized waves which extension and position are a function of the rods permittivity ε_r, radius r and the lattice constant a. A plane-wave eigensolver, Appendix B, has been used to compute the electromagnetic band structure for the TM modes of a triangular lattice of dielectric columns for several values of r, a and ε_r. The results of this parametric study can be visualized in gapmaps as shown in figure 3.3, 3.8 and 3.9.

Figure 3.3 shows the gapmap for several values of r/a as a function of rods permittivity ε_r. When r/a is chosen smaller than 0.1 a single bandgap is present; for values greater than 0.15 several bandgaps of narrower extension appear, therefore a value in the 0.1-0.15 region would provide the widest single bandgap regardless of the rods permittivity.

Several simulations were run to select the dielectric permittivity and geometrical parameters a and r of a set of possibile candidates for the realization of an antenna prototype, figure 3.4. Following a similar approach to Chapter 2, we focused our attention on permittivity values of ceramics available on the market. The multilayer CEBG antenna presented and analysed in Chapter 2 was build using a ceramic material with dielectric permittivity ε_r=76.5; simulations shown that lower dielectric permittivity ceramics could

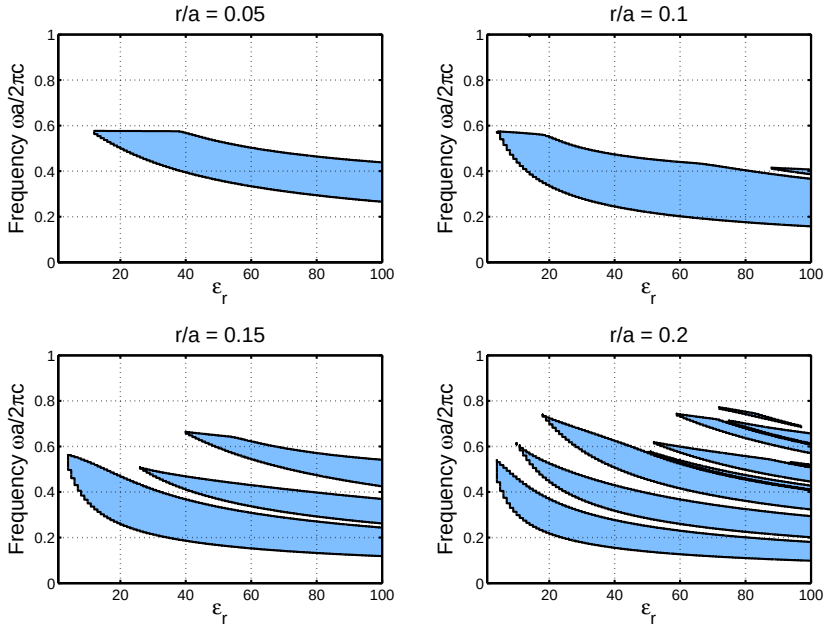

Figure 3.3: *Simulated electromagnetic gapmaps as a function of rods permittivity ε_r for several values of r/a.*

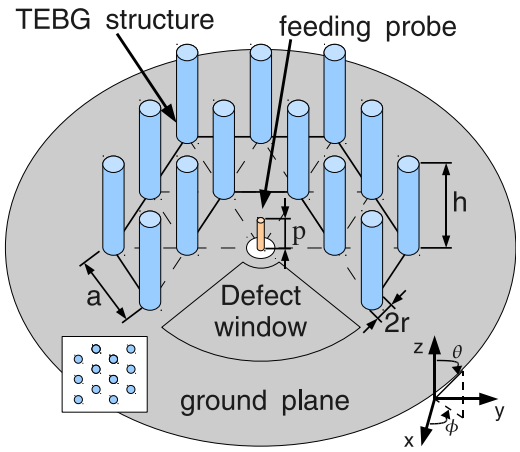

Figure 3.4: *TEBG antenna geometry and triangular lattice of circular dielectric rods (inset).*

be used though, figure 2.25-2.26, and we therefore considered ceramic materials with ε_r <40 to prove the concept (low dielectric permittivity materials are usually cheaper as well). The best preliminary results were achieved with the combinations of a, r and ε_r summarised in table 3.1.

The S_{11} response, radiation patterns (at frequencies within the bandgaps), gain and FTBR of the selected candidates are shown in figure 3.5-3.7. At frequencies within the individual bandgap, all models have radiation patterns with a main beam on the azimuthal plane in the angular aperture direction presenting a high gain and FTBR. In the 8GHz-9GHz frequency range, all models achieved similar performances in terms of gain and FTBR, figure 3.7, but sidelobes level and beamwidth tend to be respectively lower and

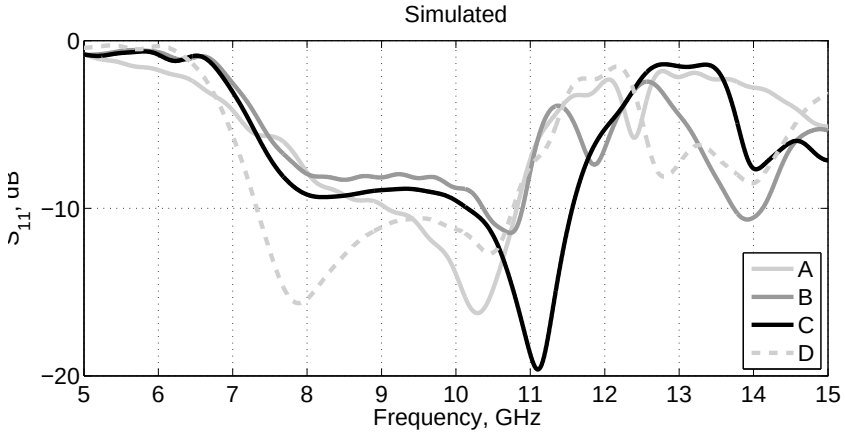

Figure 3.5: *TEBG antenna with N_L=2 and h=20mm, selected models simulated S_{11} (feeding probe length was adjusted in each case for optimal matching):*
A - a=15mm, r=2mm and ε_r=9.8;
B - a=12mm, r=2mm and ε_r=20;
C - a=12.5mm, r=1.5mm and ε_r=30;
D - a=13mm, r=1.5mm and ε_r=37.

narrower for models with a higher dielectric permittivity. In terms of impedance matching, model *D* achieved the wider bandwidth although the other models performances could be improved by tuning the feed geometry or dimensions rather than using the standard coaxial transition modeled in the simulations and used to build prototypes (see Section 3.3.3).

Therefore, in order to achieve the best overall performances in terms of impedance bandwidth and radiative properties, we adopted model *D* as a base for prototype analysis and design using dielectric rods made with modified zirconium tin titanate D36 supplied by Morgan Electroceramics [81]; as in Chapter 2, ceramic rods were simulated using the dielectric permittivity and loss tangent values supplied on the manufacturer catalogue, ie $\varepsilon_r = 37 \pm 1$ and $tan\delta = 0.24 \cdot 10^{-3}$.

In figure 3.8 are presented gapmaps for several values of *a* as a function of *r* with ε_r=37. As *r* is increased, new bandgaps appear; bandgaps frequency and extensions are generally decreasing as *r* is increased. Figure 3.9 (gapmaps are plotted as a function of *a* for several values of *r* with ε_r=37) shows that, when *r* is fixed, a minimum value of *a* is

Name	*a*, mm	*r*, mm	ε_r	$tan\delta$	Bandgap, GHz
A	15	2	9.8	$10 \cdot 10^{-3}$	7.51-10.86
B	12	2	20	$0.14 \cdot 10^{-3}$	6-10.85
C	12.5	1.5	30	$0.1 \cdot 10^{-3}$	5.98-11.69
D	13	1.5	37	$0.24 \cdot 10^{-3}$	5.28-10.95

Table 3.1: *TEBG antenna with N_L=2, selected candidates geometrical properties and dielectric permittivity.*

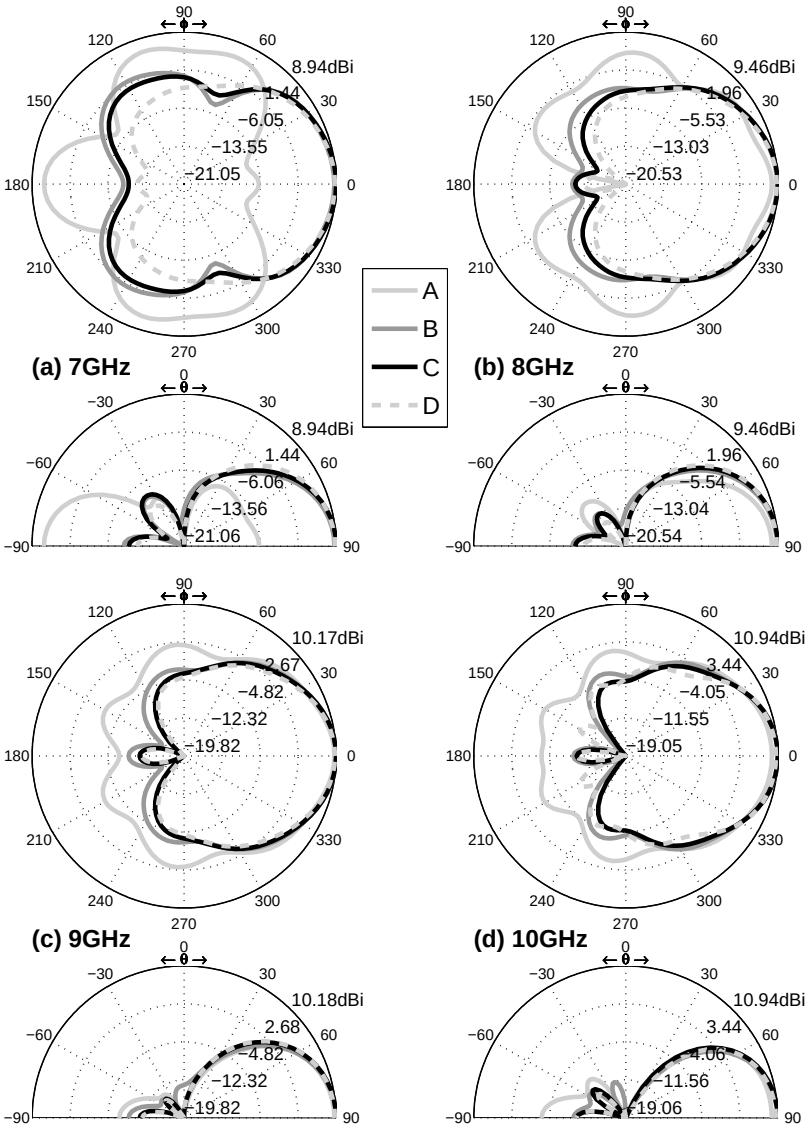

Figure 3.6: *TEBG antenna with N_L=2 and h=20mm, selected models simulated radiation patterns within the bandgap:*
A - a=15mm, r=2mm and ε_r=9.8;
B - a=12mm, r=2mm and ε_r=20;
C - a=12.5mm, r=1.5mm and ε_r=30;
D - a=13mm, r=1.5mm and ε_r=37.

required for bandgaps to appear; bandgaps extension initially grows as r is increased and after reaching a maximum is then reduced.

These gapmaps are very useful to design the geometrical parameters of the antenna. When ε_r is equal to 37, a maximum extension for a single bandgap is obtained when r/a=0.115; r and a can be set using figure 3.8 and figure 3.9 according to the required frequency of operation. Figure 3.10 shows the electromagnetic band structure for a triangular lattice with a=13mm, r=1.5mm ($r/a = 0.1154$) and ε_r=37: a 69.9% complete TM bandgap is present from 5.28GHz to 10.95GHz, making this structure very attractive to build wideband TEBG antennas.

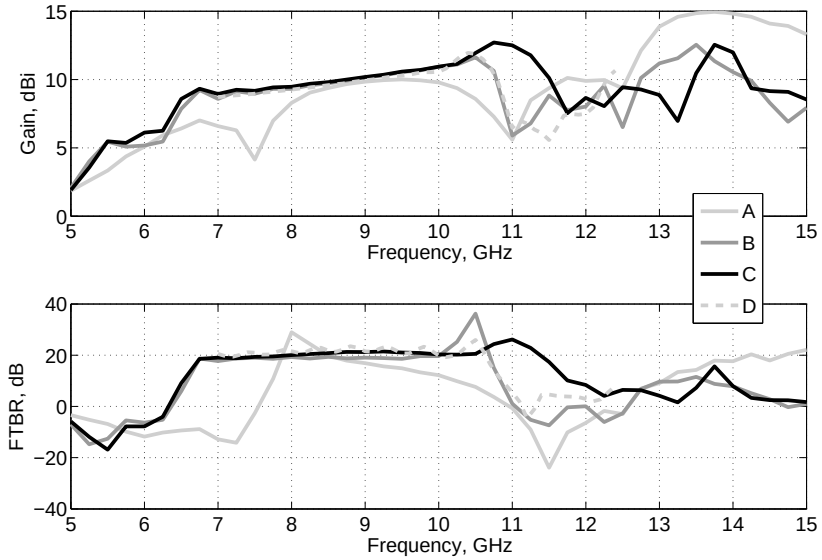

Figure 3.7: *TEBG antenna with N_L=2 and h=20mm, selected models simulated gain and FTBR:*
A - a=15mm, r=2mm and ε_r=9.8;
B - a=12mm, r=2mm and ε_r=20;
C - a=12.5mm, r=1.5mm and ε_r=30;
D - a=13mm, r=1.5mm and ε_r=37.

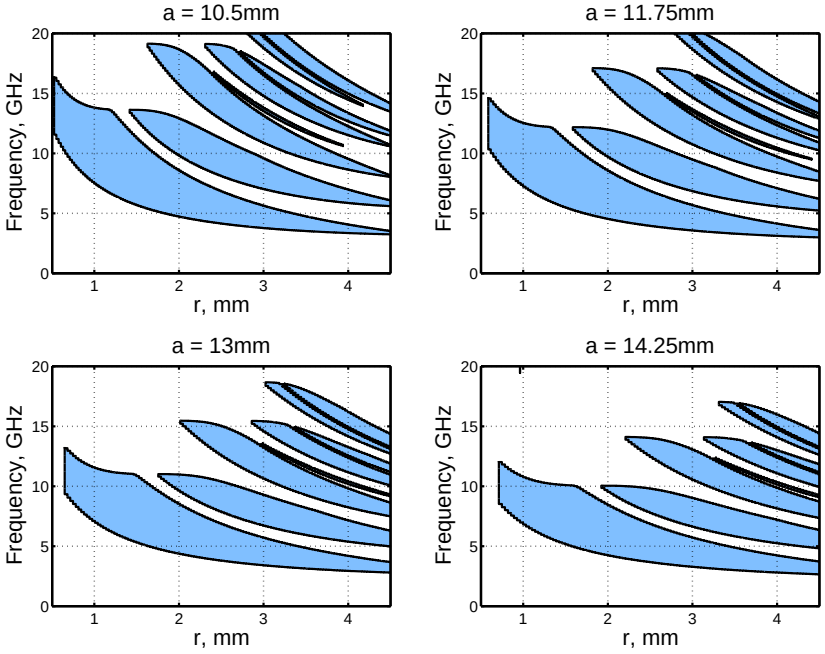

Figure 3.8: *Simulated electromagnetic gapmaps as a function of rods radius r for several values of lattice constant a, ε_r=37.*

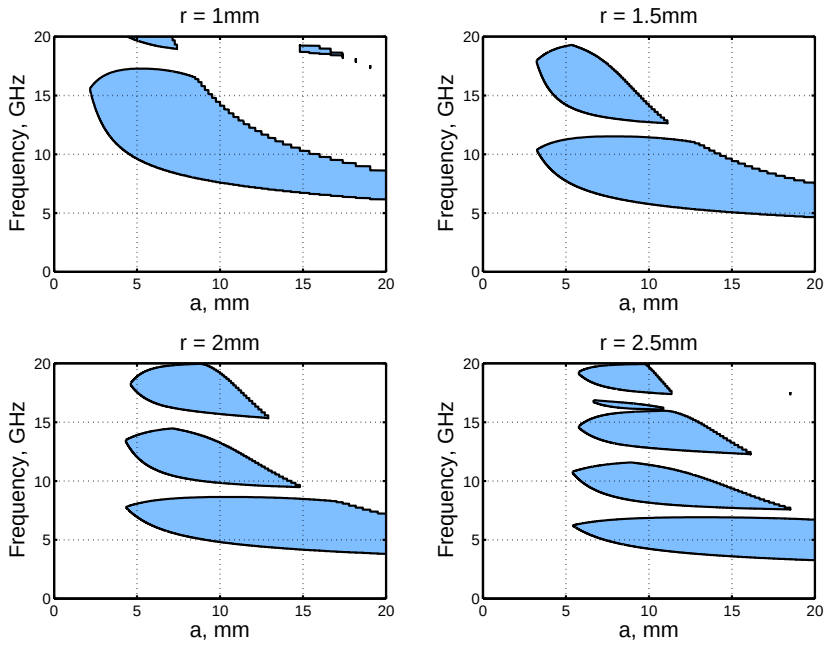

Figure 3.9: *Simulated electromagnetic gapmaps as a function of lattice constant a for several values of rods radius r, ε_r=37.*

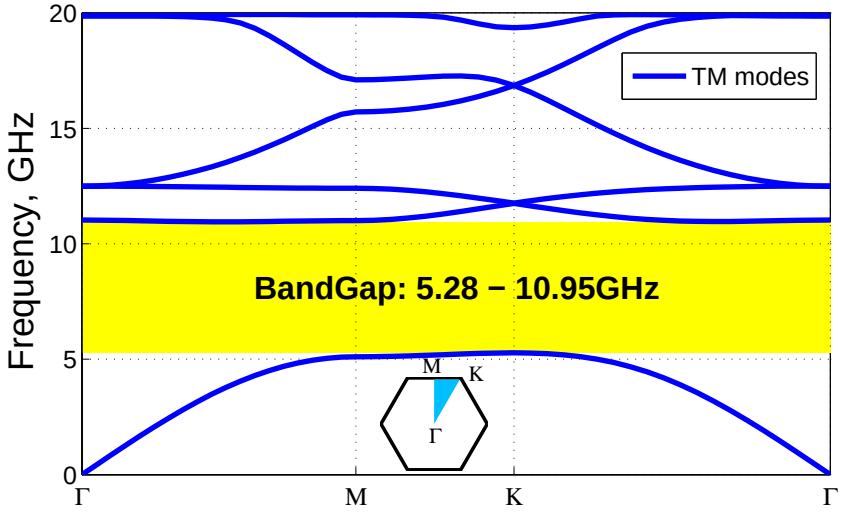

Figure 3.10: *Simulated electromagnetic band structure for the TM modes of a two-dimensional triangular lattice of dielectric columns with a=13mm, r=1.5mm,ε_r=37.*

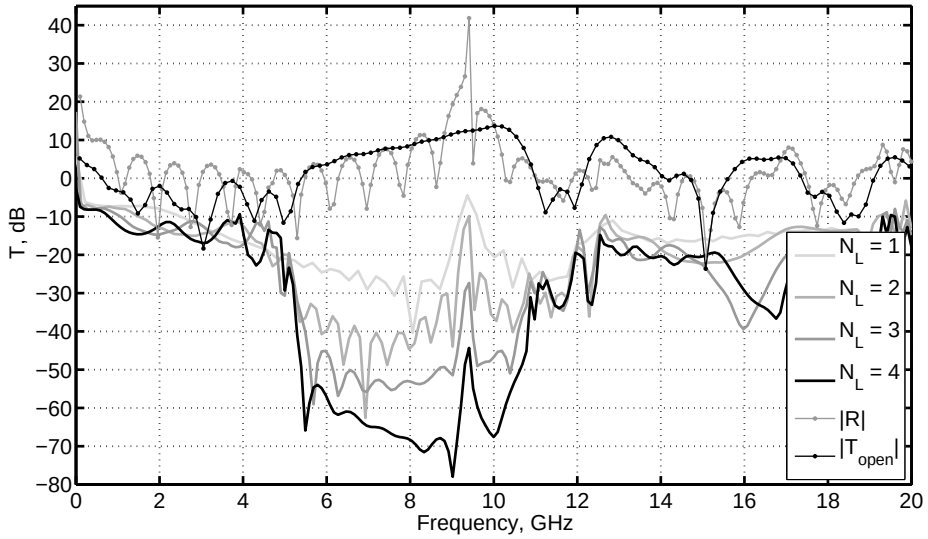

Figure 3.11: *Simulated transmission coefficient T as a function of number of layers N_L; a=13mm, r=1.5mm and ε_r=37.*

3.2.2 Transmission coefficients of a finite number of layers

The electromagnetic band structure computed in the previous section is valid for a 2D structure of infinite extension. Since the antennas cannot be realized using an infinite structure, the transmission coefficient of a 2D TEBG structure with a finite number of layers, figure 3.2a, has been computed.

The structure is fed by an infinite long current line source (J) placed in the axis which excites a TM cylindrical wave. The transmission coefficient T is extracted by normalizing the transverse electric field $E(x_p,y_p)|_{TEBG}$ recorded when the TEBG structure is present with the transverse electric field $E(x_p,y_p)|_0$ recorded when the TEBG structure is not present:

$$T = \frac{E(x_p,y_p)|_{TEBG}}{E(x_p,y_p)|_0} \tag{3.4}$$

Figure 3.11 shows the computed transmission coefficient as a function of number of layers N_L as well as the normalized field magnitude inside the cavity R, and the transmission coefficient T_{open} computed in front of the structure when a defect window is introduced. A clear stop-band behaviour is visible from 5GHz to 12GHz, which is very close to the bandgap frequencies computed in the previous section. The peaks at 9.5GHz are caused by the cavity resonance as demonstrated by the inner field distribution R and by the transmission coefficient T_{open}: once the cavity is opened the peak is not visible any more.

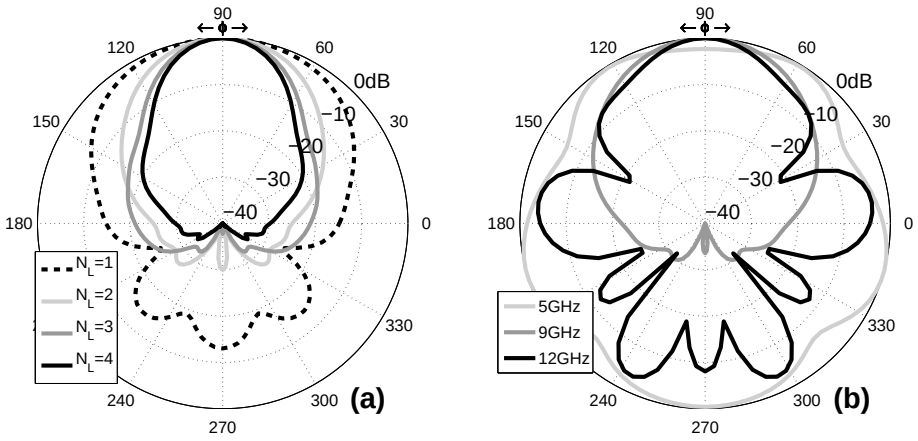

Figure 3.12: *2D TEBG antenna simulated radiation patterns, a=13mm, r=1.5mm and ε_r=37: a) as a function of number of layers N_L at 10GHz; b) as a function of frequency for a 2 layers structure (bandgap at 5.28-10.95GHz, figure 3.10).*

A 2D TEBG structure with a defect window can be therefore used to realize an antenna with directive patterns expected at bandgap frequencies. Figure 3.2b shows the 2D TEBG antenna structure; simulated radiation patterns as a function of number of layers N_L and frequency are shown in figure 3.12 whilst the normalised electric field distribution as a function of frequency is reported in figure 3.13. Two layers were found again a good compromise in terms of directivity and antenna dimensions, figure 3.12a. As expected, the antenna is very directive at frequencies within the 2D TEBG structure bandgap: figure 3.12b shows that at lower frequencies, 5GHz, the antenna presents a quasi-omnidirectional behaviour whilst at higher frequencies, 12GHz, the radiation pattern presents several lobes with comparable magnitude; at 9GHz, within the bandgap, the antenna is very directive.

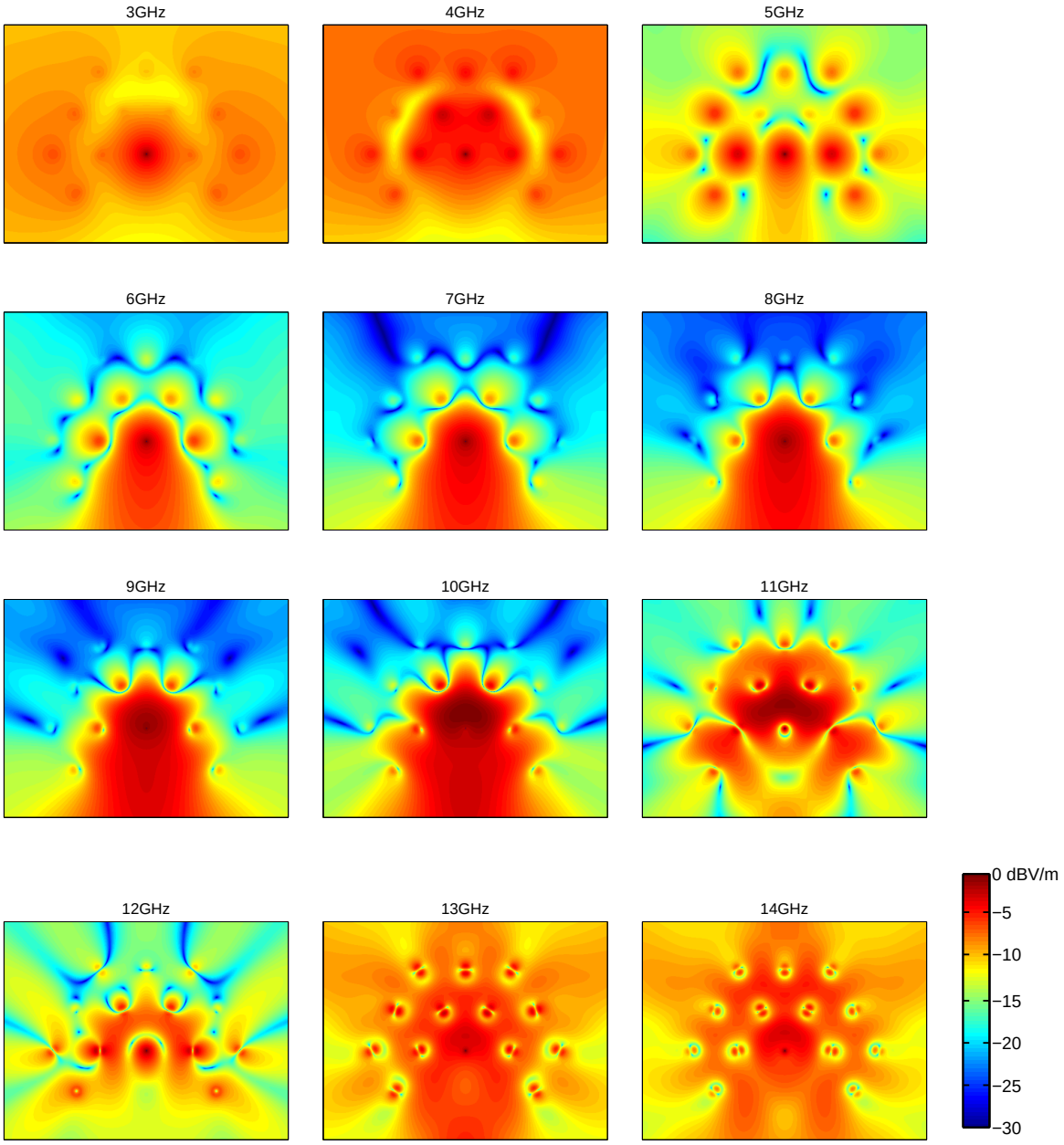

Figure 3.13: *2D TEBG antenna, simulated normalised electric field distribution, a=13mm, r=1.5mm and* ε_r*=37.*

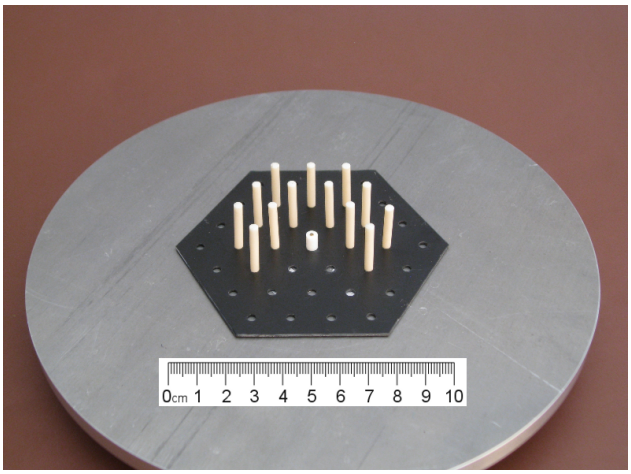

Figure 3.14: *Single-feed TEBG antenna prototype.*

3.3 Single-feed TEBG Antenna

A 3D TEBG antenna, figure 3.14, has been realized with dielectric rods of length h=20mm, radius r=1.5mm and ε_r=37$\pm$1 (D36 modified zirconium tin titanate [81]) arranged in a triangular lattice with a=13mm; excitation is given through a monopole feed of length p=6.9mm. This structure, as mentioned in the previous section, is based on the approximation of a 2D triangular lattice (made with infinite long dielectric rods) using ceramic rods of height h. For low elevation angles, the excited fields have a distribution very similar to the 2D configuration: the 3D TEBG structure is a good approximation of the 2D structure and, at frequency within the bandgap, a high attenuation is expected in the TEBG structure direction. For increasing elevation angles, the 3D TEBG structure approximation of the 2D structure progressively fails; however, given the intrinsic configuration of the excited fields (the electric field magnitude is decreasing as the elevation angle increases), low radiated fields are expected anyway. Gain is therefore expected in the same angular direction of the defect window whilst in the opposite direction, where the structure is intact, the radiation is attenuated.

In figure 3.15-3.16 simulations and measurements results of a built prototype, figure 3.14, are compared showing good agreement: 31% fractional bandwidth is achieved from 7.63GHz to 10.4GHz with an average gain and front-to-back-ratio of 11.5dBi and 27dB respectively, the measured half power beamwidth (HPBW) varies between 50° and 60° on the H-plane and is smaller than 30° on the E-plane. The antenna is very directive in the H-plane, reaching a peak gain and front-to-back-ratio of 12dBi and 34dB respectively in the 10GHz region. Discrepancies between simulations and measurements can be mainly attributed to the different dimensions of the ground plane used for the prototype (round with 200mm diameter) and in the simulations (infinite), Section 2.2.4.4. Tolerances in rods dimensions and position could also play a minor role, Section 3.3.6. The gain decreasing shown in the measurements at low elevation angles, figure 3.16, is also caused by the finite ground plane used for the prototype.

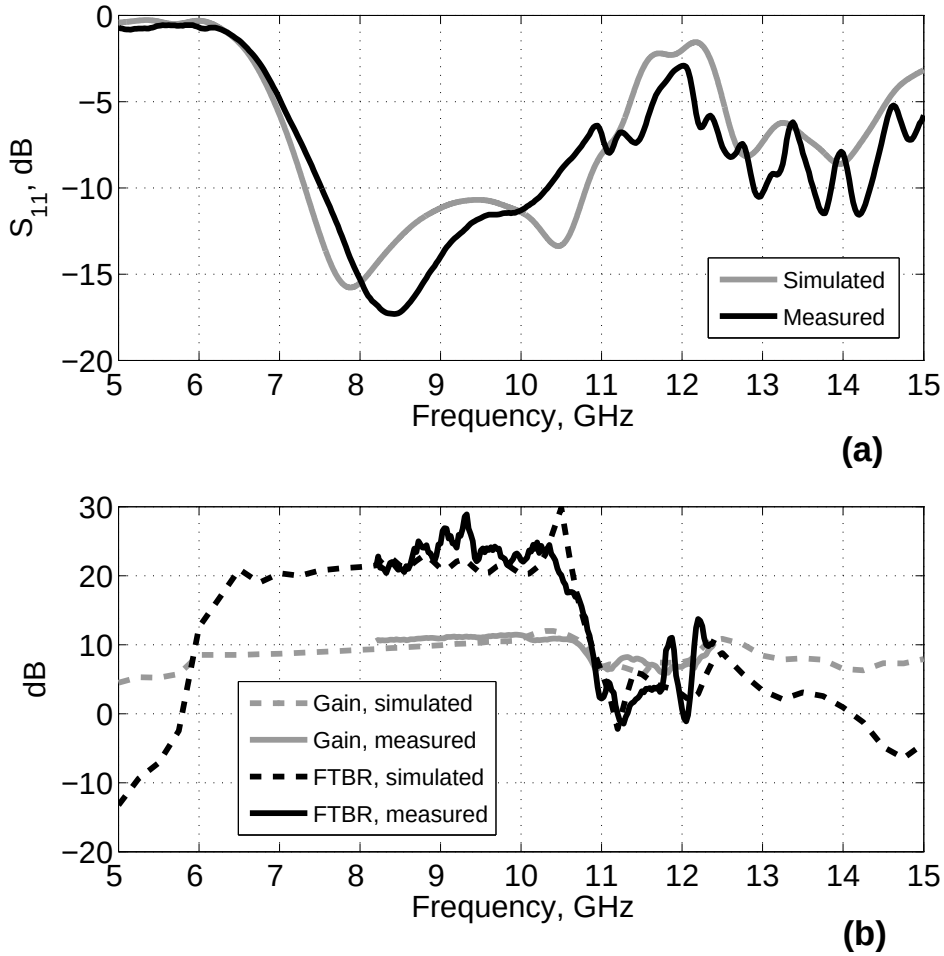

Figure 3.15: *TEBG antenna with a=13mm, r=1.5mm, ε_r=37 and h=20mm, simulated and measured: a) S_{11}; b) gain and front-to-back-ratio (FTBR).*

As shown in figure 3.15, the TEBG antenna is very directive between 5.9GHz and 10.8GHz where the FTBR is greater than 10dB and the gain varies between 8.5dBi and 12dBi. If we compare figure 3.15 with figure 3.10, we can see that the high FTBR frequency range, 5.9-10.8GHz, almost coincide with the 2D lattice bandgap frequencies, 5.28-10.95GHz, confirming the design assumptions that the 3D TEBG structure is a good approximation of the 2D TEBG structure. The normalised electric field distribution on the azimuthal plane is shown in figure 3.17 as a function of frequency. At frequencies within the bandgap, 6GHz-10GHz, the TEBG structures re-direct the excited fields toward the angular aperture; below the bandgap, 3GHz-5GHz, there is little interaction between excited fields and the TEBG structure, whilst at frequency above the bandgap, 11GHz-14GHz, the excited fields interact with the TEBG structure resulting in multiple beams radiation patterns, figure 3.18d.

The directivity of radiation patterns does not vary significantly within the high FTBR frequency range apart for two peaks at 9GHz and around 9.4GHz where the FTBR is almost 10dB higher than the average. At frequencies above 10.5GHz, the directivity of the radiation patterns deteriorates rapidly: although figure 3.15 shows a high gain value even outside the bandgap frequency range, a single high directivity beam in the desired

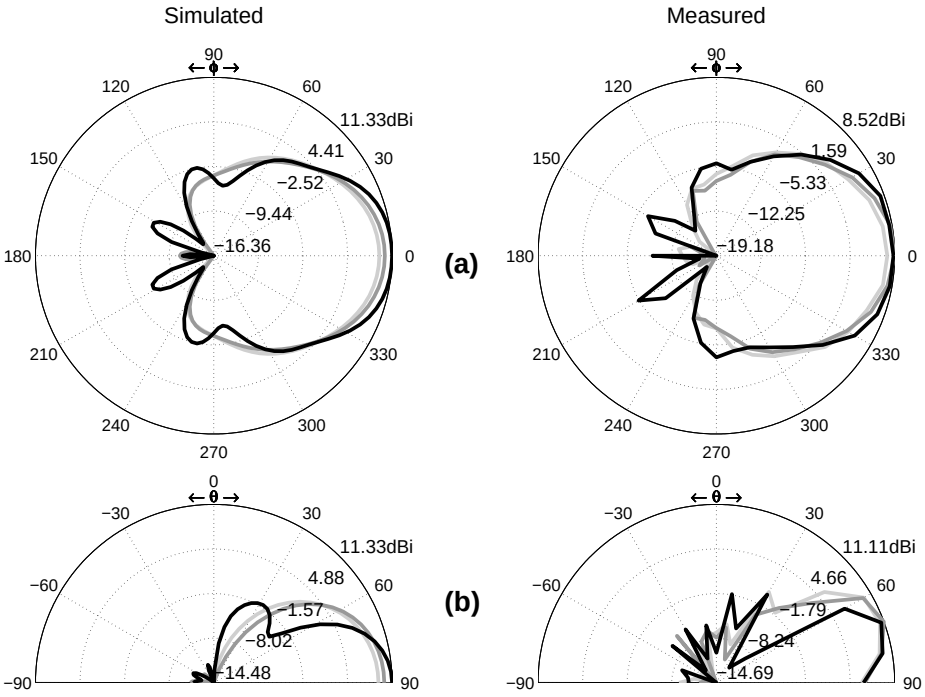

Figure 3.16: *TEBG antenna simulated and measured radiation patterns, a=13mm, r=1.5mm, ε_r=37 and h=20mm: a) H-plane; b) E-plane.*

direction is not present any more as for the 2D TEBG antenna, figure 3.12b. Radiation patterns are also quite stable in the whole impedance bandwidth as shown in figure 3.16 and figure 3.18.

In the next sections the results of a parametric study focused on the number of layers N_L and the dielectric rods length h are presented.

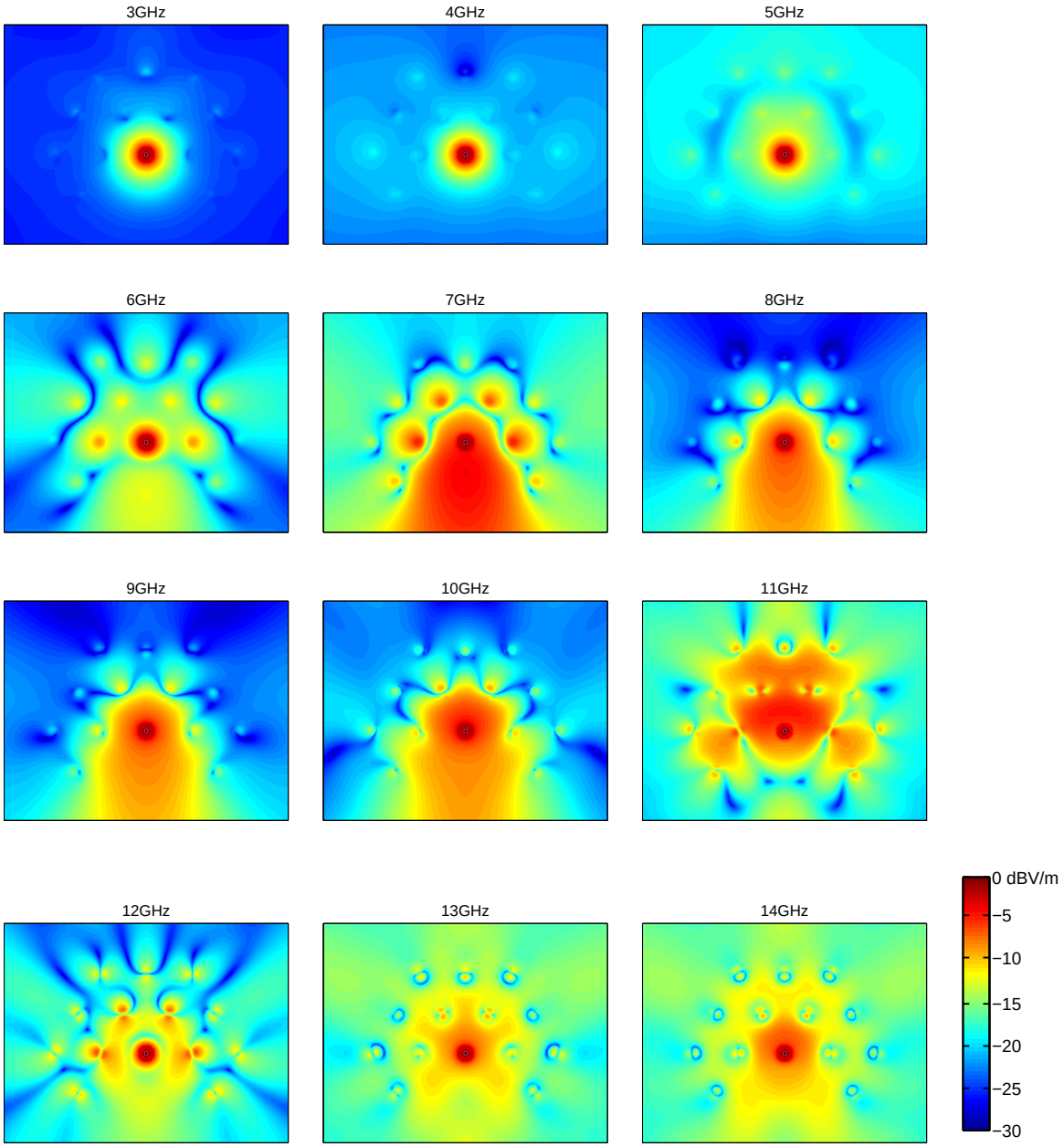

Figure 3.17: *3D TEBG antenna, simulated normalised electric field distribution on the azimuthal plane, a=13mm, r=1.5mm, ε_r=37 and h=20mm.*

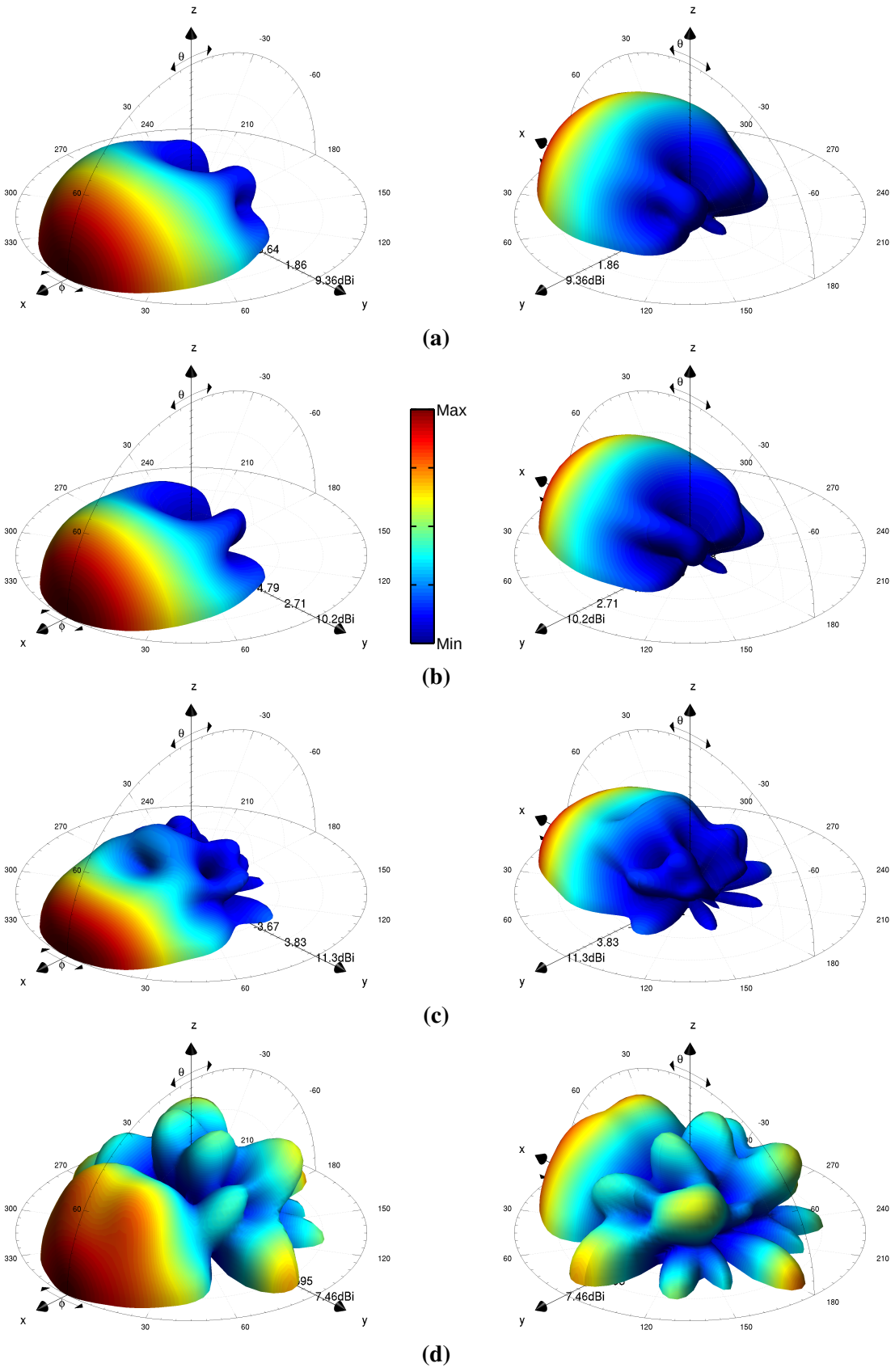

Figure 3.18: *3D TEBG antenna simulated 3D radiation patterns, P_r=13mm, r=1.5mm, ε_r=37 and h=20mm: a) 8.2GHz, b) 9.4GHz, c) 10.6GHz; d) 12GHz (outside the bandgap).*

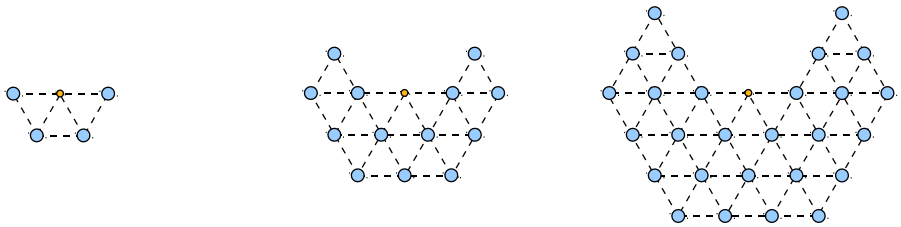

(a) **(b)** **(c)**

Figure 3.19: *3D TEBG antenna geometry as a function of number of layers: a) N_L=1; b) N_L=2; b) N_L=3.*

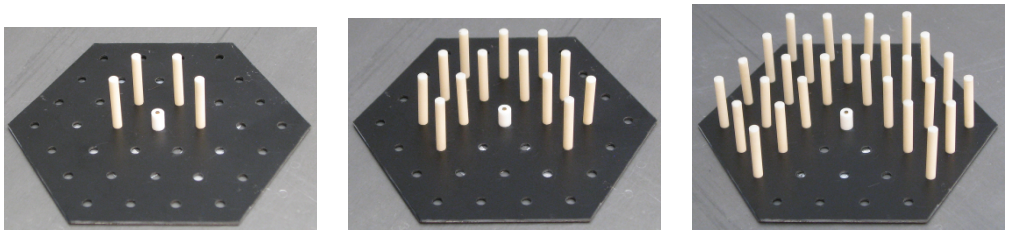

(a) **(b)** **(c)**

Figure 3.20: *3D TEBG antenna photos as a function of number of layers: a) N_L=1; b) N_L=2; b) N_L=3.*

3.3.1 Number of Layers N_L

In figure 3.21 the simulated and measured S_{11} as a function of N_L with h=20mm is shown. The impedance bandwidth presents two main resonances: increasing the number of layers improves the matching at the first resonance whilst at the second resonance is decreased. The difference between 1 or 2 layers is small and adding extra layers only marginally affects the S_{11} response. At frequencies within the bandgap, gain is increasing with the number of layers; the FTBR is reduced ad lower frequencies and increased at higher frequencies, figure 3.22. Radiation patterns are compared in figure 3.23, showing that increasing the number of layers narrows the main beam and reduces the radiation in the backward direction. The improvements introduced when passing from N_L=2 to N_L=3 are little whilst the number of required dielectric rods N_{rods} is more than doubled and the maximum dimension is also increased by 50%, suggesting that N_L=2 is a good compromise in terms of performance and overall dimensions and complexity.

Table 3.2 summarizes the effect of the number of layers N_L on the antenna performance.

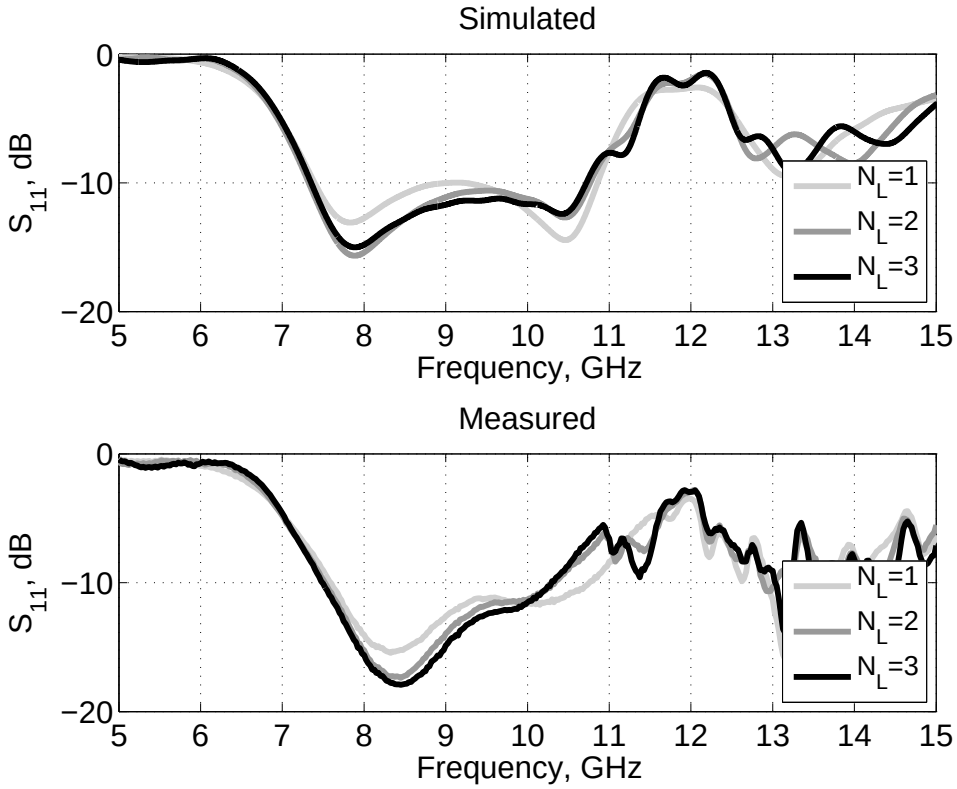

Figure 3.21: *TEBG antenna simulated and measured S_{11} as a function of numbers of layers N_L; a=13mm, r=1.5mm, h=20mm, ε_r=37.*

N_L	Gain, dBi	FTBR, dB	Bandwidth	N_{rods}	Max dim.
1	10.7 (9.0)	31.3 (19.4)	34.2% 7.6-10.8GHz	4	$2 \cdot a$ $0.78 \cdot \lambda_c$
2	11.5 (11.0)	28.9 (23.4)	31.8% 7.5-10.4GHz	13	$4 \cdot a$ $1.56 \cdot \lambda_c$
3	12.5 (12.0)	33.1 (26.8)	31% 7.5-10.3GHz	27	$6 \cdot a$ $2.34 \cdot \lambda_c$

Table 3.2: *3D TEBG antenna measured performance as a function of number of layers N_L; a=13mm, r=1.5mm, ε_r=37 and h=20mm (in brackets are reported the average values within the impedance bandwidth); $\lambda_c = \lambda_{(f_c=9GHz)}=33.3mm$.*

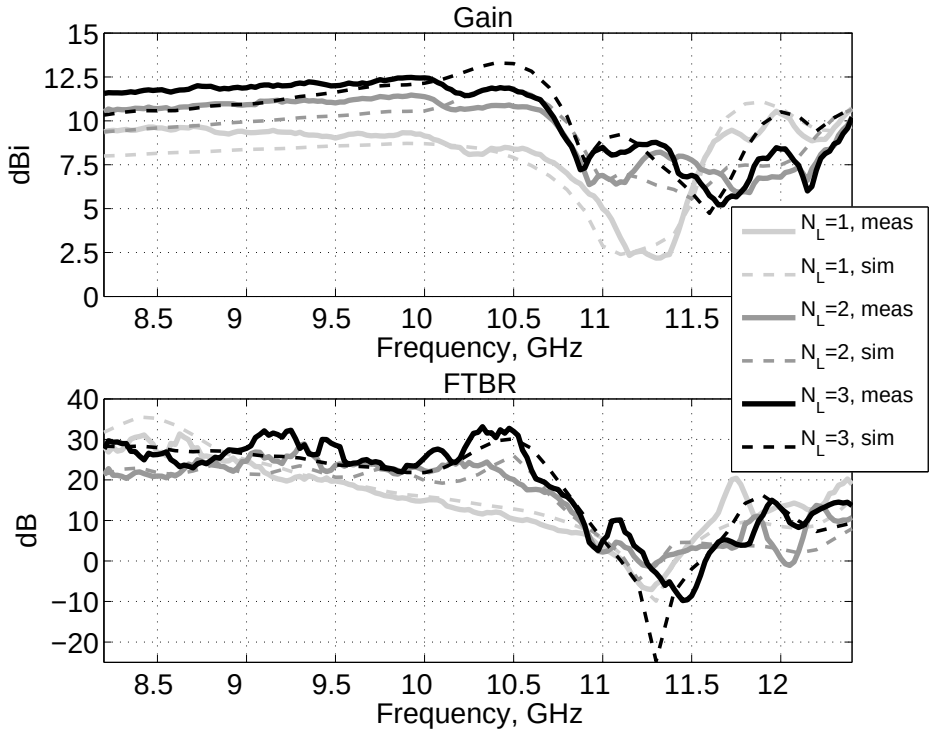

Figure 3.22: *TEBG antenna simulated and measured gain and FTBR as a function of numbers of layers N_L; a=13mm, r=1.5mm, h=20mm, ε_r=37.*

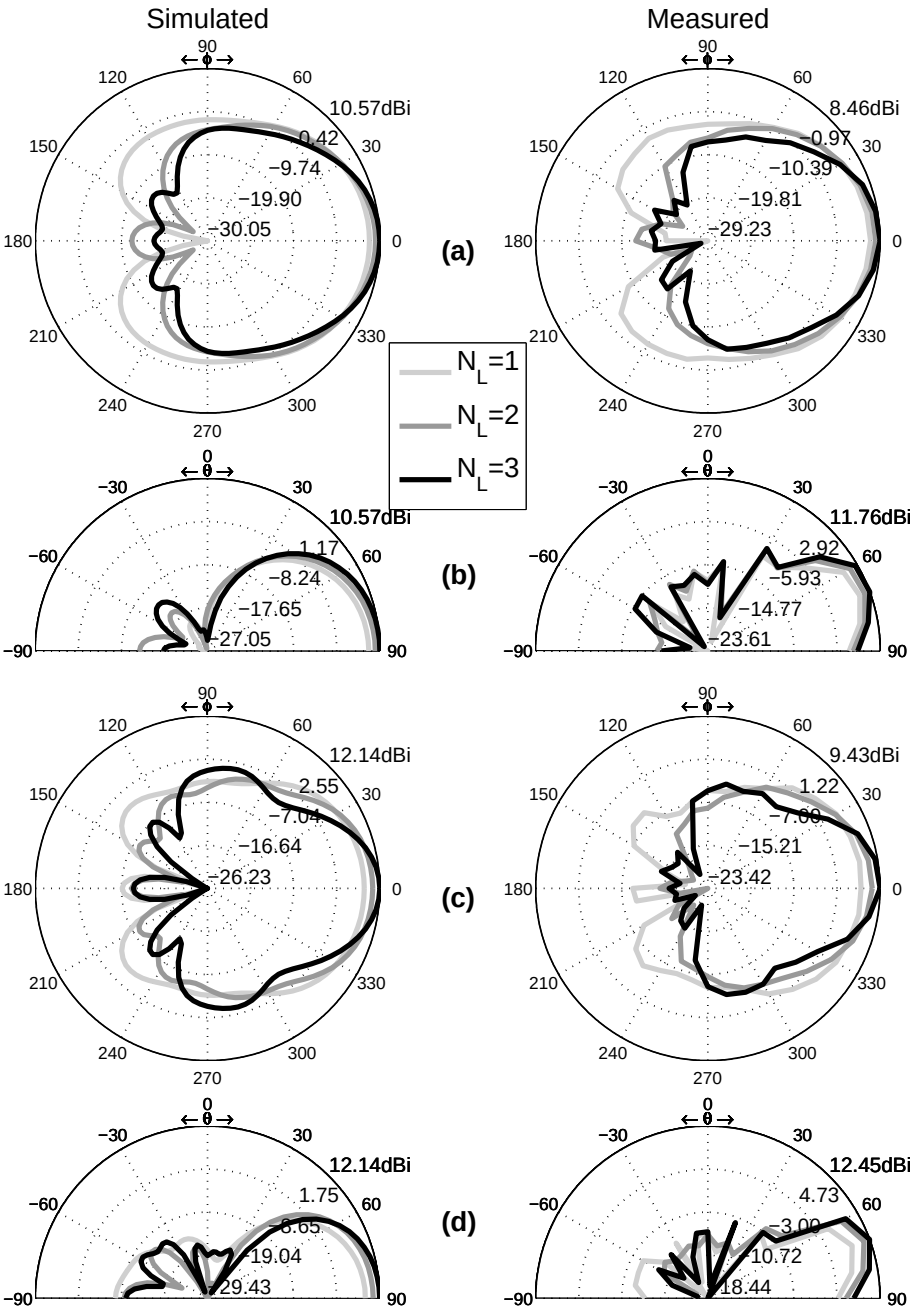

Figure 3.23: *TEBG antenna simulated (left) and measured (right) radiation patterns as a function of numbers of layers N_L; a=13mm, r=1.5mm, h=20mm, ε_r=37: a) H-plane at 8.5GHz; b) E-plane at 8.5GHz; c) H-plane at 10GHz; d) E-plane at 10GHz.*

3.3.2 *Rods length* h

The rods length h has a strong influence on the antenna matching: figure 3.24 shows that increasing h generally improves the S_{11} response also widening the -10dB impedance bandwidth. Gain is improved at lower frequencies (difference between h=20mm and h=30mm is marginal though) and decreased toward the end of the bandgap; the FTBR is generally improved at frequencies within the bandgap, figure 3.25.

As the rods length is increased, the H-plane radiation patterns present a narrower beam, figure 3.26a,3.26c; on the E-plane is narrower at lower frequencies but at higher frequencies a middle value for the rods length present the narrowest beam, figure 3.26b and figure 3.26d.

Simulations shown that a further increase to rods length, $h = 40mm, 50mm$ not shown in figure 3.24-figure 3.26, leaves the S_{11} unaffected, further narrows the beamwidth and increases the FTBR whilst the gain is slightly reduced.

Results are summarized in table 3.3.

h, mm	Gain, dBi	FTBR, dB	Bandwidth
10 $0.3 \cdot \lambda_c$	10.2 (8.9)	25.3 (19.2)	20.2% 8.7-10.6GHz
20 $0.6 \cdot \lambda_c$	11.5 (11.0)	28.9 (23.4)	31.8% 7.5-10.4GHz
30 $0.9 \cdot \lambda_c$	11.6 (10.8)	35.9 (22.7)	41.1% 7.4-11.2GHz

Table 3.3: *3D TEBG antenna measured performance as a function of rods length h; N_L=2, a=13mm, r=1.5mm, ε_r=37 (in brackets are reported the average values within the impedance bandwidth); $\lambda_c = \lambda_{(f_c=9GHz)}$=33.3mm.*

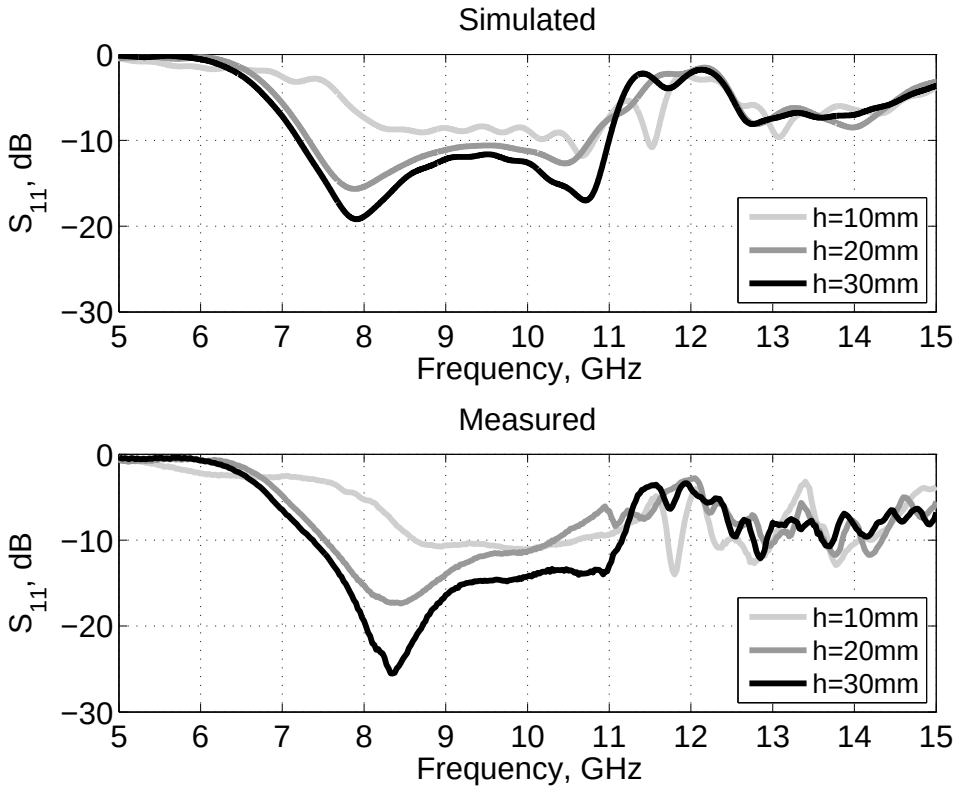

Figure 3.24: *TEBG antenna simulated and measured S_{11} as a function of rods length h; a=13mm, r=1.5mm, N_L=1, ε_r=37.*

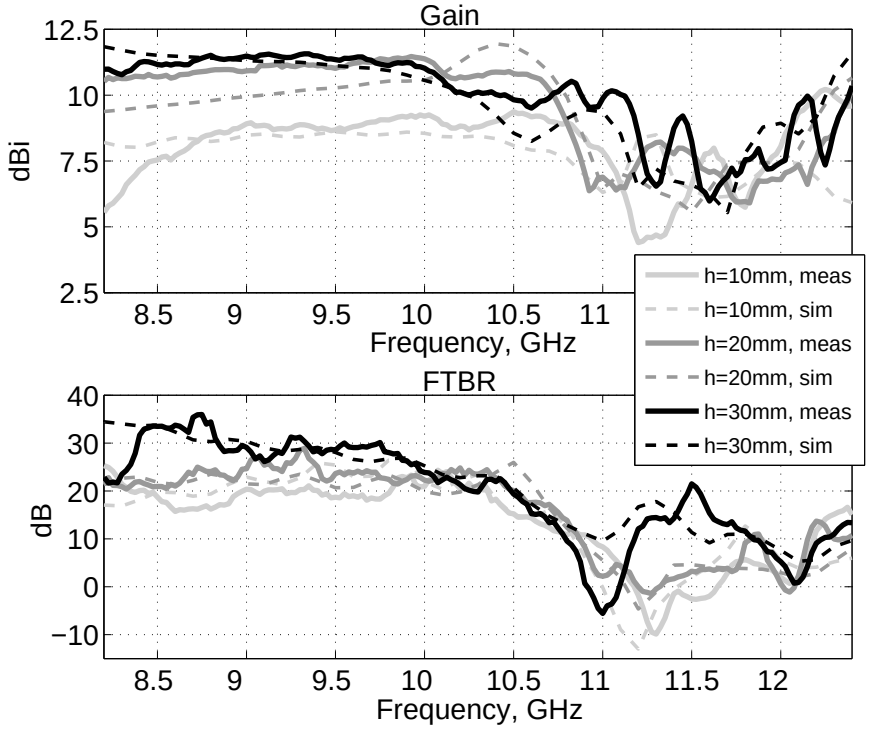

Figure 3.25: *TEBG antenna simulated and measured gain and FTBR as a function of rods length h; a=13mm, r=1.5mm, N_L=1, ε_r=37.*

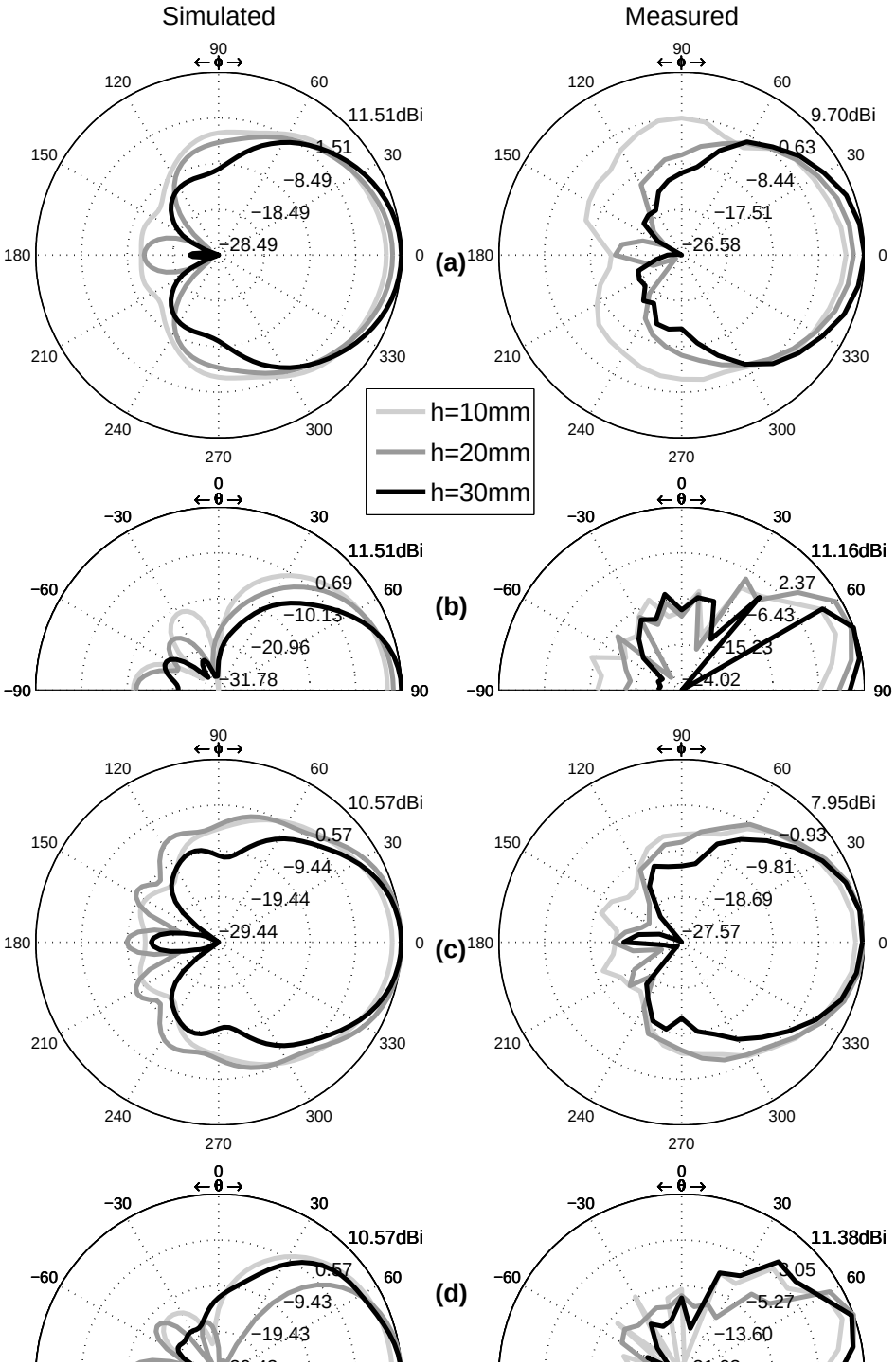

Figure 3.26: *TEBG antenna simulated (left) and measured (right) radiation patterns as a function of rods length h; a=13mm, r=1.5mm, N_L=1, ε_r=37: a) H-plane at 8.5GHz; b) E-plane at 8.5GHz; c) H-plane at 10GHz; d) E-plane at 10GHz.*

(a) (b) (c)

Figure 3.27: *Standard coaxial transitions/monopole feeds.*

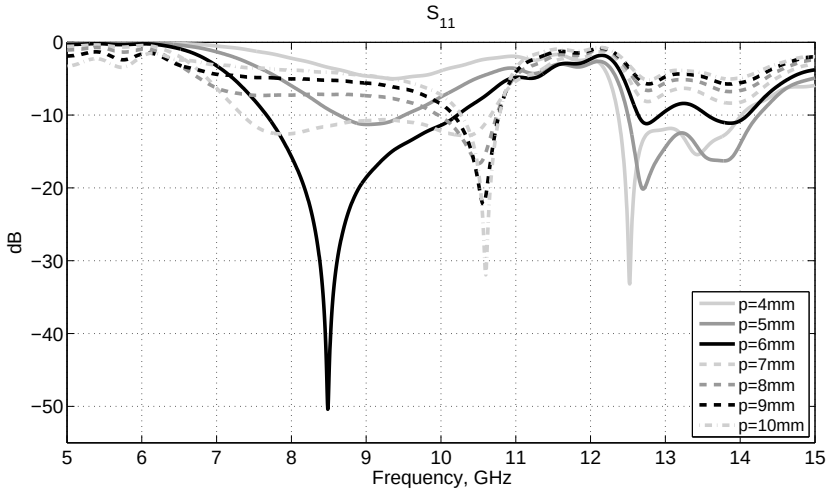

Figure 3.28: *3D TEBG antenna, simulated S_{11} as a function of probe length p with a=13mm, r=1.5mm, ε_r=37, h=20mm and r_p=0.635mm (standard SMA transition probe radius).*

3.3.3 Improving antenna matching and bandwidth

Antenna prototypes were fed using standard SMA transitions, as those shown in figure 3.27, connected to a metal ground plane. Impedance matching was tuned by cutting the monopole feed at a specific length p; the monopole radius r_p is fixed and equal to 0.635mm.

Figure 3.28 reports the simulated S_{11} response as a function of probe length p for a TEBG antenna with a=13mm and r=1.5mm, showing that impedance matching, as expected, can be varied significantly by tuning the monopole length p.

Impedance matching could be also improved by tuning the monopole feed radius r_p as shown in figure 3.29. Therefore, by tuning monopole feed length p and radius r_p (as well as using other bandwidth enlargement techniques), it should be possible to tune the impedance matching to cover the whole bandgap extension hence maximizing the operational bandwidth.

As abovementioned, the monopole radius was fixed by the available SMA transitions and it is been a major constraint in choosing TEBG structure geometrical parameters a and r. In fact, the chosen values (a=13mm, r=1.5mm) are not an optimal choice

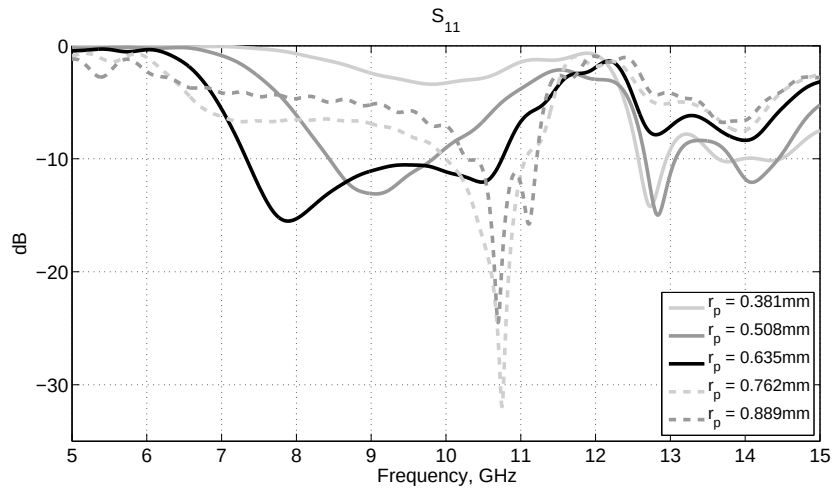

Figure 3.29: *3D TEBG antenna, simulated S_{11} as a function of probe radius r_p with a=13mm, r=1.5mm, ε_r=37, h=20mm and p=7mm.*

in terms of X-band frequency range coverage, as shown in figure 3.8 and figure 3.9. Simulated TEBG antennas made with smaller EBG structures failed to achieve impedance matching at the required frequency band. The trade-off between bandgap position, extension and antenna impedance matching was therefore biased by the monopole feed radius r_p=0.635mm; the geometrical parameters were chosen in order to maximize the coverage of the X-band frequency range by the TEBG antenna impedance bandwidth and best results were achieved with a=13mm and r=1.5mm.

3.3.4 Scaling antenna geometrical dimensions

As already mentioned, an EBG structure geometrical dimensions can be scaled down or up in order to respectively scale up or down bandgaps position and extension. In figure 3.30 is shown the simulated S_{11} responses of the analysed TEBG antenna, here refered as $TEBG2$ (a=13mm, r=1.5mm, h=20mm, p=6.9mm and r_p=0.635mm), along with a scaled down version $TEBG1$ (a=10.5mm, r=1.2mm, h=16.2mm, p=5.65mm and r_p=0.513mm): $TEBG1$ bandwidth is shifted at higher frequencies and it is larger in terms of absolute value but it remained constant in relative value (center frequency has been also shifted at a higher value). Figure 3.31 also compares the radiation patterns, showing $TEBG1$ performing better than $TEBG2$ at higher frequencies and worse at lower frequencies as expected.

All $TEBG1$ geometrical parameters were scaled down, including monopole feed height p and radius r_p in order to preserve impedance matching. Scaling down only the TEBG structure parameters would not preserve the impedance matching and therefore the antenna would present directive radiation patterns at higher frequencies although not properly matched.

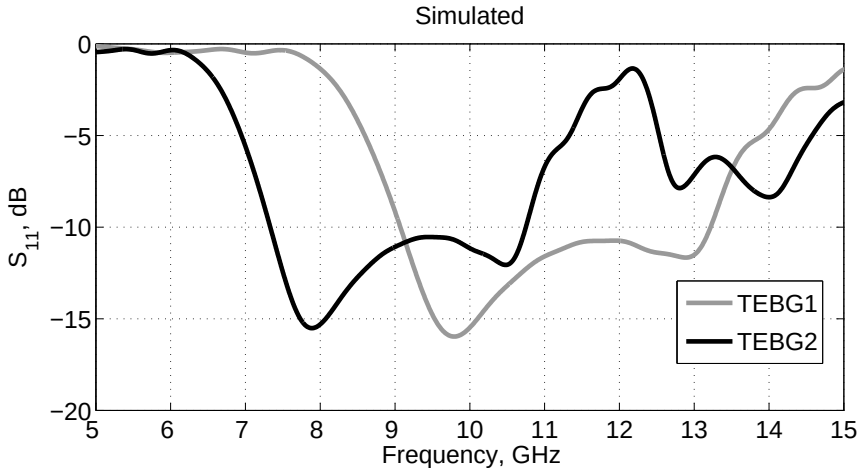

Figure 3.30: *3D TEBG antenna, simulated S_{11} of scaled prototypes: TEBG1 - a=10.5mm, r=1.2mm, h=16.2mm, p=5.65mm, r_p=0.513mm, ε_r=37; TEBG2 - a=15mm, r=1.5mm, h=20mm, p=6.9mm, r_p=0.635mm, ε_r=37.*

3.3.5 Effect of the dielectric loss tangent on antenna performance

The effect of the dielectric loss tangent on the antenna performance have been assessed by simulating a TEBG antenna made with constant dielectric permittivity $\varepsilon_r = 37$ and a variable $tan\delta$ spanning from the ideal lossless case, $tan\delta = 0$, to a 100 times larger loss tangent compared to the nominal value $tan\delta = 0.24 \cdot 10^{-3}$; the results are presented in figure 3.32-3.34.

There is virtually no difference between a lossless case and the reference case with a nominal $tan\delta = 0.24 \cdot 10^{-3}$: the S_{11} response, radiation patterns and achieved gain and FTBR are practically identical.

When $tan\delta$ is set 10 times higher than the nominal case, ie $tan\delta = 2.4 \cdot 10^{-3}$, there is a very little influence on antennas performance although hardly noticeable in figure 3.32-3.34.

Further increasing $tan\delta$ to a value 100 times higher than the reference case, ie $tan\delta = 24 \cdot 10^{-3}$, has a small impact on antenna S_{11} response with a gain reduction mainly at frequency outside the bandgap; the effect on the FTBR is heterogeneous: at low frequencies is slightly reduced, basically uneffected at bandgap frequencies and slightly improved at higher frequencies. There is also a small effect on radiation patterns but it is still hardly noticeable in figure 3.34.

To summarize, the effect of the dielectric loss tangent on the performances is hardly noticeable for $tan\delta$ values up to 100 times higher than the reference case. At bandgap frequencies, the effect of $tan\delta$ is negligible also in the worst considered scenario $tan\delta = 24 \cdot 10^{-3}$: the TEBG structure bandgap is not influenced by the higher losses and the excited fields are still effectively not allowed to propagate through the EBG structure; since propagation is forbidden, the influence of a higher $\tan\delta$ is limited and therefore

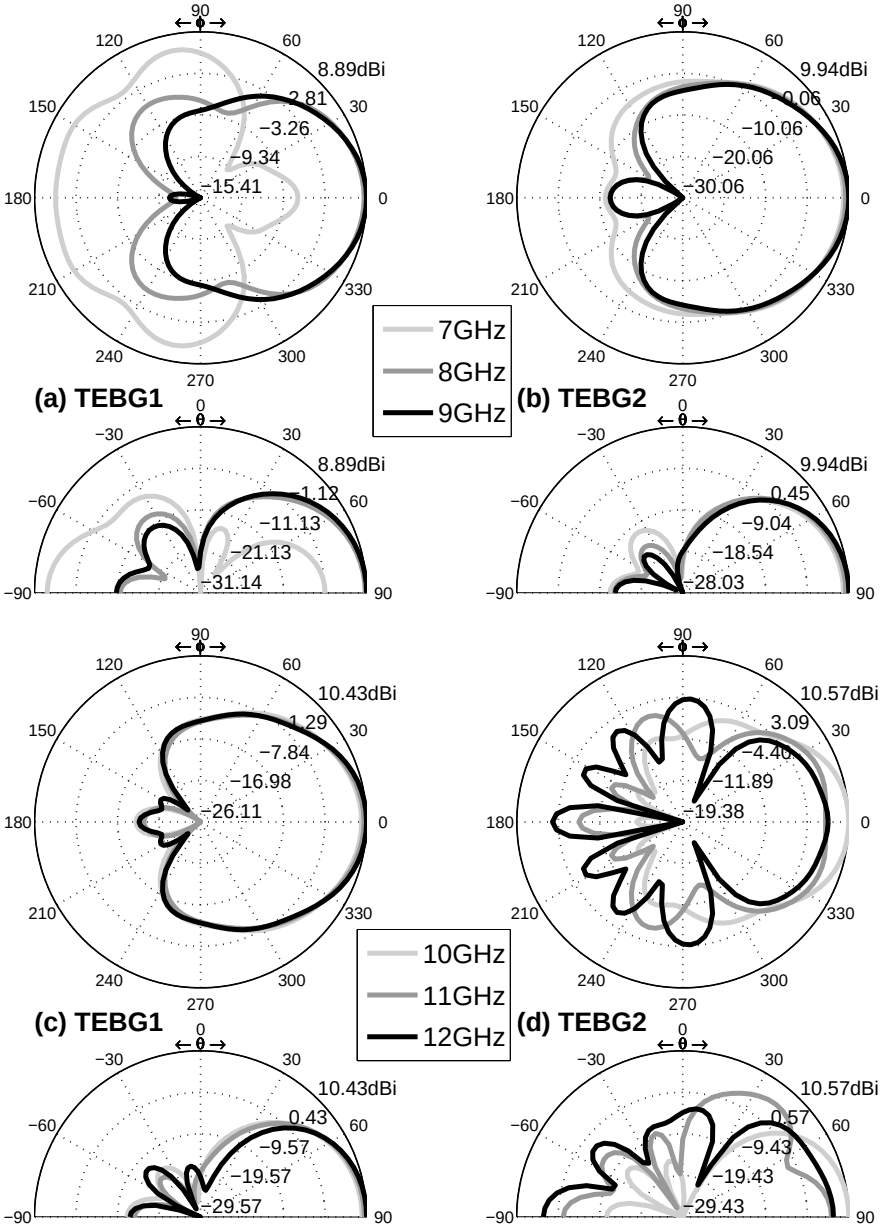

Figure 3.31: *3D TEBG antenna simulated radiation patterns comparison of scaled prototypes:*
TEBG1 - a=10.5mm, r=1.2mm, h=16.2mm, p=5.65mm, r_p=0.513mm, ε_r=37;
TEBG2 - a=15mm, r=1.5mm, h=20mm, p=6.9mm, r_p=0.635mm, ε_r=37.

losses are minimised. Thus, the TEBG antenna radiative performance are almost as good as the reference case.

With a $tan\delta$ linearly increasing with frequency (see for example [83]), simulation results could be also interpreted as if the TEBG antenna was designed to operate at frequencies 10 and 100 times higher than the reference case (simulation results though, would not take into account all other loss mechanisms such as metal losses, etc). We can therefore expect good performances from the TEBG structure (appropriately scaled in dimensions) even at frequency in the 100GHz region.

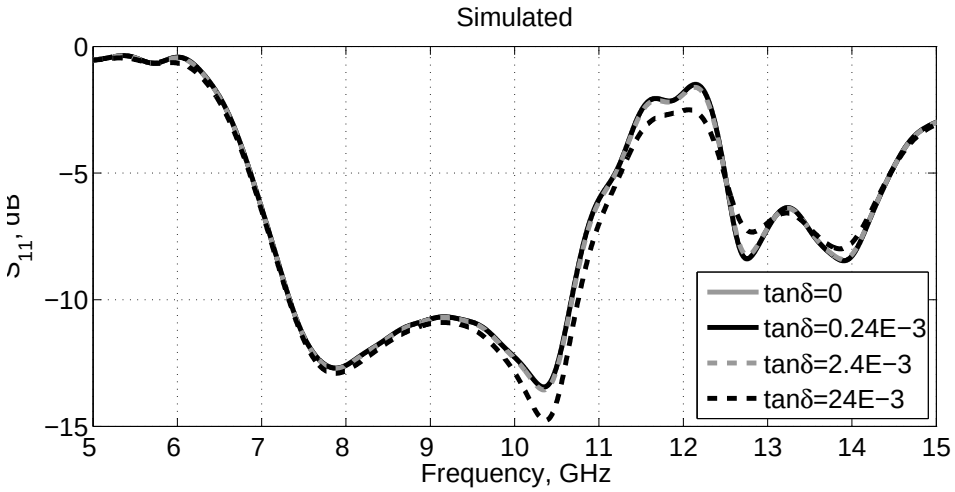

Figure 3.32: *3D TEBG antenna, simulated S_{11} as a function of dielectric loss tangent, a=13mm, r=1.5mm, h=20mm and ε_r=37.*

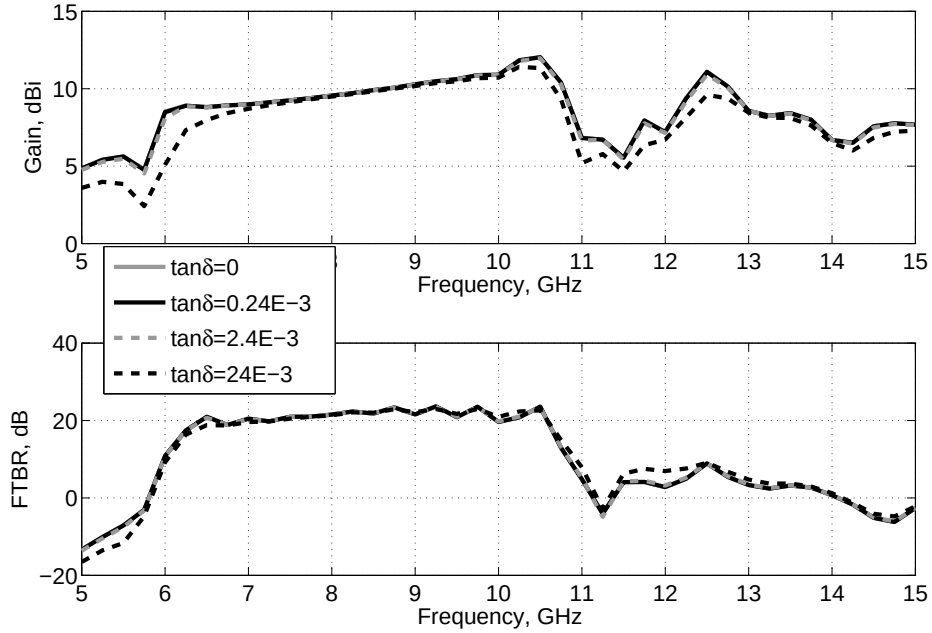

Figure 3.33: *3D TEBG antenna, simulated gain and FTBR as a function of dielectric loss tangent, a=13mm, r=1.5mm, h=20mm and ε_r=37.*

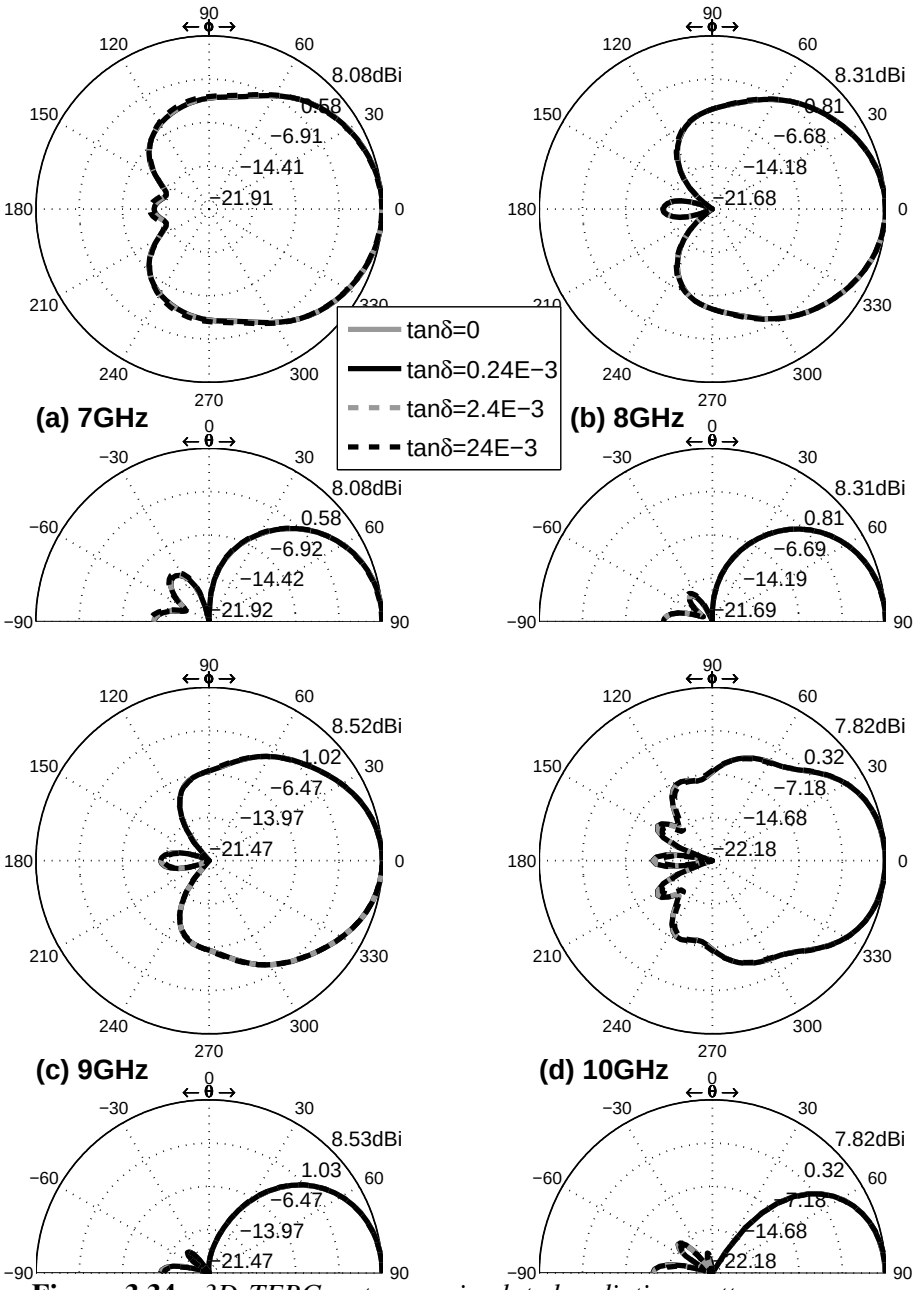

Figure 3.34: *3D TEBG antenna, simulated radiation patterns as a function of dielectric loss tangent, a=13mm, r=1.5mm, h=20mm and* ε_r*=37.*

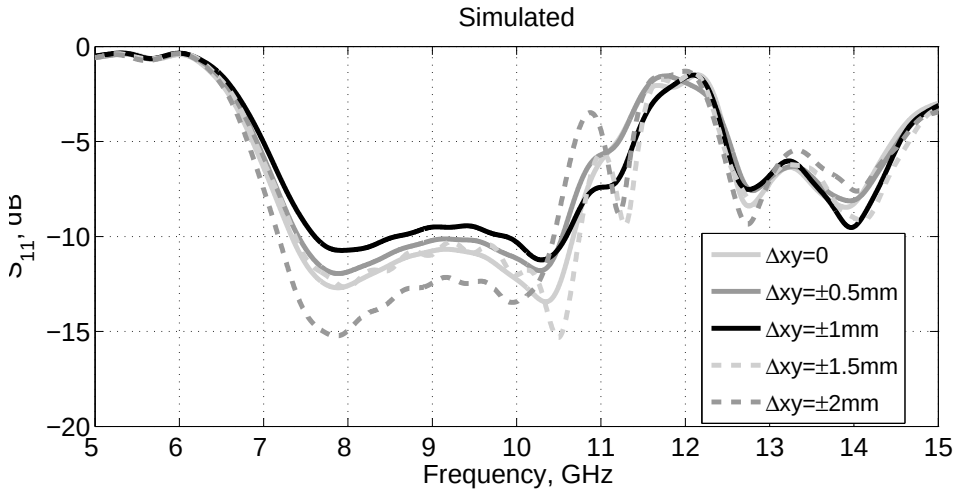

Figure 3.35: *3D TEBG antenna, simulated S_{11} as a function of dielectric rods indivual random displacement Deltaxy, a=13mm, r=1.5mm, h=20mm and ε_r=37.*

3.3.6 Sensitivity analysis on dielectric rods position

A set of simulations has been run to carry on a sensitivity analysis on the dielectric rods position in order to qualitatively characterize the influence on the performance of the antenna. Each dielectric rod has been locally displaced along the x and y directions of a random displacement Δxy of maximum value equals to $\pm 0.5, \pm 1, \pm 1.5, \pm 2mm$ which correspond to a relative displacement of about 3.75%, 7.5%, 11.25% and 15% respectively; simulation results have been then compared to a perfectly arranged structure, ie $\Delta xy = 0mm$, in order to assess the influence of rods displacement on impedance matching, radiation patterns, achieved gain and FTBR.

Rods displacement can have a substantial influence on the impedance matching: figure 3.35 shows that in one case, $\Delta xy = 1mm$, a significant mismatch is introduced and the -10dB bandwidth is reduced. Impedance matching is mainly influenced by the absolute displacement of the first layer dielectric rods, especially when rods are displaced toward the monopole feed: the (open) cavity geometry is disrupted and matching can be seriously compromised. Among the simulated structures which results are shown in figure 3.35, the one with $\Delta xy = 1mm$ had the highest absolute displacement toward the monopole feed.

The overall influence on radiation patterns, gain and FTBR at frequency within the badgap is less critical: figure 3.36 and figure 3.37 show that the radiative performance are very similar in all cases although gain tends to deteriorate when the displacement is increased. It is interesting to note that at 6.5GHz some of the structures had a FTBR improvement greater than 10dB.

The TEBG antenna is therefore quite robust to rods misplacement in terms of radiative performance but it could suffer in terms of impedance matching and bandwidth.

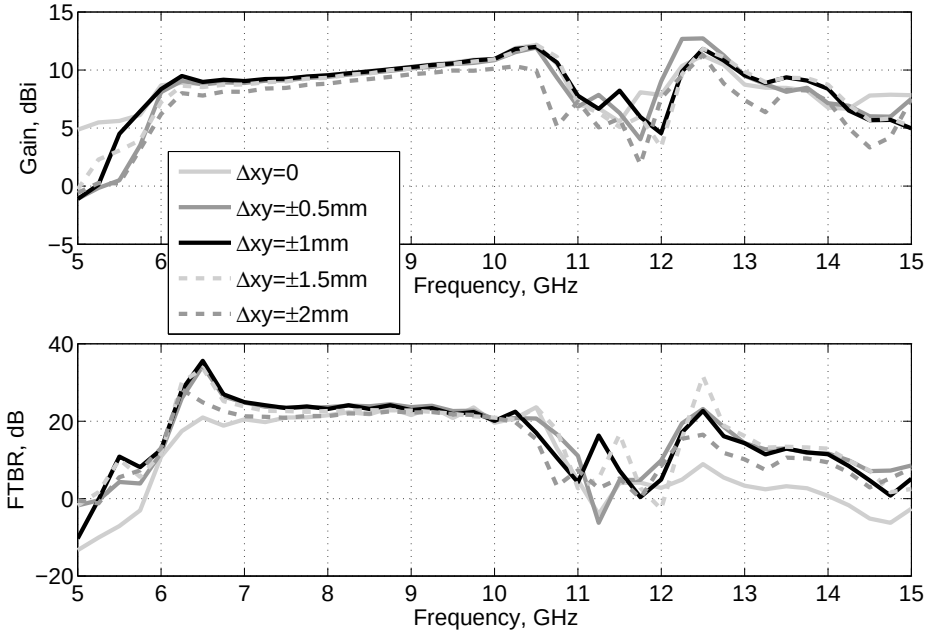

Figure 3.36: *3D TEBG antenna, simulated gain and FTBR as a function of dielectric rods indivual random displacement Deltaxy, a=13mm, r=1.5mm, h=20mm and* ε_r*=37.*

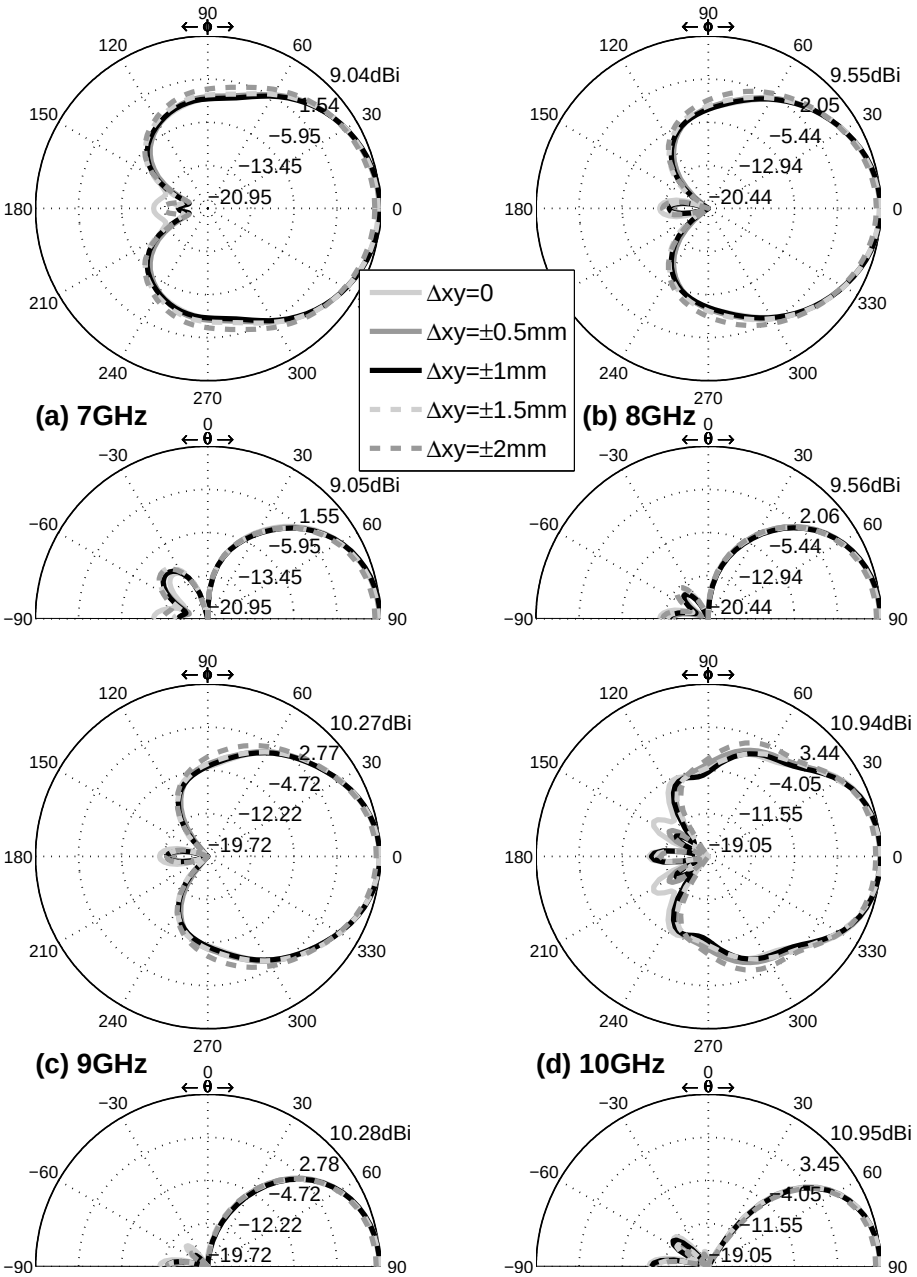

Figure 3.37: *3D TEBG antenna, simulated radiation patterns as a function of dielectric rods indivual random displacement Deltaxy, a=13mm, r=1.5mm, h=20mm and* ε_r*=37.*

3.3.7 Discussion

The CEBG antenna presented in Chapter 2 has similar characteristics to the presented TEBG antenna. Both configurations take advantage of an angular defect window to achieve high gain and FTBR in that particular direction; nevertheless the EBG structure and its characterization are different. The CEBG structure was characterised in terms of transmittivity by normalizing the electric field simulated when the structure is present with the electric field simulated when the structure is not present; the TEBG structure presents a more regular lattice which can be characterized in terms of electromagnetic band structure by analysing the sole unit cell. Although the radial and transverse periods are kept constant in the CEBG antenna, the relative distance between neighbouring rods is not constant and can vary significantly; on the contrary, the triangular lattice is very regular and the distance between neighbouring rods is always the lattice constant a. Moreover, the triangular lattice can be used to develop multi-feed antennas and arrays by adding extra dielectric rods and extra feeding probes in the lattice; the CEBG lattice does not present such advantage, in fact a feeding probe can only be placed in the centre of the lattice. Defect window configuration is also different: for the CEBG antenna, it was created by removing $2n-1$ rods form the n-th layer whilst for the TEBG antenna $n+1$ rods are removed from the n-th layer: the former configuration presents a wider defect window (120°), and the probe feed is more enclosed by the first layer (only 1 rod is missing); the latter presents a defect window with opposite characteristics, i.e. a narrower angular extension (60°) and the probe feed is less enclosed (2 rods are missing). The TEBG antenna also achieved better performance: wider bandwidth (31% against 11%), higher gain (11.5dBi against 9.5dBi) and FTBR (27dB against 13dB).

The TEBG antenna parametric study shown that increasing the number of layers N_L slightly influences the antenna impedance matching and improves gain and FTBR, although improvements for more than 2 layers are minimal. Rods length h has a bigger impact on antenna matching and it can be chosen to maximize the bandwidth; gain and FTBR are also generally improved by increasing the rods length. Not surprisingly, the TEBG antenna parametric study results are very similar to the CEBG antenna parametric results presented in the previous chapter. The influence of monopole feed dimensions where also analysed, showing that feed length and radius can be tuned in order to optimize antenna matching and impedance bandwidth.

Planar multilayer [7, 9], woodpile [13]-[17] or more complex EBG structures [38, 39] of dielectric rods can achieve higher peak gain and narrower beamwidth, although the practical operating frequency range for high directivity patterns is usually narrower compared to the presented TEBG antenna: for example, Weily et al woodpile EBG resonator antenna achieved a peak gain greater than 20dBi, 13% impedance bandwidth but only 1% directivity bandwidth [13]; a woodpile EBG horn antenna, [38] achieved a peak gain of 13.8dBi and a -10dB reflection coefficient bandwidth of 4.7%. An exception

is given by [10], where the simulated directivity bandwidth of a cross-rod EBG superstrate with a defect layer reached 30%. The presented TEBG antenna directivity patterns have similar characteristics within the whole 31% impedance bandwidth, moreover the triangular geometry is much simpler compared to the aforementioned structures.

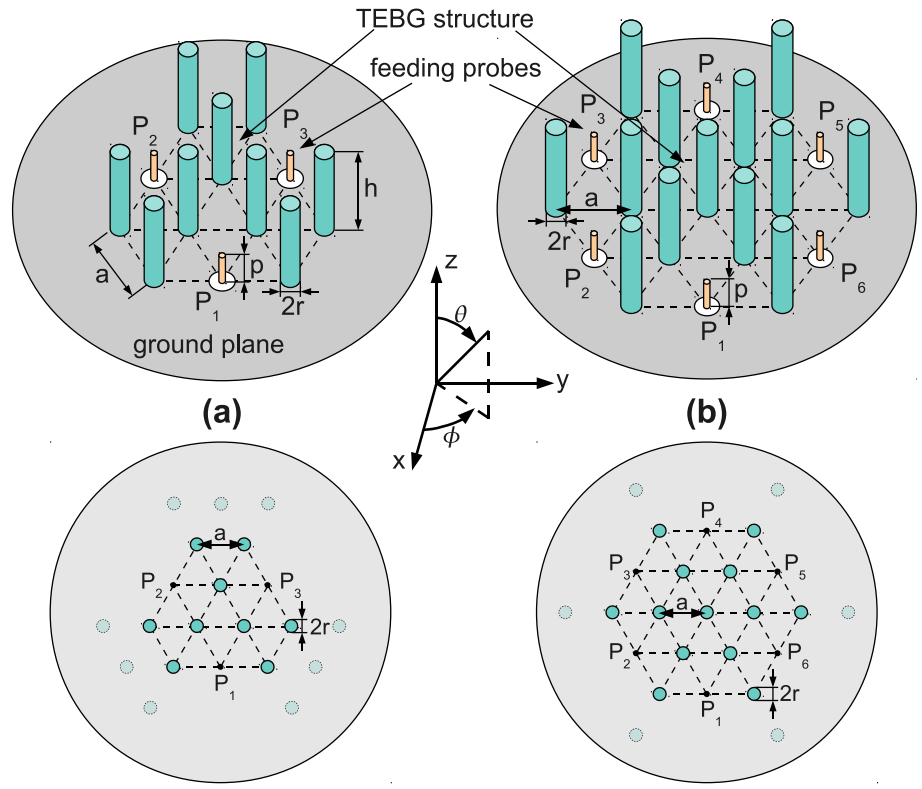

Figure 3.38: *Multi-feed TEBG antenna geometry, 3D view and top view: a) 3-feeds configuration, MF_3; b) 6-feeds configuration, MF_6.*

3.4 Multiple-feed TEBG Antennas

The intrinsic symmetry of the TEBG antenna analysed in the previous sections can be used to create multiple-feed antennas, as the ones shown in figure 3.38. As for single-feed prototypes, dielectric rods of length h=20mm, radius r=1.5mm and ε_r=37$\pm$1 (D36 modified zirconium tin titanate [81]) arranged in a triangular lattice with a=13mm over a circular ground plane have been used to build the prototypes, figure 3.39. The two configurations, 3-feeds and 6-feeds, will be respectively referred as MF_3 and MF_6. Three or six rods, MF_3 and MF_6 respectively, have been removed and replaced by monopole feeds P_i of length p=6.9mm; each feed is located in the center of an open cavity.

Multiple-feed antennas are based on the same principle of operation of the single-feed TEBG antenna: fields at frequency within the TEBG structure bandgap are directed toward the cavity apertures creating directive radiation patterns on the azimuthal plane. Moreover, given the intrinsic geometry, the radiation patterns can be rotated by 120° (MF_3) or 60° steps (MF_6) by feeding the corresponding monopole feed, figure 3.40. The TEBG structure also provides a high decoupling between the close-spaced feeding probes.

In all the following simulations and measurements, the non-excited feeds were terminated on a 50Ω load. Measurements though, have shown basically no difference whether the non-excited feeds were terminated on matched loads or open circuits.

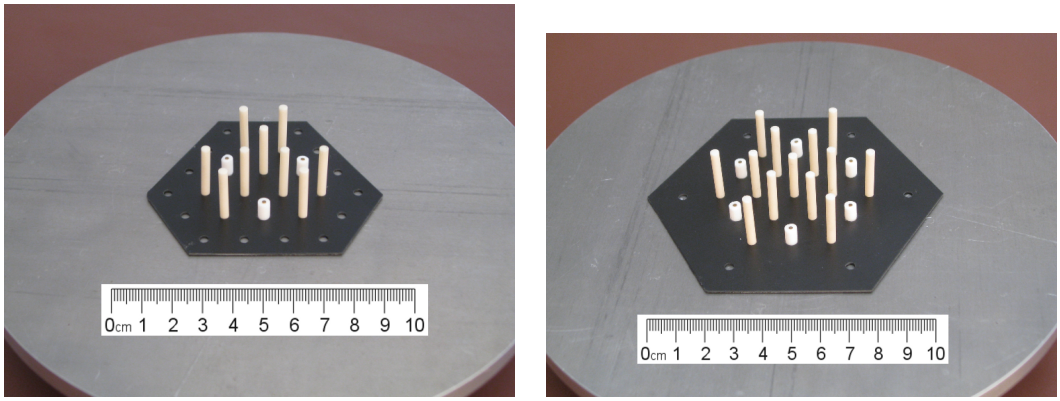

(a) **(b)**

Figure 3.39: *Multi feed TEBG antenna prototypes: a) 3-feeds configuration, MF_3; b) 6-feeds configuration, MF_6.*

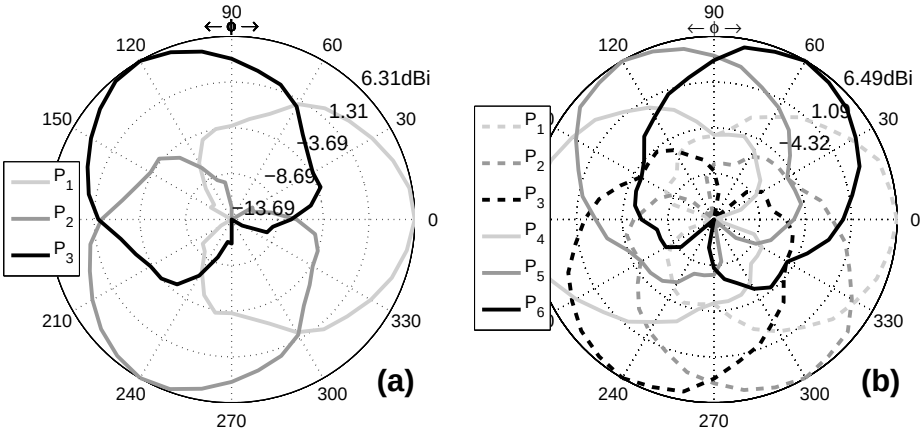

Figure 3.40: *Measured radiation patterns at 9GHz as a function of excited probe: a) 3-feeds configuration, MF_3; b) 6-feeds configuration, MF_6.*

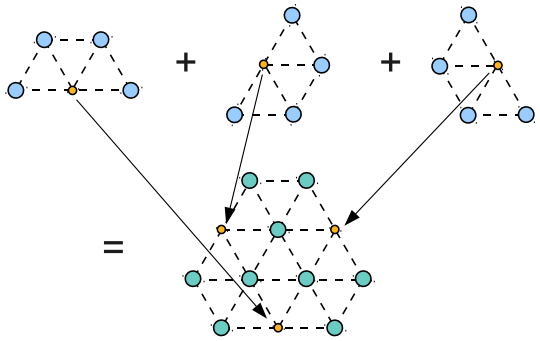

Figure 3.41: *MF_3 antenna built using 3 superimposed single feed TEBG antennas with N_L=1.*

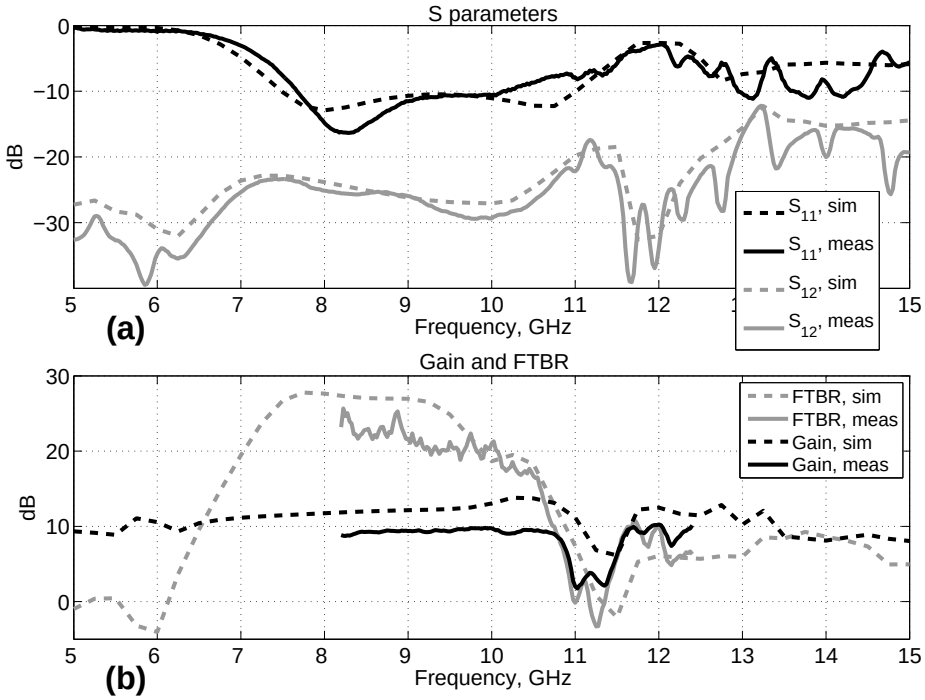

Figure 3.42: *MF_3 configuration (3 feeds), simulated and measured: a) scattering parameters; b) gain and front-to-back-ratio (FTBR) when P_1 is fed.*

MF_3 Antenna (3 feeds configuration)

In figure 3.42 and figure 3.43 simulations and measurements results of an MF_3 antenna prototype (figure 3.39a and figure 3.41) are compared showing a good agreement. 28.4% fractional bandwidth is achieved from 7.7GHz to 10.2GHz with an average gain and front-to-back-ratio (FTBR) of 9.4dBi and 21.3dB respectively (only P_1 was fed); monopole feeds are also highly decoupled, showing a forward transmission coefficient $S_{12} \leq$ -23.8dB within the impedance bandwidth. Given the antenna intrinsic geometry, only one set of scattering parameters are shown in figure 3.42; all reflection coefficients S_{ii} (with i=1,2,3) and all forward transmission coefficient S_{ij} (with i,j=1,2,3 and i≠j) are identical for symmetry reasons.

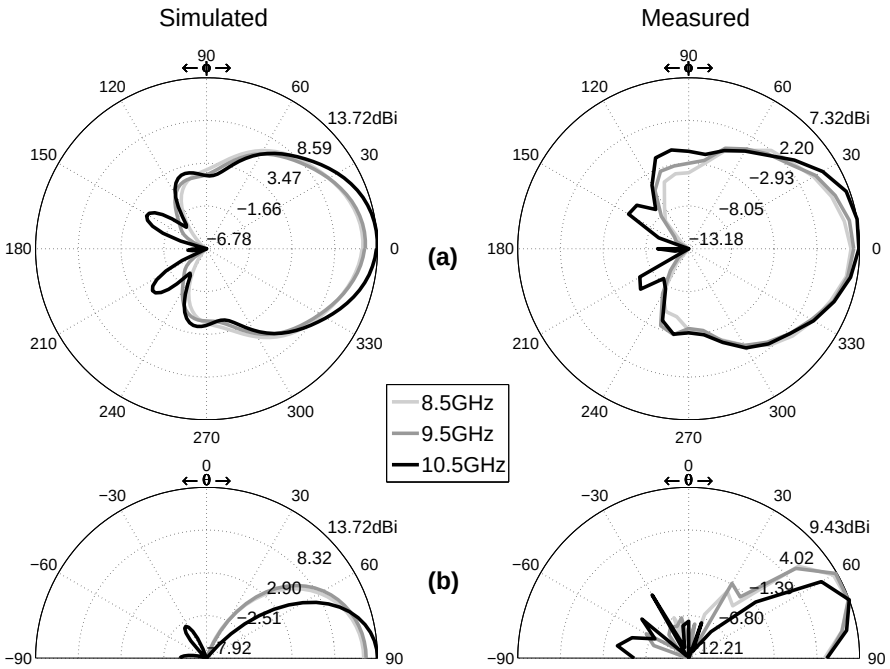

Figure 3.43: *MF_3 configuration (3 feeds) simulated and measured radiation patterns when P_1 is fed: a) H-plane; b) E-plane.*

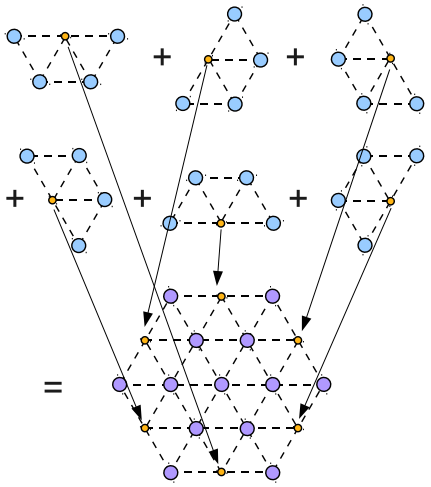

Figure 3.44: *MF_6 antenna built using 6 superimposed single feed TEBG antennas with N_L=1.*

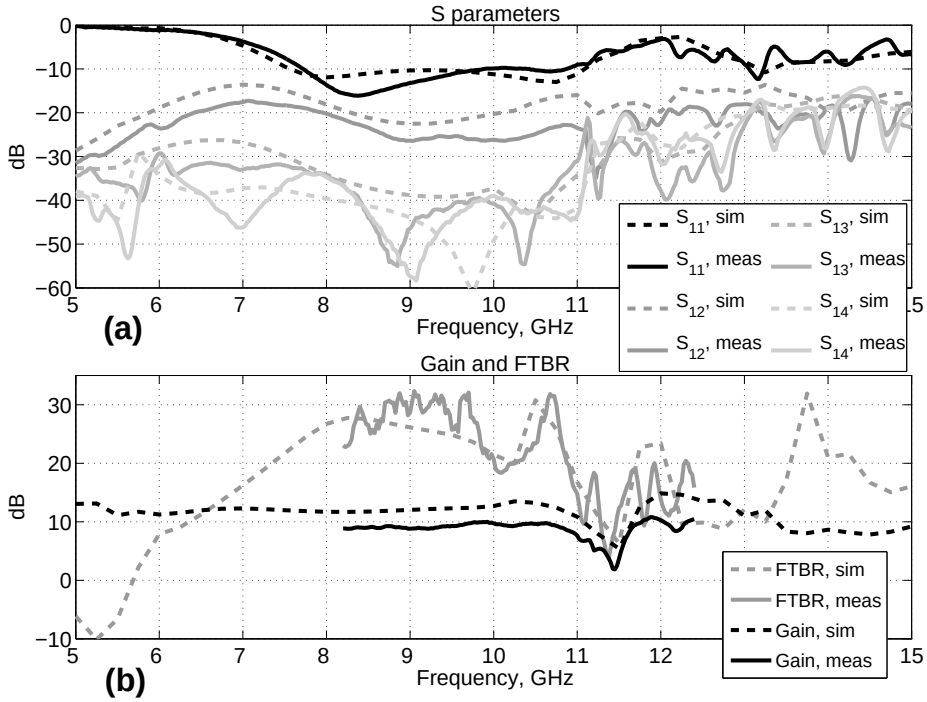

Figure 3.45: *MF_6 configuration (6 feeds), simulated and measured: a) scattering parameters; b) gain and front-to-back-ratio (FTBR) when P_1 is fed.*

MF_6 Antenna (6 feeds configuration)

MF_6 prototype (figure 3.39b and figure 3.44) measurements and simulations are compared in figure 3.45 and figure 3.46. There is a good agreement between simulated and measured results: the antenna is well matched from 7.8GHz to 10.9GHz, 33.7% fractional bandwidth, the average gain and FTBR are respectively 9.3dBi and 26.2dB (only P_1 was fed). There is a good decoupling between close feeds, $S_{12} \leq$ -19.1dB, and better for more distant feeds, S_{13} and $S_{14} \leq$ -32.5dB. As for the MF_3 antenna, only one set of S parameters is shown (S_{15} and S_{16} are not shown because equal to S_{13} and S_{12} respectively).

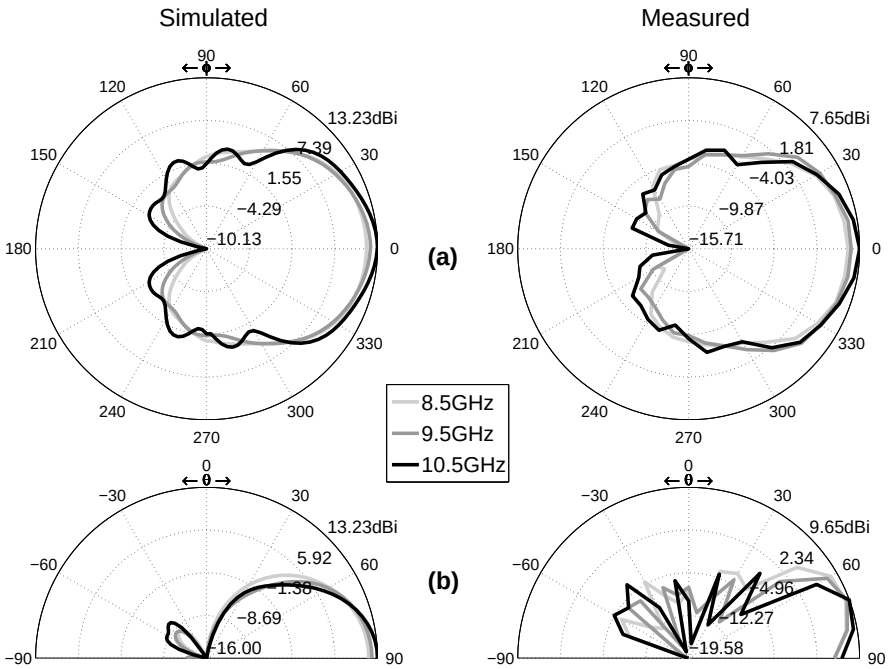

Figure 3.46: *MF_6 configuration (6 feeds) simulated and measured radiation patterns when P_1 is fed: a) H-plane; b) E-plane.*

Simulations and measurements, figure 3.42-3.46, shown that the presented antennas have similar bandwidth characteristics and are very directive on the azimuthal plane between 6.5GHz and 10.5GHz with stable radiation patterns. Outside this frequency range, the FTBR drops considerably and although the gain may appear still reasonable, radiation patterns do not present any more a single high directivity beam in the desired direction. The average half-power-beamwidth (HPBW) varies between 50° and 60° on the H-plane and is smaller than 40° on the E-plane. The overall characteristics are very similar to the single-feed TEBG antenna presented in the previous Sections.

Comparing figure 3.10 with figure 3.42 and figure 3.45, shows that the high FTBR frequency range, 6.5-10.5GHz, is within the 2D lattice bandgap, 5.31-10.94GHz, confirming also in this case the design assumptions that the TEBG structure is a good approximation of the 2D triangular lattice.

The multiple-feed structures have been parametrically studied, as for the single-feed case, focusing on the dielectric rods length h and the number of layers N_L.

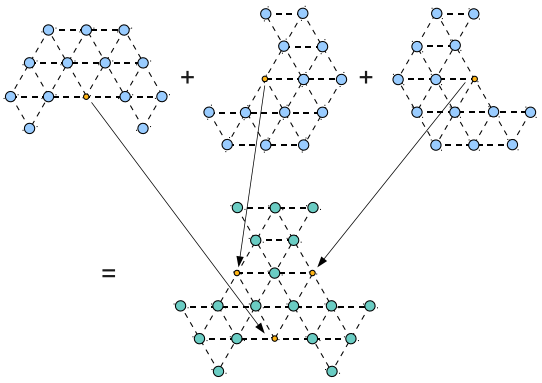

Figure 3.47: *MF_3 antenna built using 3 superimposed single feed TEBG antennas with N_L=2.*

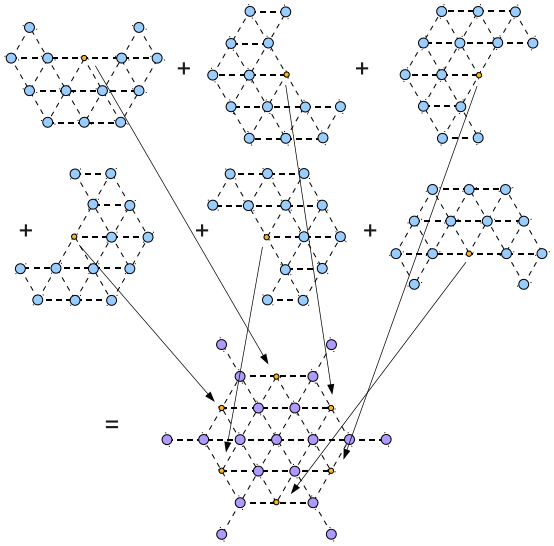

Figure 3.48: *MF_6 antenna built using 6 superimposed single feed TEBG antennas with N_L=2.*

3.4.1 Number of Layers N_L

In this parametric study, monopole feeds relative positions have been kept constant and extra dielectric rods have been placed in between. We focused our attention on N_L=1,2, where N_L is referred to the number of layers of the single feed TEBG antennas rotated and superimposed, as shown in figure 3.41, 3.44, 3.47 and 3.48, to build the MF_3 and MF_6 antennas.

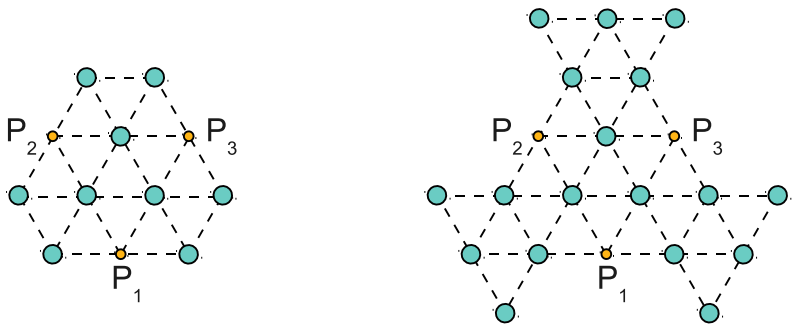

(a) **(b)**

Figure 3.49: *MF_3 configuration: a) N_L=1; b) N_L=2.*

MF_3 Antenna

The analysed configurations are shown in figure 3.49. Contrary to simulations, figure 3.50, the S_{11} response of the MF_3 antenna is not much influenced by the number of layers; mutual coupling between adjacent feed is slightly improved by around 2dB. Average gain and FTBR, figure 3.51, are also improved respectively by 1.5dB and 2.5dB; Radiation patterns present lower side lobes when N_L=2 but the HPBW is not much influenced. Measurement results, summarised in table 3.4, therefore suggest that N_L=1 is a good compromise in terms of performance, maximum dimensions ($3 \cdot a$ against $5 \cdot a$) and number of required dielectric rods N_{rods} (9 rods against 18).

N_L	Gain, dBi	FTBR, dB	Bandwidth	S_{12}, dB	N_{rods}	Max dim.
1	10.2 (9.4)	25.7 (21.3)	28.4% 7.7-10.2GHz	$\leq$-23.8 (-26.8)	9	$3 \cdot a$ $1.17 \cdot \lambda_c$
2	11.5 (10.9)	31.1 (23.8)	25.5% 7.7-9.9GHz	$\leq$-26.4 (-28.3)	18	$5 \cdot a$ $1.97 \cdot \lambda_c$
no EBG	NA	NA	NA	$\leq$-13.4 (-16.9)	NA	NA

Table 3.4: *MF_3 configuration measured performance as a function of number of layers N_L; a=13mm, r=1.5mm, ε_r=37 and h=20mm (in brackets are reported the average values within the impedance bandwidth); $\lambda_c = \lambda_{(f_c=9GHz)}$=33.3mm.*

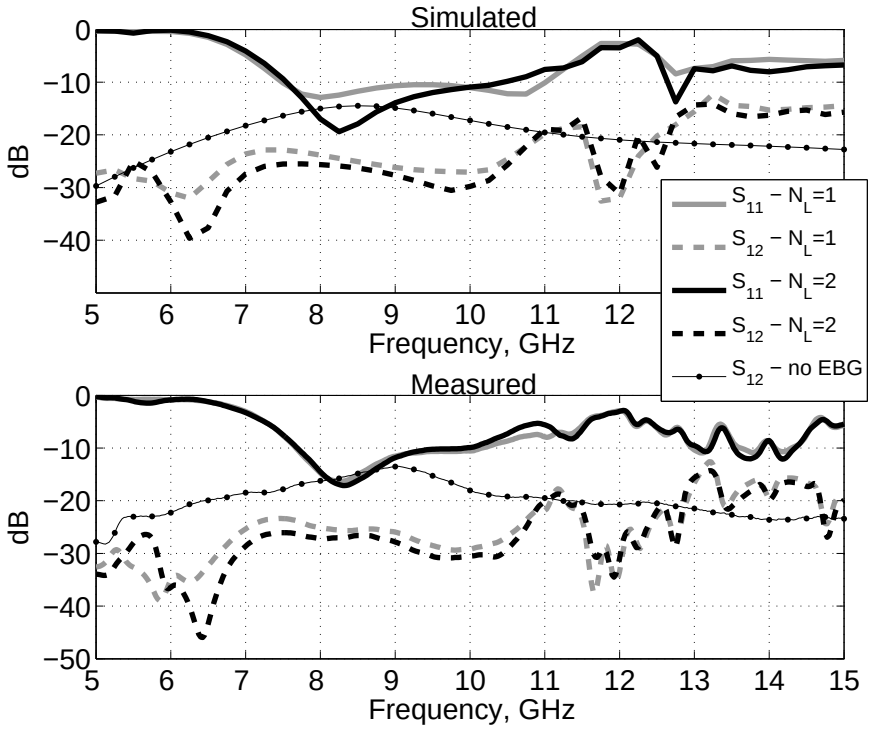

Figure 3.50: *MF_3 configuration (3 feeds), simulated and measured scattering parameters as a function of numbers of layers N_L; a=13mm, r=1.5mm, h=20mm, ε_r=37.*

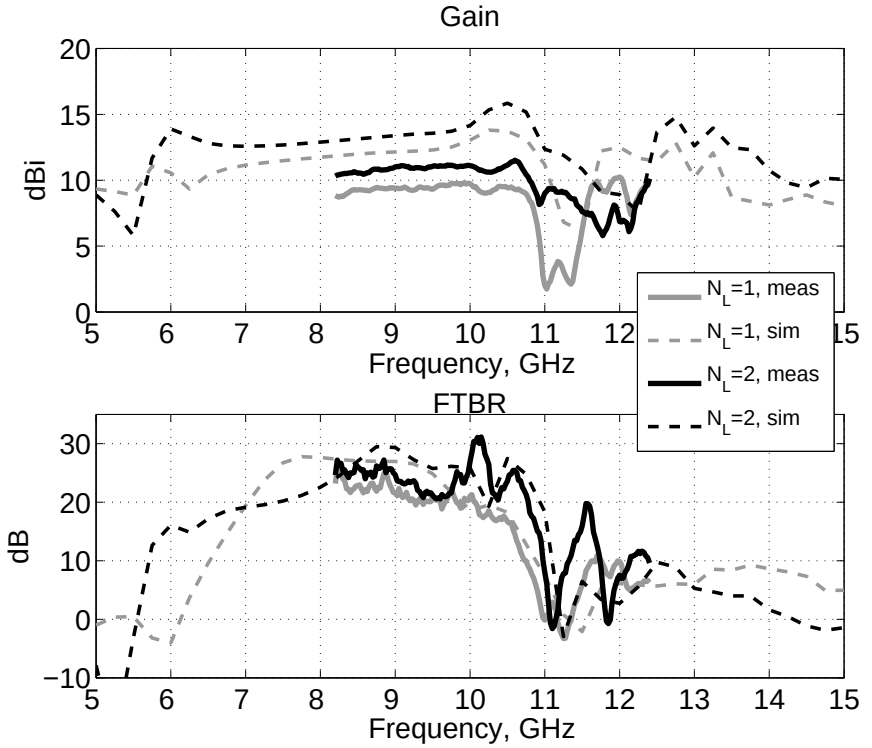

Figure 3.51: *MF_3 configuration (3 feeds), simulated and measured gain and FTBR as a function of numbers of layers N_L; a=13mm, r=1.5mm, h=20mm, ε_r=37.*

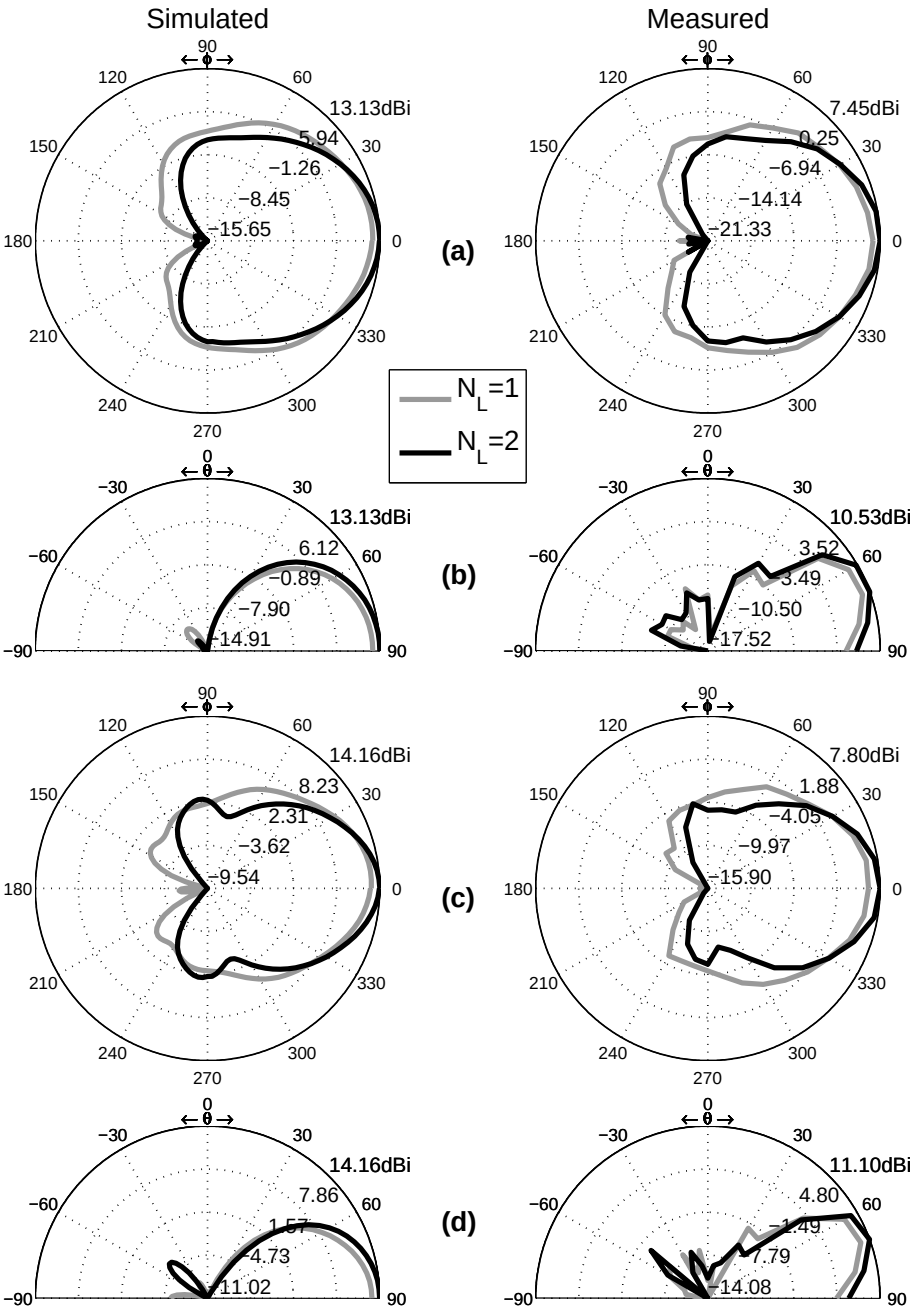

Figure 3.52: *MF_3 configuration (3 feeds), simulated and measured radiation patterns as a function of numbers of layers N_L; a=13mm, r=1.5mm, h=20mm, ε_r=37: a) H-plane at 8.5GHz; b) E-plane at 8.5GHz; c) H-plane at 10GHz; d) E-plane at 10GHz.*

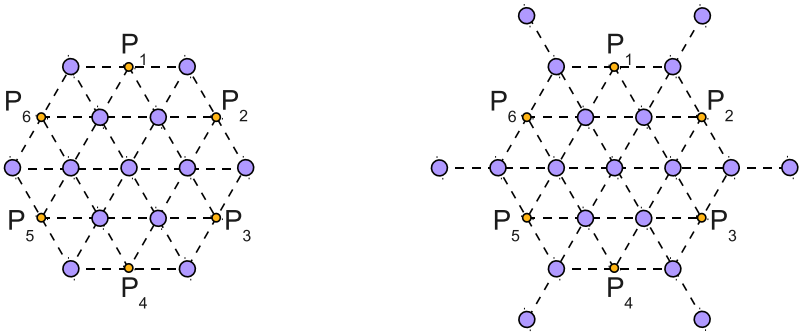

(a) **(b)**

Figure 3.53: *MF_6 configuration: a) N_L=1; b) N_L=2.*

MF_6 Antenna

The analysed configurations are shown in figure 3.53. The S_{11} response is slightly influenced, nevertheless the bandwidth is decreased from 33.7% to 24% (this reduction could be mitigated by tuning the probe length p), figure 3.54; decoupling between adjacent feeds, S_{12}, is also slightly influenced, whilst between more distant feeds, S_{13} and S_{14}, the reduction is greater than 10dB. As for the MF_3 configuration, increasing the number of layer does not have a big influence on gain and FTBR, figure 3.55.

Measurements results are summarised in table 3.5: as for the 3 feeds configuration, increasing the number of layers does not introduce big enough improvements to justify extra dielectric rods and larger maximum dimensions.

N_L	Gain dBi	FTBR dB	Bandwidth	S_{12} dB	S_{13} dB	S_{14} dB	N_{rods}	Max dim.
1	10.8 (9.3)	32.3 (26.2)	33.7% 7.8-10.9GHz	$\leq$-19.1 (-24.3)	$\leq$-32.5 (-41.8)	$\leq$-33.9 (-43.2)	13	$5 \cdot a$ $1.97 \cdot \lambda_c$
2	11.2 (10.3)	35.4 (25.7)	24% 7.7-9.8GHz	$\leq$-21.2 (-24.8)	$\leq$-43.5 (-50.0)	$\leq$-45.1 (-51.6)	19	$7 \cdot a$ $2.76 \cdot \lambda_c$
no EBG	NA	NA	NA	$\leq$-13.8 (-17.6)	$\leq$-19.1 (-23.0)	$\leq$-15.3 (-17.3)	NA	NA

Table 3.5: *MF_6 configuration measured performance as a function of number of layers N_L; a=13mm, r=1.5mm, ε_r=37 and h=20mm (in brackets are reported the average values within the impedance bandwidth); $\lambda_c = \lambda(f_c=9GHz)=33.3mm$.*

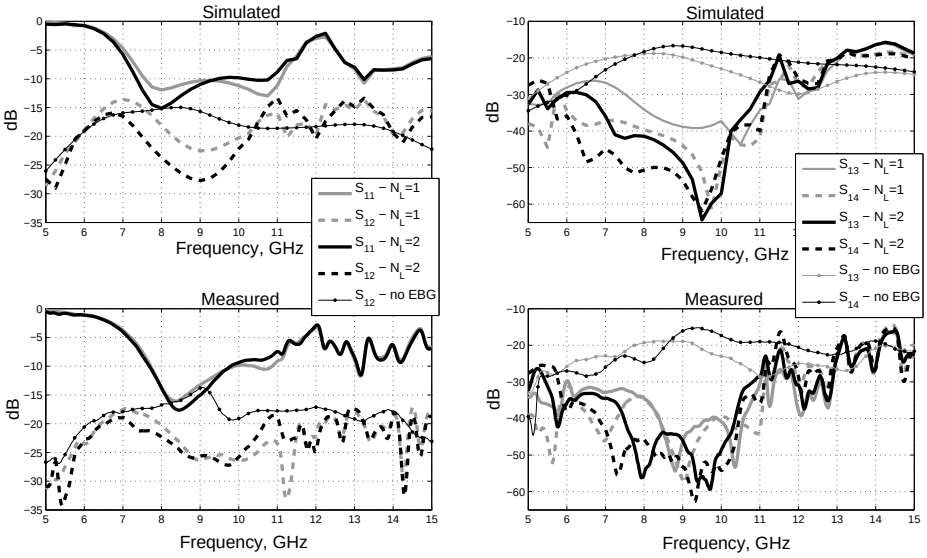

Figure 3.54: *MF_6 configuration (6 feeds), simulated and measured scattering parameters as a function of numbers of layers N_L; a=13mm, r=1.5mm, h=20mm, ε_r=37.*

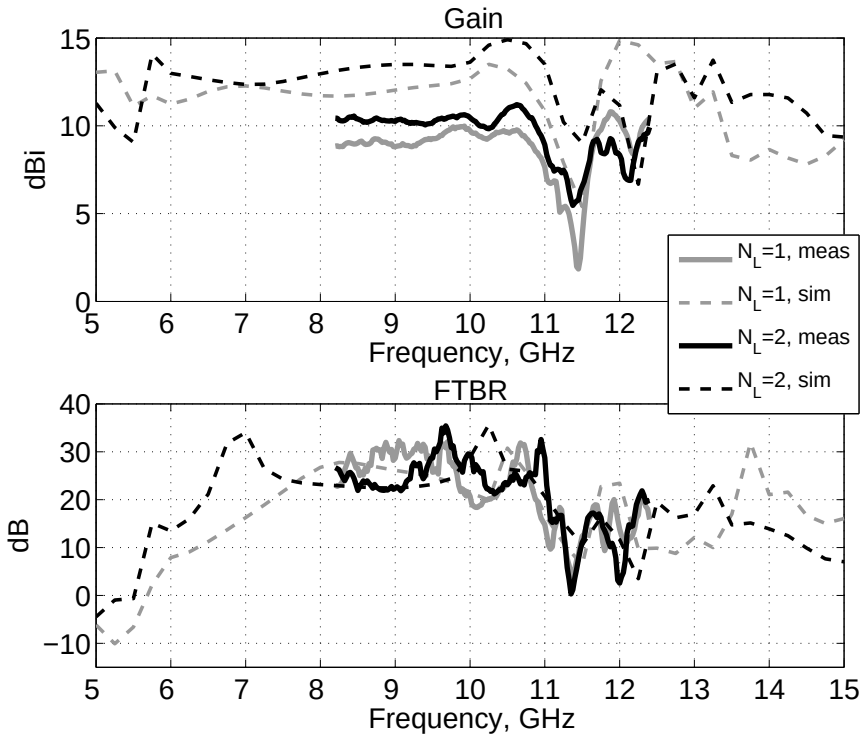

Figure 3.55: *MF_6 configuration (6 feeds), simulated and measured gain and FTBR as a function of numbers of layers N_L; a=13mm, r=1.5mm, h=20mm, ε_r=37.*

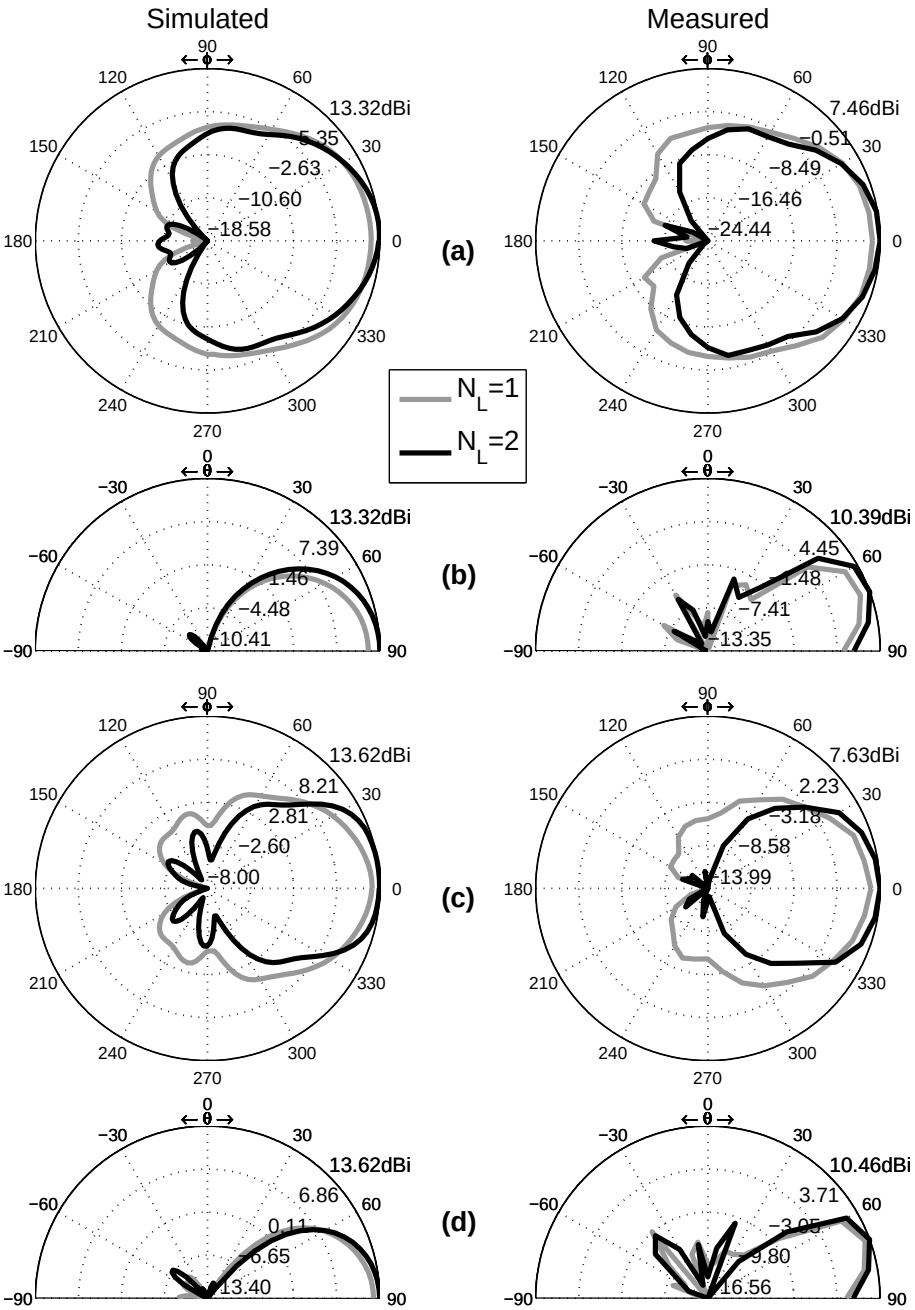

Figure 3.56: *MF_6 configuration (6 feeds), simulated and measured radiation patterns as a function of numbers of layers N_L; a=13mm, r=1.5mm, h=20mm, ε_r=37: a) H-plane at 8.5GHz; b) E-plane at 8.5GHz; c) H-plane at 10GHz; d) E-plane at 10GHz.*

3.4.2 Rods length h

The basic MF_3 and MF_6 configurations, figure 3.49a and figure 3.53b respectively, have been parametrically studied as a function of rods length h=10,20,30mm.

MF_3 Antenna

The influence of rods height on the MF_3 antenna S_{11} is shown in figure 3.57: as h is increased, antenna matching and impedance bandwidth are improved; decoupling between adjacent feeds is also increased, although the improvement introduced by passing from h=20mm to h=30mm is minimal. Gain is also generally increasing with h whilst the FTBR reaches a maximum value at an intermediate value, figure 3.58. Radiation patterns are also influenced by h: sidelobes magnitude is generally reduced as well as mainlobe beamwidth at frequencies toward the upper limit of the bandwidth, figure 3.59.

Measurements results are summarised in table 3.6.

h, mm	Gain, dBi	FTBR, dB	Bandwidth	S_{12}, dB
10 $0.3\cdot\lambda_c$	9.8 (8.6)	25.7 (10.9)	20.6% 9.1-11.2GHz	$\leq$-14.5 (-21.1)
20 $0.6\cdot\lambda_c$	10.2 (9.4)	25.7 (21.3)	28.4% 7.7-10.2GHz	$\leq$-23.8 (-26.5)
30 $0.9\cdot\lambda_c$	10.7 (9.9)	21.5 (15.9)	40.1% 7.5-11.2GHz	$\leq$-16.7 (-27.0)
no EBG	NA	NA	NA	$\leq$-13.4 (-16.9)

Table 3.6: *MF_3 configuration measured performance as a function of number of rods length h; N_L=1, a=13mm, r=1.5mm, ε_r=37 (in brackets are reported the average values within the impedance bandwidth); $\lambda_c = \lambda(f_c=9GHz)=33.3mm$.*

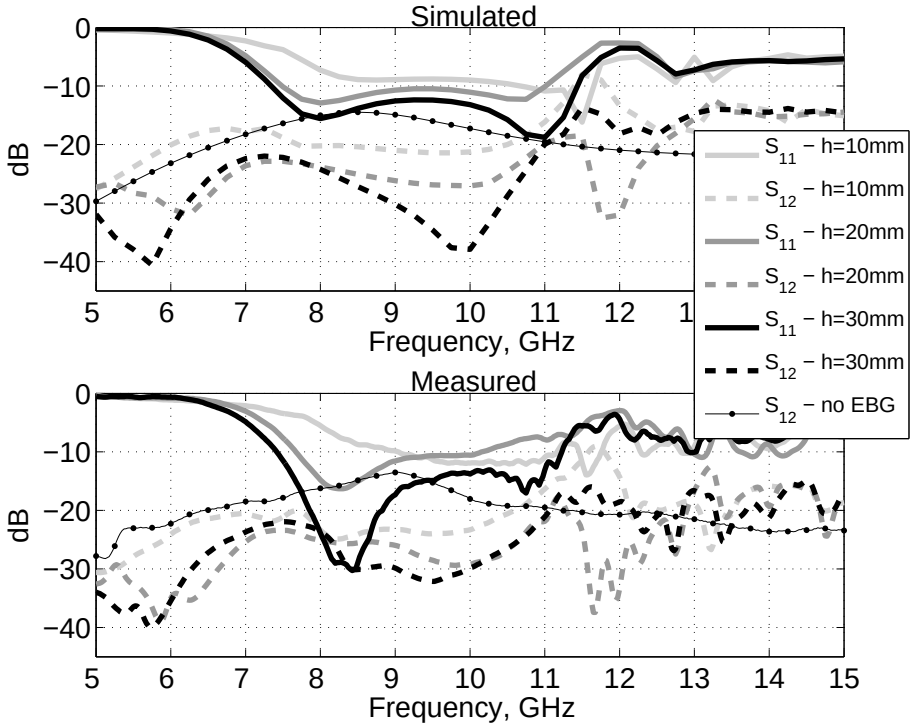

Figure 3.57: *MF_3 configuration (3 feeds), simulated and measured scattering parameters as a function of rods length h; a=13mm, r=1.5mm, N_L=1, ε_r=37.*

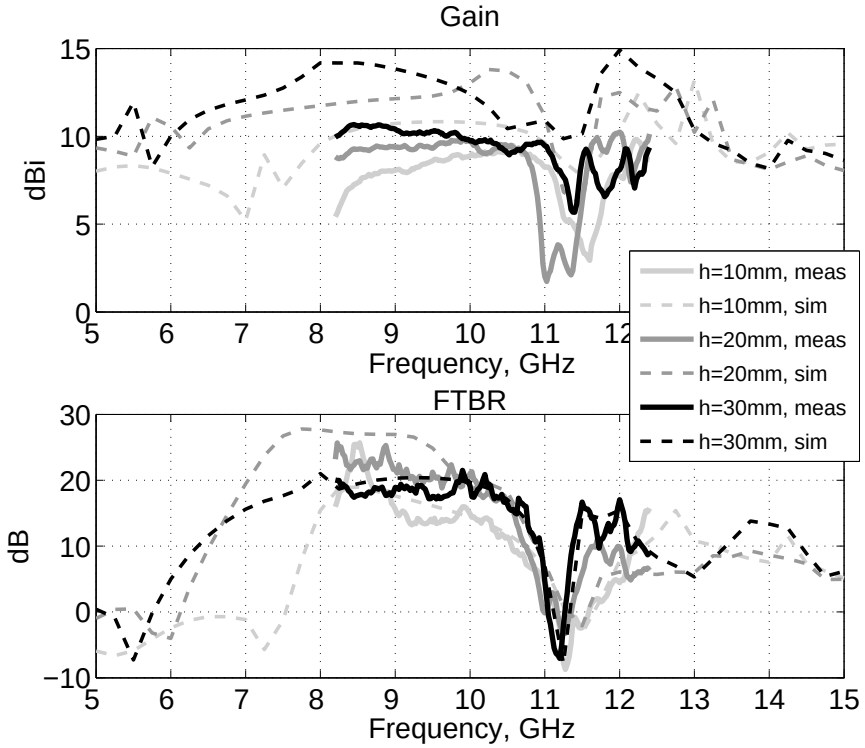

Figure 3.58: *MF_3 configuration (3 feeds), simulated and measured gain and FTBR as a function of rods length h; a=13mm, r=1.5mm, N_L=1, ε_r=37.*

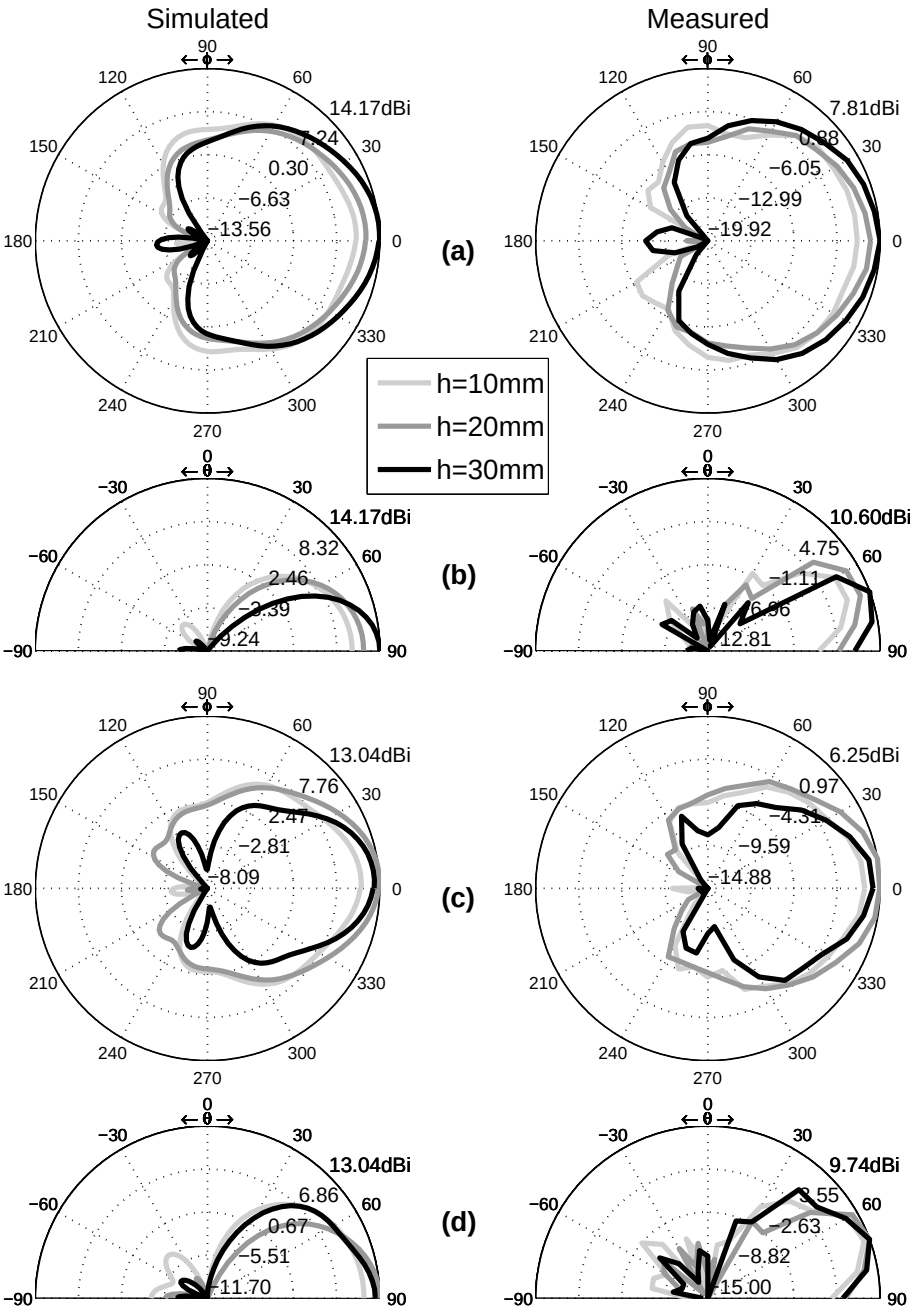

Figure 3.59: *MF_3 configuration (3 feeds), simulated and measured radiation patterns as a function of rods length h; a=13mm, r=1.5mm, N_L=1, ε_r=37: a) H-plane at 8.5GHz; b) E-plane at 8.5GHz; c) H-plane at 10GHz; d) E-plane at 10GHz.*

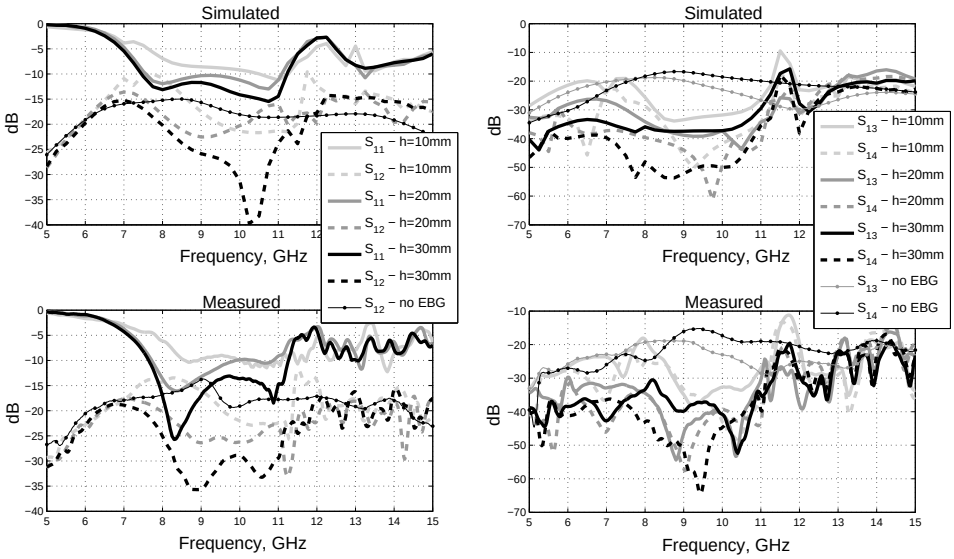

Figure 3.60: *MF_6 configuration (6 feeds), simulated and measured scattering parameters as a function of rods length h; a=13mm, r=1.5mm, N_L=1, ε_r=37.*

MF_6 Antenna

The influence of rods length *h* on the MF_6 antenna is very similar as for the MF_3 configuration: matching and bandwidth are generally improved as well as decoupling between feeds, figure 3.60. The average gain is also increasing but the FTBR is maximum at an intermediate value of *h*, figure 3.61. Radiation patterns sidelobes magnitude is decreasing with *h* but the mainlobe width is increased, figure 3.62.

Measurements results are summarised in table 3.7.

h, mm	Gain, dBi	FTBR, dB	Bandwidth	S_{12}, dB	S_{13}, dB	S_{14}, dB
10	10.0 (8.3)	29.9 (12.2)	9.2%	≤-21.9	≤-25.7	≤-35.6
$0.3\cdot\lambda_c$			10.1-11.1GHz	(-22.6)	(-31.3)	(-42.7)
20	10.8 (9.3)	32.3 (26.2)	33.7%	≤-18.8	≤-32.7	≤-33.9
$0.6\cdot\lambda_c$			7.8-10.9GHz	(-23.8)	(-41.5)	(-43.6)
30	10.4 (9.7)	24.0 (16.1)	37.9%	≤-21.6	≤-30.4	≤-26.4
$0.9\cdot\lambda_c$			7.7-11.3GHz	(-30.1)	(-38.2)	(-45.5)
no EBG	NA	NA	NA	≤-13.8	≤-19.1	≤-15.3
				(-17.6)	(-23.0)	(-17.3)

Table 3.7: *MF_6 configuration measured performance as a function of number of rods length h; N_L=1, a=13mm, r=1.5mm, ε_r=37 (in brackets are reported the average values within the impedance bandwidth); $\lambda_c = \lambda(f_c=9GHz)=33.3mm$.*

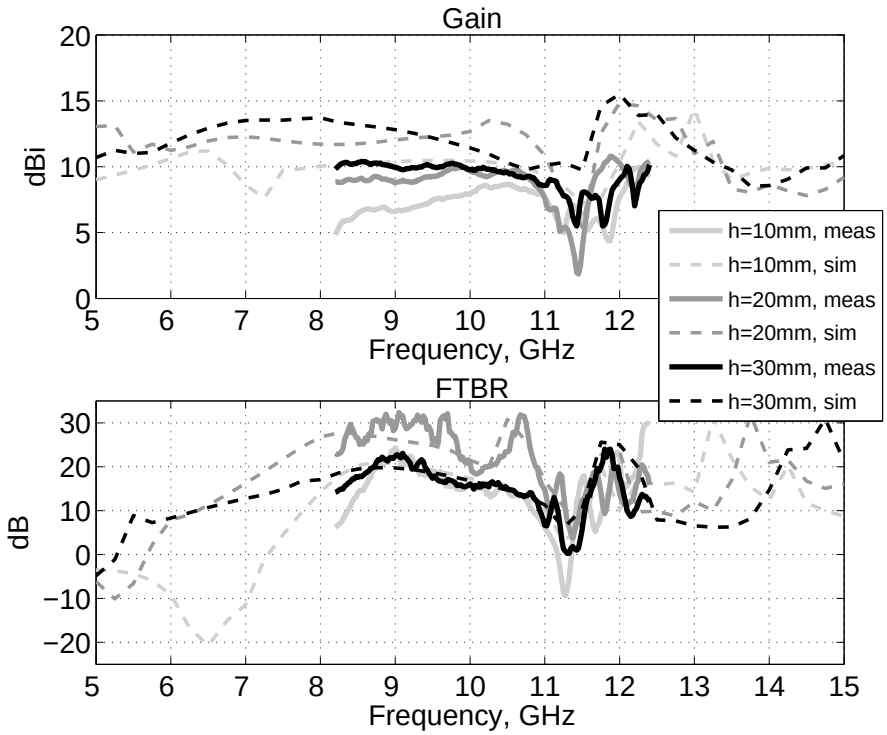

Figure 3.61: *MF_6 configuration (6 feeds), simulated and measured gain and FTBR as a function of rods length h; a=13mm, r=1.5mm, N_L=1, ε_r=37.*

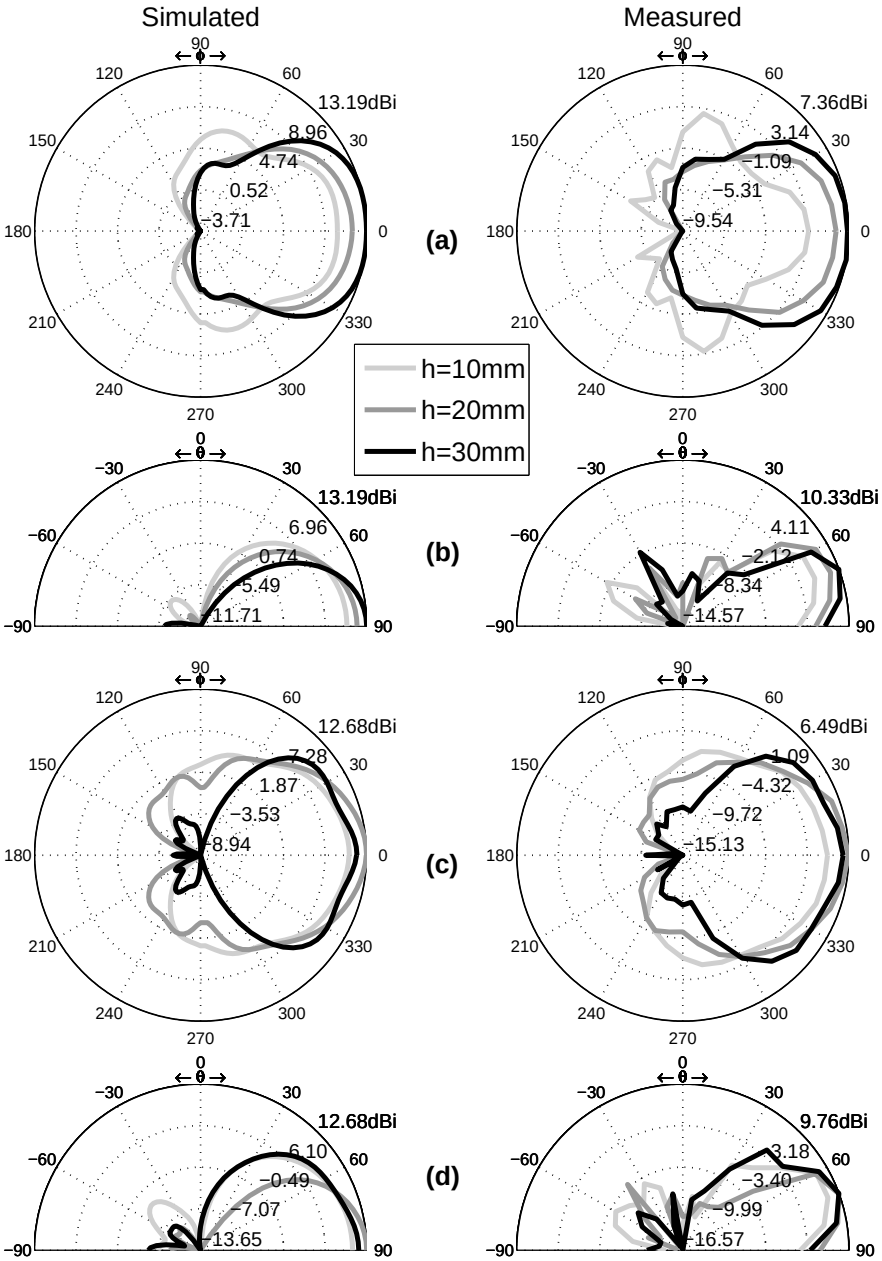

Figure 3.62: *MF_6 configuration (6 feeds), simulated and measured radiation patterns as a function of rods length h; a=13mm, r=1.5mm, N_L=1, ε_r=37: a) H-plane at 8.5GHz; b) E-plane at 8.5GHz; c) H-plane at 10GHz; d) E-plane at 10GHz.*

3.4.3 Discussion

The intrinsic symmetry of the triangular lattice can be easily exploited to design multi-feed structures as the two presented configurations. The design process is based on introducing multiple defects in a TEBG structure in order to create an axisymmetric structure with multiple open cavities; in each cavity is then placed a monopole feed. Given the structure axial symmetry, radiation patterns can be rotated by discrete angular steps according to which open cavity is fed, as demonstrated in figure 3.40.

A 3 feeds (MF_3) and a 6 feeds (MF_6) configuration were analysed and parametrically studied, showing very similar characteristics. Increasing the number of layers N_L, ie increasing the number of rods between adjacent feeds, has a little impact on performances and therefore configurations with minimum number of rods and minimum maximum dimensions are prefered. Rods heigth h has a major impact on performances: matching and bandwidth are generally increasing as well as decoupling between feeds and average gain within the impedance bandwidth. The FTBR is increasing in a first istance and then is reduced when h is further increased. Radiation patterns sidelobes are reduced when h is increased, although main lobe width is widened. In summary, h could be tuned in order to optimize performance while N_L kept minimum to minimize the requested number of rods and maximum dimensions.

The TEBG structure has a twofold purpose: increasing the gain and FTBR of the monopole feeds as well as providing high decoupling between feeds. Monopole feeds separation is $2{\cdot}a$ = 26mm (MF_3) and at least $2{\cdot}a \cdot sin(\pi/3) \simeq$ 22.5mm (MF_6), less than a wavelength, nevertheless the forward transmission coefficient S_{12} is $\leq$ -19dB within the whole impedance bandwidth. Decoupling between adjacent feeds is therefore improved by at lest 10dB for the MF_3 configuration compared to a reference case without the TEBG structure; for the MF_6 configuration the improvement is 7dB for close feeds and at least 20dB for more distant feeds.

Compared to the presented structures, other EBG antennas with multiple sources, such as linear arrays of dielectric EBG horn antennas [39], multibeam [70] and multi-feed [72] metallic EBG antennas, were able to achieve a higher maximum gain and a narrower beamwidth on the E-plane. However, the investigated multi-feed TEBG antennas present two main advantages: compactness (maximum dimensions are $\leq 1.2{\cdot}\lambda_c$ and $\leq 2{\cdot}\lambda_c$ for MF_3 and MF_6 respectively) and a much larger bandwidth (fractional bandwidth $\geq 30\%$) with stable directivity patterns.

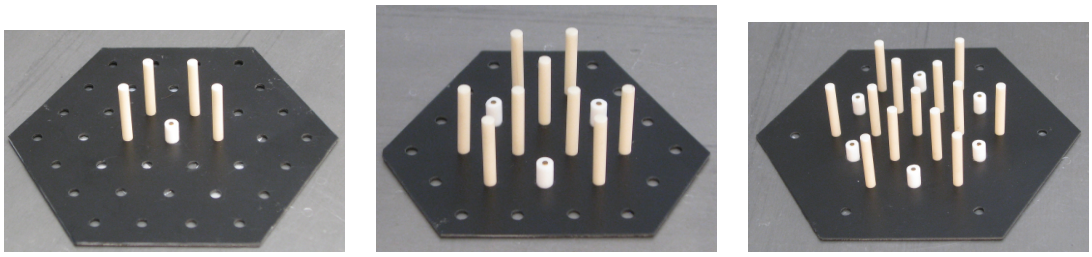

(a) *Single feed* **(b)** MF_3 **(c)** MF_6

Figure 3.63: *Single-feed and multiple-feed comparison, prototypes photo, N_L=1: a) single feed; b) 3 feeds configuration; c) 6 feeds configuration.*

3.5 Single-feed and multiple-feed comparison

Multiple feed antennas were designed using the single-feed antenna as a starting point; therefore it is reasonable to expect similarities in the performances of single feed and multiple feed configurations. In the next sections measurements results of single and multiple feed TEBG antennas are compared and analysed.

3.5.1 N_L = 1

The pictures and geometries of one layer (N_L=1) single feed and multiple feed TEBG antenna prototypes are respectively shown in figure 3.63 and figure 3.64. They present a very similar S_{11} response, figure 3.65, as well as measured gain in terms of maximum/average values and frequency behaviour, figure 3.66. FTBR frequency behaviour and maximum/average values are quite different, especially when it comes to MF_6. This can be attributed to the specific geometries of the three prototypes, especially to the different setups of dielectric rods and feeding probes on the back of the fed cavities. Radiation patterns as a function of frequency are shown in figure 3.67, all prototypes present very similar radiation patterns, especially on the azimuthal plane; differences on the elevation plane, as abovementioned, can be attributed to the different structures on the back of the fed cavities.

Prototypes characteristics and performances are summarised in table 3.8.

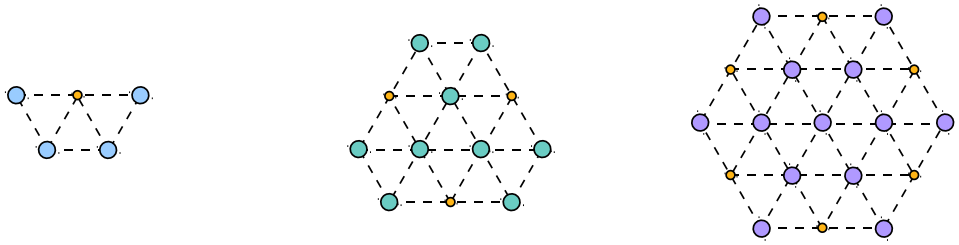

(a) *Single feed* **(b)** MF_3 **(c)** MF_6

Figure 3.64: *Single-feed and multiple-feed comparison, prototypes geometries, N_L=1: a) single feed; b) 3 feeds configuration; c) 6 feeds configuration.*

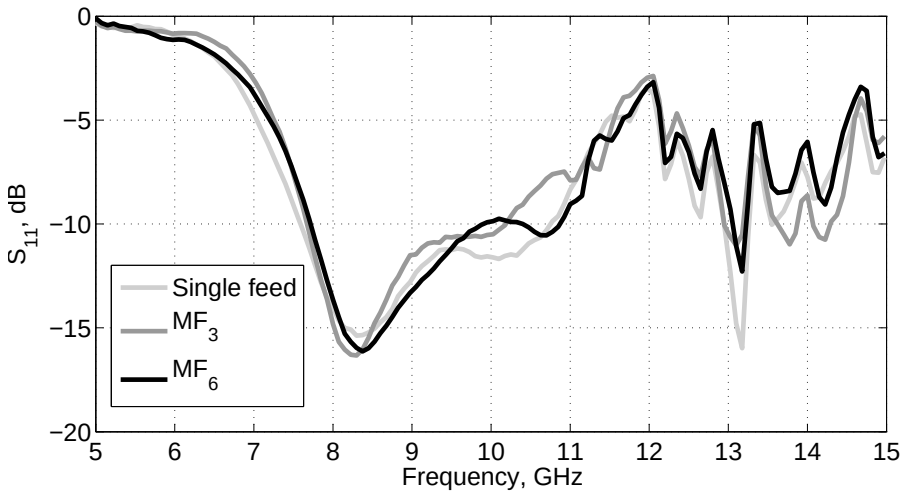

Figure 3.65: *Single-feed and multiple-feed comparison, measured S_{11}, N_L=1.*

	Single	MF_3	MF_6
Bandwidth	34.2% 7.6-10.8GHz	28.4% 7.7 - 10.2GHz	33.7% 7.8 - 10.9GHz
Gain, dBi	10.7 (9)	10.2 (9.4)	10.8 (9.3)
FTBR, dB	31.3 (19.4)	25.7 (21.3)	32.3 (26.2)
HPBW	60°	60°	60°
S_{12}, dB	N/A	≤-23.8 (-26.8)	≤-19.1 (-24.3)
S_{13}, dB	N/A	N/A	≤-32.5 (-41.8)
S_{14}, dB	N/A	N/A	≤-33.9 (-43.2)

Table 3.8: *Single-feed and multiple-feed comparison, prototypes characteristics and performances (in brackets are reported the average values within the impedance bandwidth), N_L=1.*

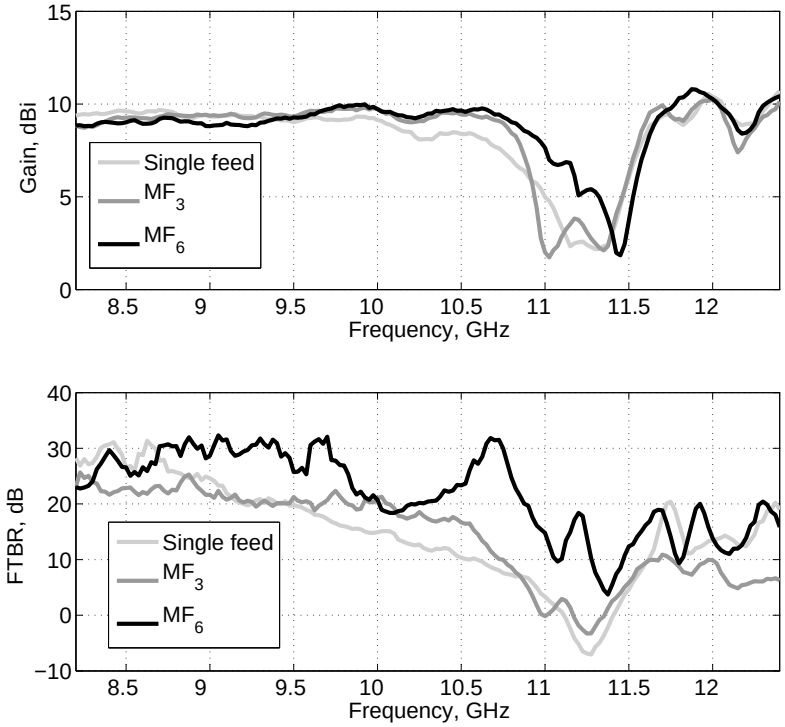

Figure 3.66: *Single-feed and multiple-feed comparison, measured gain and FTBR, $N_L=1$.*

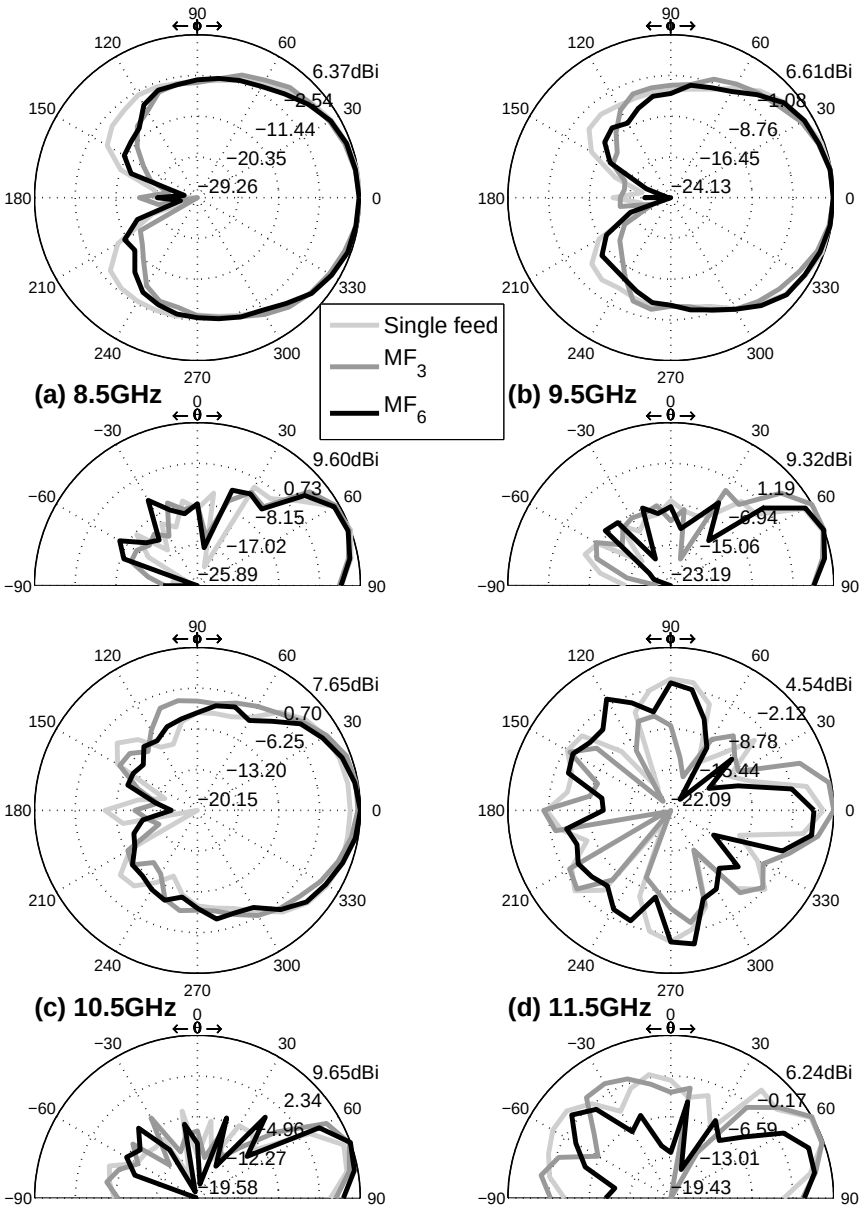

Figure 3.67: *Single-feed and multiple-feed comparison, measured radiation patterns, $N_L=1$.*

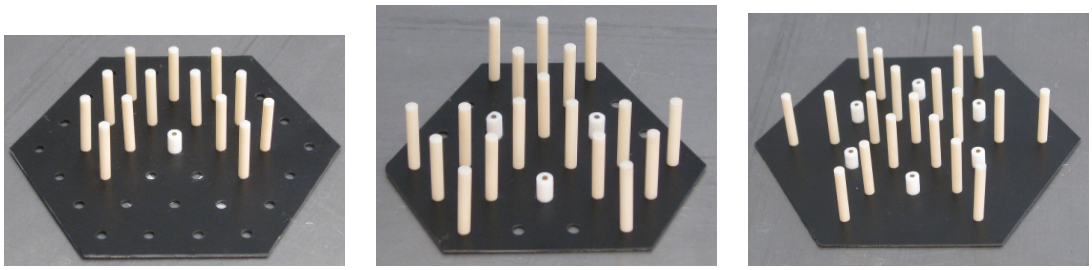

(a) *Single feed* **(b)** MF_3 **(c)** MF_6

Figure 3.68: *Single-feed and multiple-feed comparison, prototypes photo, N_L=2: a) single feed; b) 3 feeds configuration; c) 6 feeds configuration.*

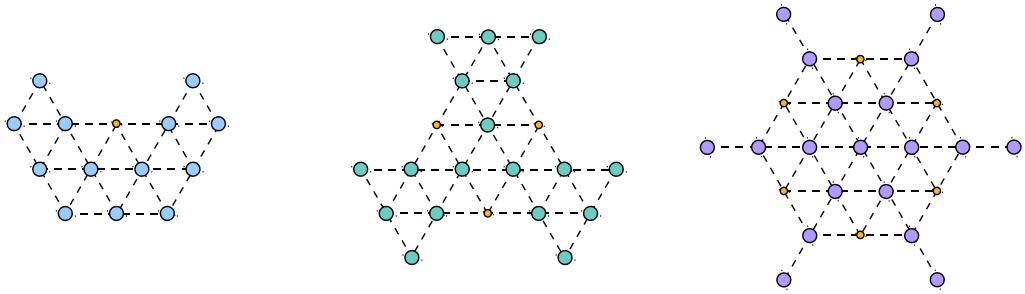

(a) *Single feed* **(b)** MF_3 **(c)** MF_6

Figure 3.69: *Single-feed and multiple-feed comparison, prototypes geometries, N_L=2: a) single feed; b) 3 feeds configuration; c) 6 feeds configuration.*

3.5.2 N_L = 2

The pictures and geometries of two layer (N_L=2) single feed and multiple feed TEBG antenna prototypes are respectively shown in figure 3.68 and figure 3.69. As in the previous case, all configurations present a very similar S_{11} response, figure 3.70 and maximum/average gain values. All prototypes show a quite stable gain at frequencies inside the bandgap, whilst at higher frequencies, gain behaviour is quite disturbed. All FTBR curves present the characteristic of rapidly falling at the bandgpad upper limit and then, as for the gain, the behavior is unpredictable.

Radiation patterns as a function of frequency are shown in figure 3.72. As in the previous case, all prototypes present very similar radiation patterns, especially on the azimuthal plane. Differences on the elevation plane can be again attributed to the different structures on the back of the fed cavities.

Prototypes characteristics and performances are summarised in table 3.9.

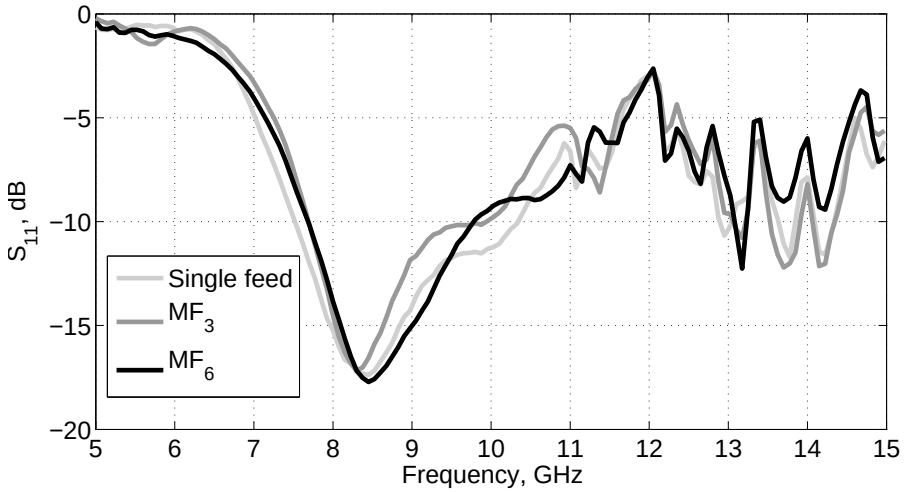

Figure 3.70: *Single-feed and multiple-feed comparison, measured S_{11}, N_L=2.*

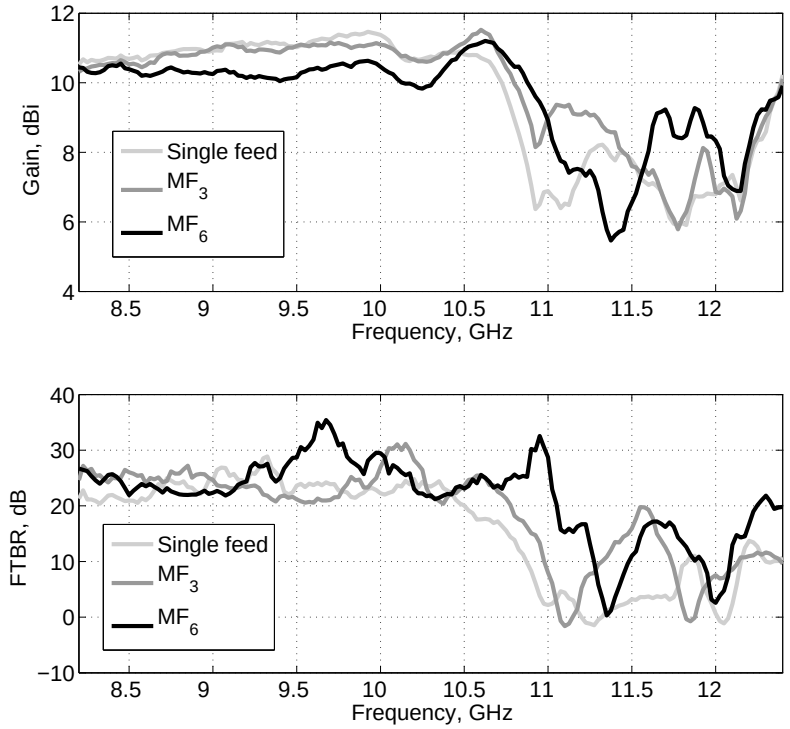

Figure 3.71: *Single-feed and multiple-feed comparison, measured gain and FTBR, N_L=2.*

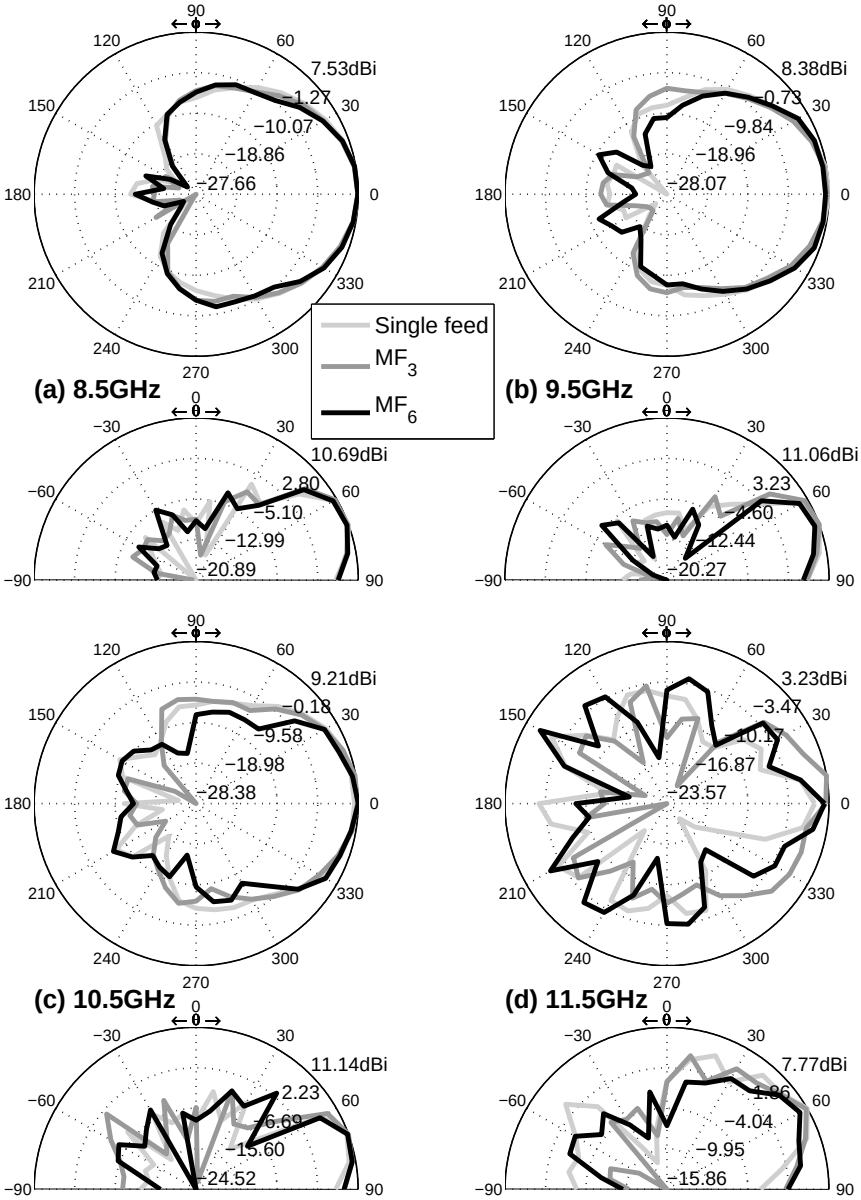

Figure 3.72: *Single-feed and multiple-feed comparison, measured radiation patterns, N_L=2.*

	Single	MF_3	MF_6
Bandwidth	31.8% 7.5 - 10.4GHz	25.5% 7.7 - 9.9GHz	24% 7.7 - 9.8GHz
Gain, dBi	11.5 (11)	11.5 (10.9)	11.2 (10.3)
FTBR, dB	28.9 (23.4)	31.1 (23.8)	35.4 (25.7)
HPBW	60°	60°	60°
S_{12}, dB	N/A	$\leq$-26.4 (-28.3)	$\leq$-21.2 (-24.8)
S_{13}, dB	N/A	N/A	$\leq$-43.5 (-50.0)
S_{14}, dB	N/A	N/A	$\leq$-45.1 (-51.6)

Table 3.9: *Single-feed and multiple-feed comparison, prototypes characteristics and performances (in brackets are reported the average values within the impedance bandwidth), N_L=2.*

3.6 Conclusions

The design steps of single feed and multiple feed dielectric TEBG antennas have been presented and analysed. The multilayer TEBG structures are made with dielectric rods arranged in a simple triangular lattice; antennas are excited using monopole feeds placed inside cavities created by removing rods from the lattice forming angular defect windows.

The triangular lattice of dielectric rods is the approximation of a 2-D crystal (made by infinite long dielectric rods) presenting a complete bandgap for TM polarization (electric field is parallel to the rods and magnetic field is in the transverse plane). At low elevation angles, the monopole excited fields have a distribution very similar to the 2-D configuration: the 3-D TEBG structure is a good approximation of the 2-D crystal and at frequency within the bandgap excited fields are re-directed toward the angular defect creating very directive radiation patterns. For increasing elevation angles, the 3-D TEBG structure approximation of the 2-D crystal progressively fails; however, given the intrinsic configuration of the excited fields (the electric field magnitude is decreasing as the elevation angle increases), low radiated fields are expected anyway.

Several prototypes were realized (using dielectric rods made with modified barium titanate ε_r=37$\pm$1 [81]) and tested, showing a good agreement between simulations and measurements. Single feed and multiple feed configurations were found with very similar characteristics:

- $\simeq$30% impedance bandwith in the 7.5GHz-10.5GHz frequency region;
- $\simeq$11dBi peak gain and a FTBR $\geq$20dB within the impedance bandwidth;
- directive radiation patterns at the TEBG structure bandgap frequencies;
- stable radiation patterns within the whole impedance bandwidth.

The presented antennas were also compared to other EBG antennas reported in literature, Section 3.3.7 and Section 3.4.3. Although other implementations were able to achieve a higher maximum gain and narrower beamwidths (Section 1.1), both single feed and multiple feed analysed configurations presents two major advantages:

Compactness: the maximum dimensions are respectively $1.17\cdot\lambda_c$, $1.56\cdot\lambda_c$ and $1.97\cdot\lambda_c$ for the single feed, MF_3 and MF_6 configurations with a $0.6\cdot\lambda_c$ vertical profile (λ_c is the wavelength at the impedance bandwidth center frequency of 9GHz).

Operational frequency range: radiation patterns are quite stable in the whole impedance bandwidth and therefore the operational frequency range covers the whole $\simeq$30% impedance bandwidth.

Chapter 4 – Dielectric EBG corner reflector antennas

4.1 Introduction

The use of reflectors is a well-established approach in antenna design to increase the gain of an otherwise low-directivity source [74, 84]. Among the simplest types of reflectors is the dihedral corner reflector, easily realised joining together two reflective surfaces to form a corner of angle α.

The multilayer CEBG and TEBG structures presented in the previous chapters were found able to achieve high gain and FTBR on the azimuthal plane with an optimized number of layers N_L=2. Increasing the number of layers would improve the performances (given by the angular defect window presenting a larger aperture) at the expense of the required number of rods and overall dimensions. An extension to multilayer CEBG and TEBG structures are the EBG corner reflectors depicted in figure 4.1, where a triangular lattice (TEBG) of dielectric rods and a square lattice (SEBG) of dielectric rods are used to create 60°, 90° and 120° EBG corner reflectors. The principle of operation is quite simple: at bandgap frequencies, the EBG structure is expected to reflect the excited fields toward the corner aperture in a similar fashion of a metal corner reflector.

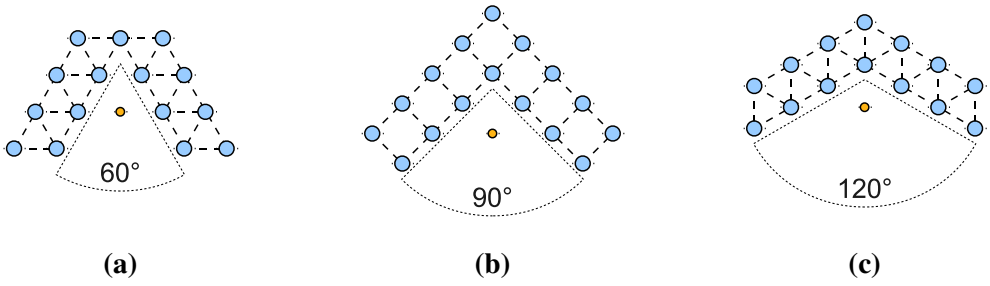

Figure 4.1: *EBG corner geometries: a)* 60° *TEBG corner reflector; b)* 90° *SEBG corner reflector; c)* 120° *TEBG corner reflector.*

Two different EBG crystals have been used, the same triangular lattice used for the TEBG antennas presented in Chapter 3 and a square lattice of dielectric rods. The triangular lattice, figure 4.2a, is composed by dielectric rods arranged according to the lattice vectors:

$$\mathbf{a}_{1T} = a(\hat{\mathbf{x}}\sqrt{3} + \hat{\mathbf{y}})/2 \tag{4.1}$$

$$\mathbf{a}_{2T} = a(\hat{\mathbf{x}}\sqrt{3} - \hat{\mathbf{y}})/2 \tag{4.2}$$

where a is the lattice constant and $\hat{\mathbf{x}}$ and $\hat{\mathbf{y}}$ are the cartesian unit vectors. The triangular lattice geometry can be easily used to create EBG reflectors with a corner aperture equal to $n \cdot \frac{\pi}{3}$ with $n = 0, 1, 2, ...$; we considered the cases $n = 1, 2$, i.e. a corner aperture of 60°

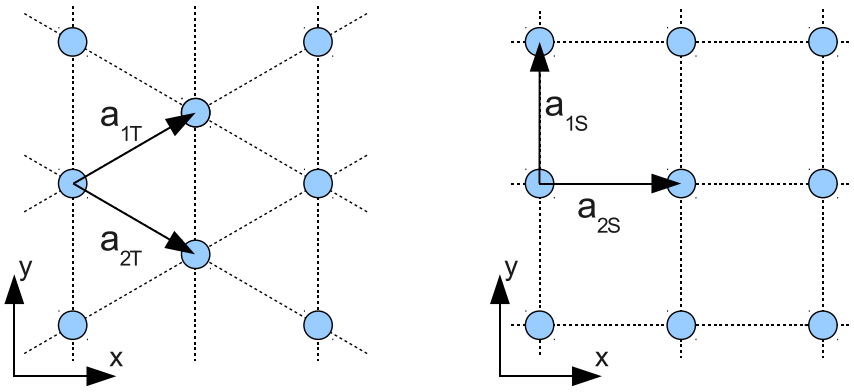

(a) **(b)**

Figure 4.2: *EBG corner lattices: a) triangular lattice; b) square lattice.*

and 120°, figure 4.1a,c. The square lattice, figure 4.2b, is composed by dielectric rods arranged according to the lattice vectors:

$$\mathbf{a}_{1S} = a\hat{\mathbf{x}} \tag{4.3}$$

$$\mathbf{a}_{2S} = a\hat{\mathbf{y}} \tag{4.4}$$

and it can be easily used to create EBG reflector with a corner aperture equal to $n\frac{\pi}{2}$ with $n = 0, 1, 2, ...$; we considered the case $n = 1$, i.e. a corner aperture of 90°, figure 4.1b.

The dielectric EBG corner reflectors have been analysed following a similar approach as for CEBG and TEBG multilayer structures:

- two-dimensional antennas were analysed and parametrically studied in order to identify the influence of geometrical parameters on radiation performances;
- previous step results were then used to design three-dimensional EBG corner antennas;
- prototypes were built and tested;
- simulations and measurements results were finally compared and analysed.

As already mentioned, the TEBG crystal is the same as the one used to design multilayer TEBG antennas and therefore has been already characterised. The SEBG crystal has been characterised in a similar fashion as for the TEBG crystal using a plane-wave eigen-solver to compute electromagnetic badgap structures as a function of the geometrical parameters and rods dielectric permittivity. Results have been collected and visualised in gapmaps.

In the next sections the design steps, simulations and measurements results of single feed and multiple feed EBG corner reflector antennas based on a triangular lattice and

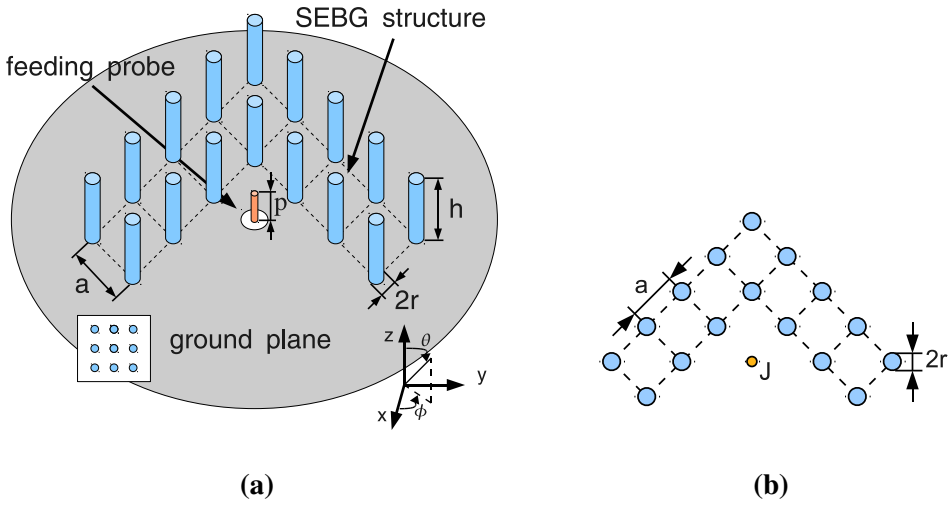

Figure 4.3: 90° *SEBG corner reflector antenna geometry: a) 3-D view and (inset) square lattice of circular dielectric rods; b) schematic view.*

a square lattice of dielectric rods are presented. The 90° SEBG corner reflector antenna will be introduced first along with the characterization of the SEBG crystal; 60° and 120° TEBG corner reflector antennas will be then analysed and finally, the three corner reflector EBG antennas compared.

4.2 90° SEBG corner reflector antenna

The 90° dielectric EBG corner antenna is realized arranging dielectric rods in a square geometry as shown in figure 4.3. The square lattice EBG (SEBG) structure presents the shape of a 90° corner reflector and a source feed is place at distance s from the reflector apex. The SEBG structure approximate a 2-D square lattice of infinite long dielectric rods of radius r arranged according to the lattice constant a. The 2-D lattice has been characterized in terms of electromagnetic band structure; a two-dimensional antenna has been then analyzed to get a first insight on the influence of the geometrical parameters on the radiation patterns.

4.2.1 SEBG Characterization

The SEBG structure may present a complete bandgap for TM polarized waves which extension and position are a function of the rods permittivity ε_r, radius r and the lattice constant a. A plane-wave eigensolver, Appendix B, has been used to compute the electromagnetic band structure for the TM modes as a function of rods radius r, lattice constant a and dielectric permittivity ε_r. The results can be visualised in gapmaps as those shown in figure 4.4-4.6. These gapmaps are quite similar to the TEBG gapmaps shown in Chapter 3, in particular the influence of geometrical parameters and rods dielectric permittivity can be summarised as:

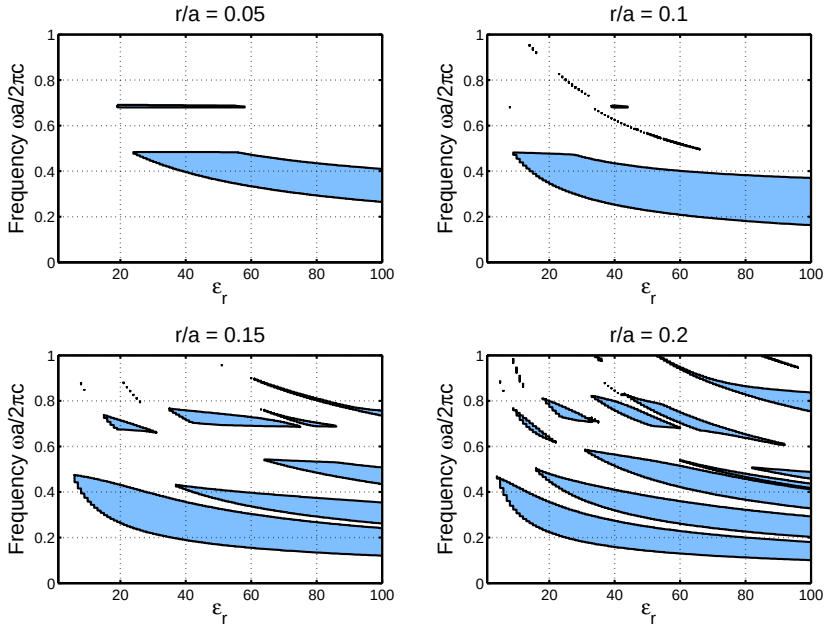

Figure 4.4: *Simulated electromagnetic gapmaps as a function of rods permittivity ε_r for several values of r/a.*

- for small values of the ratio r/a there is only one main bandgap which center frequency inversely proportional to rods ε_r, figure 4.4. For values greater than 0.15, several bandgaps of narrower extension appear;
- we focused our attention on ε_r=37 in order to reuse the ceramic dielectric rods of multilayer TEBG antennas (different ceramic materials with a different dielectric permittivity could be used though as pointed out in the previous chapters);
- when a is fixed and r is increased, figure 4.5, new bandgaps appear with centre frequency and extensions generally inversely proportional to r;
- when r is fixed, figure 4.6, a minimum value of a is required for bandgaps to appear; bandgaps extension initially grows as r is increased and after reaching a maximum is then reduced.

These gapmaps are very useful to design the geometrical parameters of the antenna. The maximum extension of the first bandgap is reached at r/a=0.122 for ε_r=37; r and a can be then set using figure 4.5 and figure 4.6 according to the required frequency of operation. Figure 4.7 show the electromagnetic band structure for a square lattice with a=12mm, r=1.5mm ($r/a = 0.125$) and ε_r=37: a 64% complete TM bandgap is present from 5.5GHz to 10.63GHz.

4.2.2 2-D 90° SEBG corner reflector characterization

If we excite a TM mode in front of the 90° SEBG corner reflector, energy at frequencies outside the bandgap will be free to propagate through the structure whilst energy at

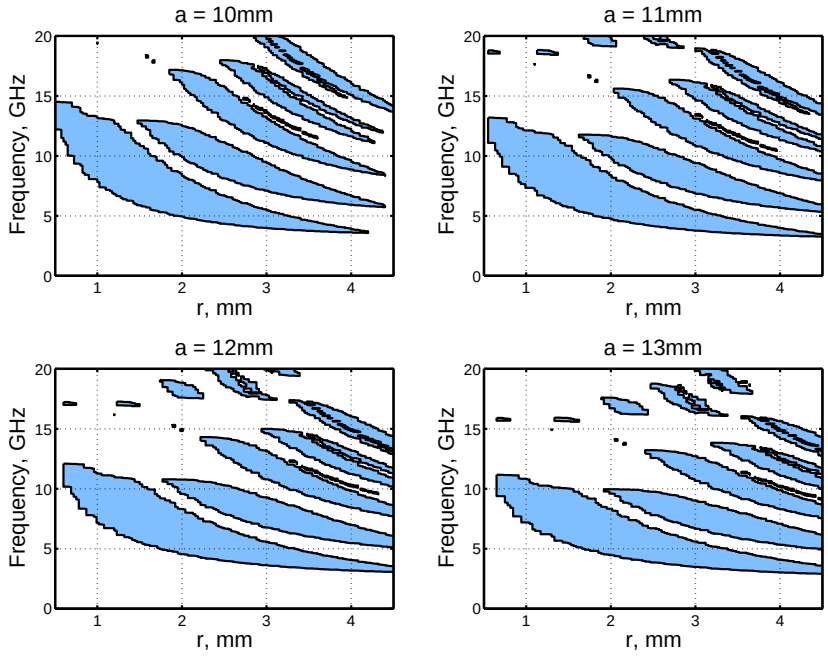

Figure 4.5: *Simulated electromagnetic gapmaps as a function of rods radius r for several values of lattice constant a, ε_r=37.*

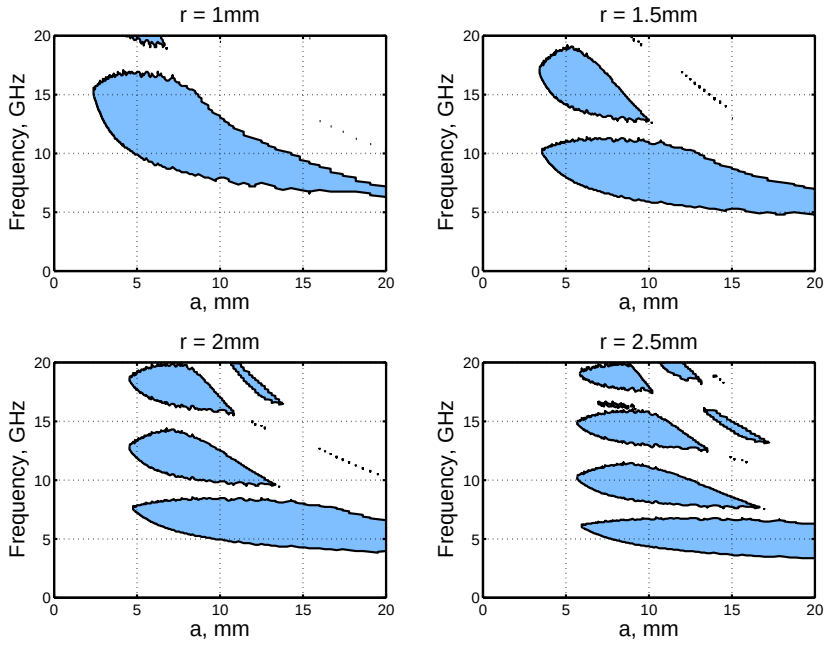

Figure 4.6: *Simulated electromagnetic gapmaps as a function of lattice constant a for several values of rods radius r, ε_r=37.*

frequencies within the bandgap will be reflected back enhancing the radiated fields in the aperture D_a direction.

A two-dimensional 90° SEBG corner reflector antenna has been parametrically studied focusing on: the reflector width w; the reflector internal length L; the distance between source feed and corner apex s.

The reflector width w is proportional to the deployed numbers of layers N_w : $w =$

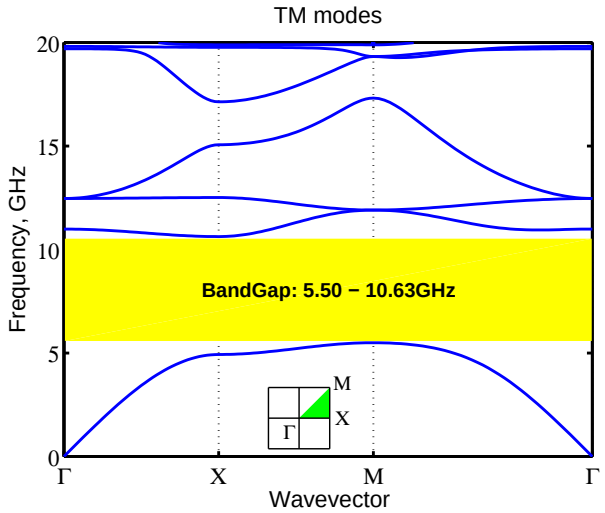

Figure 4.7: *Simulated electromagnetic band structure for the TM modes of a two-dimensional square lattice of dielectric columns with r=1.5mm, a=12mm, ε_r=37.*

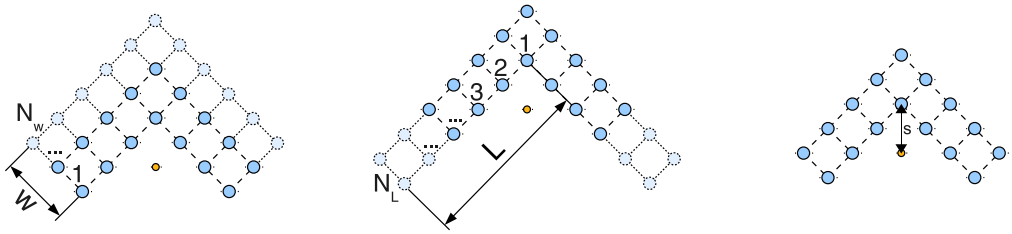

(a) **(b)** **(c)**

Figure 4.8: *2-D 90° SEBG corner reflector antenna, parametrical study: a) reflector width w; b) reflector internal length L; c) feed distance from corner apex s.*

$(N_w - 1) \cdot a$, figure 4.8a. Simulations shown that the radiation patterns are slightly influenced by the reflector width, figure 4.9: the difference between 2 or more layers is very small and for $w \geq 2 \cdot a$ radiation patterns are practically identical.

The reflector internal length L is proportional to the deployed numbers of layers N_L: $L = (N_L - 1) \cdot a$, figure 4.8b. Increasing the length L increases the front-to-back-ratio (FTBR) and narrows the radiation patterns main beam, figure 4.10. For $L \geq 5 \cdot a$ radiation patterns are practically identical.

The distance between source feed and corner apex s, figure 4.8c, has a big impact on the radiation patterns, as shown in figure 4.11. A short distance provides better performance at high frequencies but worse FTBR at low frequencies; conversely a longer distance provides worse perfomance at high frequencies and better FTBR at low frequencies. The most stable radiation patterns for the widest frequency range were achieved with a feed displacement $s = 2 \cdot a \cdot \cos\left(\frac{\alpha}{2}\right) = a \cdot \sqrt{2}$, where α is the corner enclosed angle, i.e. 90°.

The normalised electric field distribution is shown in figure 4.12 for a 2-D 90°

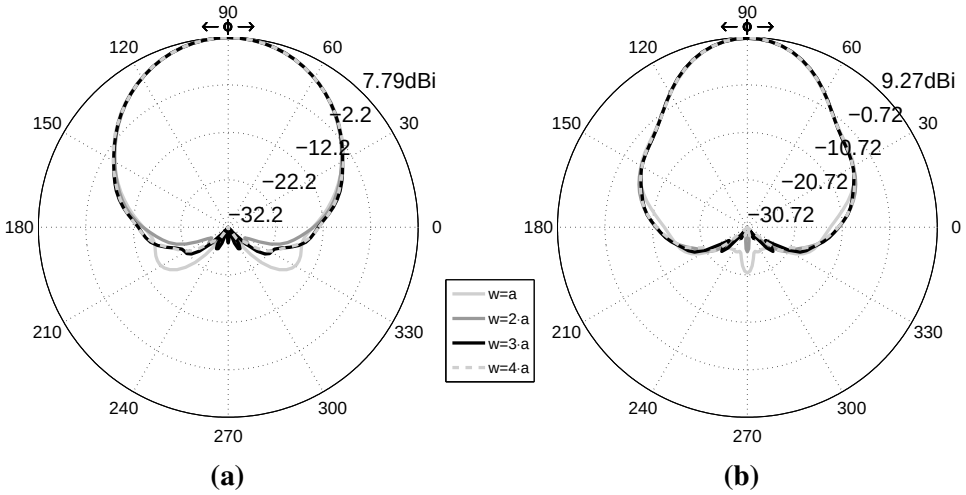

Figure 4.9: *2-D* 90° *SEBG corner reflector antenna, simulated (normalised) radiation patterns as a function of the reflector width w, N_L=3: a) 7GHz, b) 9GHz.*

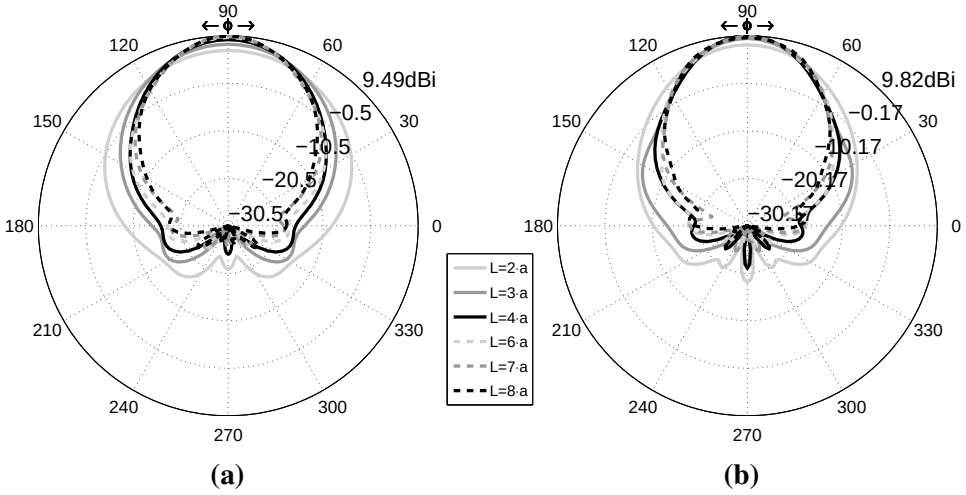

Figure 4.10: *2-D* 90° *SEBG corner reflector antenna, simulated (normalised) radiation patterns as a function of the reflector internal length L, N_w=2: a) 7GHz, b) 10GHz.*

SEBG corner reflector antenna with N_L=3 and N_w=2. At frequencies inside the bandgap, 6GHz-10GHz, the electric field is re-directed toward the corner aperture; at frequency below and above the bandgap, respectively 3GHz-5GHz and 11GHz-14GHz, there is either little interaction between the excite fields and the SEBG structure or the excited fields are scattered in every direction leading to radiation patterns with multiple beams.

The parametric study revealed that the most influent parameter is the source distance *s*, which must be chosen properly to guarantee directive radiation patterns with a high FTBR within the whole bandgap frequency range. The reflector width *w* and internal length *L* have a smaller influence on the radiation patterns; they can be then chosen according to the antenna dimension requirements.

In figure 4.14 and figure 4.15 the radiation patterns, gain and FTBR of a 2-D

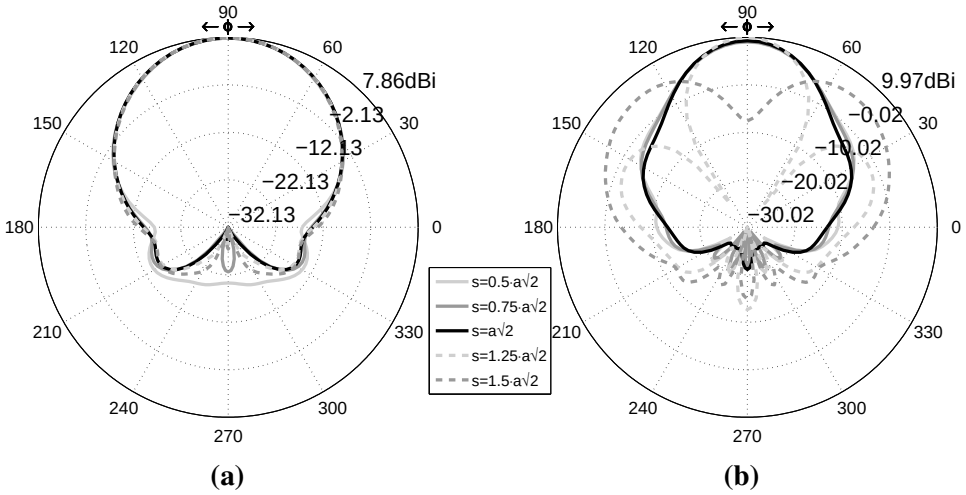

Figure 4.11: *2-D* 90° *SEBG corner reflector antenna, simulated (normalised) radiation patterns as a function of the feed distance s from the corner apex,* N_L*=3 and* N_w*=2: a) 7GHz, b) 10GHz.*

90° SEBG corner reflector antenna and 2-D 90° metal corner reflector antenna of similar dimensions are compared, figure 4.13. At bandgap frequencies, 5.5-10.63GHz, the two antennas present very similar characteristics: the main beam of the radiation patterns nicely overlap for at least 90° and the two antennas present the same directivity. Therefore, at bandgap frequencies the SEBG corner reflector is as good as a metallic reflector. Differencies in FTBR and radiation patterns at angles outside the main beam can be attribuited to fields diffracted by the edges of the SEBG corner as well as fields propagating, although attenuated, through the SEBG structure.

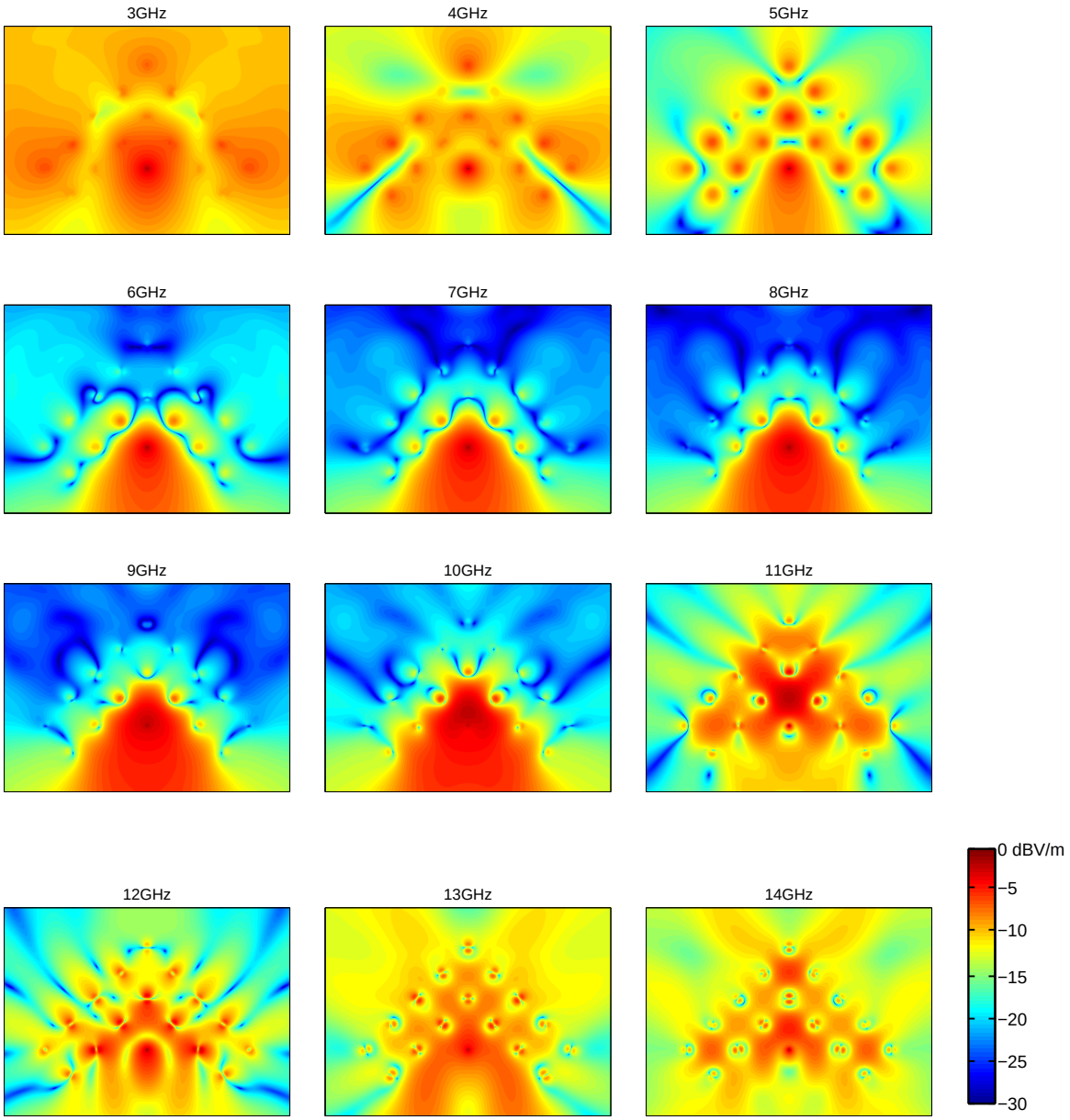

Figure 4.12: *2-D SEBG antenna, simulated normalised electric field distribution on the azimuthal plane, a=12mm, r=1.5mm, ε_r=37, N_L=3 and N_w=2.*

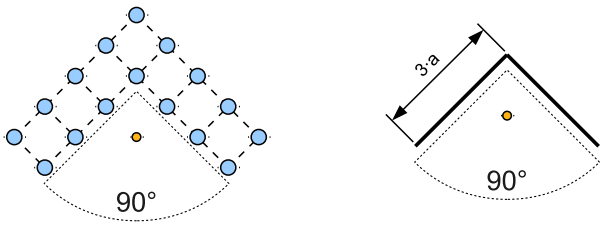

(a) **(b)**

Figure 4.13: *a) 2-D 90° SEBG corner reflector antenna; b) 2-D 90° metal corner reflector antenna.*

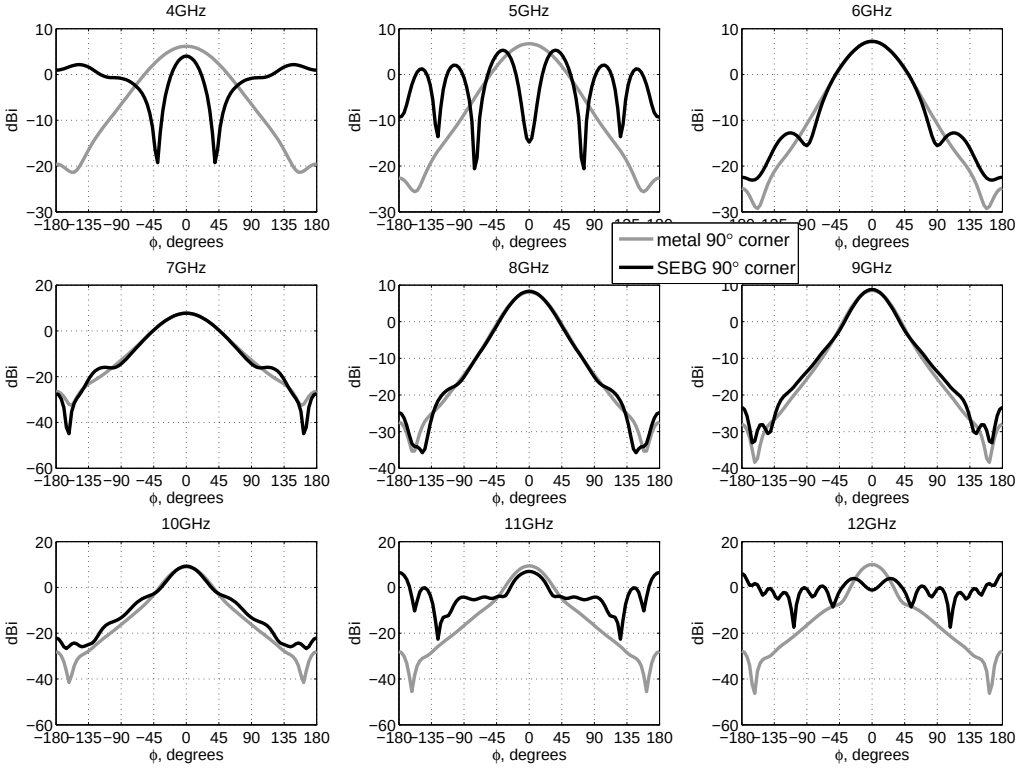

Figure 4.14: *2-D 90° SEBG corner reflector antenna and 90° metal corner reflector antenna comparison: simulated directivity patterns as a function of frequency, a=12mm, r=1.5mm, ε_r=37, N_L=3 and N_w=2.*

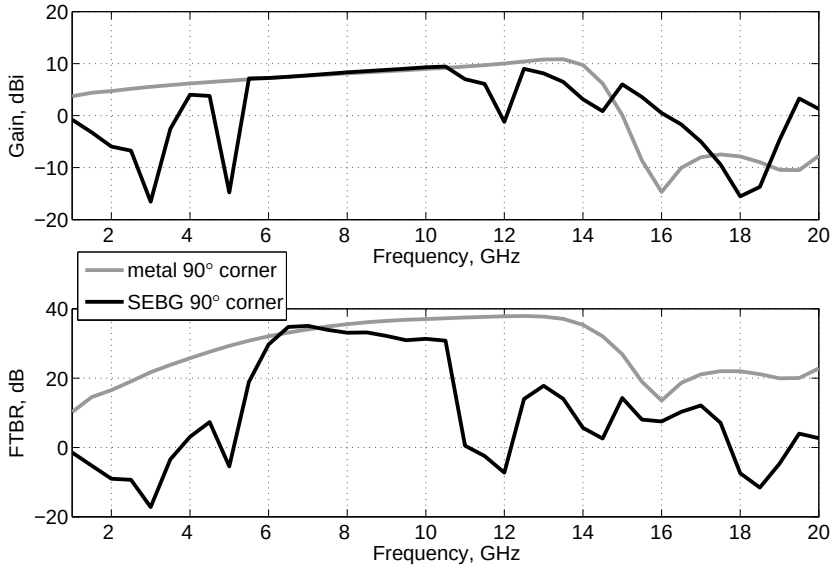

Figure 4.15: *2-D 90° SEBG corner reflector antenna and 90° metal corner reflector antenna simulated gain and FTBR comparison, a=12mm, r=1.5mm, ε_r=37, N_L=3 and N_w=2.*

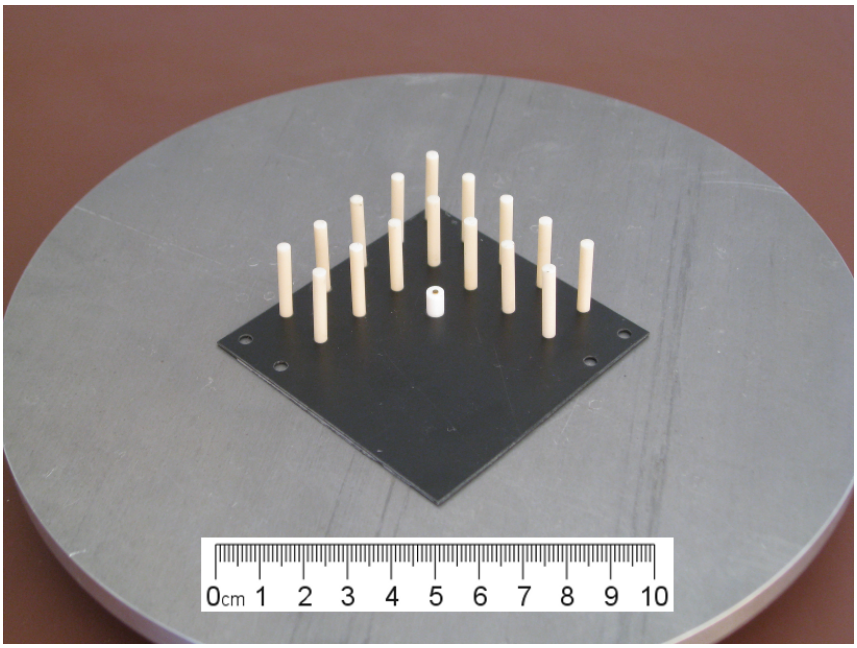

Figure 4.16: *3-D* 90° *SEBG corner reflector antenna prototype.*

4.2.3 3-D SEBG design

A dielectric 90° SEBG corner reflector antenna, Fig. 4.3, has been designed using the results of the two-dimensional parametric study. A reflector width w and internal length L respectively equal to $a = 12mm$ (N_w=2) and $3 \cdot a = 36mm$ (N_L=3) have been chosen along with a source distance s from the apex equals to $a \cdot \sqrt{2}$.

The SEBG structure is realized using dielectric rods of length h=20mm, radius r=1.5mm and ε_r=37±1 (D36 modified zirconium tin titanate [81]) arranged in a square lattice with a=12mm; excitation is given through a monopole feed of length p=6.9mm.

As mentioned in the previous section, the SEBG structure is based on the approximation of a 2-D square lattice (made with infinite long dielectric rods) using ceramic rods of height h. For low elevation angles, the excited fields have a distribution very similar to the 2-D configuration: the 3-D SEBG structure is a good approximation of the 2-D structure and, at frequency within the bandgap, the SEBG structure reflects the imping fields toward the aperture D_a. For increasing elevation angles, the 3-D SEBG structure approximation of the 2-D structure progressively fails; however, given the intrinsic configuration of the excited fields (the electric field magnitude is decreasing as the elevation angle increases), low radiated fields are expected anyway. Gain is therefore expected in the same direction of the corner reflector aperture D_a whilst in the opposite direction, toward the reflector, the radiation is attenuated. The principle of operation is therefore the same as for CEBG and TEBG multilayer antenna structures.

A prototype designed to operate in the X-band has been built and tested, figure 4.16, showing a good agreement with simulation results, figure 4.17-4.18; the achieved -10dB fractional bandwidth is 40% (7.5GHz - 11.3GHz) with an average gain and FTBR respectively equal to 12.5dBi and 22dB. Radiation patterns are quite stable up to 10.5GHz,

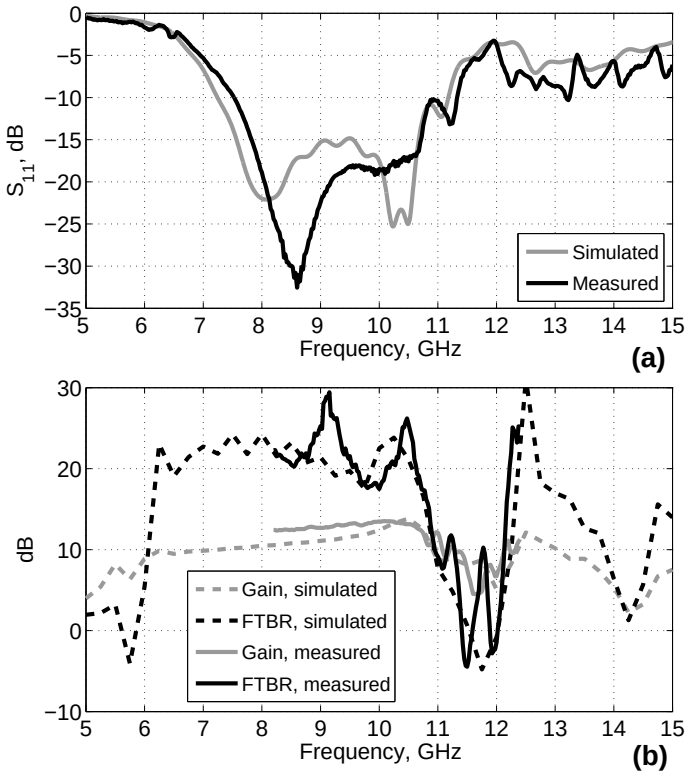

Figure 4.17: *3-D 90° SEBG corner reflector antenna simulated and measured: a) S_{11}; b) gain and front-to-back-ratio (FTBR).*

figure 4.18 and figure 4.19, with a measured half power beamwidth (HPBW) around 30°. From 10.5GHz upward, radiation patterns lose directivity and sidelobes level increases.

Discrepancies between simulations and measurements can be mainly attributed to the different dimensions of the ground plane used for the prototype (round with 200mm diameter) and in the simulations (infinite). Tolerances in rods dimensions and position could also play a minor role. The gain decreasing shown in the measurements at low elevation angles, figure 4.18, is also caused by the finite ground plane used for the prototype, Section 2.2.4.4.

4.2.4 Discussion

Simulations and measurements, figure 4.17-4.18, shown that the presented antenna is very directive between 6.2GHz and 10.6GHz where the FTBR is greater than 20dB and the gain varies between 9.5dBi and 13.85dBi. This frequency band almost coincide with the 2-D lattice bandgap, 5.5-10.63GHz, confirming the design assumptions that the 3-D SEBG structure is a good approximation of the 2-D SEBG structure.

Figure 4.20 shows the normalised electric field magnitude just above the ground plane: at frequencies within the bandgap, 7GHz-10GHz, the SEBG corner structure reflects the excited fields toward the aperture direction; before the bandgap, 3GHz-5GHz there is little interaction between the excited fields and the SEBG structure; at frequencies above the bandgap, 11GHz-14GHz, the excited fields escapes from the rear of the reflector

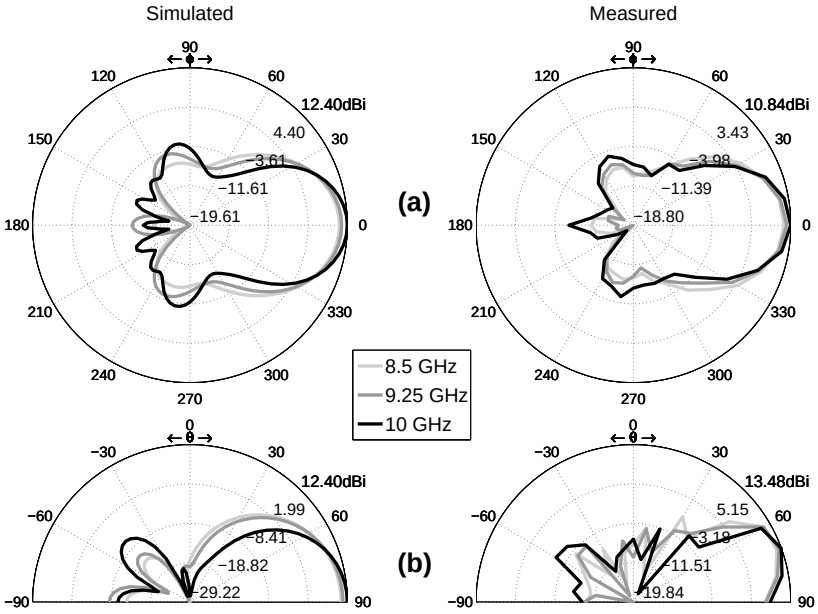

Figure 4.18: *3-D* 90° *SEBG corner reflector antenna simulated (left) and measured (right) radiation patterns: a) H-plane; b) E-plane.*

creating a non directive radiation patterns with multiple beams.

Metallic 90° corner reflector antennas have been extensively analyzed in literature [85–87, 84, 74]; in figure 4.21-4.23 the simulated 3-D 90° SEBG corner reflector antenna is compared with a simulated metallic corner reflector antenna of similar dimensions, i.e. side length $L = 3 \cdot a = 36mm$, corner heght $h = 20mm$ and feed distance from the apex $s = a \cdot \sqrt{2}$; reflector thickness was chosen equal to 0.5mm. The metallic corner reflector antenna achieved a larger bandwidth and an average FTBR 5dB higher, figure 4.21; it is interesting to note that at frequency within the bandgap, 5.5GHz-10.63GHz, the two antennas present the same gain, figure 4.22; moreover the main beams are almost identical on the H-plane and very similar on the E-plane, figure 4.23. Simulations results therefore suggest that at bandgap frequencies the 3-D 90° SEBG corner reflector is as good as a metallic reflector. Discrepancies on the azimuthal plane could be attribuited to the different thickness of the simulated reflectors (12mm for the SEBG reflector and 0.5mm for the metallic reflector); discrepancies on the elevation plane could be caused by the SEBG structure failing to stop the propagation of impinging fields at non-normal incidence.

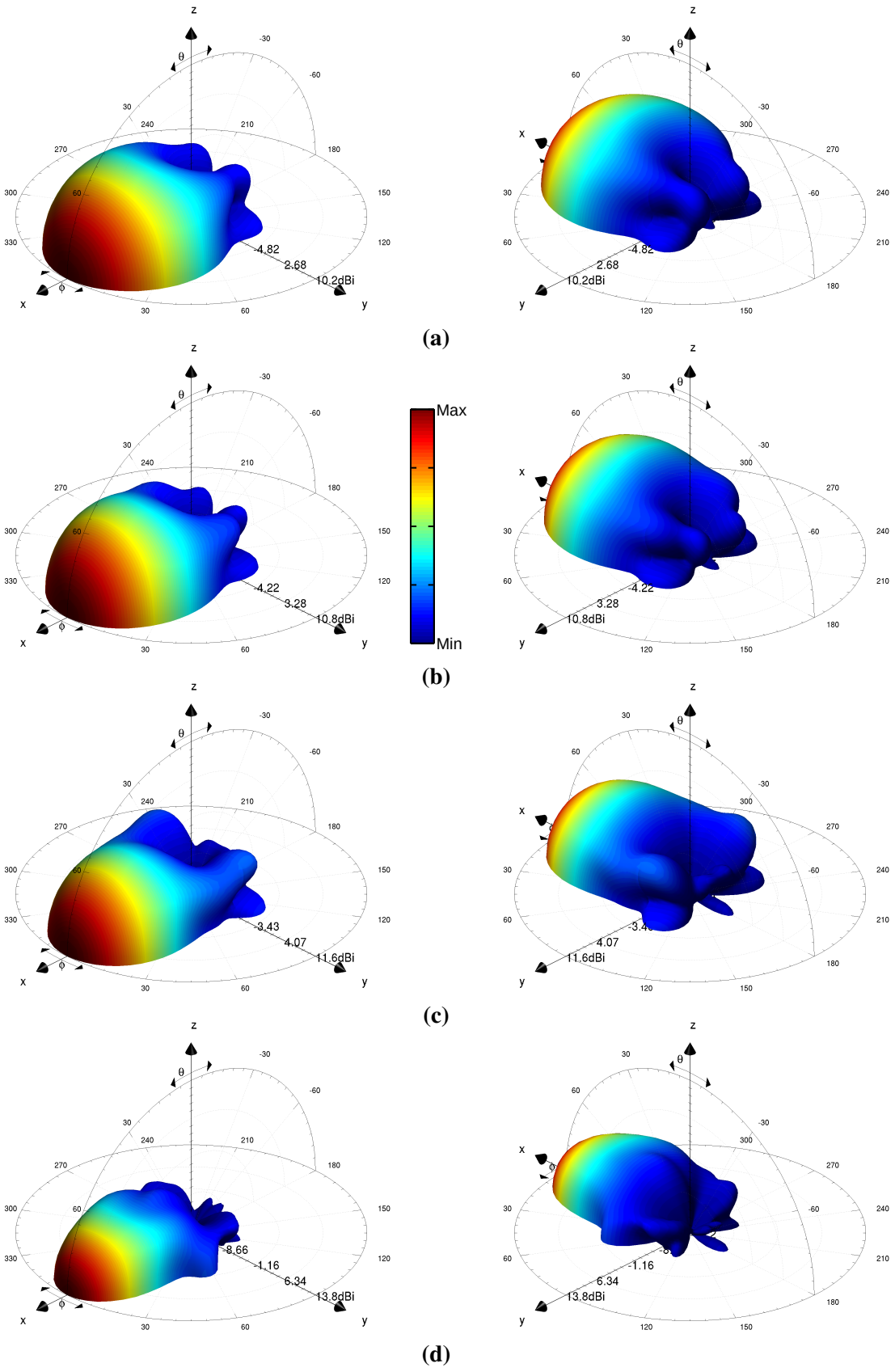

Figure 4.19: *3-D TEBG antenna simulated 3-D radiation patterns, P_r=13mm, r=1.5mm, ε_r=37 and h=20mm: a) 7.5GHz, b) 8.5GHz, c) 9.5GHz, c) 10.5GHz.*

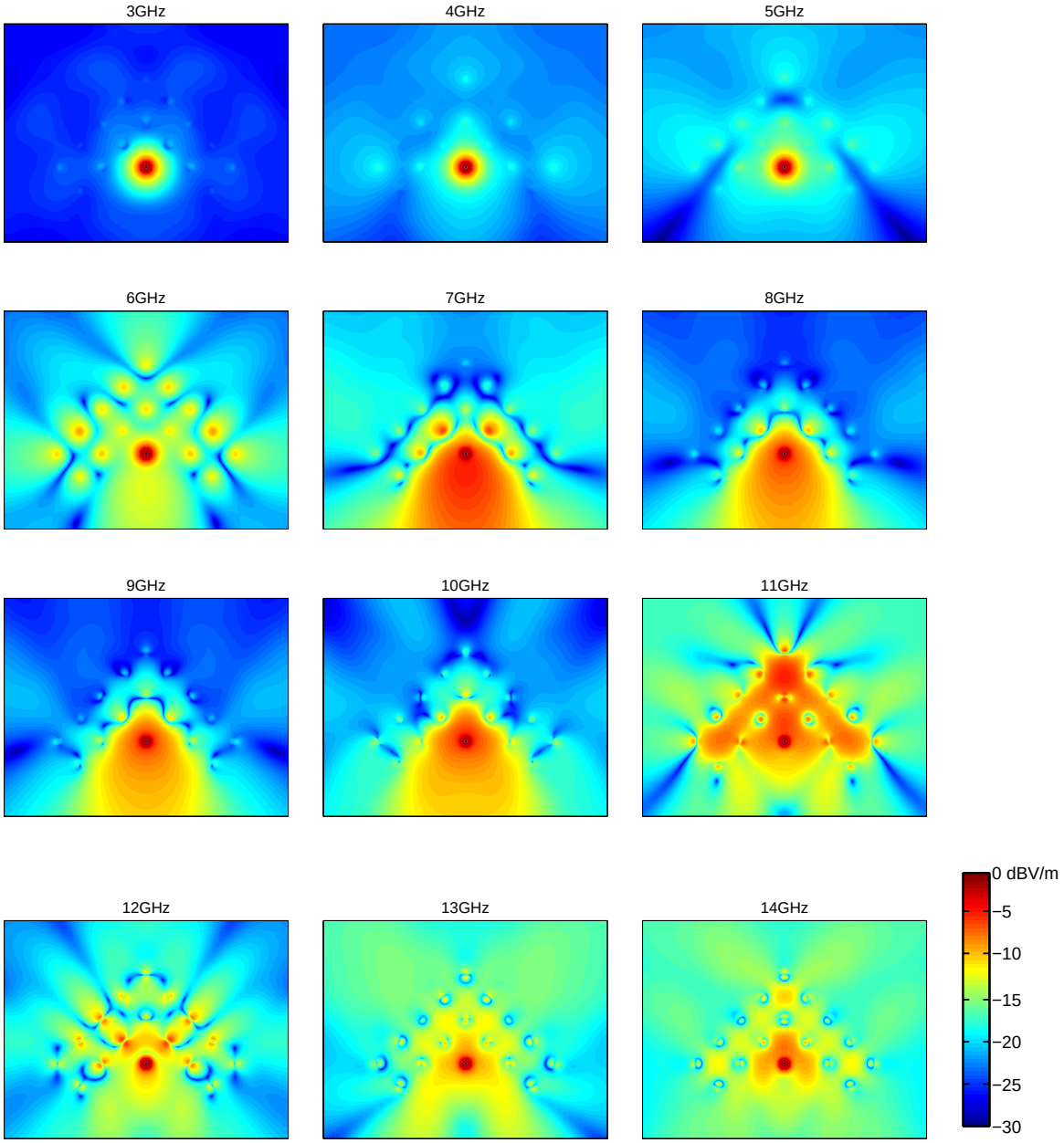

Figure 4.20: *3-D SEBG antenna, simulated normalised electric field distribution on the azimuthal plane, a=12mm, r=1.5mm, ε_r=37 and h=20mm.*

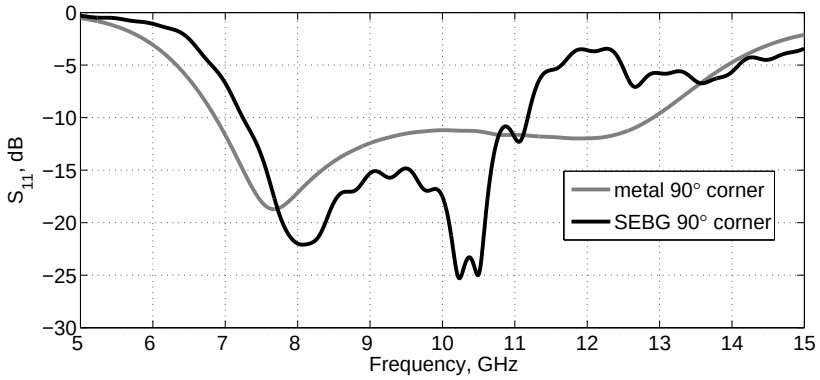

Figure 4.21: *3-D 90° SEBG corner reflector antenna and metallic corner reflector antennas simulated S_{11}.*

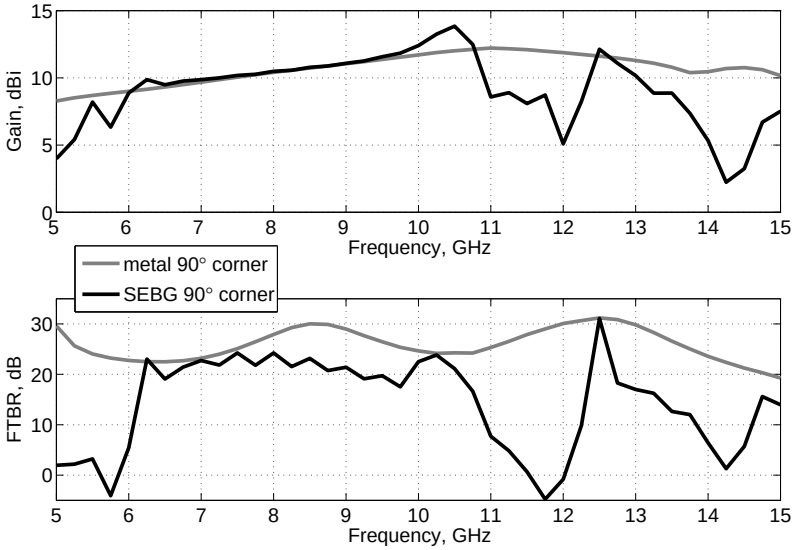

Figure 4.22: *3-D* 90° *SEBG corner reflector antenna and metallic corner reflector antennas simulated gain and front-to-back-ratio (FTBR).*

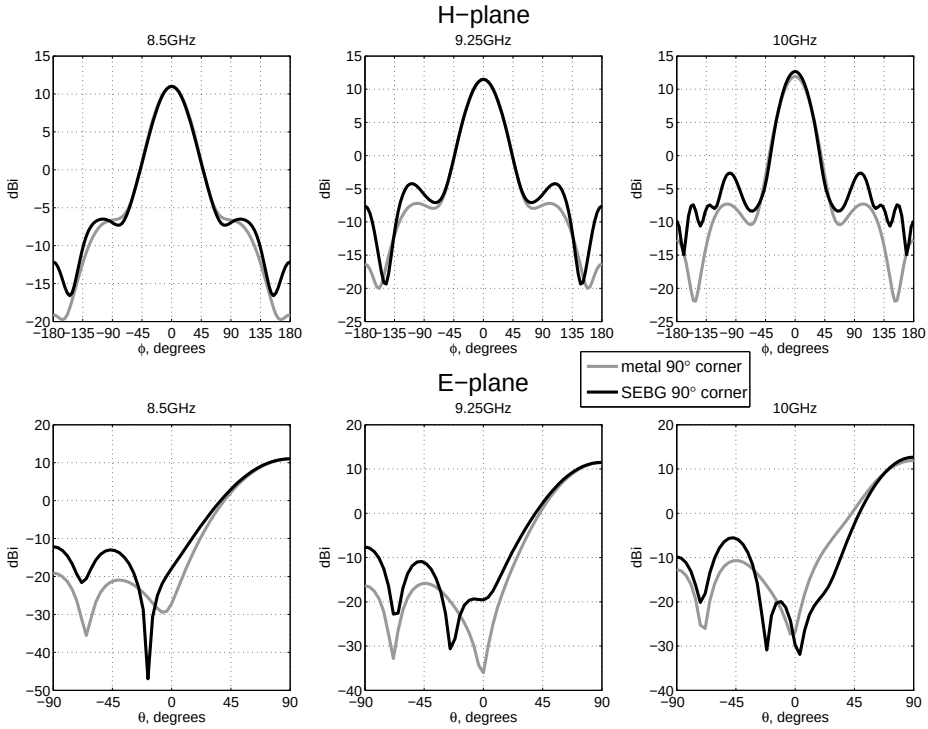

Figure 4.23: *3-D* 90° *SEBG corner reflector antenna and metallic corner reflector antennas simulated radiation patterns.*

4.2.5 Parametric study

The 90° SEBG corner reflector have been parametrically studied focusing on:

- feed distance from the corner apex s;
- corner length L;
- dielectric rods heigth h.

4.2.5.1 Feed displacement s

For 90° metal corner, feed displacement is a very important parameter and it is usually set $s = 0.25 - 0.7\lambda_c$ [85, 84] where λ_c is the central frequency wavelength. When s is greater than $0.7\lambda_c$ the azimuthal radiation pattern presents multiple beams whilst for too small s, less than $0.2\lambda_c$, bandwidth is reduced and radiation resistance is also decreased reducing the antenna efficiency.

A 3-D 90° SEBG corner reflector antenna with $L = 3 \cdot a$ was parametrically studied as a function of feed distance from the corner apex s. The feed displacement s has a big influence on impedance matching and radiation patterns. The impedance matching is improved as the displacement is increased, reaching an optimal value at around $s = a \cdot \sqrt{2} = 0.54\lambda_c$ where $\lambda_c = \lambda\left(f_c{=}9.5GHz\right) = 31.5mm$; a further increase of s would then reduce the impedance bandwidth and matching, figure 4.24. Displacements smaller than $a \cdot \sqrt{2}$ present very similar radiation patterns at frequency within the bandgap, figure 4.26, as well as similar gain and FTBR, figure 4.25. Larger displacements fail to achieve high directivity, also leading to radiation patterns with multiple beams as shown in figure 4.26d.

Best overall results in terms of matching, impedance bandwidth and directivity radiation patterns were achieved with $s = 2 \cdot a \cdot \cos\left(\frac{\alpha}{2}\right) = a \cdot \sqrt{2}$, where α is the corner enclosed angle, i.e. 90°.

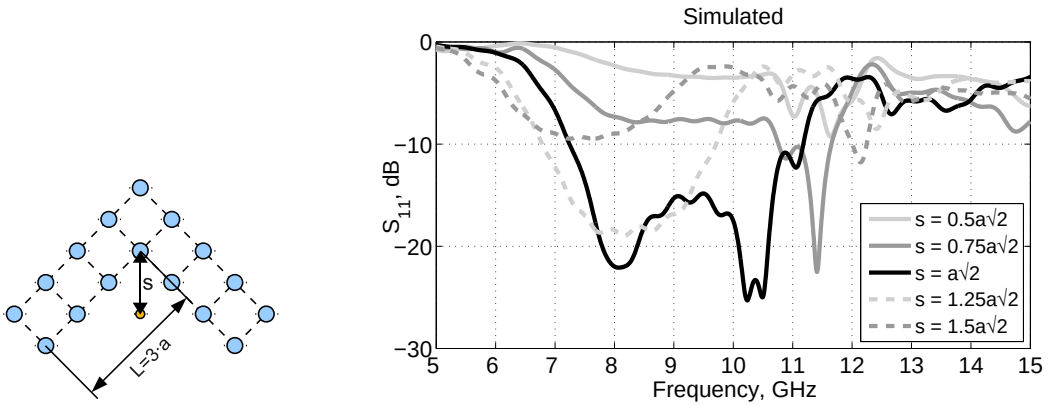

(a) **(b)**

Figure 4.24: *3-D 90° SEBG corner reflector antenna as a function of feed displacement s, $L = 3 \cdot a$, a=12mm, r=1.5mm, ε_r=37 and h=20mm: a) geometry; b) simulated S_{11}.*

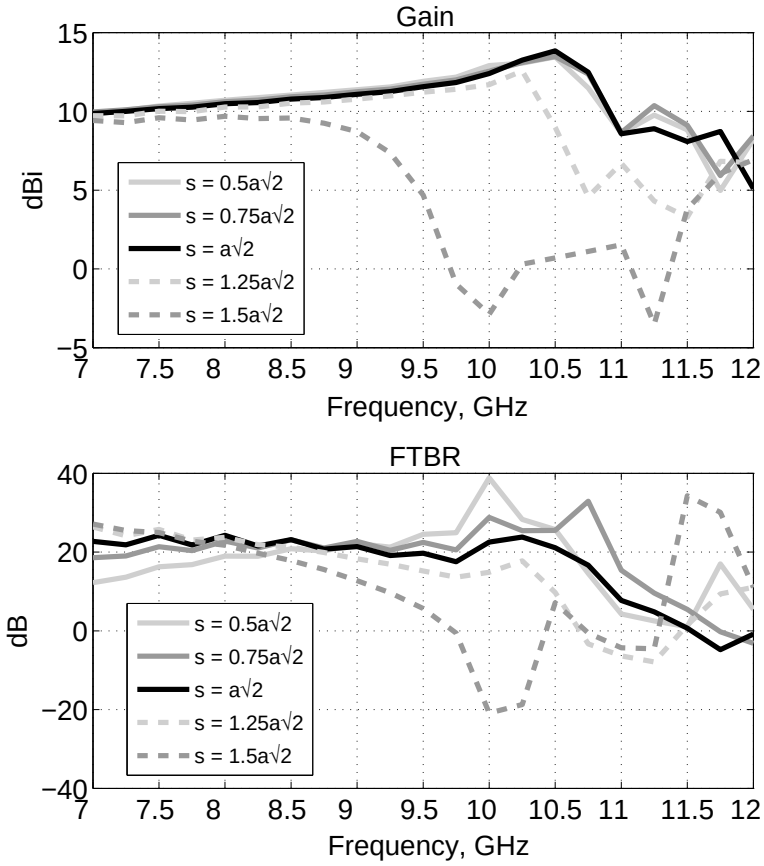

Figure 4.25: *3-D 90° SEBG corner reflector antenna simulated gain and FTBR as a function of side feed displacement s, $L = 3 \cdot a$, a=12mm, r=1.5mm, ε_r=37 and h=20mm.*

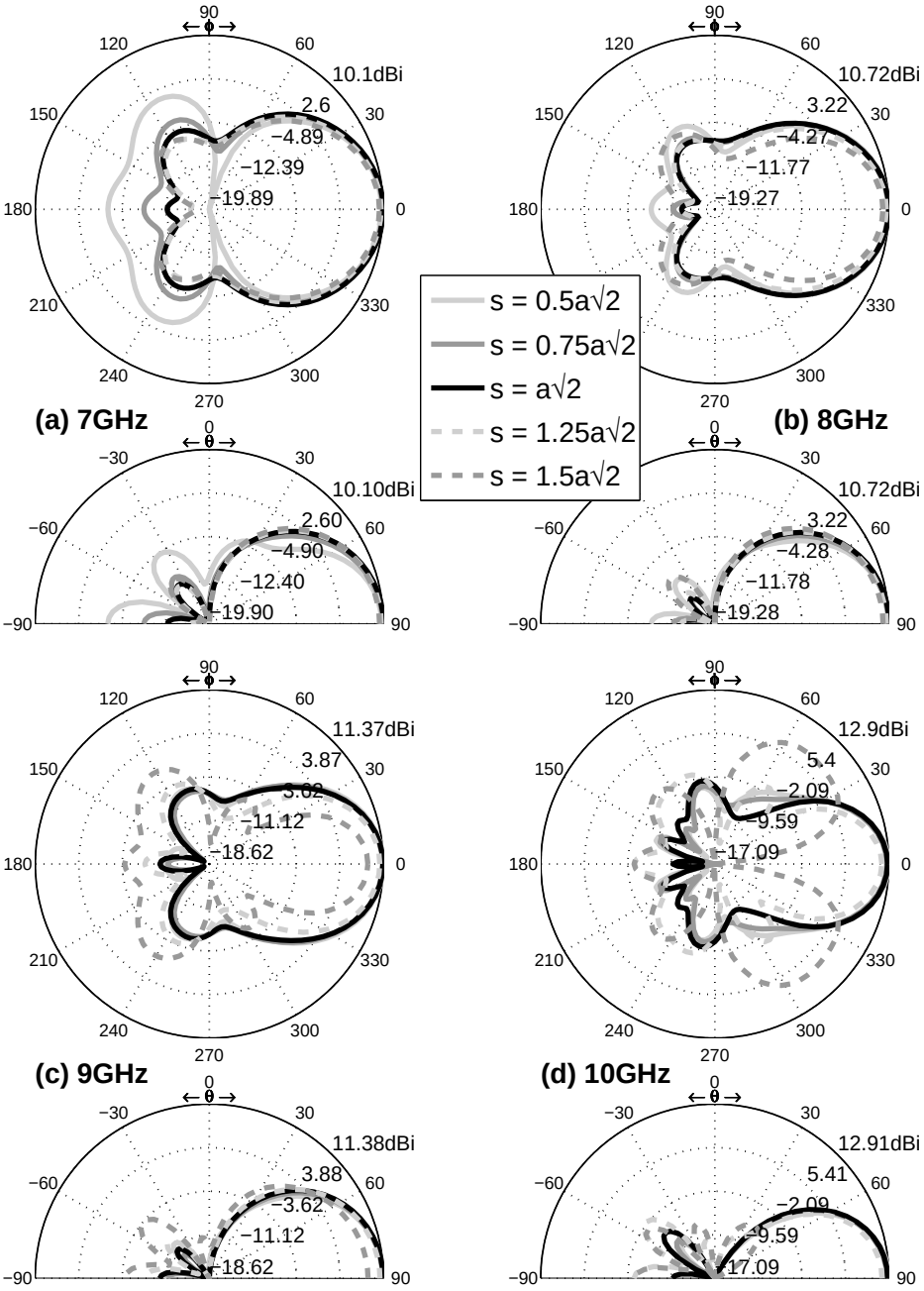

Figure 4.26: *3-D* 90° *SEBG corner reflector antenna simulated radiation patterns as a function of side feed displacement s,* $L = 3 \cdot a$*, a=12mm, r=1.5mm,* ε_r*=37 and h=20mm: a) 7GHz; b) 8GHz; c) 9GHz; d) 10GHz.*

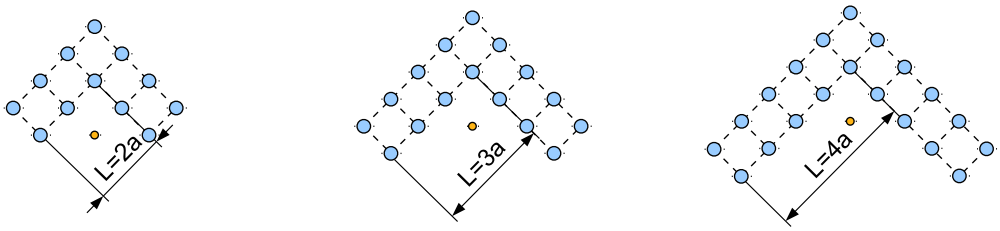

(a) **(b)** **(c)**

Figure 4.27: *3-D 90° SEBG corner reflector antenna geometries as a function of corner length L: a) $L = 2 \cdot a$; b) $L = 3 \cdot a$; c) $L = 4 \cdot a$.*

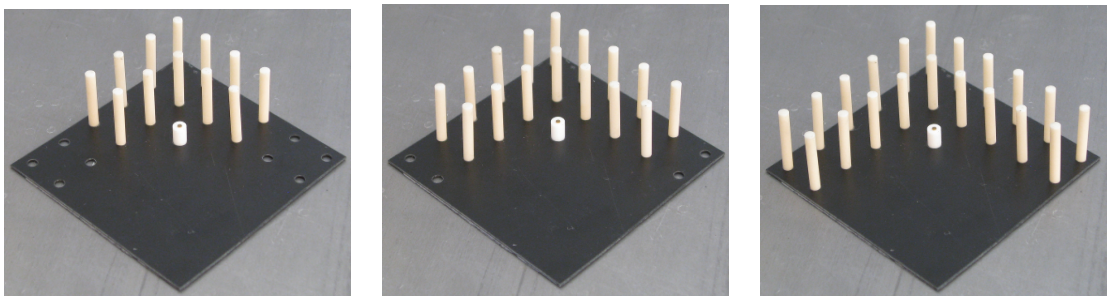

(a) **(b)** **(c)**

Figure 4.28: *3-D 90° SEBG corner reflector antenna geometries as a function of corner length L: a) $L = 2 \cdot a$; b) $L = 3 \cdot a$; c) $L = 4 \cdot a$.*

4.2.5.2 Side length L

For a 90° metal corner the side length L is usually set equal to $2 \cdot s$ [85, 87, 84, 74]; a greater side length would just slightly increase the gain and therefore $L = 2 \cdot s$ is a good compromise in terms of overall dimensions and performance.

A 3-D 90° SEBG corner reflector antenna was parametrically studied as a function of side length L; results are summarised in table 4.1. As L is increased, impedance bandwidth and matching are not much influenced, figure 4.29; radiation patterns directivity and gain are improved when L is increased from $2 \cdot a$ to $3 \cdot a$, but the relative improvement for $L = 4 \cdot a$ is very little. The major impact of side length L is on the maximum dimensions and required number of dielectric rods.

The results of this parametric study are collected in table 4.1.

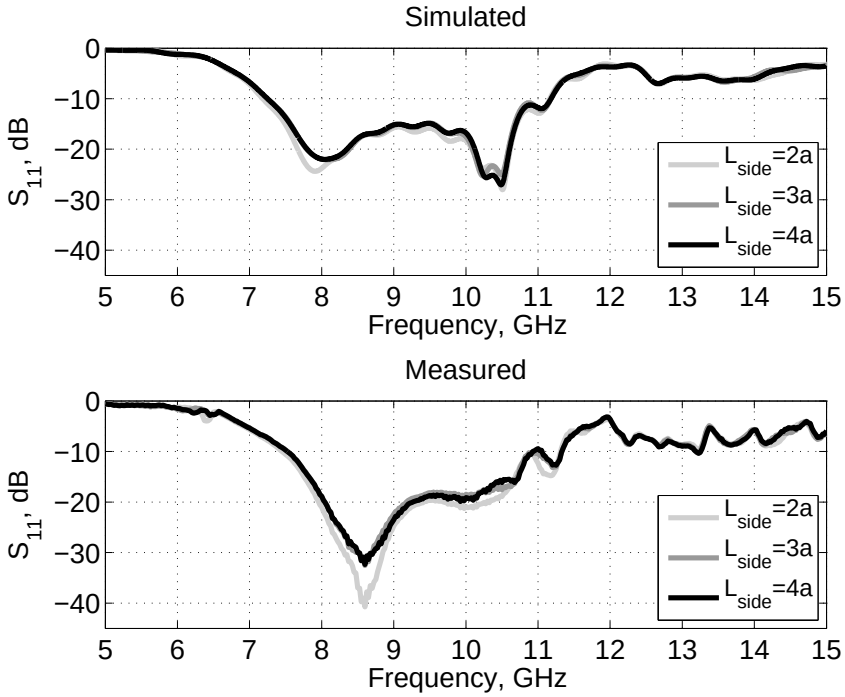

Figure 4.29: *3-D* 90° *SEBG corner reflector antenna simulated and measured S_{11} as a function of side length L, a=12mm, r=1.5mm, ε_r=37 and h=20mm.*

L	Gain, dBi	FTBR, dB	Bandwidth	N_{rods}	Max dim.
$2{\cdot}a$	12.7 (11.4)	37.7 (25.1)	41.4%	12	$3 \cdot a \cdot \sqrt{2}$
			7.5-11.4GHz		$1.61{\cdot}\lambda_c$
$3{\cdot}a$	13.5 (12.5)	29.4 (19.5)	40.4%	16	$4 \cdot a \cdot \sqrt{2}$
			7.5-11.4GHz		$2.15{\cdot}\lambda_c$
$4{\cdot}a$	14.1 (12.9)	35.8 (21.2)	40.4%	20	$5 \cdot a \cdot \sqrt{2}$
			7.5-11.4GHz		$2.69{\cdot}\lambda_c$

Table 4.1: *3D* 90° *SEBG corner reflector antenna measured performance as a function of side length L; a=12mm, r=1.5mm, ε_r=37 and h=20mm (in brackets are reported the average values within the impedance bandwidth);* $\lambda_c = \lambda_{(f_c=9.5GHz)=31.5mm}$.

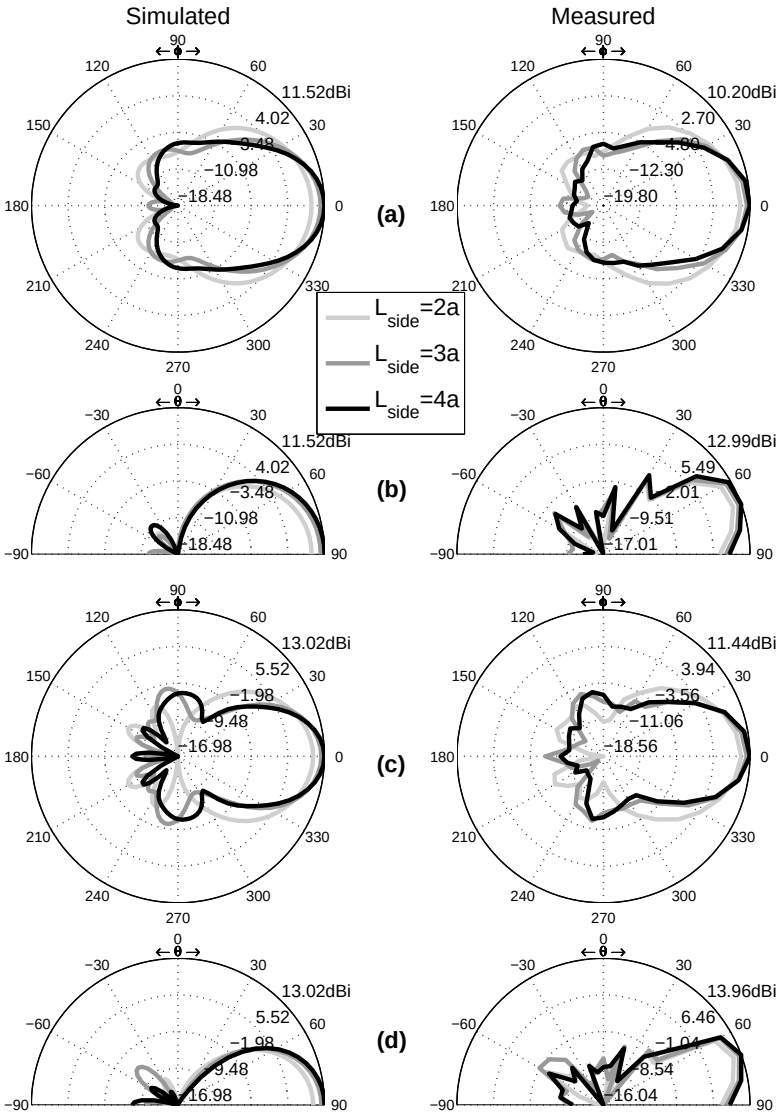

Figure 4.30: *3-D 90° SEBG corner reflector antenna simulated and measured radiation patterns as a function of side length L, a=12mm, r=1.5mm, ε_r=37 and h=20mm: a) H-plane 8.5GHz; b) E-plane 8.5GHz; c) H-plane 10GHz; d) E-plane 10GHz.*

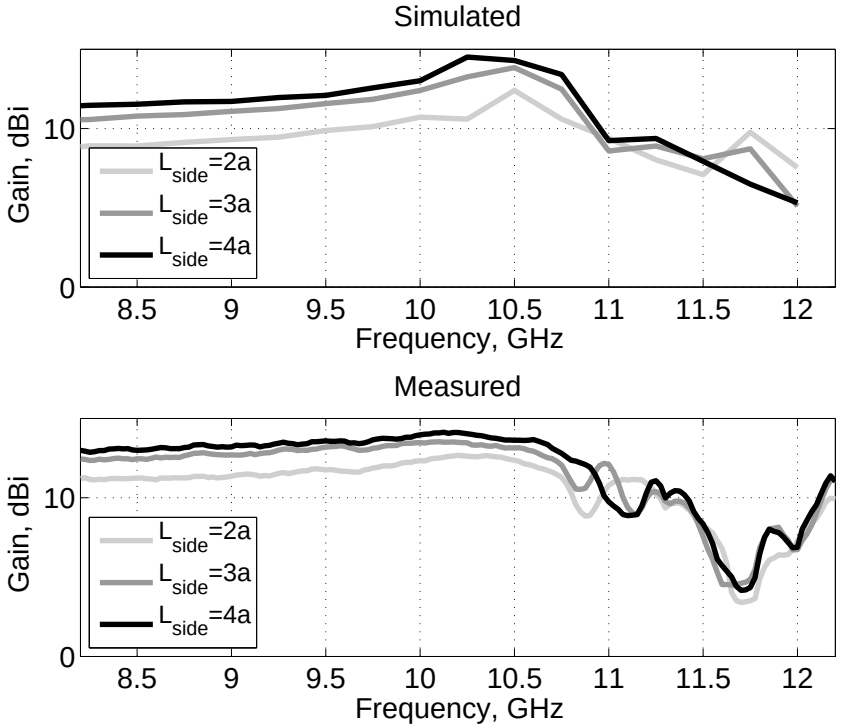

Figure 4.31: *3-D 90° SEBG corner reflector antenna simulated and measured gain as a function of side length L, a=12mm, r=1.5mm, ε_r=37 and h=20mm.*

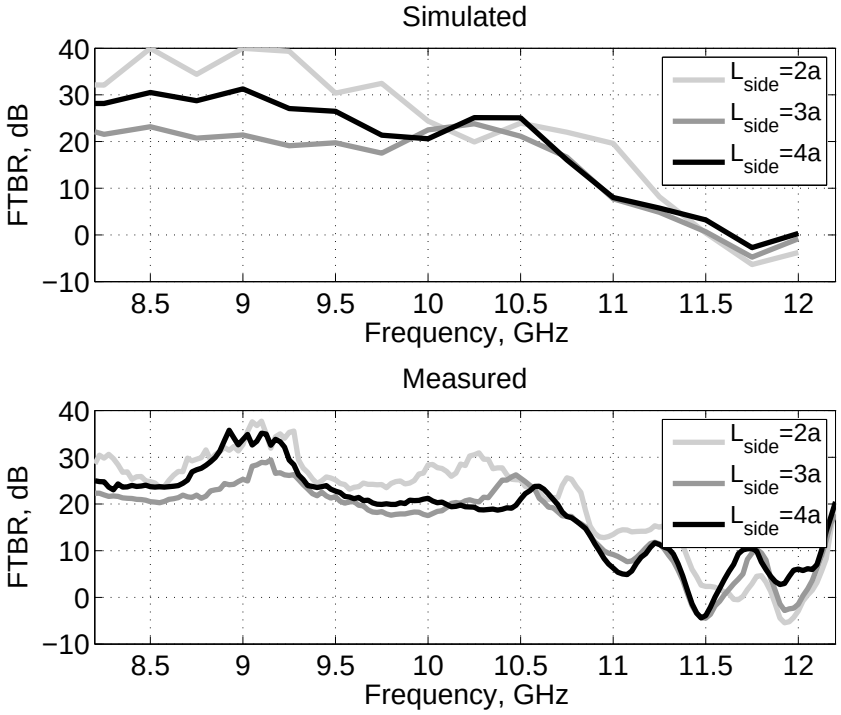

Figure 4.32: *3-D 90° SEBG corner reflector antenna simulated and measured FTBR as a function of side length L, a=12mm, r=1.5mm, ε_r=37 and h=20mm.*

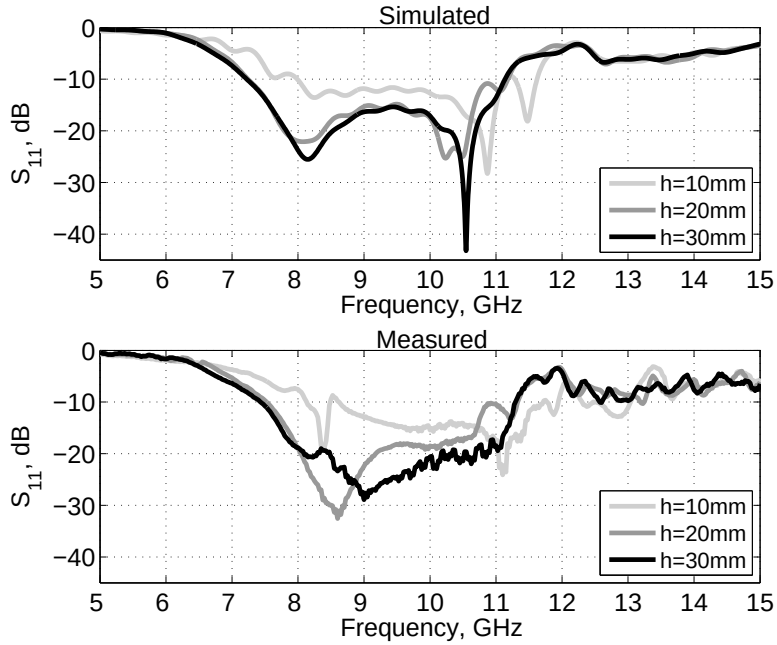

Figure 4.33: *3-D 90° SEBG corner reflector antenna simulated and measured S_{11} as a function of rods heigth h, $L = 3 \cdot a$, a=12mm, r=1.5mm, ε_r=37.*

4.2.5.3 Rods length h

A 3-D 90° SEBG corner reflector antenna was parametrically studied as a function of rods length, focusing on *h*=10,20 and 30mm. The influenece of *h* on the SEBG corner antenna is shown in figure 4.33-4.36: impedance bandwidth and matching are increased with *h* as well as gain and FTBR, even though the latter has a more complex frequency behaviour (locally the FTBR is actually decreasing with *h*). Rods length *h* can be therefore set to optimize the frequency behaviour of gain and FTBR.

The results of this parametric study are collected in table 4.2.

h, mm	Gain, dBi	FTBR, dB	Bandwidth
10 $0.317 \cdot \lambda_c$	13.1 (11.4)	36.7 (20.4)	38.0% 8.2-12.0GHz
20 $0.633 \cdot \lambda_c$	13.5 (12.5)	29.4 (19.5)	40.4% 7.5-11.4GHz
30 $0.95 \cdot \lambda_c$	13.7 (13.1)	39.1 (25.1)	40.7% 7.5-11.3GHz

Table 4.2: *3-D SEBG antenna measured performance as a function of rods length h; $L = 3 \cdot a$, a=12mm, r=1.5mm, ε_r=37 (in brackets are reported the average values within the impedance bandwidth); $\lambda_c = \lambda\left(f_c=9.5GHz\right)=31.5mm$.*

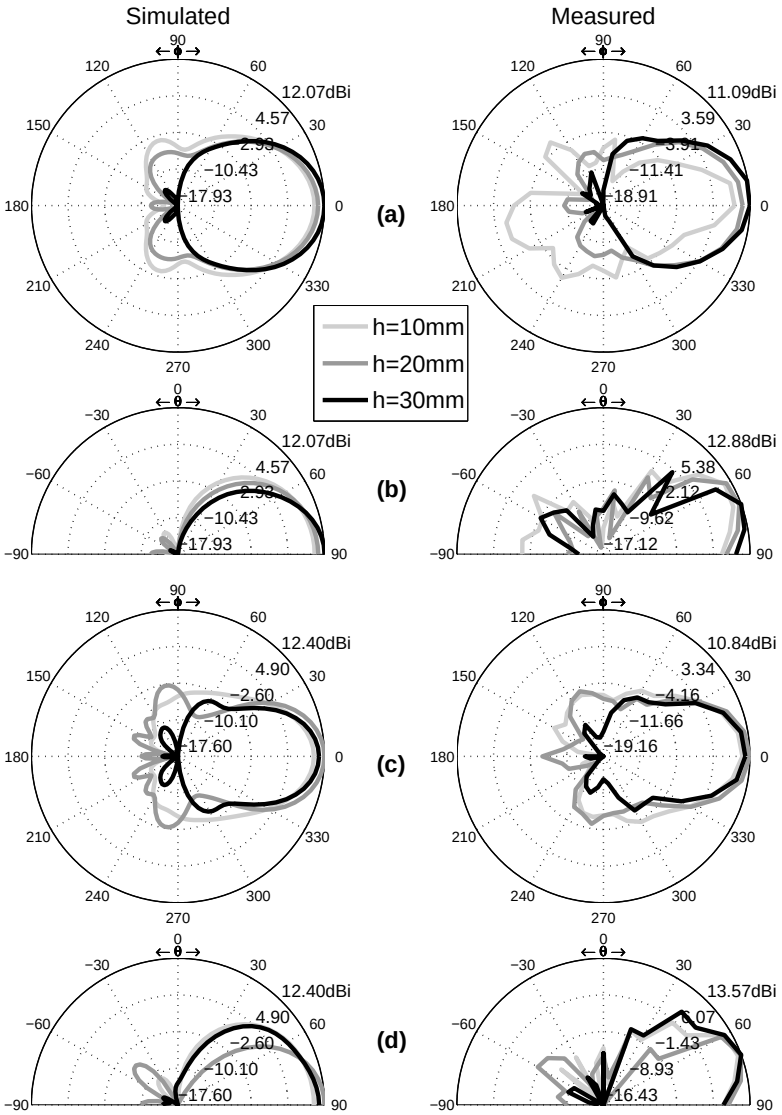

Figure 4.34: *3-D 90° SEBG corner reflector antenna simulated and measured radiation patterns as a function of rods heigth h, $L = 3 \cdot a$, a=12mm, r=1.5mm, ε_r=37: a) H-plane 8.5GHz; b) E-plane 8.5GHz; c) H-plane 10GHz; d) E-plane 10GHz.*

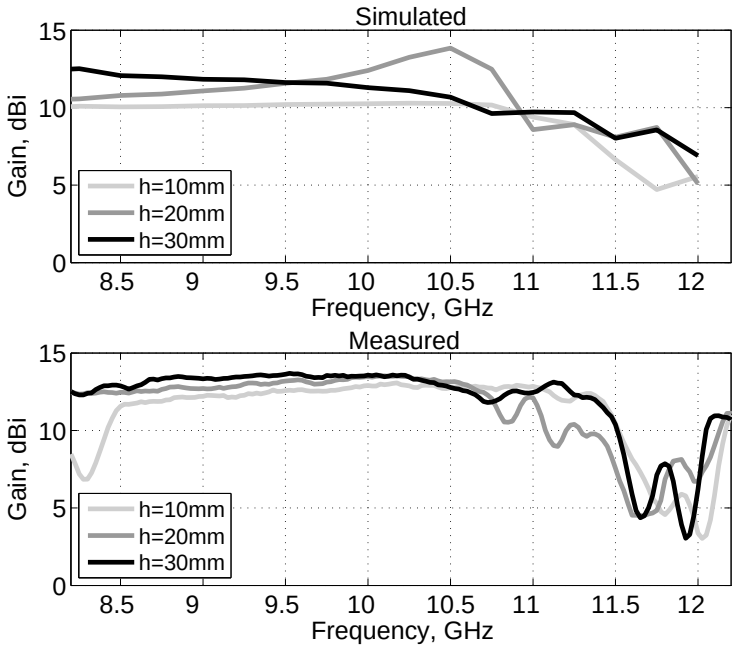

Figure 4.35: *3-D 90° SEBG corner reflector antenna simulated and measured gain as a function of rods heigth h, $L = 3 \cdot a$, a=12mm, r=1.5mm, ε_r=37.*

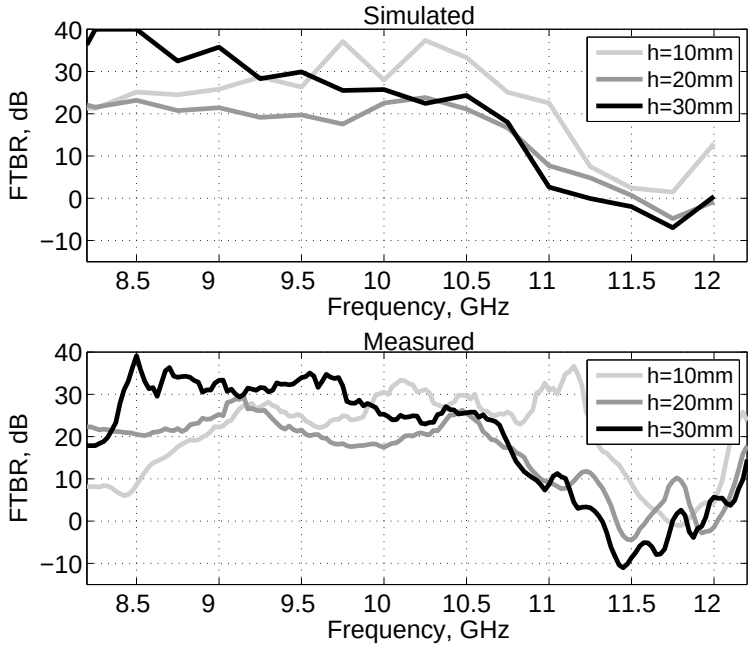

Figure 4.36: *3-D 90° SEBG corner reflector antenna simulated and measured FTBR as a function of rods heigth h, $L = 3 \cdot a$, a=12mm, r=1.5mm, ε_r=37.*

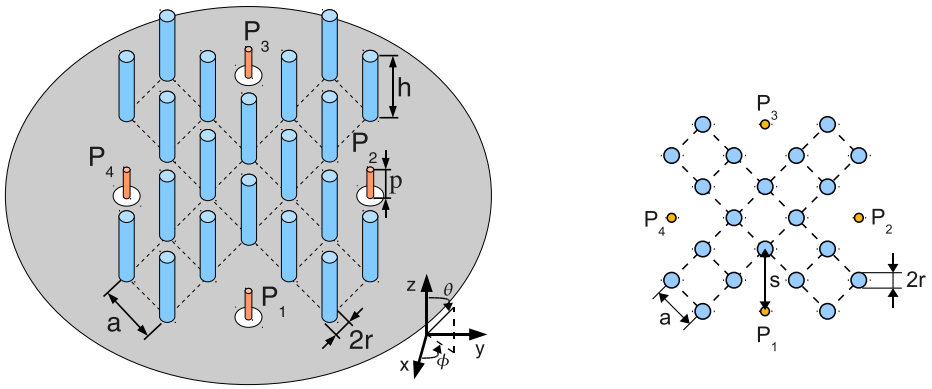

(a) **(b)**

Figure 4.37: *Multiple feed 90° SEBG corner reflector antenna geometry: a) 3-D view; b) schematic view.*

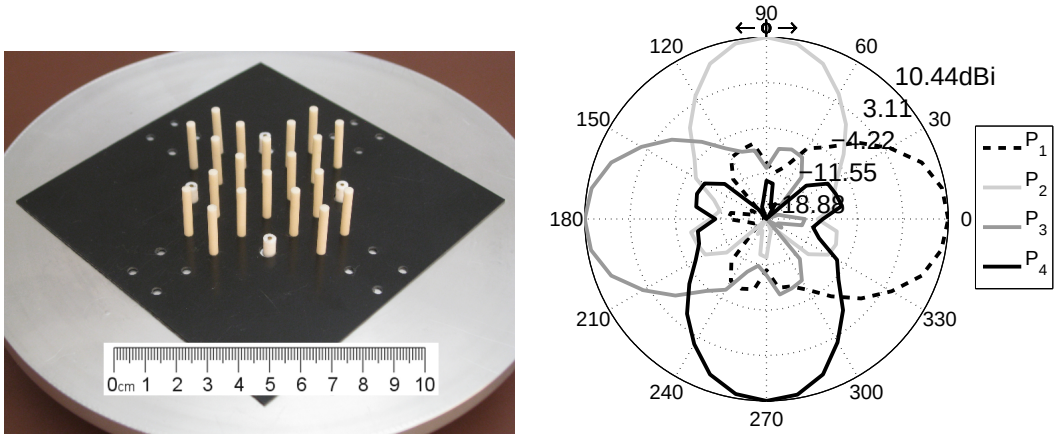

(a) **(b)**

Figure 4.38: *Multiple feed 90° SEBG corner reflector antenna: a) prototype photo; b) measured radiation patterns at 9GHz as a function of excited probe, $L = 2 \cdot a$, a=12mm, r=1.5mm, h=20mm, ε_r=37.*

4.2.6 Multiple feed SEBG corner reflector antennas

A multiple feed 90° SEBG corner reflector antenna can be easily created by arranging dielectric rods in a cross-shaped structure as shown in figure 4.37; in a similar fashion to the multiple feed TEBG antennas presented in Section 3.4, radiation patterns can be rotated on the azimuthal plane by 90° discrete steps by exciting the corresponding monopole feed, figure 4.38b. The SEBG structure has again a two-fold purpose, acting as a corner reflector, as for the single feed structure, and also increase the decoupling between monopole feeds.

The multiple feed 90° SEBG corner reflector antenna depicted in figure 4.37 has been parametrically studied as a function of corner side length L and rods length H, the results are presented in the next sections.

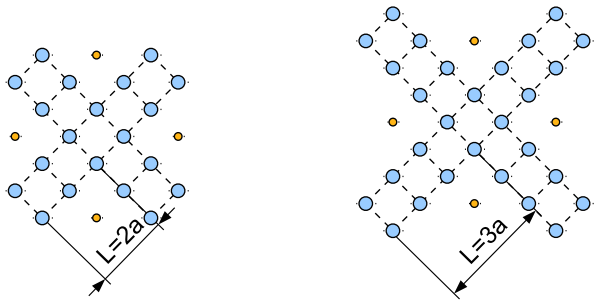

Figure 4.39: *Multiple feed* 90° *SEBG corner reflector antenna geometries: a)* $L = 2 \cdot a$*; b)* $L = 3 \cdot a$*.*

4.2.6.1 Corner length L

Two structures of corner length respectively equal to $L = 2 \cdot a$ and $L = 3 \cdot a$, figure 4.39a-b, have been simulated, prototyped and tested; simulation and measurements results are shown in figure 4.40-4.42 and summarised in table 4.3. The antenna $s-parameters$ are sligthly influenced by the corner length, figure 4.40, and its clearly visible an improvement in the decoupling between feeds in the 6GHz-11GHz frequency range (within the SEBG structure bandgap); at frequency outside the bandgap, the S_{12} and S_{13} parameters have very similar values to a reference structure without SEBG. Gain is increased by a longer corner length L whilst the FTBR is actually decreased, figure 4.41; radiation patterns beamwidth is reduced when the corner length is increased, figure 4.42

L	Gain dBi	FTBR dB	Bandwidth	S_{12} dB	S_{13} dB	N_{rods}	Max dim.
$2 \cdot a$	13.3 (12.2)	34.6 (24.2)	38.5% 7.7-11.4GHz	$\leq$-18.6 (-40.2)	$\leq$-20.7 (-39.8)	20	$5 \cdot a$ $1.9 \cdot \lambda_c$
$3 \cdot a$	14.2 (13.1)	29.9 (21.6)	38.2% 7.8-11.4GHz	$\leq$-20.0 (-42.5)	$\leq$-18.2 (-42.4)	28	$7 \cdot a$ $2.67 \cdot \lambda_c$
no EBG	N/A	N/A	N/A	$\leq$-20.77 (-22.71)	$\leq$-19.81 (-21.42)	N/A	N/A

Table 4.3: *Multiple feed* 90° *SEBG corner reflector antenna measured performance as a function of side length L; a=12mm, r=1.5mm,* ε_r*=37 and h=20mm (in brackets are reported the average values within the impedance bandwidth);* $\lambda_c = \lambda_{(f_c=9.5GHz)=31.5mm}$*.*

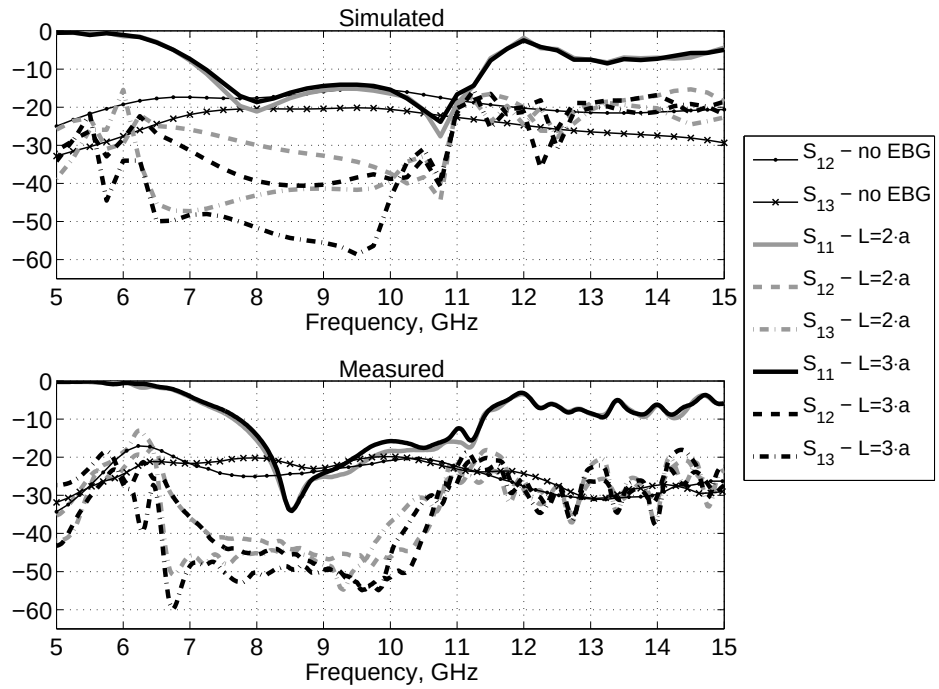

Figure 4.40: *Multiple feed 90° SEBG corner reflector antenna, simulated and measured scattering parameters as a function of corner length L; a=12mm, r=1.5mm, h=20mm, ε_r=37.*

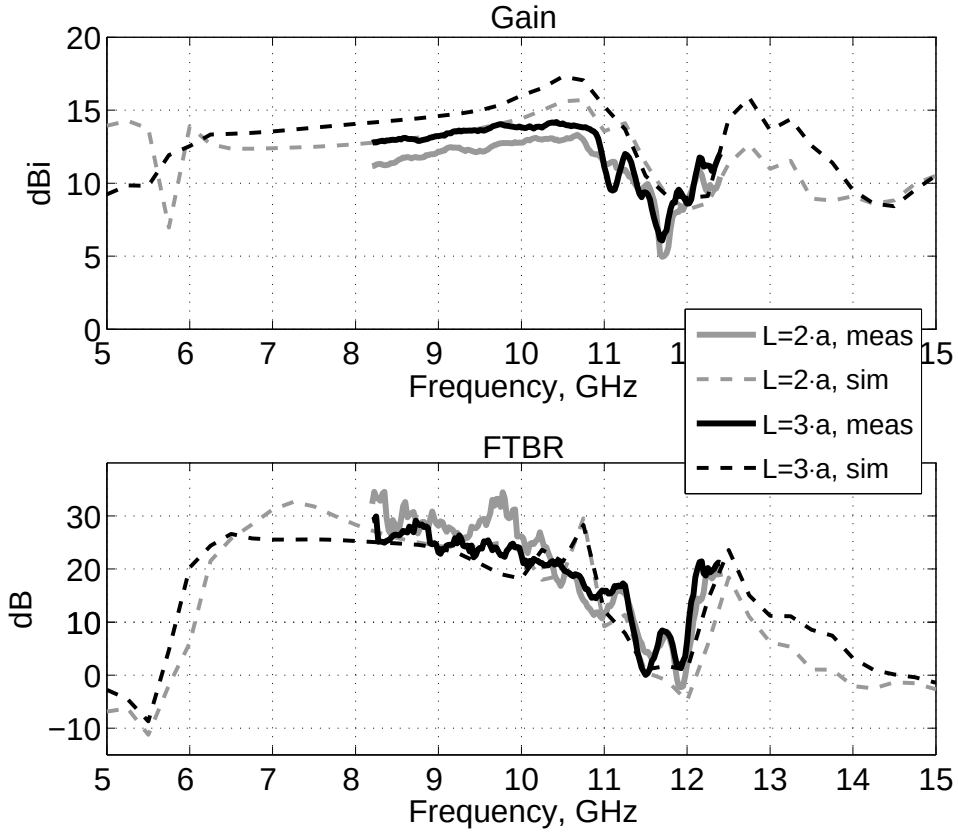

Figure 4.41: *Multiple feed 90° SEBG corner reflector antenna, simulated and measured gain and FTBR as a function of corner length L; a=12mm, r=1.5mm, h=20mm, ε_r=37.*

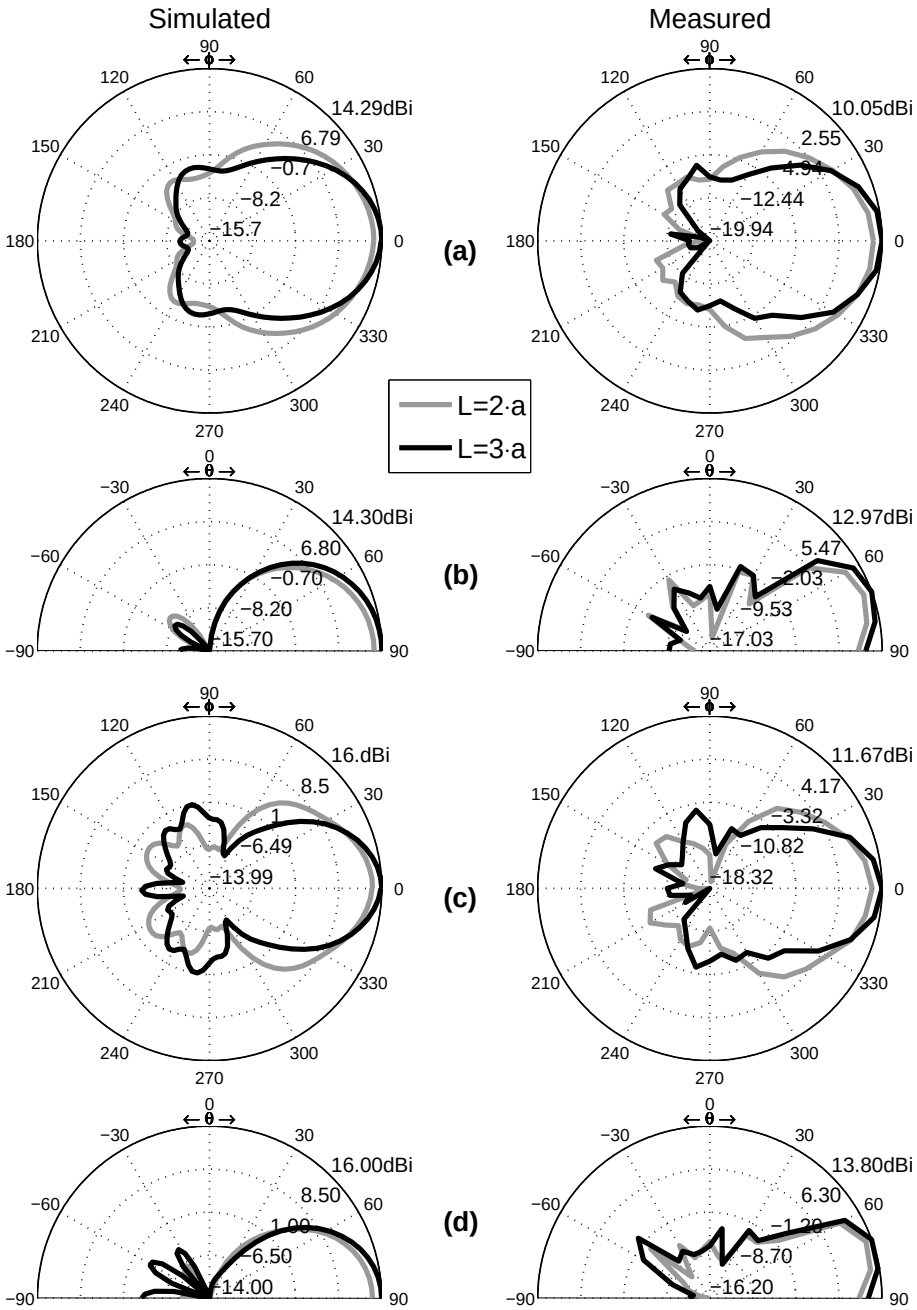

Figure 4.42: *Multiple feed 90° SEBG corner reflector antenna, simulated and measured radiation patterns as a function of corner length L; a=12mm, r=1.5mm, h=20mm, ε_r=37: a) H-plane at 8.5GHz; b) E-plane at 8.5GHz; c) H-plane at 10GHz; d) E-plane at 10GHz.*

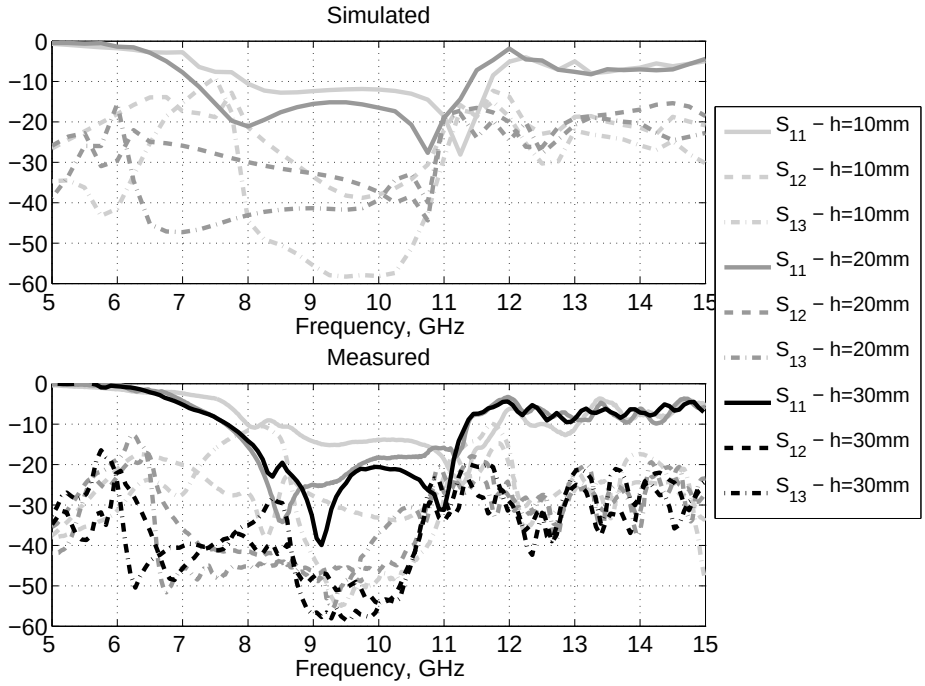

Figure 4.43: *Multiple feed* 90° *SEBG corner reflector antenna, simulated and measured scattering parameters as a function of numbers of rods length h; a=12mm, r=1.5mm,* $L = 2 \cdot a$*,* ε_r*=37.*

4.2.6.2 Rods length *h*

A multiple feed 90° SEBG corner reflector antenna with $L = 2 \cdot a$, figure 4.39a, has been parametrically studied as a function of rods length h. The results of this parametric study are shown in figure 4.43-4.45 and summarised in table 4.4; simulations with $h = 30mm$ did not converge to an accurate solution and therefore those results have not been included in the figures. Antenna S_{11} is quite influenced by h: impedance matching is progressively improved by increasing and h whilst the impedance bandwidth, after an initial extension, is not influenced anymore for h greater than 20mm, figure 4.43. Gain is also gradually improved by increasing the dielectric rods length whilst the FTBR is first improved when h is increased from 10mm to 20mm but then is deteriorated when h is further increased to 30mm, figure 4.44. Radiation patters sidelobes are generally decreased when h is increased and the main beam beamwidth is not much influenced, figure 4.45.

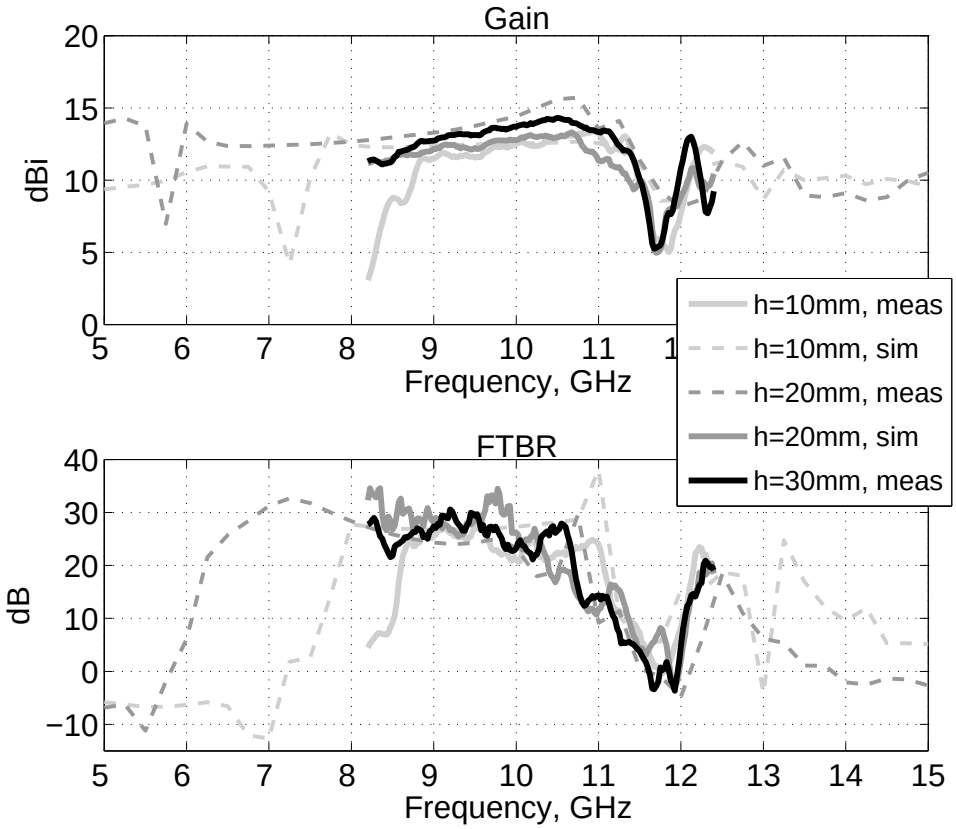

Figure 4.44: *Multiple feed* 90° *SEBG corner reflector antenna, simulated and measured gain and FTBR as a function of numbers of rods length h; a=12mm, r=1.5mm,* $L = 2 \cdot a$*,* ε_r*=37.*

h, mm	Gain, dBi	FTBR, dB	Bandwidth	S_{12}	S_{13}
10	13.4 (11.4)	27.9 (19.6)	33.3%	≤-14.7	≤-10.0
$0.317 \cdot \lambda_c$			8.4-11.8GHz	(-27.4)	(-35.6)
20	13.3 (12.2)	34.6 (24.2)	38.5%	≤-18.6	≤-20.7
$0.633 \cdot \lambda_c$			7.7-11.4GHz	(-40.2)	(-39.8)
30	14.3 (13.1)	30.6 (22.9)	38.5%	≤-23.7	≤-19.9
$0.95 \cdot \lambda_c$			7.7-11.4GHz	(-42.8)	(-42.6)
no EBG	N/A	N/A	N/A	≤-20.77	≤-19.81
				(-22.71)	(-21.42)

Table 4.4: *Multiple feed* 90° *SEBG corner reflector antenna measured performance as a function of rods length h;* $L = 3 \cdot a$*, a=12mm, r=1.5mm,* ε_r*=37 (in brackets are reported the average values within the impedance bandwidth);* $\lambda_c = \lambda_{(f_c=9.5GHz)=31.5mm}$*.*

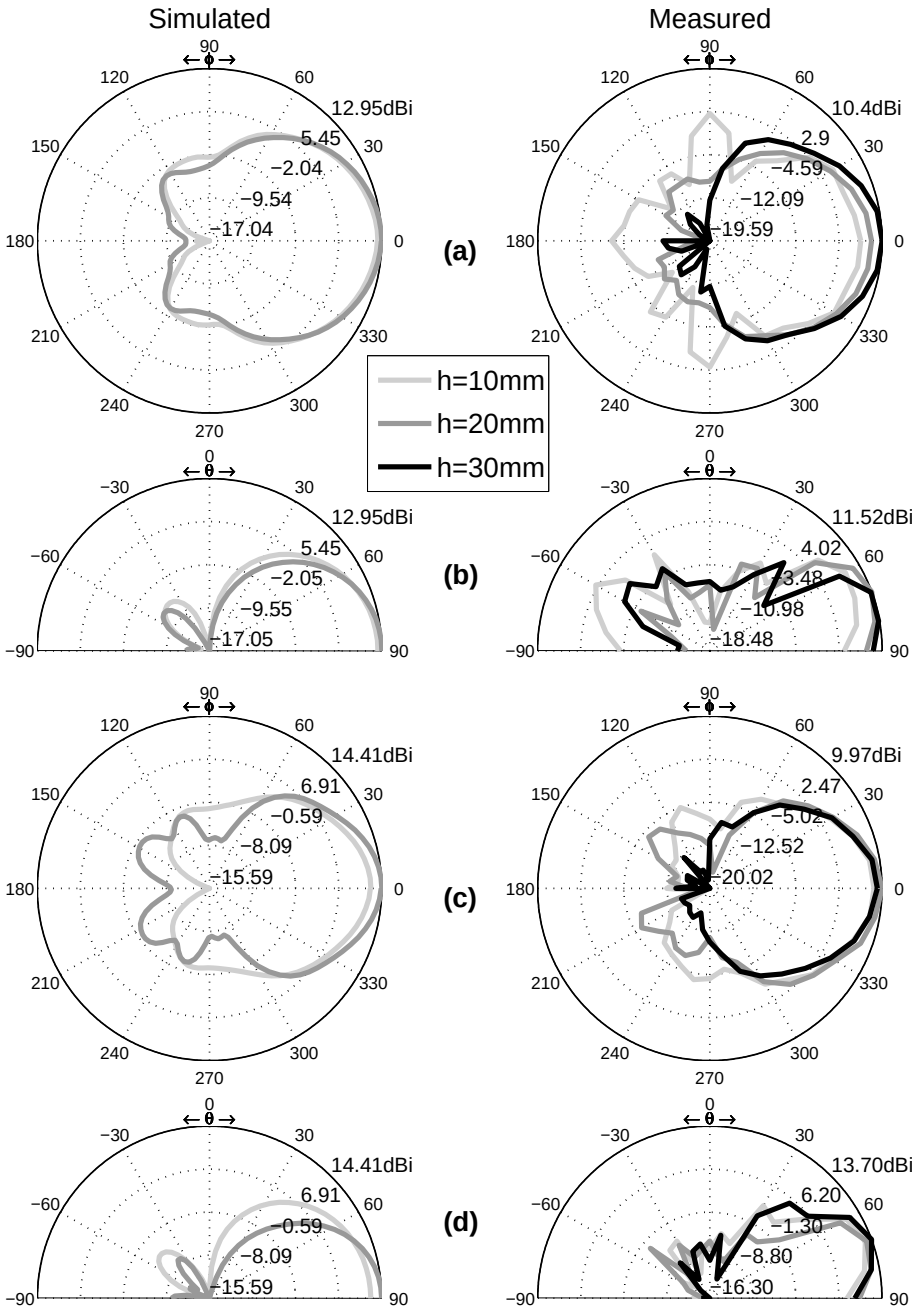

Figure 4.45: *Multiple feed 90° SEBG corner reflector antenna, simulated and measured radiation patterns as a function of numbers of rods length h; a=12mm, r=1.5mm, $L = 2 \cdot a$, ε_r=37: a) H-plane at 8.5GHz; b) E-plane at 8.5GHz; c) H-plane at 10GHz; d) E-plane at 10GHz.*

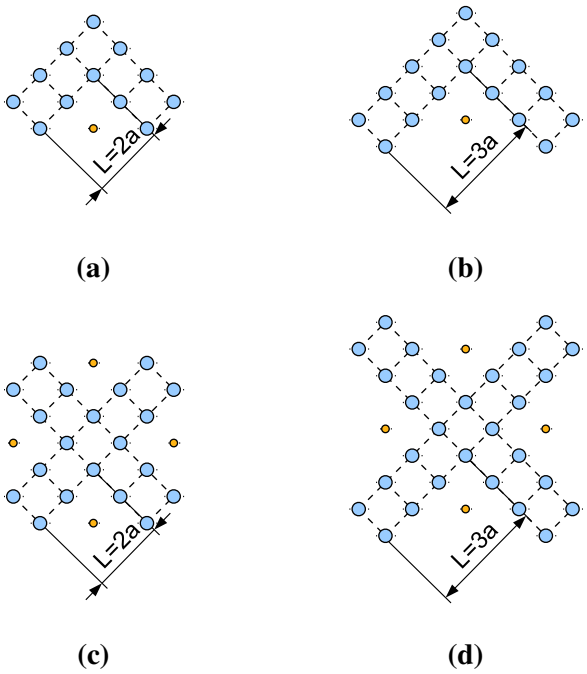

Figure 4.46: *Single-feed and multiple-feed* 90° *SEBG corner reflector antenna comparison, prototypes geometries: a) single feed* $L = 2 \cdot a$*; b) single feed* $L = 3 \cdot a$*; c) multiple feed* $L = 2 \cdot a$*; d) multiple feed* $L = 3 \cdot a$*.*

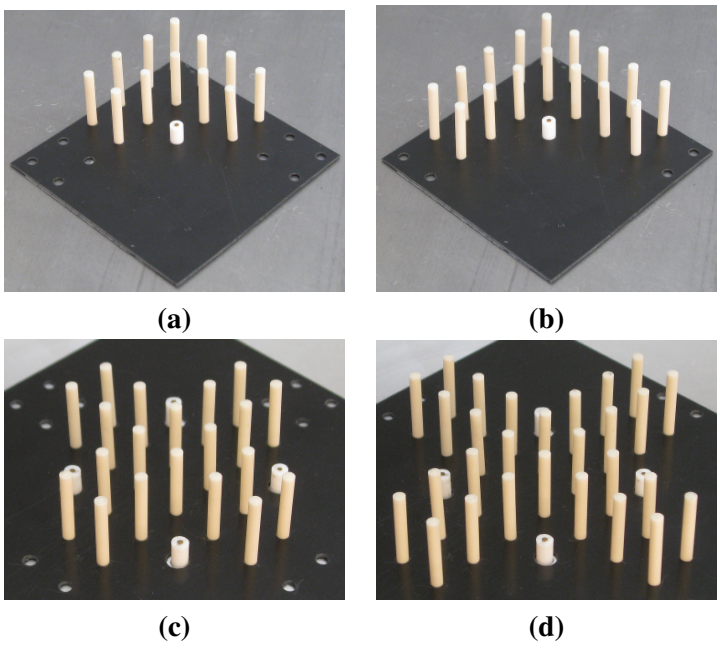

Figure 4.47: *Single-feed and multiple-feed* 90° *SEBG corner reflector antenna comparison, prototypes photos: a) single feed* $L = 2 \cdot a$*; b) single feed* $L = 3 \cdot a$*; c) multiple feed* $L = 2 \cdot a$*; d) multiple feed* $L = 3 \cdot a$*.*

4.2.6.3 Single-feed and multiple-feed comparison

As for the multiple-feed structure analysed in Section 3.4, we can expect the multiple-feed 90° SEBG corner reflector antennas to present similar performance to the single-feed

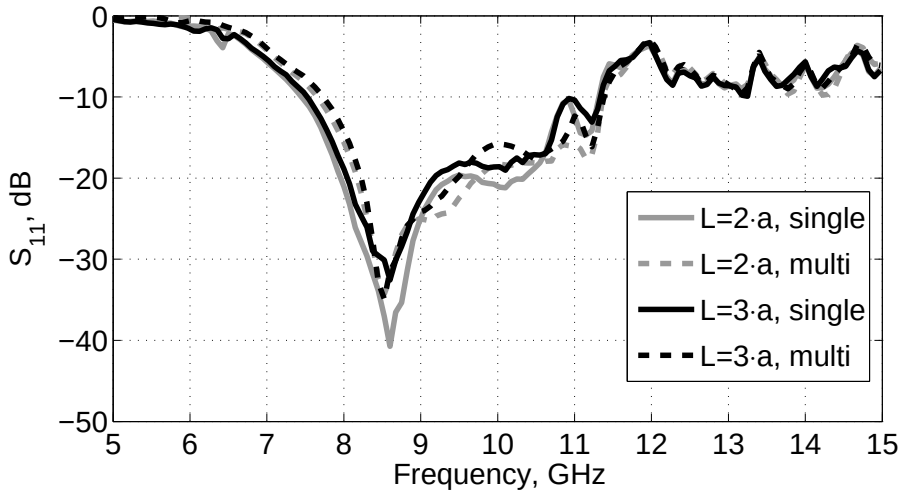

Figure 4.48: *Single-feed and multiple feed* 90° *SEBG corner reflector antenna, measured* S_{11} *as a function of corner length L; a=12mm, r=1.5mm, h=20mm,* ε_r*=37.*

antenna counterparts. Antennas geometries are shown in figure 4.46 and the measured S_{11} responses are compared in figure 4.48: all antennas have similar frequency response regardless being single-feed or multiple-feed as well as regardless the corner length, as pointed out in the parametric studies presented in the previous sections.

Radiation patterns, gain and FTBR are also quite similar, figure 4.49-4.50, the multiple feed structures also achieved very similar beamwidth and sidelobe levels to the single feed counterparts; the slightly higher gain presented by the multiple feed structures could be attributed to the extra rods in the multi feed structures themselves increasing the amount of energy reflected toward the excited aperture. Radiation patterns are again quite stable in the whole impedance bandwidth.

The results of this comparison are summarised in table 4.5: as expected, multiple feed structures present very similar characteristics to single feed structure with the extra capabilities of rotating radiation patterns by 90° discrete steps.

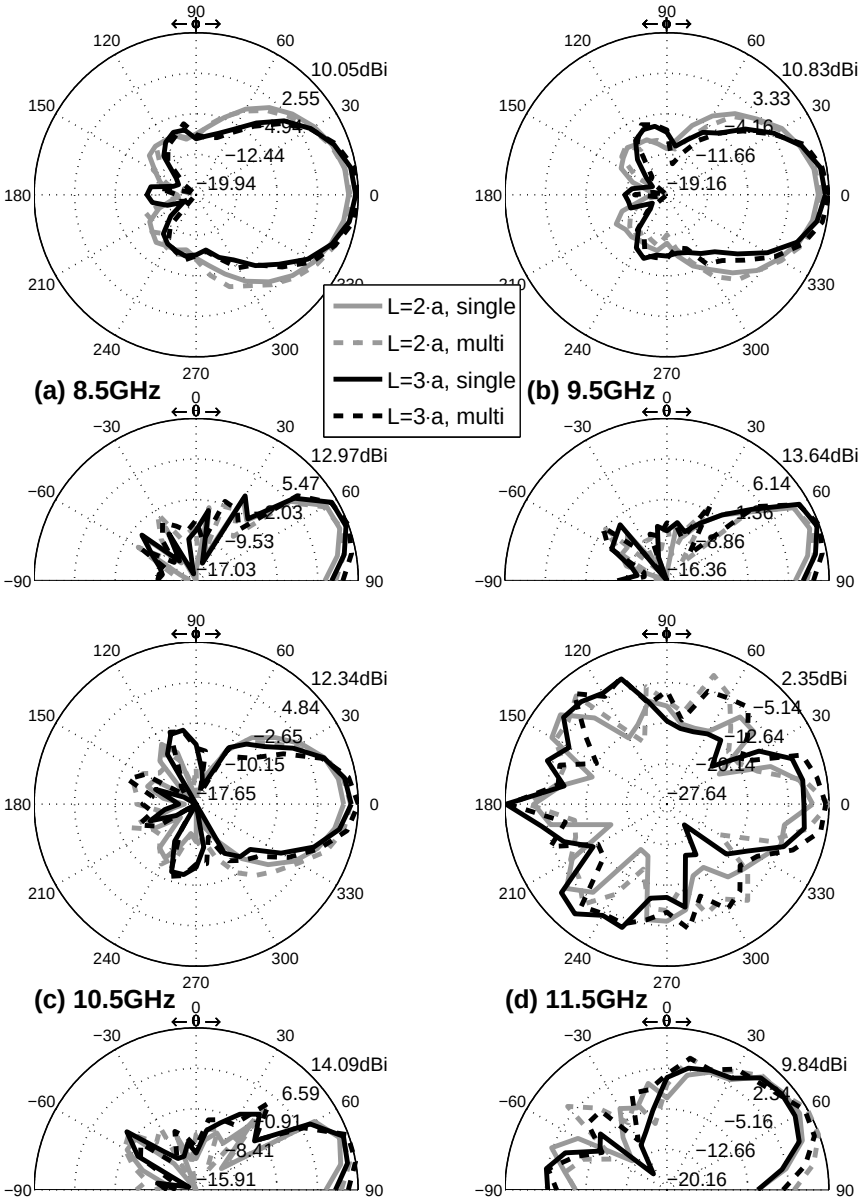

Figure 4.49: *Single-feed and multiple-feed* 90° *SEBG corner reflector antenna comparison, measured radiation patterns as a function of corner length L; a=12mm, r=1.5mm, h=20mm,* ε_r*=37..*

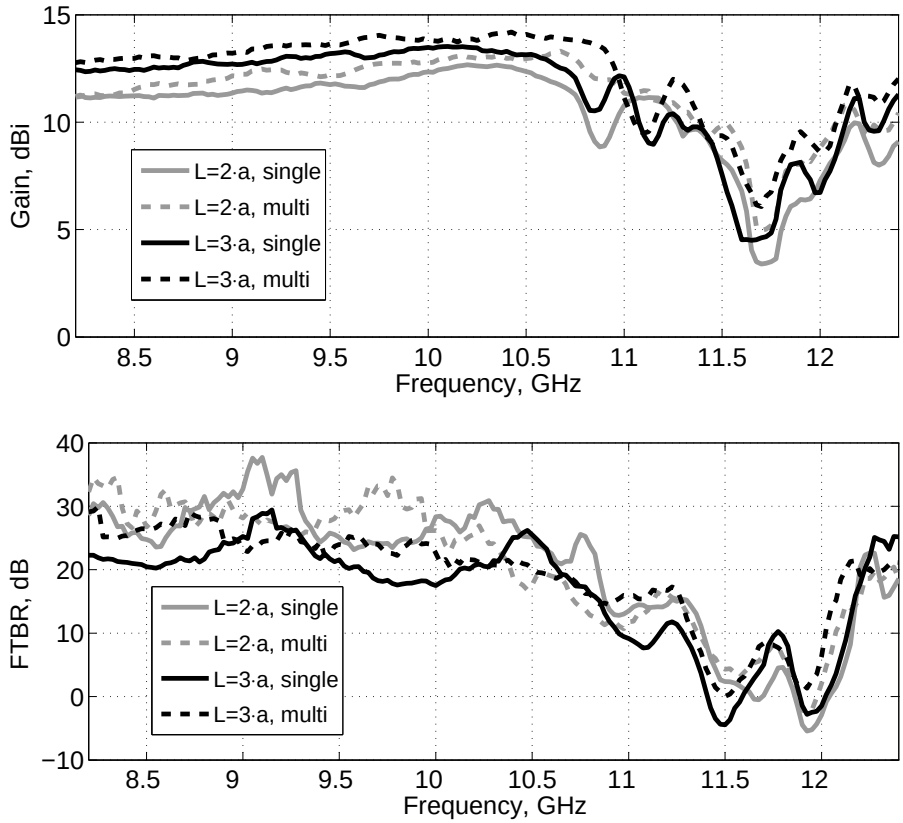

Figure 4.50: *Single-feed and multiple-feed* 90° *SEBG corner reflector antenna comparison, measured gain and FTBR as a function of corner length L; a=12mm, r=1.5mm, h=20mm,* ε_r*=37..*

	Single	Multi	Single	Multi
L	$2 \cdot a$	$2 \cdot a$	$3 \cdot a$	$3 \cdot a$
Bandwidth	41.4% 7.5-11.4GHz	38.5% 7.7-11.4GHz	40.4% 7.5-11.4GHz	38.2% 7.8-11.4GHz
Gain, dBi	12.7 (11.4)	13.3 (12.2)	13.5 (12.5)	14.2 (13.1)
FTBR, dB	37.7 (25.1)	34.6 (24.2)	29.4 (19.5)	29.9 (21.6)
S_{12}, dB	N/A	$\leq$-18.6 (-40.2)	N/A	$\leq$-20.0 (-42.5)
S_{13}, dB	N/A	$\leq$-20.7 (-39.8)	N/A	$\leq$-18.2 (-42.4)

Table 4.5: *Single-feed and multiple-feed* 90° *SEBG corner reflector antenna comparison, prototypes characteristics and performances as a function of corner length L; a=12mm, r=1.5mm, h=20mm,* ε_r*=37 (in brackets are reported the average values within the impedance bandwidth).*

4.2.7 Summary

The presented 90° SEBG corner reflector, realized using a simple square lattice of dielectric rods, was able to achieve a 40% fractional impedance bandwidth along with stable radiation patterns, average gain and FTBR respectively equal to 12.5dBi and 20dB.

Simulations and measurements shown that the deployed SEBG structure is a good approximation of a two-dimensional crystal: at frequencies within the bandgap, the SEBG structures reflects the excited fields toward the corner aperture, achieving directive radiation patterns on the azimuthal plane.

Simulated gain and radiation patterns were also found in good agreement with gain and radiation patterns of a metallic corner reflector antenna of similar dimensions, demonstrating that at bandgap frequency the SEBG corner reflector is as good as a metallic reflector, in accordance with other researchers findings: woodpile EBG horn antennas [38, 39] and a multilayer parabolic reflector [8] achieved, at bandgap frequencies, the same radiative properties of metallic structures of analogous dimensions.

A parametric study shown that the feed distance from the apex s corner length L and dielectric rods length h can be tuned to optimize the antenna performance. In particular the feed displacement s was found having the biggest impact on bandwidth and radiation patterns, in line with metal reflector characteristics. Corner length L does not influence much matching and radiative performance and can be therefore set according to minimise the required number of dielectric rods and maximum dimensions. Increasing dielectric rods length h generally increases matching and radiative properties, thus it can be tuned to optimize the overall performances.

A multiple-feed structure realised with four monopole feeds was also presented and analysed showing similar characteristics to the single-feed counterpart, achieving very similar performances in terms of impedance bandwidth, gain, FTBR as well as radiation patterns beamwidth and sidelobes level. By exciting one of the four probes at a time, the radiation patterns can be actively rotated by 90° steps on the azimuthal plane.

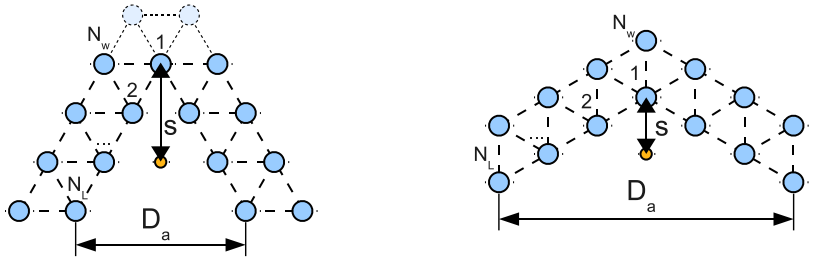

(a) **(b)**

Figure 4.51: *TEBG corner reflector geometries: a)* 60°*; b)* 120°.

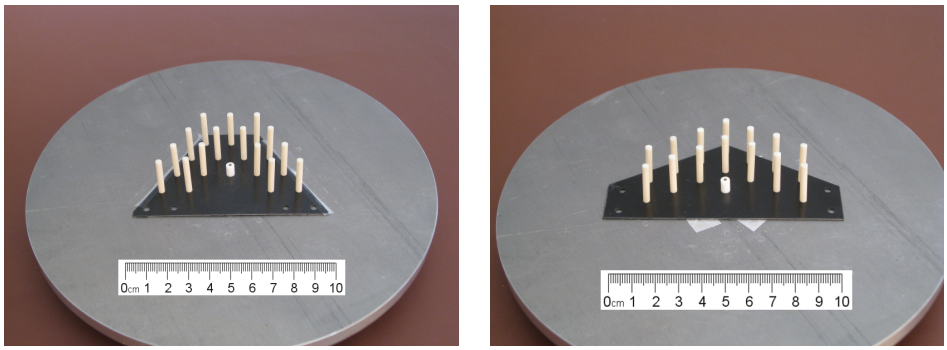

(a) **(b)**

Figure 4.52: *TEBG corner reflector photos: a)* 60°*; b)* 120°.

4.3 TEBG corner reflector antennas

A triangular lattice of dielectric rods can be used to create 60° and 120° corner reflectors as shown in figure 4.51. We focused our attention on corner reflector of 2 layers width, $w = 2 \cdot a$, arranging dielectric rods according to the TEBG lattice presented in Chapter 3, i.e. a=13mm and r=1.5mm.

Both 60° and 120° TEBG corner reflectors have been analysed following a similar procedure as for the 90° SEBG corner reflector:

- 2-D TEBG corner reflector have been parametrically studied to get a first insight on the incidence of geometrical parameters on radiative properties;
- 2-D TEBG and metal corner reflector of similar dimensions have been compared in terms of radiation patterns;
- results gathered from the 2-D analysis have been used to design 3-D TEBG corner reflector antennas;
- 3-D TEBG corner reflector antennas have been compared to analogous metal corner reflector antennas and parametrically studied to find optimum designs.

4.3.1 60° *corner reflector*

The 60° TEBG corner presents a peculiarity, the corner apex is in fact buried inside the TEBG crystal; therefore, the 2 shaded dielectric columns shown in figure 4.51a have not been included in the corner structure.

4.3.1.1 2-D 60° corner reflector antenna

The normalised electric field distribution as a function of frequency is shown in figure 4.53: the 2-D TEBG 60° corner reflector is very effective at frequencies within the bandgap, 5.28-10.95GHz Chapter 3, whilst at frequencies outside the bandgap there is a strong leakage through the TEBG structure, leading to non-directive or multiple beams radiation patterns.

The influence of the corner side length L on the radiation patterns is shown in figure 4.54: as expected, increasing the side length improves gain and narrows the beamwidth; the number of require dielectric rods is also increased, therefore leading to a trade-off between performance and dimensions.

Feed displacement s has a major impact on radiation patterns: a too small displacement is detrimental to radiation patterns at low frequencies; conversely, a too large displacement is detrimental to radiation patterns at high frequencies. Best performance was achieved when $s = 2 \cdot a \cdot \cos\left(\frac{\alpha}{2}\right) = 2 \cdot a \cdot \cos(\pi/6)$, where α is the corner enclosed angle, i.e. 60°.

The 2-D TEBG 60° corner reflector has been compared to metal reflectors of similar dimensions, in particular to a standard 60° metal corner, figure 4.56b, and to a modified "A shaped" 60° metal corner to take into account the characteristics of the TEBG structure. Simulations results are shown in figure 4.57 and figure 4.58: at bandgap frequencies, TEBG corner structure and metal corners present very similar radiation patterns (for a beamwidth of at least 90°) and basically the same realised gain.

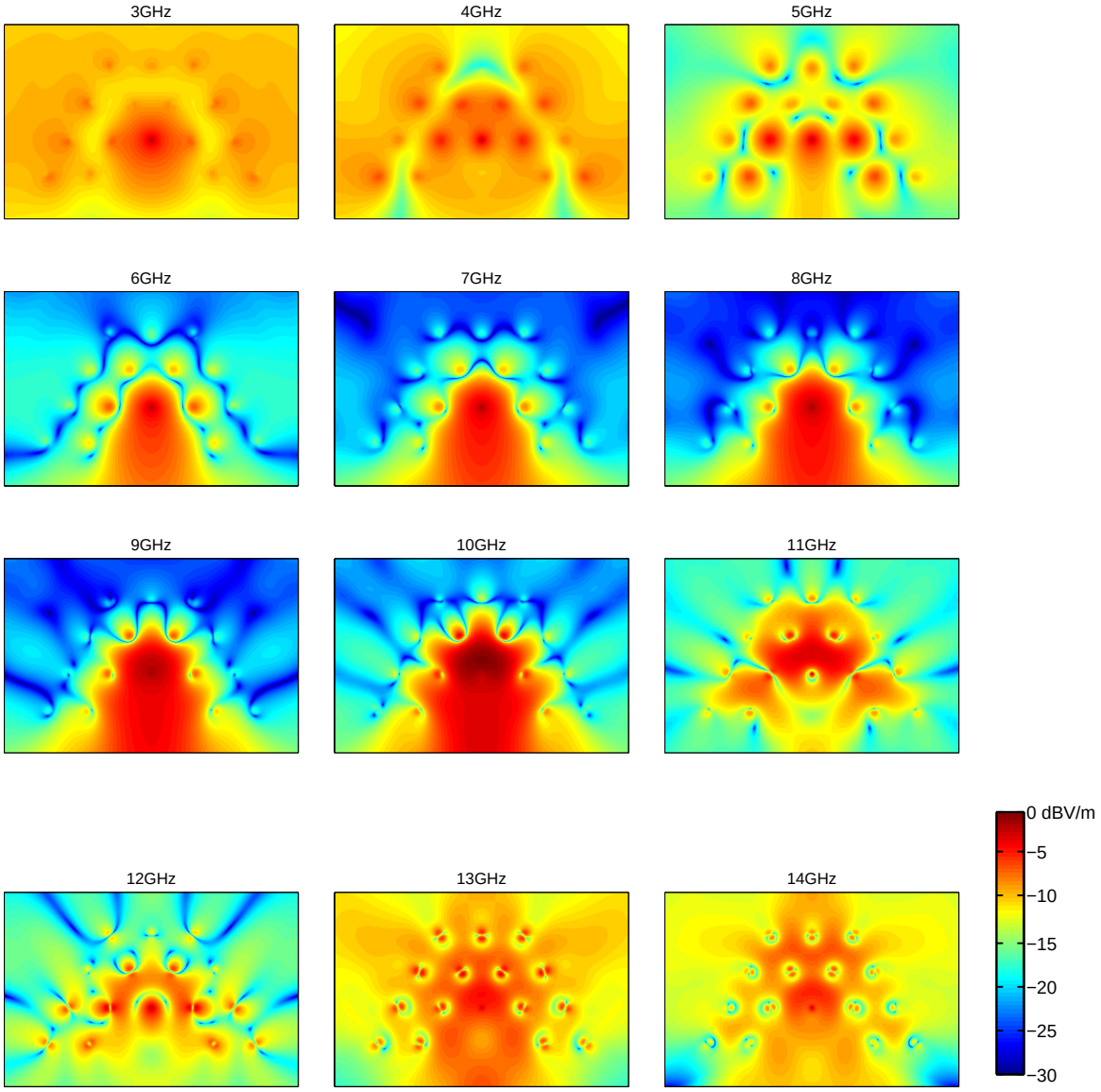

Figure 4.53: *2-D TEBG 60° corner reflector antenna, simulated normalised electric field distribution on the azimuthal plane, a=13mm, r=1.5mm, ε_r=37, N_L=3 and N_w=2.*

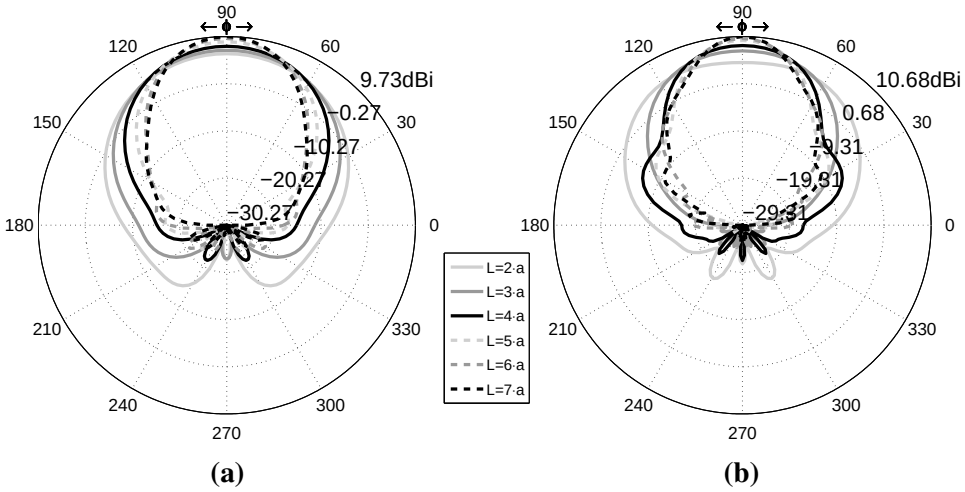

Figure 4.54: *2-D* 60° *TEBG corner reflector antenna, simulated (normalised) radiation patterns as a function of the reflector internal length L, N_w=2: a) 7GHz, b) 10GHz.*

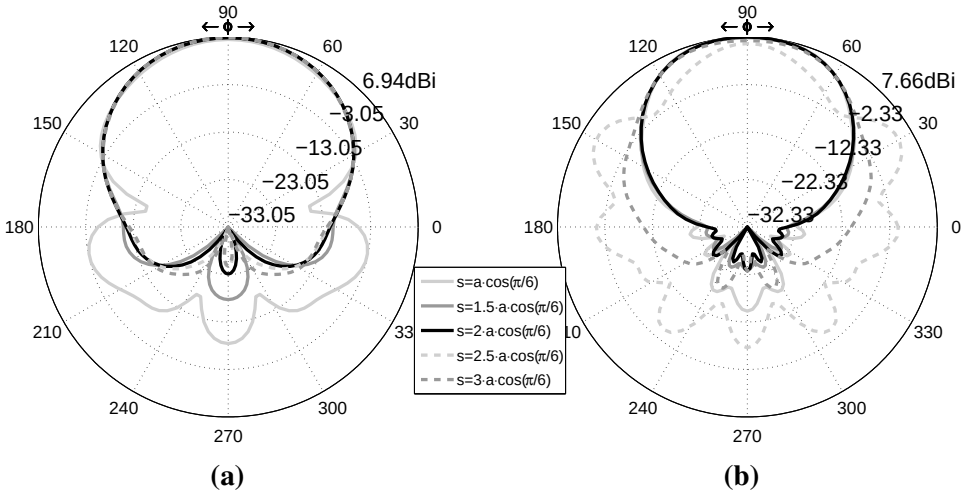

Figure 4.55: *2-D* 60° *TEBG corner reflector antenna, simulated (normalised) radiation patterns as a function of the feed distance s from the corner apex, N_L=3 and N_w=2: a) 7GHz, b) 10GHz.*

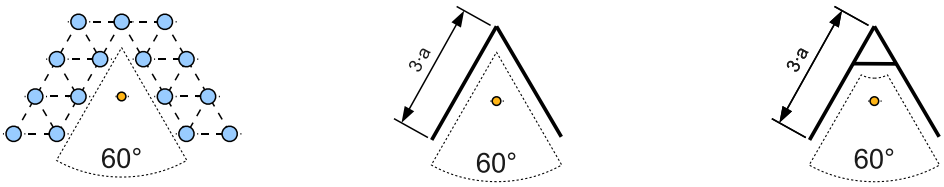

Figure 4.56: *a) 2-D* 60° *TEBG corner reflector antenna; b) 2-D* 60° *metal corner reflector antenna; c) 2-D* 60° *modified metal corner reflector antenna.*

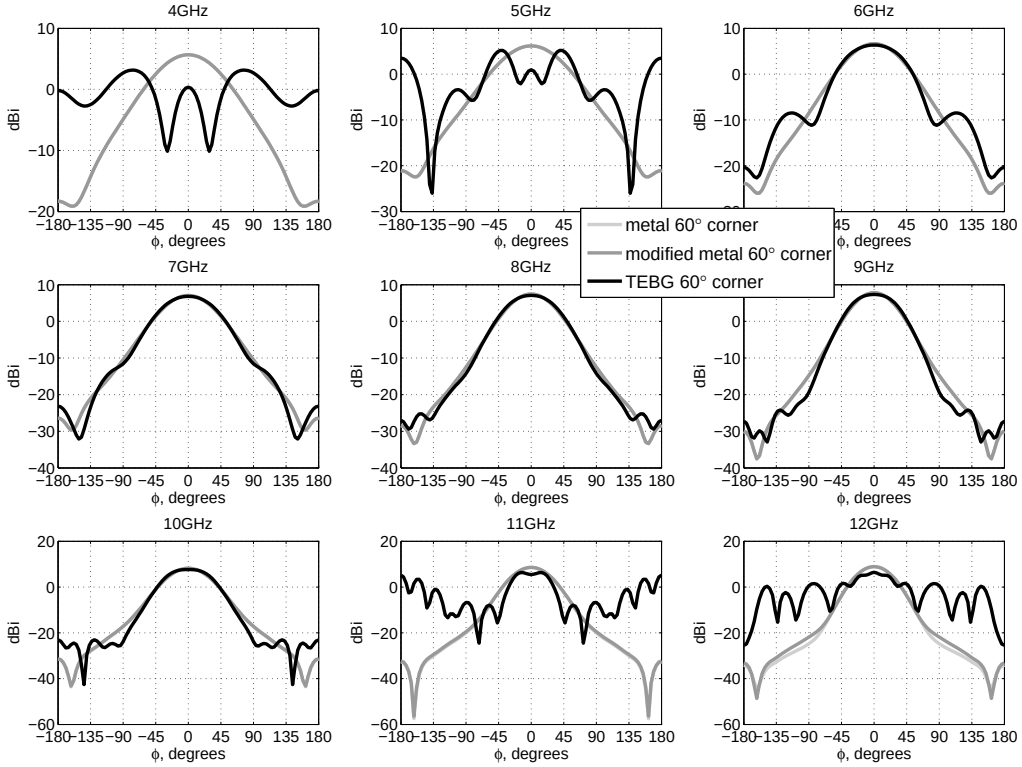

Figure 4.57: *2-D 60° TEBG corner reflector antenna and 60° metal corner reflector antennas comparison: simulated directivity patterns as a function of frequency, a=13mm, r=1.5mm, ε_r=37, N_L=3 and N_w=2.*

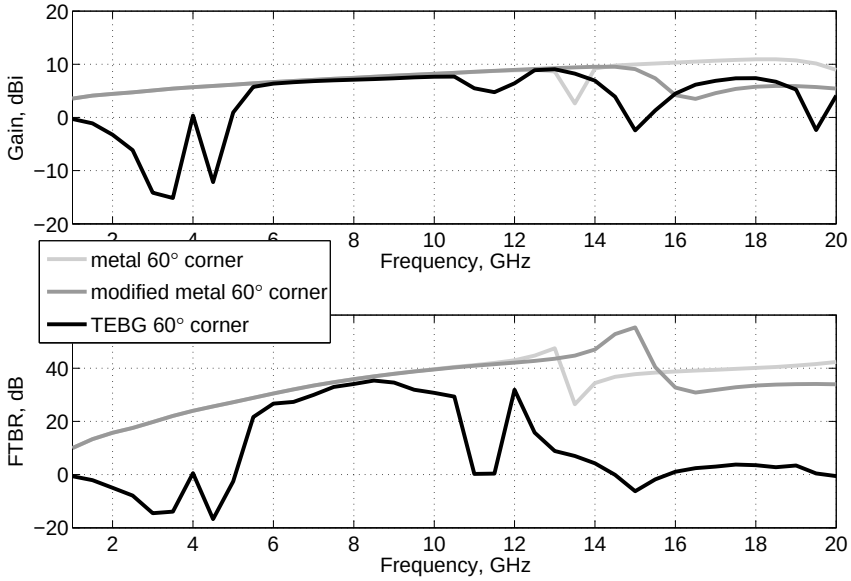

Figure 4.58: *2-D 60° TEBG corner reflector antenna and 60° metal corner reflector antennas simulated gain and FTBR comparison, a=13mm, r=1.5mm, ε_r=37, N_L=3 and N_w=2.*

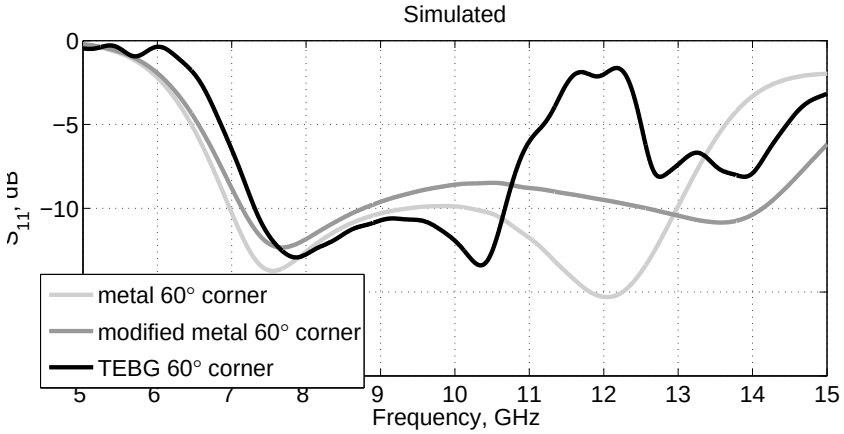

Figure 4.59: *3-D TEBG* 60° *corner reflector antenna and metallic corner reflector antenna simulated* S_{11}.

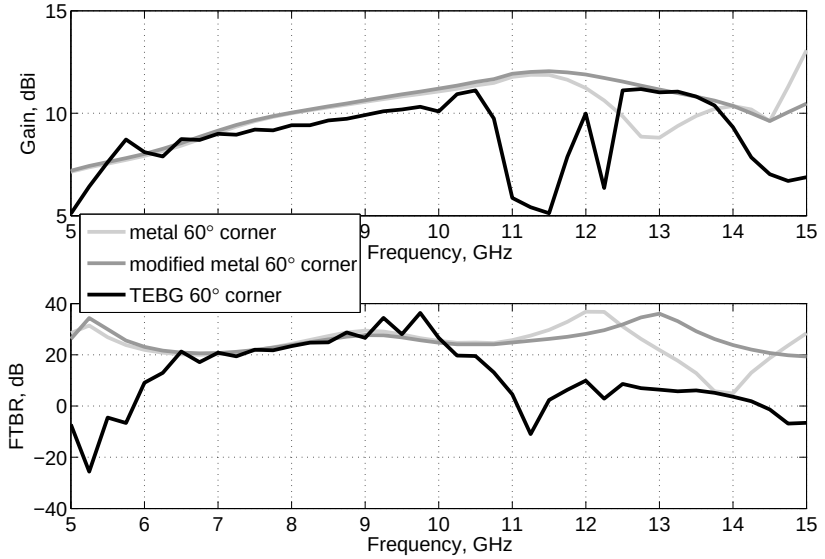

Figure 4.60: *3-D TEBG* 60° *corner reflector antenna and metallic corner reflector antenna simulated gain and front-to-back-ratio (FTBR).*

4.3.1.2 3-D 60° corner reflector antenna

A 3-D TEBG 60° corner reflector antenna has been simulated and compared against the two analogous metal corner reflector antennas. Reflector width w and internal length L respectively equal to $a = 13mm$ (N_w=2) and $3 \cdot a = 39mm$ (N_L=3) have been chosen along with a source distance s from the apex equals to $2 \cdot a \cdot \cos \pi/6$. The S_{11} responses are quite different, figure 4.59, but gain, FTBR and radiation patterns are quite similar at frequencies within the bandgap figure 4.60-4.61.

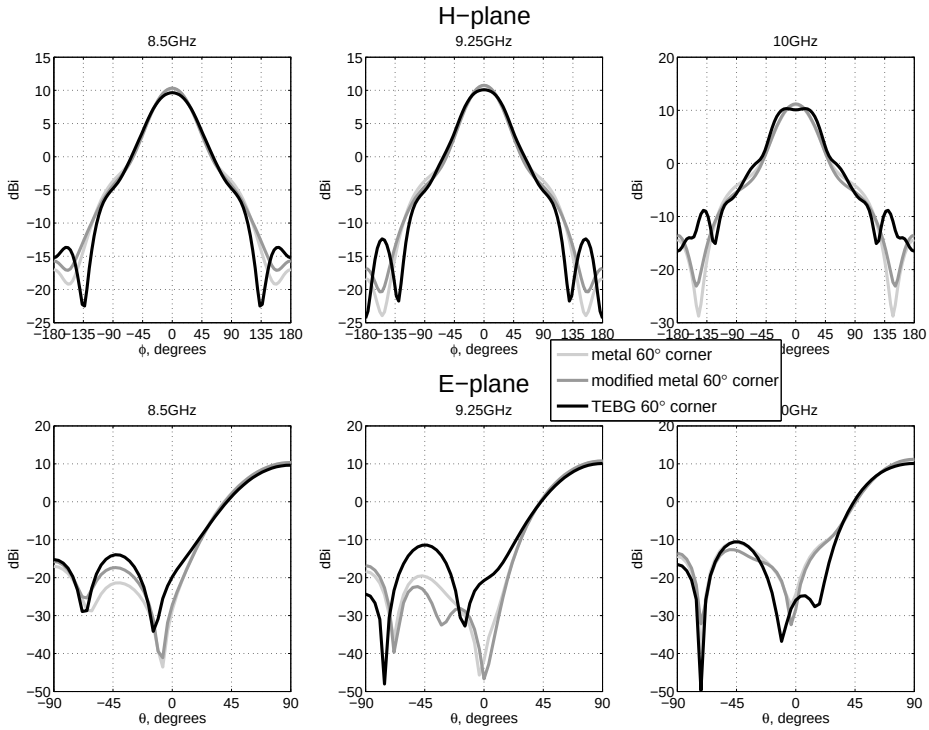

Figure 4.61: *3-D TEBG* 60° *corner reflector antenna and metallic corner reflector antenna simulated radiation patterns.*

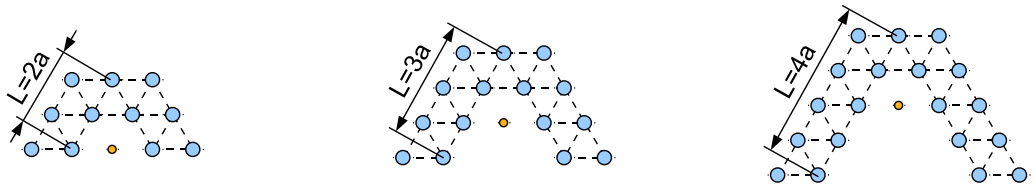

(a) **(b)** **(c)**

Figure 4.62: *3-D 60° TEBG corner reflector antenna geometries as a function of corner length L: a) $L = 2 \cdot a$; b) $L = 3 \cdot a$; c) $L = 4 \cdot a$.*

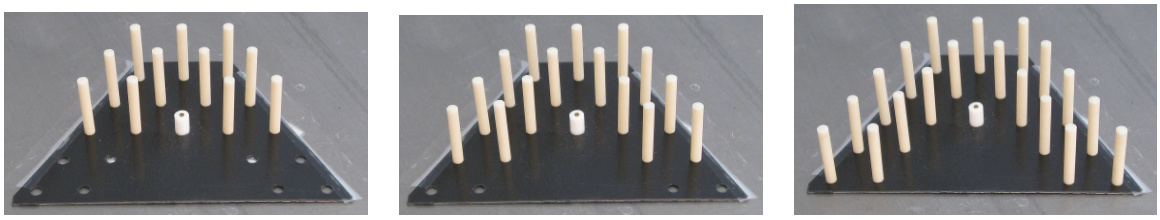

(a) **(b)** **(c)**

Figure 4.63: *3-D 60° TEBG corner reflector antenna photos as a function of corner length L: a) $L = 2 \cdot a$; b) $L = 3 \cdot a$; c) $L = 4 \cdot a$.*

The 3-D 60° TEBG corner reflector antenna has been parametrically studied as a function of the corner side length L, figure 4.62; the results are summarised in table 4.6. Antenna matching and bandwidth are moderatly influenced by the side length L, figure 4.64; a 25% or greater impedance bandwidth is easily achieved, with matching generally improving with L. Simulated and measured radiative performance are in very good agreement: increasing L improves the achieved gain, greater than 11.9dBi, and narrows the beamwidth; the FTBR though, is maximum with an intermediate side length $L = 3 \cdot a$ when it reaches a maximum and average value of 31.7dB and 26dB respectively. Maximum dimensions and the required number of rods are obviously increasing with L, leading to a trade-off between performance and geometrical dimensions/complexity.

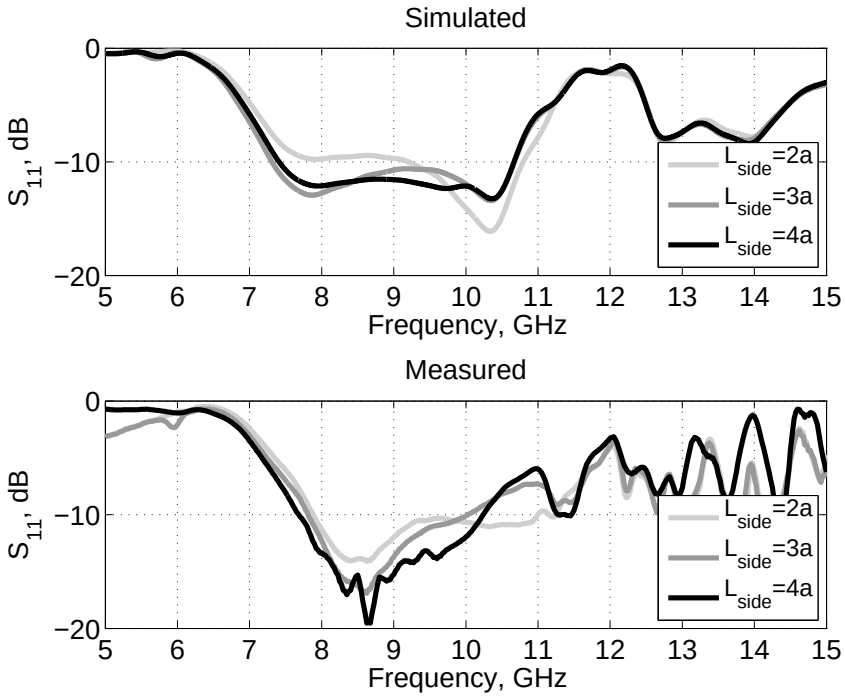

Figure 4.64: *3D TEBG* 60° *corner reflector antenna simulated and measured* S_{11} *as a function of side length L.*

L	Gain, dBi	FTBR, dB	Bandwidth	N_{rods}	Max dim.
$2{\cdot}a$	11.9 (8.9)	26.0 (15.7)	35.1%	11	$4 \cdot a$
			7.9-11.3GHz		$1.65{\cdot}\lambda_c$
$3{\cdot}a$	12.5 (11.9)	31.7 (26.0)	25.1%	15	$5 \cdot a$
			7.8-10.1GHz		$2.06{\cdot}\lambda_c$
$4{\cdot}a$	13.8 (13.2)	28.7 (23.9)	28.4%	19	$6 \cdot a$
			7.7-10.2GHz		$2.48{\cdot}\lambda_c$

Table 4.6: *3-D TEBG* 60° *corner reflector antenna measured performance as a function of side length L; a=13mm, r=1.5mm,* ε_r*=37 and h=20mm (in brackets are reported the average values within the impedance bandwidth);* $\lambda_c = \lambda_{(f_c=9.5GHz)=31.5mm}$.

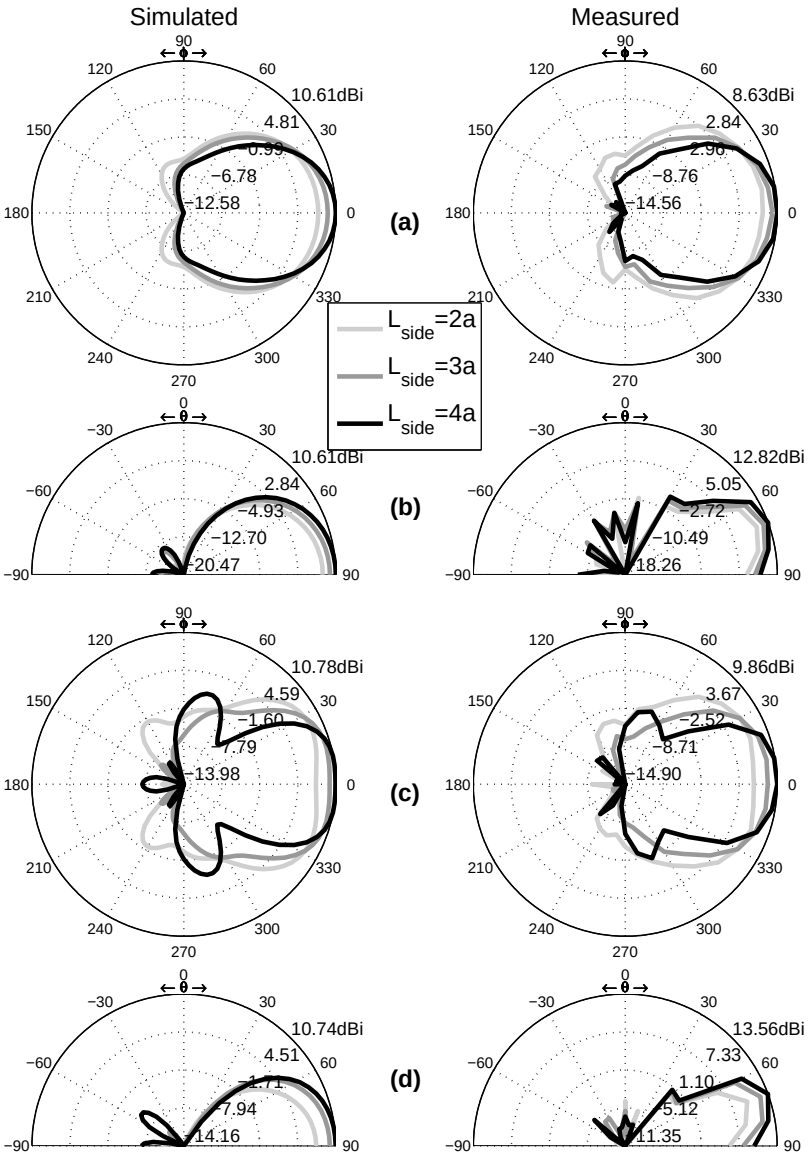

Figure 4.65: *3D TEBG* 60° *corner reflector antenna simulated and measured radiation patterns as a function of side length L: a) H-plane 8.5GHz; b) E-plane 8.5GHz; a) H-plane 10GHz; b) E-plane 10GHz.*

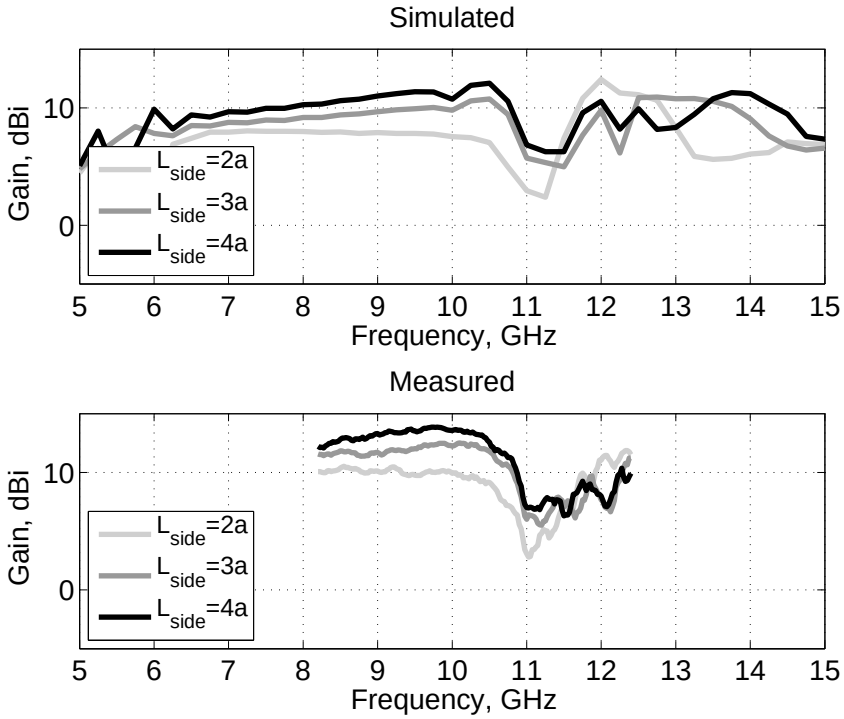

Figure 4.66: *3D TEBG* 60° *corner reflector antenna simulated and measured gain as a function of side length L.*

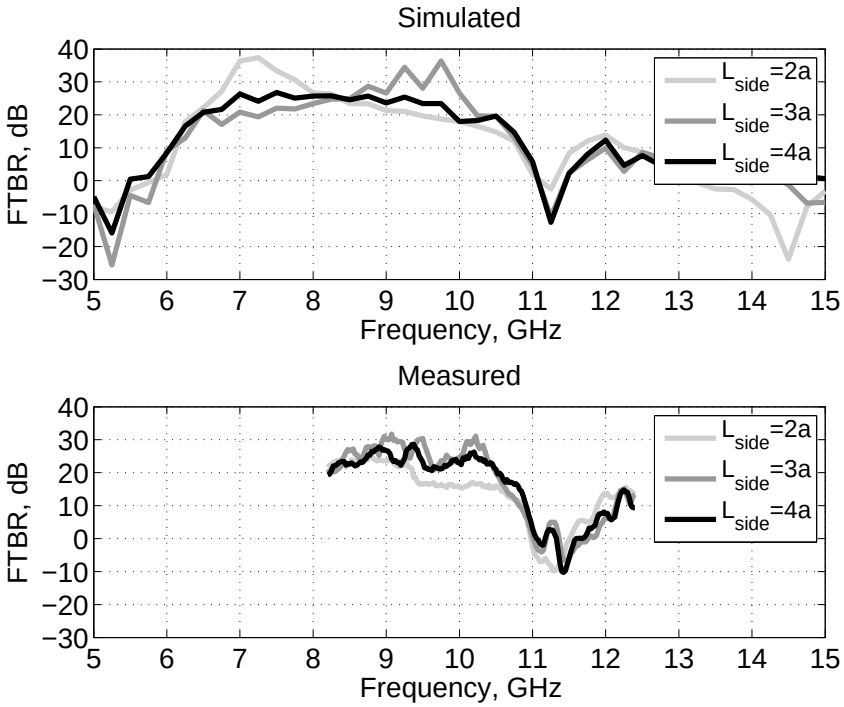

Figure 4.67: *3D TEBG* 60° *corner reflector antenna simulated and measured FTBR as a function of side length L.*

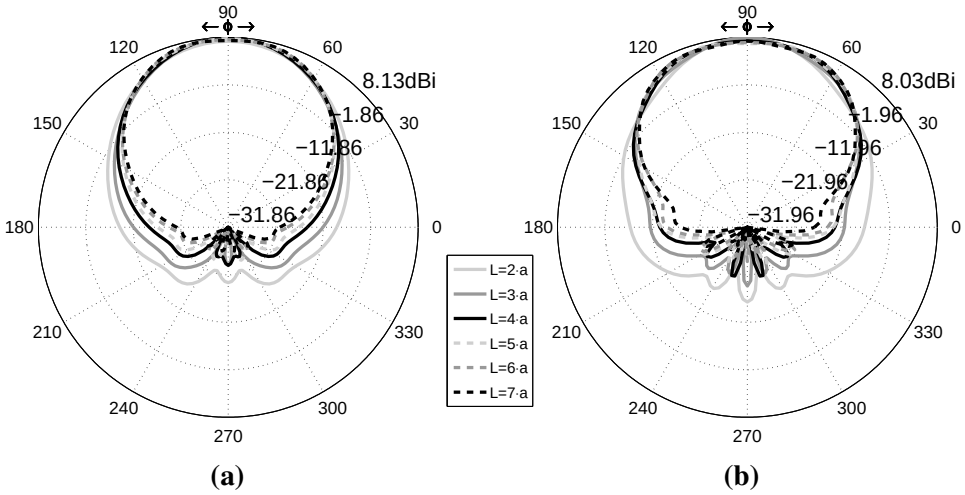

Figure 4.68: *2-D* 120° *TEBG corner reflector antenna, simulated (normalised) radiation patterns as a function of the reflector internal length L, N_w=2: a) 7GHz, b) 10GHz.*

4.3.2 120° *corner reflector*

4.3.2.1 2-D 120° corner reflector antenna

A TEBG crystal can be also used to create 120° corner reflectors are shown in figure 4.51b. The influence of corner side length L and feed displacement s on the radiation patterns are respectively shown in figure 4.68 and figure 4.70. We focused our attention on a corner width $w = a$. Increasing the corner side length L improves radiation patterns directivity in terms of maximum gain and narrower beamwidth; a good compromise in terms of performance and dimensions is $L = 3 \cdot a$.

The normalised electric field distribution as a function of frequency is shown in figure 4.69: at frequencies within the TEBG structure bandgap (5.28-10.95GHz), the 2-D 60° corner is very effective to reflect the excited fields toward the corner aperture leading to directive radiation patterns; at frequencies outside the bandgap, energy is free to propagate through the reflector leading to not directive radiation patterns.

The feed displacement s has a minor impact compared to 60° and 90° EBG corner reflectors but the same influence: at low frequencies radiation patterns are disrupted by a too small displacement whilst at high frequency radiation patterns are disrupted by a too large displacement. The minor impact is partially caused by the fact that even though the relative displacements we tested are the same in all cases ($s = 0.5 - 1.5\bar{s}$ where $\bar{s}$ is the average displacement), the absolute displacements are quite different, and in the 120° reflector case are minimum (in particular s=7.5-22.5mm, whilst for the 60° corner s=11.26-33.78mm and for the 90° corner s=8.48-25.46mm). Best results are obtained again when $s = 2 \cdot a \cdot \cos\left(\frac{\alpha}{2}\right) = a$, where α is the corner enclosed angle, i.e. 120°.

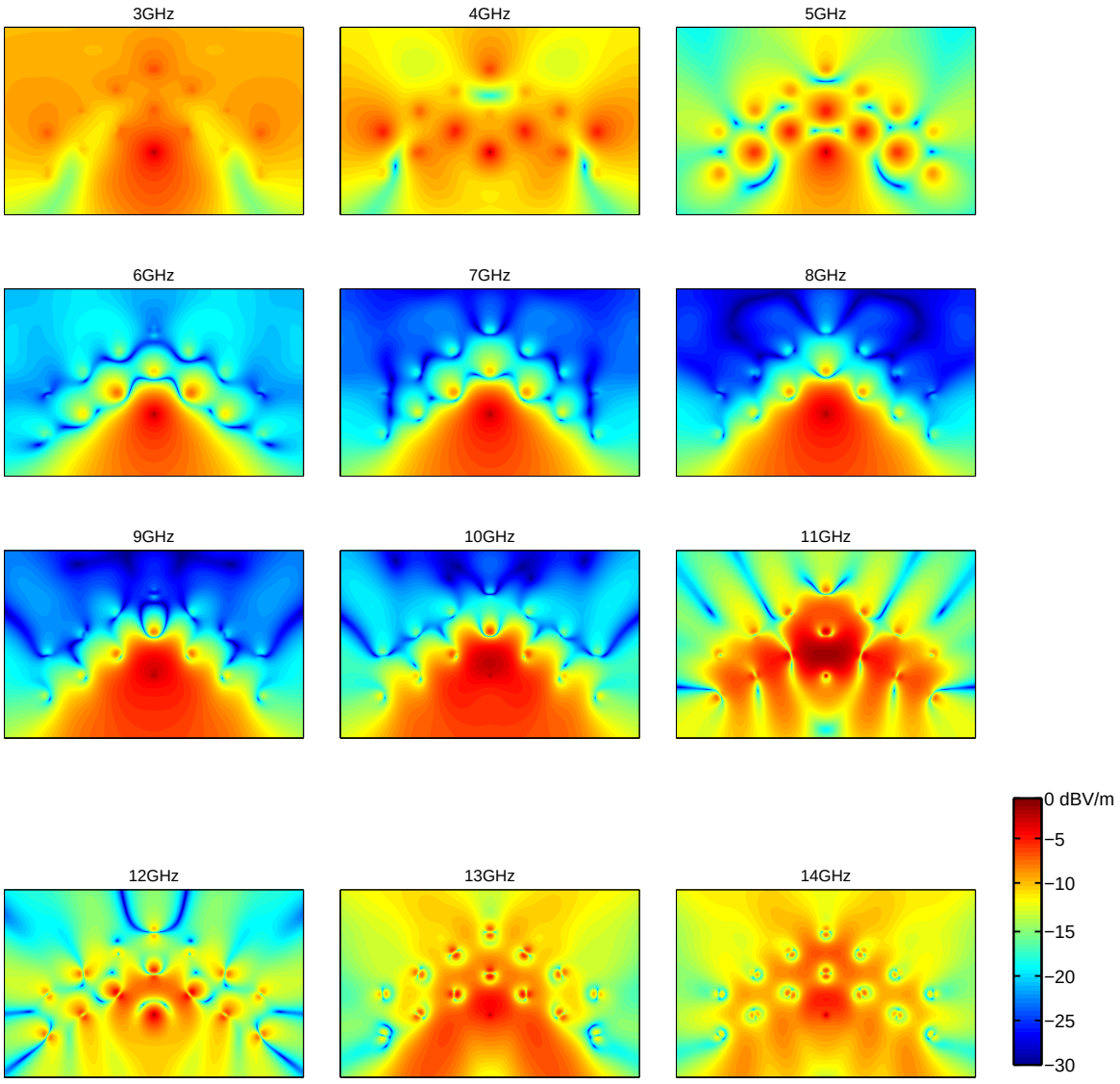

Figure 4.69: *2-D TEBG* 120° *corner reflector antenna, simulated normalised electric field distribution on the azimuthal plane, a=13mm, r=1.5mm,* ε_r*=37,* N_L*=3 and* N_w*=2.*

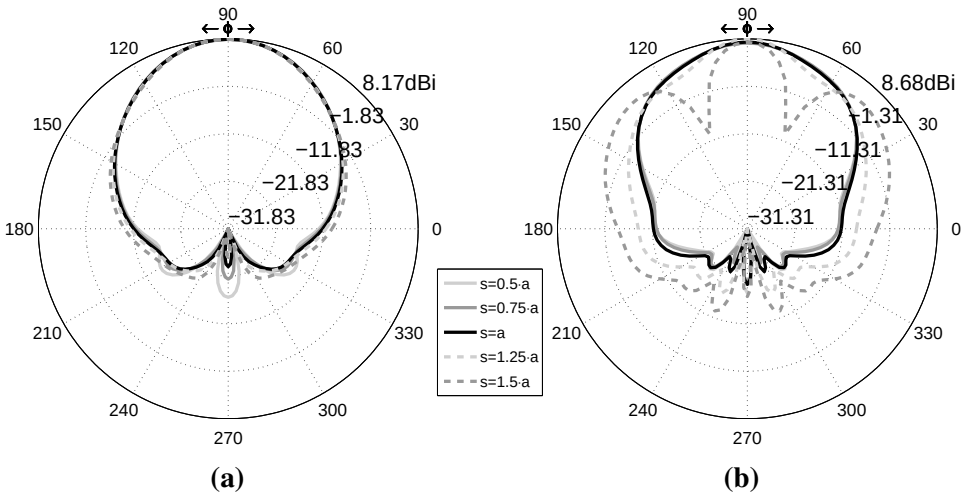

Figure 4.70: *2-D* 120° *TEBG corner reflector antenna, simulated (normalised) radiation patterns as a function of the feed distance s from the corner apex,* N_L*=3 and* N_w*=2: a) 7GHz, b) 10GHz.*

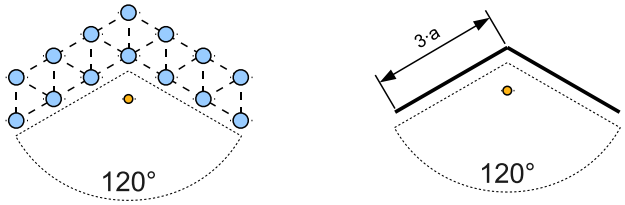

(a) **(b)**

Figure 4.71: *a) 2-D* 120° *TEBG corner reflector antenna; b) 2-D* 120° *metal corner reflector antenna.*

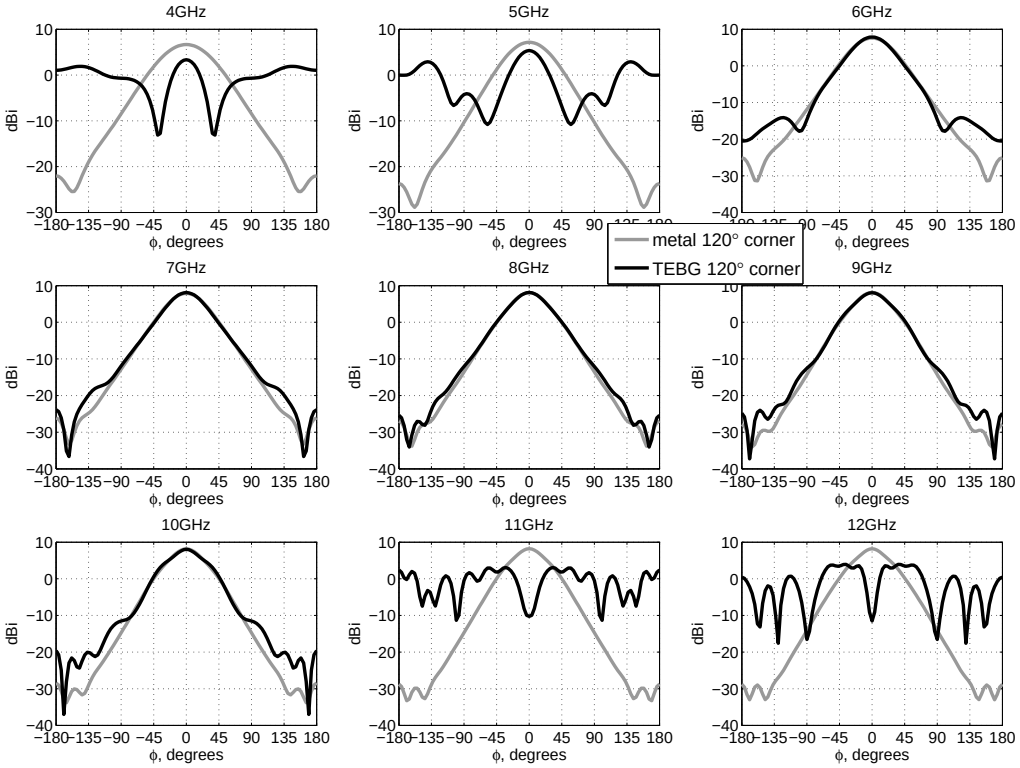

Figure 4.72: *2-D* 120° *SEBG corner reflector antenna and* 120° *metal corner reflector antenna comparison: simulated directivity patterns as a function of frequency, a=13mm, r=1.5mm,* ε_r*=37,* N_L*=3 and* N_w*=2.*

In figure 4.72 and figure 4.73 a 2-D 120° TEBG corner reflector antenna with $s = a$, N_L=3 and N_w=2 is compared with a metal reflector of similar dimensions, figure 4.71, in terms of radiation patterns, gain and FTBR. At bandgap frequencies, radiation patterns are quite similar for a beam extension of circa 150° and the realised gain is practically the same. The TEBG corner reflector is therefore as good as a metal reflector (at bandgap frequencies).

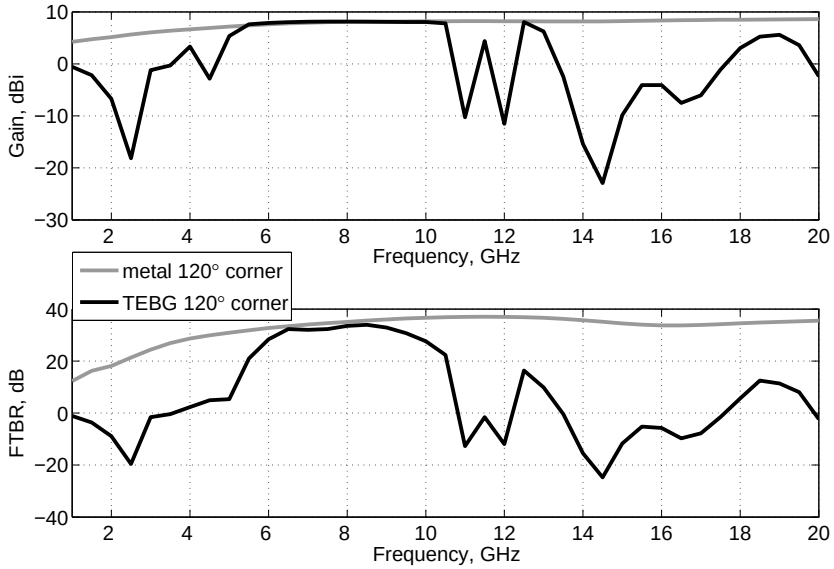

Figure 4.73: *2-D* 120° *SEBG corner reflector antenna and* 120° *metal corner reflector antenna comparison: simulated gain and FTBR, a=13mm, r=1.5mm,* ε_r*=37,* N_L*=3 and* N_w*=2.*

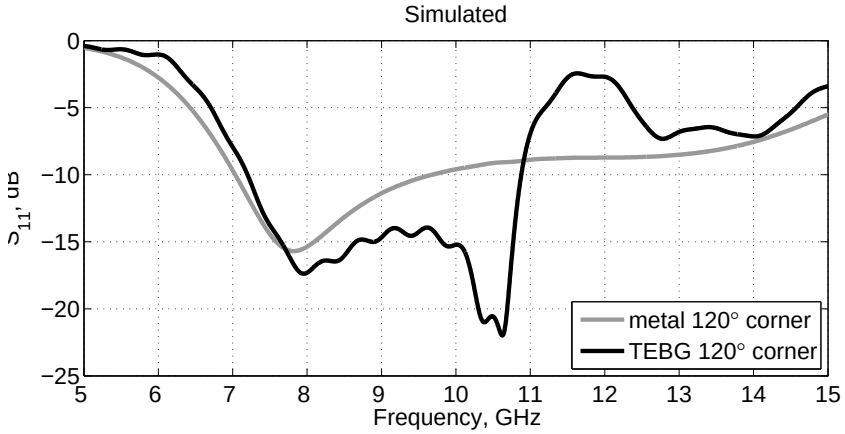

Figure 4.74: *3-D TEBG* 120° *corner reflector antenna and metallic corner reflector antenna simulated* S_{11}.

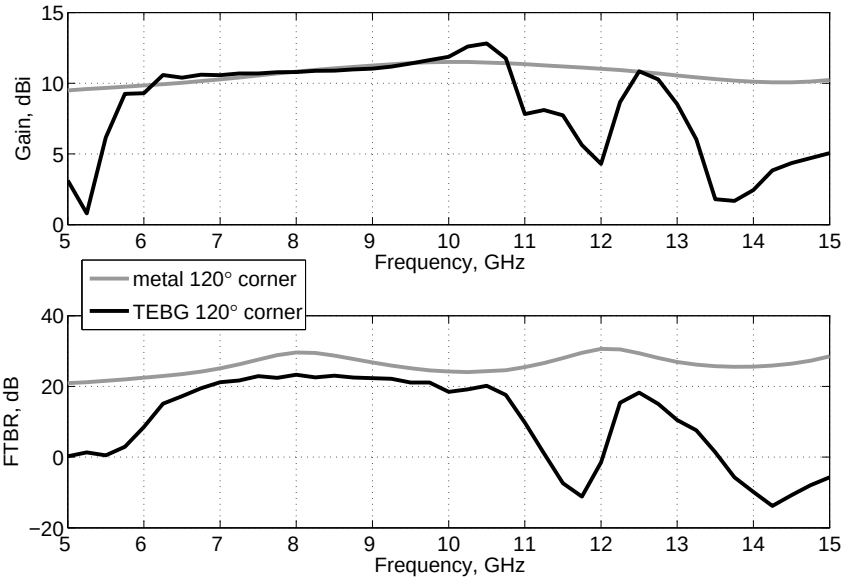

Figure 4.75: *3-D TEBG* 120° *corner reflector antenna and metallic corner reflector antenna simulated gain and front-to-back-ratio (FTBR).*

4.3.2.2 3-D 120° corner reflector antenna

A 3-D TEBG 120° corner reflector antenna has been simulated and compared against a metal corner reflector antenna of similar dimensions. The chosen geometrical parameters are width $w = a = 13mm$ (N_w=2), corner side length $L3 \cdot a = 39mm$ (N_L=3), feed displacement from the apex $s = a$. The S_{11} responses are quite different, figure 4.74, but gain, FTBR and radiation patterns are very similar at frequencies within the bandgap figure 4.75-4.76; TEBG and metal reflectors have again the same radiative characteristics (at bandgap frequencies) as in the previous cases.

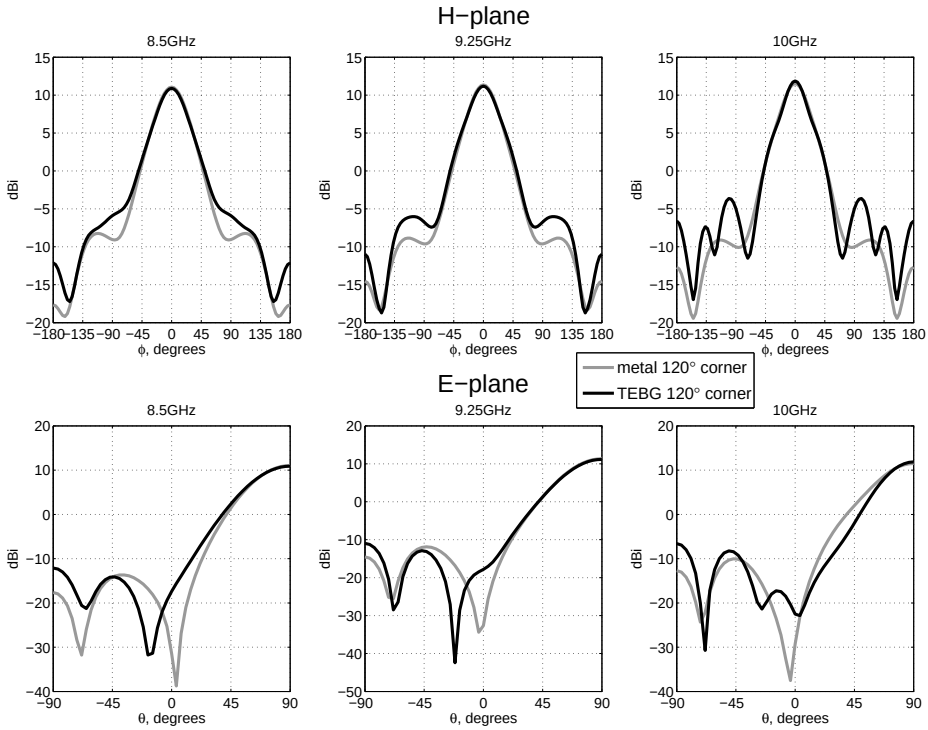

Figure 4.76: *3-D TEBG* 120° *corner reflector antenna and metallic corner reflector antenna simulated radiation patterns.*

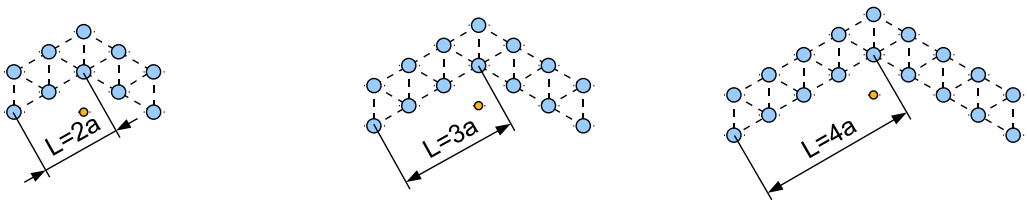

(a) **(b)** **(c)**

Figure 4.77: *3-D* 120° *TEBG corner reflector antenna geometries as a function of corner length L: a)* $L = 2 \cdot a$*; b)* $L = 3 \cdot a$*; c)* $L = 4 \cdot a$*.*

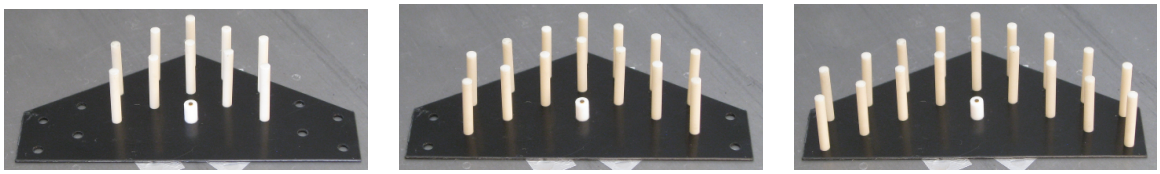

(a) **(b)** **(c)**

Figure 4.78: *3-D* 120° *TEBG corner reflector antenna photos as a function of corner length L: a)* $L = 2 \cdot a$*; b)* $L = 3 \cdot a$*; c)* $L = 4 \cdot a$*.*

The results of a parametric study focused on the corner side length L are summarised in table 4.77. Impedance bandwidth and gain are practically not influenced at all when L is increased from $2 \cdot a$ to $4 \cdot a$, figure 4.79 and figure 4.81; only the FTBR is moderatly influenced with best performance achieved when L is minimum, i.e. $L = 2 \cdot a$, figure 4.82. Radiation patterns are also mildly influenced by L: as the side length is increased, side lobes level is sligthly decreased, figure 4.80. A configuration with $L = 2 \cdot a$ is therefore the optimum choice in terms of antenna performance and geometrical dimensions.

L	Gain, dBi	FTBR, dB	Bandwidth	N_{rods}	Max dim.
$2 \cdot a$	13.4 (12.6)	31.8 (23.4)	37.9% 7.7-11.3GHz	10	$4 \cdot a \cdot \sin \pi/3$ $1.43 \cdot \lambda_c$
$3 \cdot a$	13.6 (12.7)	26.8 (20.3)	37.9% 7.7-11.3GHz	14	$6 \cdot a \cdot \sin \pi/3$ $2.14 \cdot \lambda_c$
$4 \cdot a$	13.4 (12.3)	28.0 (20.1)	37.9% 7.7-11.3GHz	18	$8 \cdot a \cdot \sin \pi/3$ $2.86 \cdot \lambda_c$

Table 4.7: *3-D TEBG* 120° *corner reflector antenna measured performance as a function of side length L; a=13mm, r=1.5mm,* ε_r*=37 and h=20mm (in brackets are reported the average values within the impedance bandwidth);* $\lambda_c = \lambda_{(f_c=9.5GHz)=31.5mm}$*.*

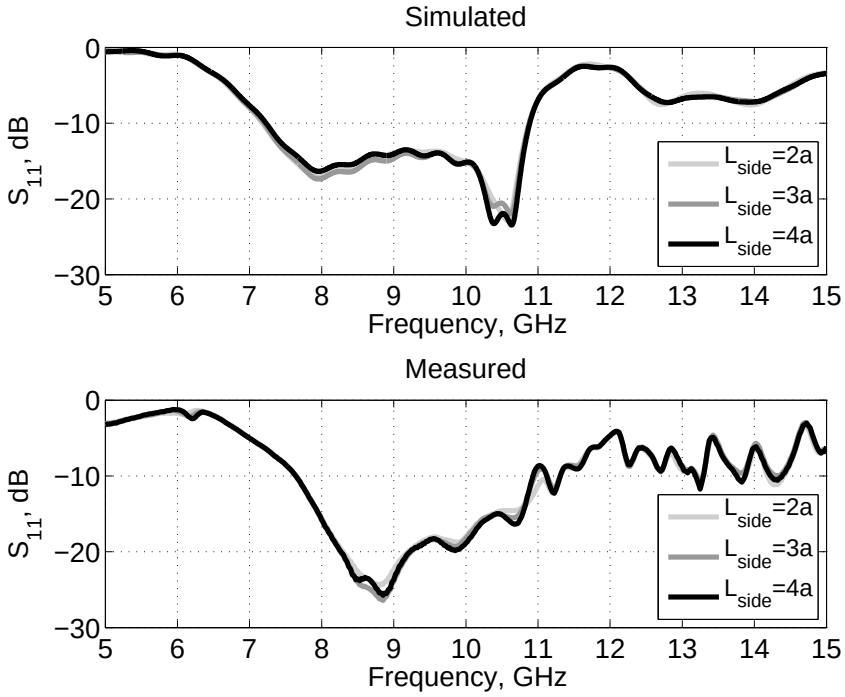

Figure 4.79: *3D TEBG* 120° *corner reflector antenna simulated and measured* S_{11} *as a function of side length L.*

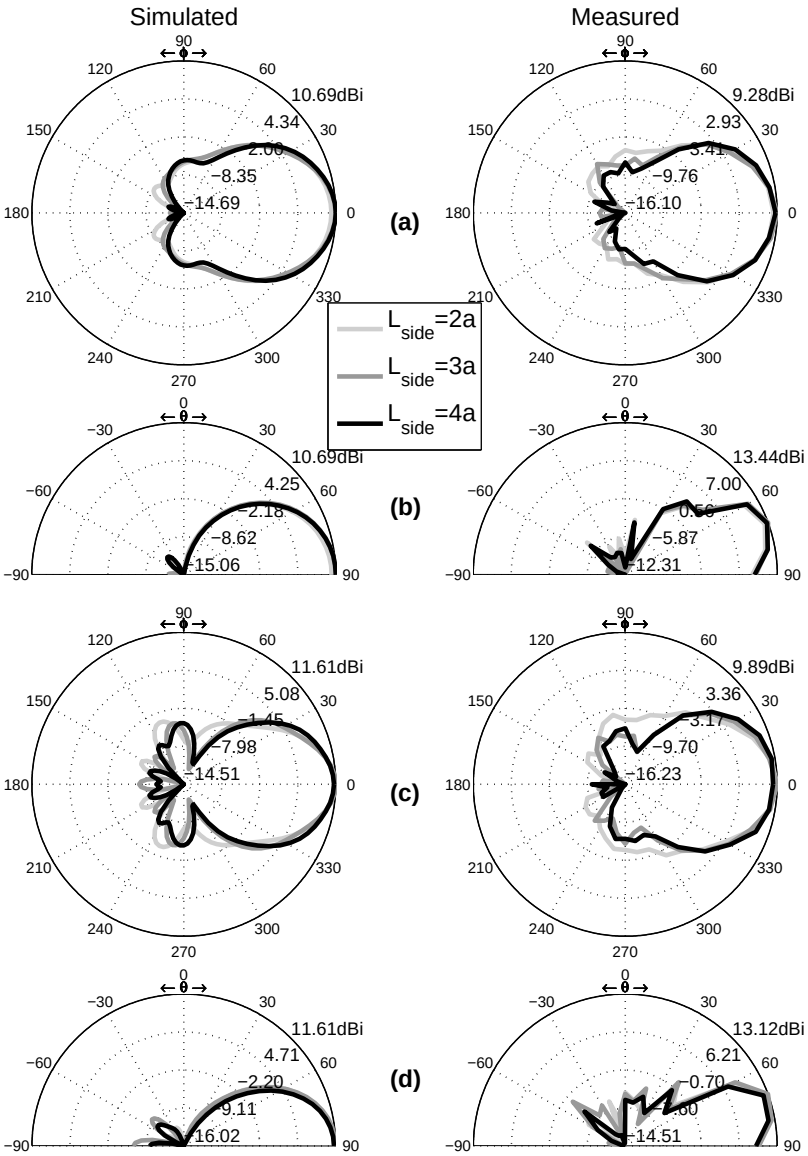

Figure 4.80: *3D TEBG* 120° *corner reflector antenna simulated and measured radiation patterns as a function of side length L: a) H-plane 8.5GHz; b) E-plane 8.5GHz; a) H-plane 10GHz; b) E-plane 10GHz.*

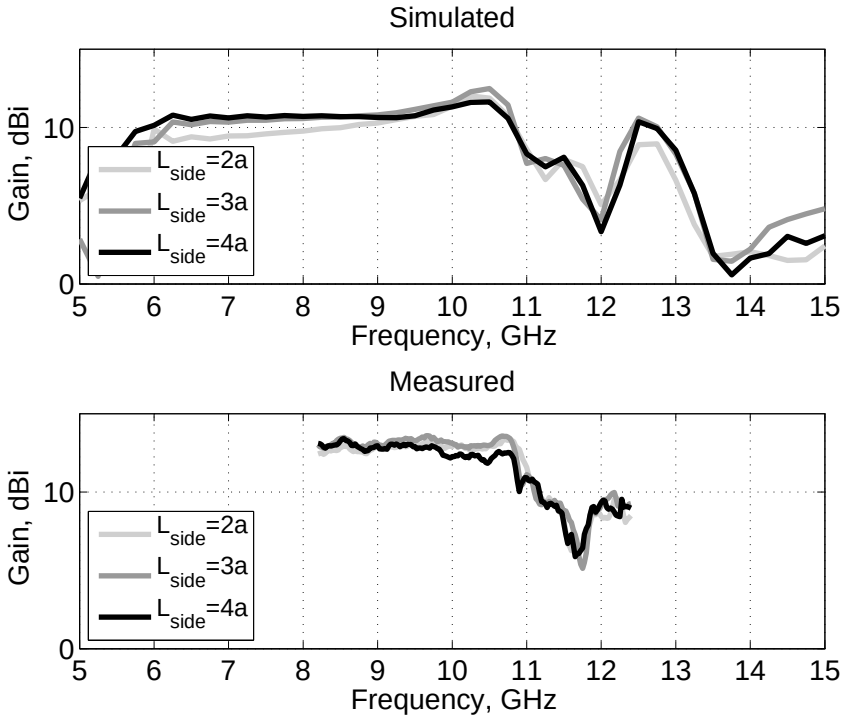

Figure 4.81: *3D TEBG* 120° *corner reflector antenna simulated and measured gain as a function of side length L.*

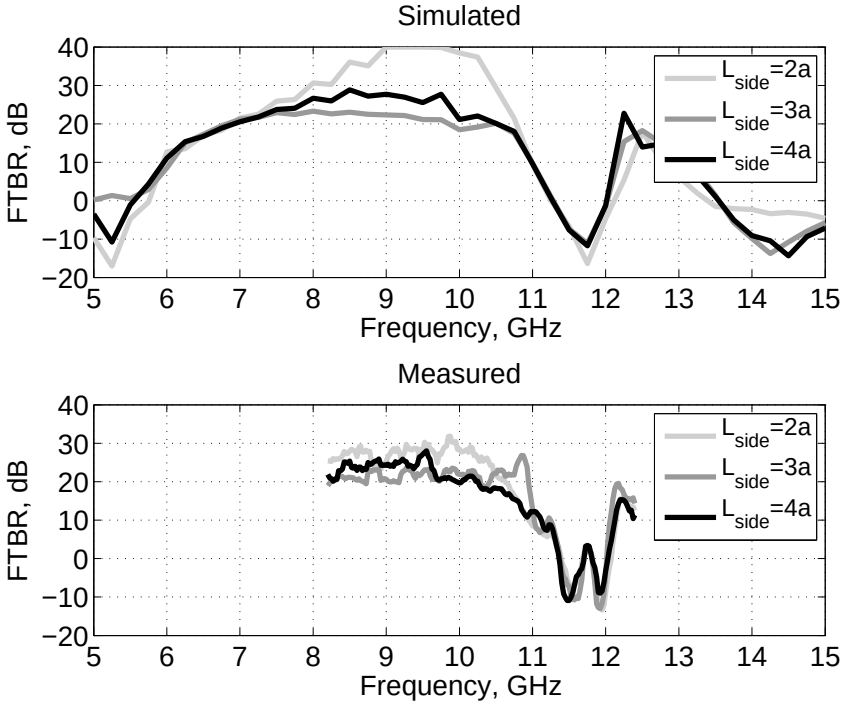

Figure 4.82: *3D TEBG* 120° *corner reflector antenna simulated and measured FTBR as a function of side length L.*

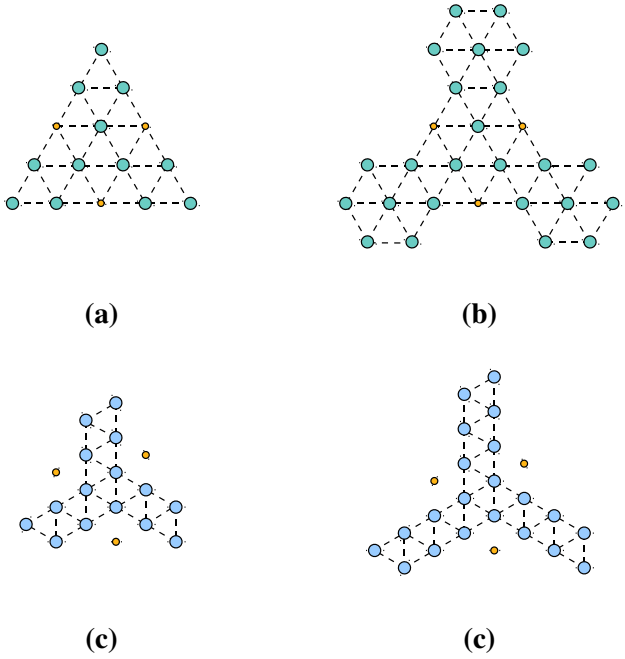

Figure 4.83: *Multiple feed TEBG corner reflector antenna geometries: a)* 60°, $L = 2 \cdot a$*; b)* 60°, $L = 3 \cdot a$*; a)* 120°, $L = 2 \cdot a$*; b)* 120°, $L = 3 \cdot a$*.*

4.3.3 Multiple feed TEBG corner reflector antennas

Multiple-feed corner TEBG antennas could be also created following the same procedure used in the previous sections, i.e. overlap multiple rotated copy of a 60° or 120° TEBG corner reflector antennas as shown in the examples depicted in figure 4.83.

As already demonstrated by multilayer and by 90° SEBG corner reflector antennas, we can expect very similar performance to the single-feed counterpart, with the addition of rotating radiation patterns by discrete angular steps according to the excited monopole feed.

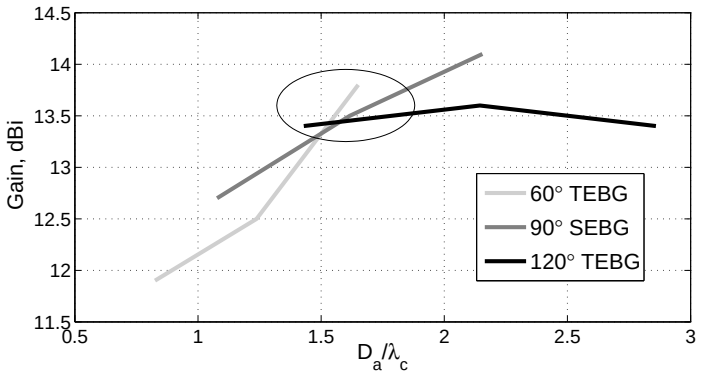

Figure 4.84: *3-D EBG corner reflector antennas measured gain as a function of corner aperture D_a, $\lambda_c = \lambda(f_c=9.5GHz)=31.5mm$):*
TEBG 60°*, a=13mm, r=1.5mm, ε_r=37 and h=20mm;*
SEBG 90°*, a=12mm, r=1.5mm, ε_r=37 and h=20mm;*
TEBG 120°*, a=13mm, r=1.5mm, ε_r=37 and h=20mm.*

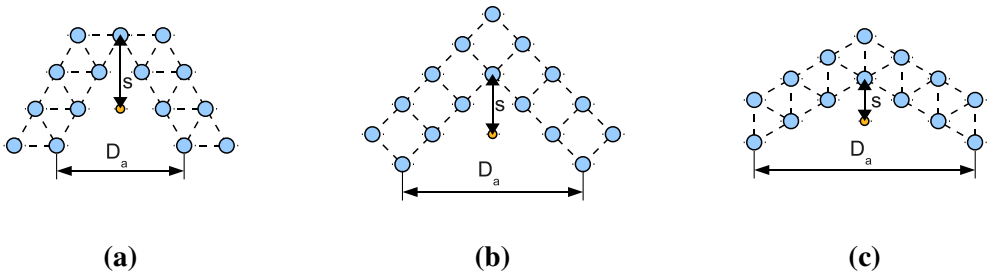

(a) **(b)** **(c)**

Figure 4.85: *3-D EBG corner reflector antenna geometries: a)* 60° *TEBG; b)* 90° *SEBG; c)* 120° *TEBG.*

4.4 EBG corner reflectors comparison

The achieved gain as a function of corner aperture dimension (normalised to the center frequency wavelength λ_c) for the 60° TEBG, 90° SEBG and 120° TEBG corner reflector antennas is shown in figure 4.84 and summarised in table 4.8; the EBG reflector antennas achieved similar gain values when the apertures had similar extension. For the former two structures, gain is linearly increasing with the aperture, whilst for the latter structure is basically constant regardless the corner aperture. Gain is influenced by the corner reflector geometry, ie side length L, corner angle α and aperture size D_a (which can be expressed as a function of the formers).

The influence of the corner side length L can be explained by analogy with metal reflectors. In figure 4.86 are shown three metal corner reflectors, respectively 60°, 90° and 120°; the feed displacement is the same as the analogous EBG counterpart, respectively $2 \cdot a \cdot \cos \pi/6$, $a \cdot \sqrt{2}$ and a. For each reflector there is a distance l from the apex to a point A located on the reflector side for which the fields excited by the source are reflected parallel to the axis. Fields reflected at points located between A and the apex, are reflected toward the axis whilst fields impinging at points located beyond A are reflected away from the

axis. Therefore, in order to optimize the amount of energy reflected toward the corner axis, the reflector side length L must be long at least l. The minimum side length l can be expressed as a function of the corner angle α:

$$l = 2 \cdot s \cdot \cos\left(\frac{\alpha}{2}\right) \tag{4.5}$$

the feed displacement s was set for all analysed EBG reflectors equal to:

$$s = 2 \cdot a \cdot \cos\left(\frac{\alpha}{2}\right) \tag{4.6}$$

therefore:

$$l = 2 \cdot 2 \cdot a \cdot \cos\left(\frac{\alpha}{2}\right) \cdot \cos\left(\frac{\alpha}{2}\right) = a \cdot \left[2 \cdot \cos\left(\frac{\alpha}{2}\right)\right]^2 \tag{4.7}$$

leading to:

$$\alpha = 60^\circ = \frac{\pi}{3} \qquad l = a \cdot \left[2 \cdot \cos\left(\frac{\pi}{6}\right)\right]^2 = a \cdot \left(2 \cdot \frac{\sqrt{3}}{2}\right)^2 = 3 \cdot a \tag{4.8}$$

$$\alpha = 90^\circ = \frac{\pi}{2} \qquad l = a \cdot \left[2 \cdot \cos\left(\frac{\pi}{4}\right)\right]^2 = a \cdot \left(2 \cdot \frac{\sqrt{2}}{2}\right)^2 = 2 \cdot a \tag{4.9}$$

$$\alpha = 120^\circ = \frac{2}{3}\pi \qquad l = a \cdot \left[2 \cdot \cos\left(\frac{\pi}{3}\right)\right]^2 = a \cdot \left(2 \cdot \frac{1}{2}\right)^2 = a \tag{4.10}$$

A side longer than l is usually required in practice to avoid the detrimental effects of fields diffracting from the corner edges. Increasing the corner side length L therefore increases

model	$L = 2 \cdot a$	$L = 3 \cdot a$	$L = 4 \cdot a$
60° TEBG	11.9 dBi ($D_a = 2 \cdot a = 0.83\lambda_c$)	12.5 dBi ($D_a = 3 \cdot a = 1.24\lambda_c$)	13.8 dBi ($D_a = 4 \cdot a = 1.65\lambda_c$)
90° SEBG	12.7 dBi ($D_a = 2 \cdot a\sqrt{2} = = 1.08\lambda_c$)	13.5 dBi ($D_a = 3 \cdot a\sqrt{2} = = 1.62\lambda_c$)	14.1 dBi ($D_a = 4 \cdot a\sqrt{2} = = 2.16\lambda_c$)
120° TEBG	13.4 dBi ($D_a = 4 \cdot a \sin \pi/3 = = 1.43\lambda_c$)	13.6 dBi ($D_a = 6 \cdot a \sin \pi/3 = = 2.14\lambda_c$)	13.4 dBi ($D_a = 8 \cdot a \sin \pi/3 = = 2.86\lambda_c$)

Table 4.8: *EBG corner reflector antennas measured gain comparison,*
$\lambda_c = \lambda(f_c{=}9.5GHz){=}31.5mm$*:*
TEBG 60°*, a=13mm, r=1.5mm,* ε_r*=37 and h=20mm;*
SEBG 90°*, a=12mm, r=1.5mm,* ε_r*=37 and h=20mm;*
TEBG 120°*, a=13mm, r=1.5mm,* ε_r*=37 and h=20mm.*

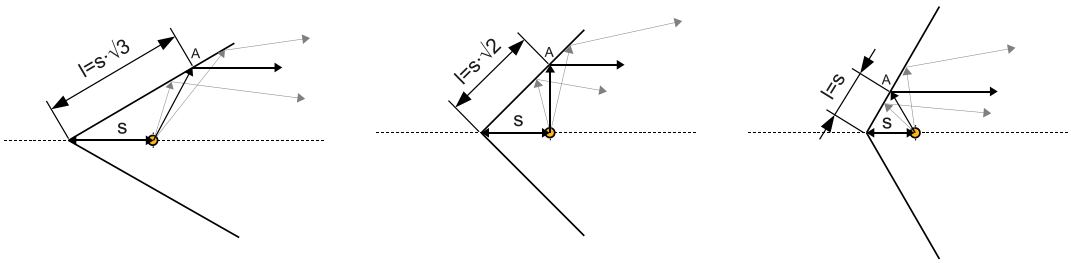

(a) **(b)** **(c)**

Figure 4.86: *Corner reflector geometries: a)* 60°*; b)* 90°*; c)* 120°.

the amount of energy reflected toward the axis and ultimately increases the gain; when L becomes greater than l though, fields impinging at points beyond l are reflected away from the axis and their influence on the gain becomes gradually smaller and eventually dies out.

Gain is also influenced by the excited fields magnitude and phase on the corner aperture D_a, which is linked to the corner side length L and angle α by:

$$D_a = 2 \cdot L \cdot \sin\left(\frac{\alpha}{2}\right) \tag{4.11}$$

for the analysed EBG reflectors:

$$\begin{aligned} \alpha = 60^\circ) \quad & D_a = L \\ \alpha = 90^\circ) \quad & D_a = \sqrt{2} \cdot L \\ \alpha = 120^\circ) \quad & D_a = \sqrt{3} \cdot L \end{aligned} \tag{4.12}$$

The electric field magnitude and phase distribution of the analysed 2-D EBG corner reflector antennas are shown in figure 4.87. In all cases the electric field magnitude is quite uniform on the aperture. For the 60° TEBG corner also the phase is quite uniform on the aperture whilst for the 120° TEBG the phase front is more curved leading to a quite variable phase on the aperture D_a; the 90° SEBG sits in an intermediate position. For a given corner aperture size D_a, small angles can provide a more uniform phase distribution leading to more directive radiation patterns but a longer side length L is generally required.

In figure 4.88 are reported the electric field magnitude and phase distribution of metal corner of analogue dimensions to the EBG corners analysed in figure 4.87: both magnitude and phase distribution are very similar inside the corners, suggesting again that EBG corners are as good as metal corners at frequencies within the bandgap although the reflection mechanism is based on different concepts. Behind the EBG corners, the phase distribution is quite "disturbed" due to the mutual interaction of the (attenuated) fields propagating through the EBG structures and diffracted at the corner edges; behind

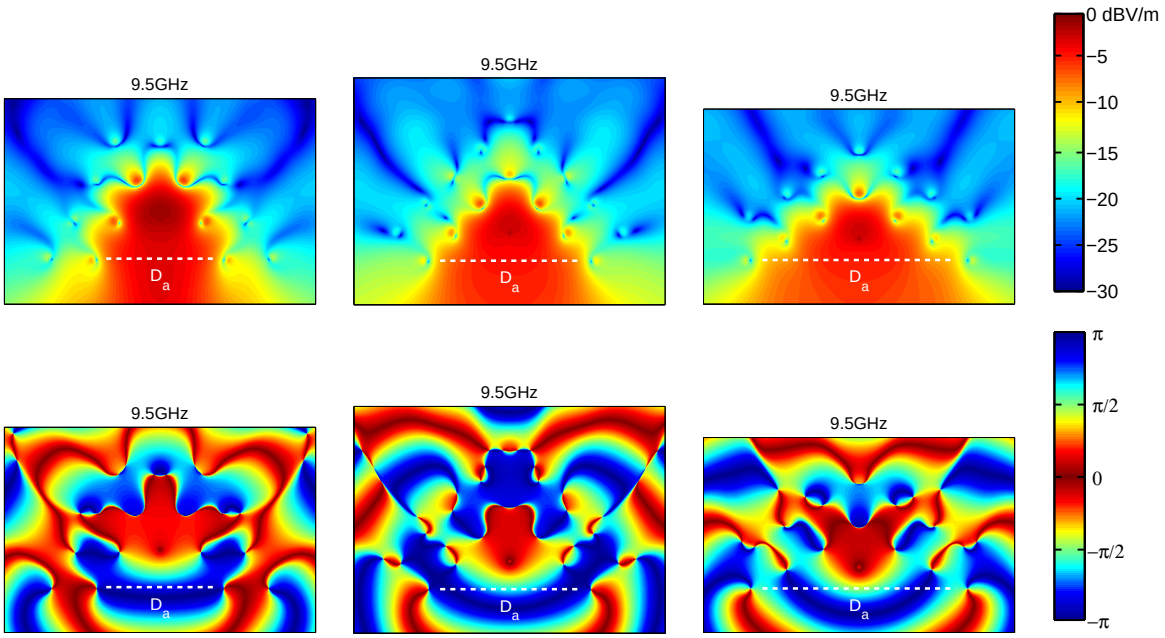

Figure 4.87: *2-D EBG corner reflector antennas, simulated electric field magnitude (above) and phase (below) distribution at f_c=9.5GHz, $L = 3 \cdot a$, $w = a$: a) 60° TEBG; b) 90° SEBG; c) 120° TEBG.*

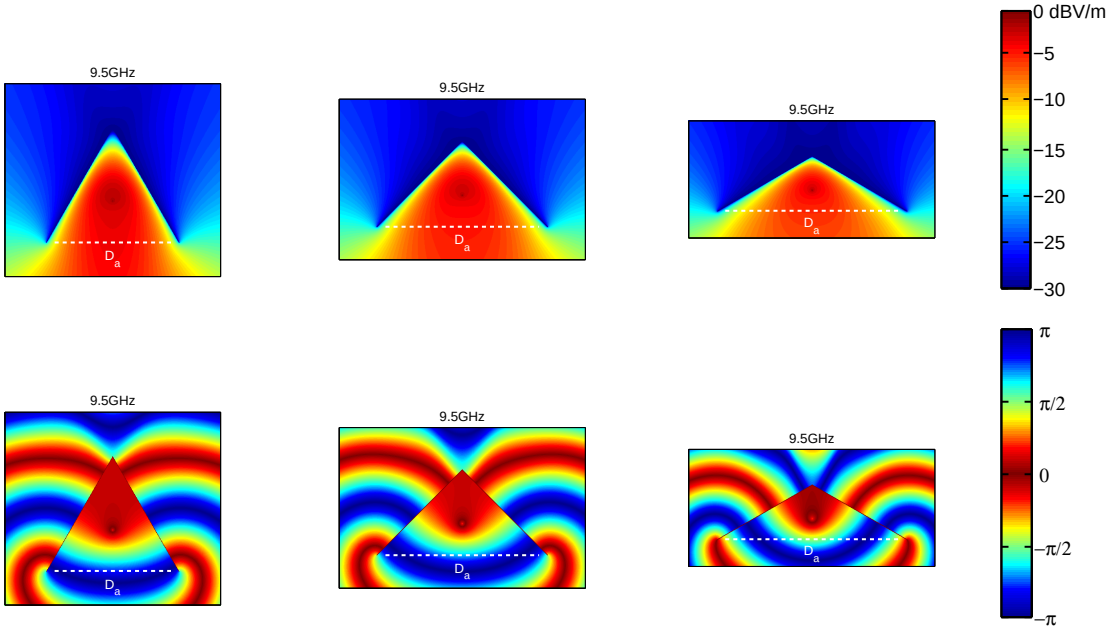

Figure 4.88: *2-D metal corner reflector antennas, simulated electric field magnitude (above) and phase (below) distribution at f_c=9.5GHz, $L = 3 \cdot a$: a) 60°; b) 90°; c) 120°.*

the metal corners the phase distribution is continuous and it is mainly associated to the diffracted fields propagating round the metal corner edges.

Therefore the gain is mainly influenced by:

- the corner side length L, in terms of amount of energy re-directed toward the axis. A minimum length l function of the corner angle α is required to optimize the amount of reflected energy;
- the corner angle α, in terms of its influence on the electric field phase and magnitude distribution on the corner aperture.

In figure 4.84 the points for which the analysed corner reflector antennas achieved similar measured performance have been enclosed by a circle; in particular the three corner antennas parameters are:

60° **TEBG:** $L = 4 \cdot a$, a=13mm, r=1.5mm, ε_r=37 and h=20mm;

90° **SEBG:** $L = 3 \cdot a$, a=12mm, r=1.5mm, ε_r=37 and h=20mm;

120° **TEBG:** $L = 2 \cdot a$, a=13mm, r=1.5mm, ε_r=37 and h=20mm;

The antennas geometries are shown in figure 4.89 and the geometrical characteristics and the achieved measured performance are summarised in table 4.9 and compared in figure 4.91 and figure 4.92. The 90° SEBG corner reflector achieved the widest impedance bandwidth, 40.4%, the 120° TEBG S_{11} response is quite similar though. The achieved gain is quite similar for all models and the measured FTBRs also presents very similar values. Radiation patterns are quiet similar at low frequencies, figure 4.92, but at high frequencies the 90° SEBG corner reflector presents the narrower beamwidth. The best overall performance, including geometrical dimensions and required number of dielectric rods, were achieved by the 120° TEBG corner reflector antenna, although the 90° SEBG model would be the best choice when narrower beamwidth are required. If the required number of rods or maximum dimensions were not an issue, the 60° TEBG and the 90° SEBG models could be used to achieve a higher gain than 120° TEBG models though, figure 4.84.

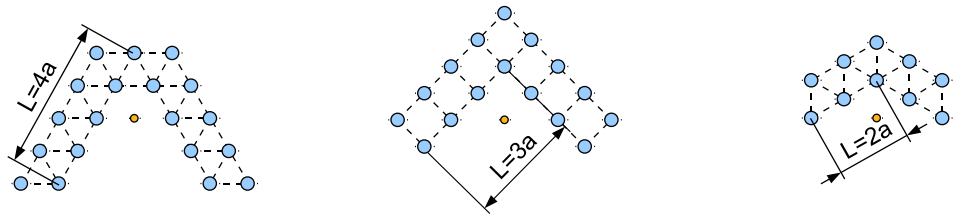

(a) **(b)** **(c)**

Figure 4.89: *3-D EBG corner reflector antenna geometries:*
a) 60° *TEBG,* $L = 4 \cdot a$*, a=13mm, r=1.5mm,* ε_r*=37 and h=20mm;*
b) 90° *SEBG,* $L = 3 \cdot a$*, a=12mm, r=1.5mm,* ε_r*=37 and h=20mm;*
c) 120° *TEBG,* $L = 2 \cdot a$*, a=13mm, r=1.5mm,* ε_r*=37 and h=20mm.*

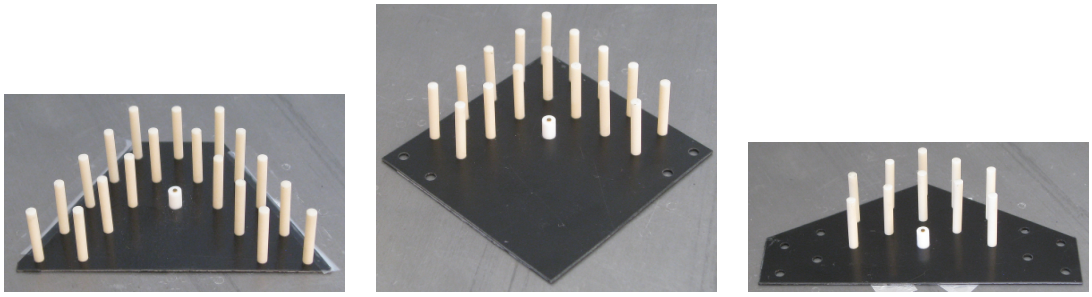

(a) **(b)** **(c)**

Figure 4.90: *3-D EBG corner reflector antenna photos:*
a) 60° *TEBG,* $L = 4 \cdot a$*, a=13mm, r=1.5mm,* ε_r*=37 and h=20mm;*
b) 90° *SEBG,* $L = 3 \cdot a$*, a=12mm, r=1.5mm,* ε_r*=37 and h=20mm;*
c) 120° *TEBG,* $L = 2 \cdot a$*, a=13mm, r=1.5mm,* ε_r*=37 and h=20mm.*

model	Gain, dBi	FTBR, dB	Bandwidth	N_{rods}	Max dim.	D_a
60° TEBG	13.8 (13.2)	28.7 (23.9)	28.4%	19	$6 \cdot a$	$4 \cdot a$
			7.7-10.2GHz		$2.48 \cdot \lambda_c$	$1.65 \cdot \lambda_c$
90° SEBG	13.5 (12.5)	29.4 (19.5)	40.4%	16	$4 \cdot a \cdot \sqrt{2}$	$3 \cdot a \cdot \sqrt{2}$
			7.5-11.4GHz		$2.15 \cdot \lambda_c$	$1.61 \cdot \lambda_c$
120° TEBG	13.4 (12.6)	31.8 (23.4)	37.9%	10	$4 \cdot a \cdot \sin \pi/3$	$4 \cdot a \cdot \sin \pi/3$
			7.7-11.3GHz		$1.43 \cdot \lambda_c$	$1.43 \cdot \lambda_c$

Table 4.9: *EBG corner reflector antennas measured performance comparison (in brackets are reported the average values within the impedance bandwidth,* $\lambda_c = \lambda_{(f_c=9.5GHz)=31.5mm}$*):*
TEBG 60°*,* $L = 4 \cdot a$*, a=13mm, r=1.5mm,* ε_r*=37 and h=20mm;*
SEBG 90°*,* $L = 3 \cdot a$*, a=12mm, r=1.5mm,* ε_r*=37 and h=20mm;*
TEBG 120°*,* $L = 2 \cdot a$*, a=13mm, r=1.5mm,* ε_r*=37 and h=20mm.*

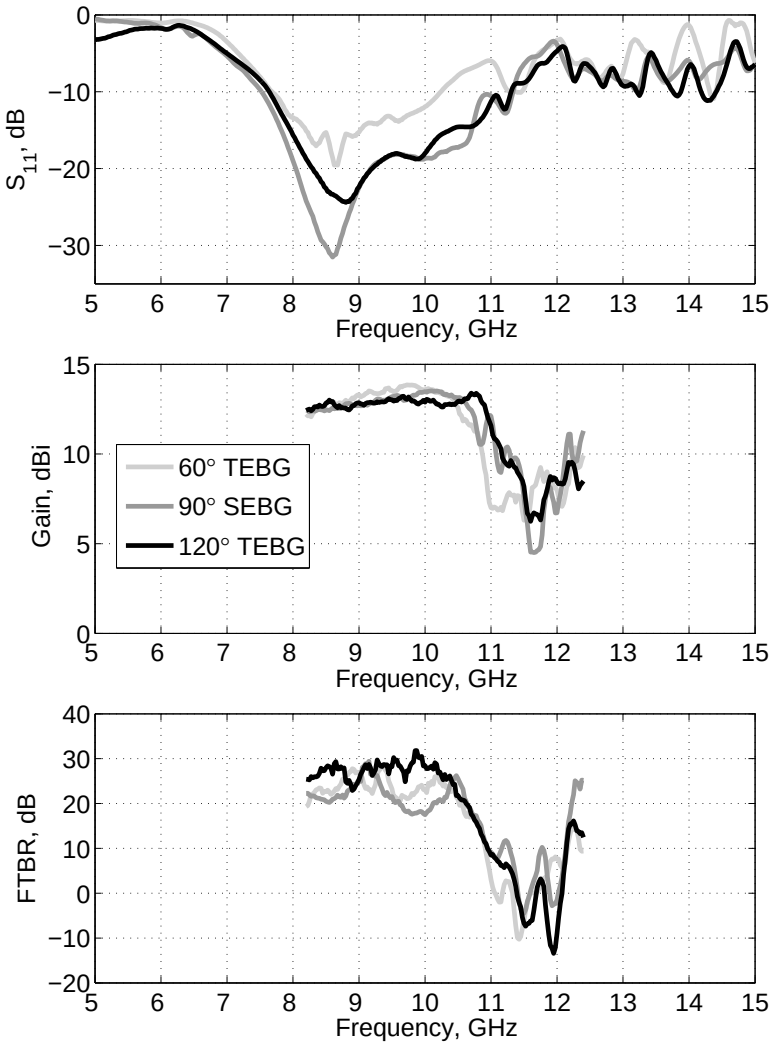

Figure 4.91: *Dielectric EBG corner reflector antennas measured S_{11}, gain and FTBR:*
TEBG 60°, $L = 4 \cdot a$, *a=13mm, r=1.5mm,* ε_r*=37 and h=20mm;*
SEBG 90°, $L = 3 \cdot a$, *a=12mm, r=1.5mm,* ε_r*=37 and h=20mm;*
TEBG 120°, $L = 2 \cdot a$, *a=13mm, r=1.5mm,* ε_r*=37 and h=20mm.*

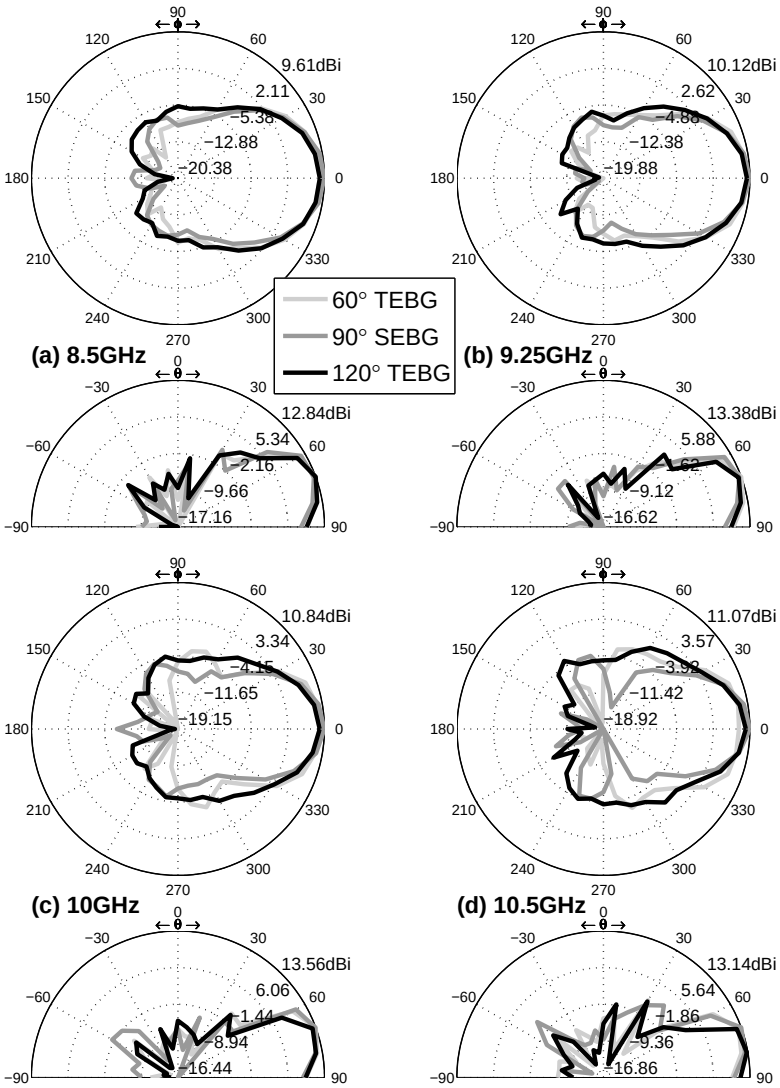

Figure 4.92: *Dielectric EBG corner reflector antennas measured radiation patterns: a) 8.5GHz; b)9.25GHz; c) 10GHz; d) 10.5GHz;*
TEBG 60°*,* $L = 4 \cdot a$*, a=13mm, r=1.5mm,* ε_r*=37 and h=20mm;*
SEBG 90°*,* $L = 3 \cdot a$*, a=12mm, r=1.5mm,* ε_r*=37 and h=20mm;*
TEBG 120°*,* $L = 2 \cdot a$*, a=13mm, r=1.5mm,* ε_r*=37 and h=20mm.*

4.5 Conclusions

Novel dielectric EBG corner reflector antennas based on ceramic rods arranged according to simple two-dimensional triangular and square lattice geometries have been presented and analysed. We focused our attention on a corner angle α equal to 60°, 90° and 120° in order to take advantage of the intrinsic geometrical properties of the triangular and square lattices. The principle of operation is the same as for metallic reflectors: at bandgap frequencies, the excited fields are reflected toward the corner aperture enhancing the radiation patterns in that privileged direction.

Several prototypes were built and tested using ceramic rods of radius r=1.5mm, length h=20mm and dielectric permittivity ε=37, achieving an impedance bandwidth greater than 30% with stable radiation patterns within, a measured gain and FTBR respectively greater than 12dBi and 25dB.

A parametric study revealed that the most influent parameter on antennas radiative performances is the feed distance from the corner apex s: an optimized feed displacement $s = 2 \cdot a \cdot \cos\left(\frac{\alpha}{2}\right)$ was found able to achieve stable and directive radiation patterns for the largest frequency range.

The influence of corner side length L was also investigated showing that, in a similar fashion to metal corner, a minimum side length $l = a \cdot \left[2 \cdot \cos\left(\frac{\alpha}{2}\right)\right]^2$ is required to optimize the amount of energy reflected toward the corner aperture D_a. The corner angle α has also an influence on the antenna performances: small angles provide a more uniform electric field phase distribution on the corner aperture D_a; a longer side length L would be required though.

A comparison between the analysed reflectors shown that the achieved gain is similar when the individual corner apertures have similar extension and, in these conditions, the best performances in terms of geometrical dimensions and required number of dielectric rods were achieved by the 120° TEBG corner reflector antenna. The 60° TEBG and the 90° SEBG models though, can be used to achieve a narrower beamwidth and a higher gain at the expense of larger geometrical dimensions and required number of dielectric rods.

Multiple-feed dielectric corner EBG antenna were also presented and investigated; these structures are created by overlapping multiple copy of a single-feed EBG corner antenna rotated by discrete angular steps according to the structure lattice geometry: 60° or 120° angular steps when using a TEBG lattice, 90° when using an SEBG lattice. A parametric study on multiple-feed 90° SEBG corner reflector antennas revealed that these structures can achieve very similar performances to the single-feed counterpart (in a similar fashion to the multiple-feed antennas presented in Chapter 3); the main addition to single-feed structure is the ability of actively rotate radiation patterns of discrete angular steps by exciting the corresponding monopole feed.

The analysed dielectric EBG reflectors were found basically equivalent (at bandgap frequencies) to metal reflectors of analogous dimensions, achieveing the same gain and very similar radiation patterns as well as very similar electric field magnitude and phase distributions inside the corner reflectors, suggesting them as possible substitutes for high frequencies applications for taking advantage of the low-loss characteristics of dielectric ceramic materials.

Chapter 5 – Discussion and Conclusion

In this work the design steps of two novel classes of EBG antennas based on dielectric EBG structures have been presented, analysed and validated by measurements. Simulations and measurements have shown that the presented structures can easily achieve a large impedance bandwidth greater than 30% with stable radiation patterns within. Radiation patterns achieved a gain greater than 12dBi with a high FTBR greater than 25dB.

Multilayer Cylindrical and Triangular EBG antennas: the first class of EBG antennas is based on a multilayer structure realised with a 2-D EBG crystal made of dielectric rods arranged according to a cylindrical (CEBG) or triangular (TEBG) geometry. A cavity is created by removing one dielectric rod and a monopole feed is placed in its stead; an angular defect window is also introduced in the EBG structure in order to allow the propagation of the excited fields (at bandgap frequencies) toward the angular defect to achieve directive radiation patterns with a high FTBR.

Multilayer CEBG antennas were developed to extend to dielectric structures the concepts presented by Boutayeb et al applied to metallic structures [43–45]. Multilayer TEBG antenna have been then developed to overcome the intrinsic limitations of the cylindrical geometry regarding electromagnetic band structure computation and hosting multiple feeds. In fact, bandgaps position and extension of a multilayer CEBG cavity structure was computed by means of the structure's transmission coefficient T, ie two simulations had to be run: one with the structure in place and one without the structure; the electric field recorded with the structure in place would be then normalised by the electric field recorded in the same point when no structure was present. A dip in the transmission coefficient T would then indicate the presence of a bandgap in that frequency range. Although this procedure predicted quite well bandgap position and extension, a series of assumptions had to be made, ie we set the separation between passband and stopband at $T = -20dB$ and we choose a four layers structure as a "standard structure" to compute T. Hosting multiple feeds is also not feasible with a cylindrical geometry built around a privileged axis: radial and transverse periodicity can be defined around only one feed; the others feeds would be in general surrounded by an asymmetryc crystal.

Multilayer TEBG antennas, compared to multilayer CEBG antennas, present a more regular geometry. Bandgaps position and extension were characterised using the same approach used for CEBG antennas as well as computing more rigorously the electromagnetic band structure of the EBG crystal using a plane-wave eigen-solver, Appendix B. The former presents the same limitations of above, ie setting a stopband threshold and a "standard structure" to compute T from; moreover, when computing the transmission coefficient T using the former approach, attention must be paid to distinguish peaks produced by resonances in the cavity from pass-band peaks between two bandgaps, Section 3.2.2. The latter is based on a sound analytical approach where the eigen-values of the unit

cell are computed, nevertheless also this approach present a limitation: the unit cell approach assumes a periodic structure of infinite dimensions. Despite the limitations of each approach, results of the two characterization methods were found in good agreement. Regarding hosting multiple feeds, a TEBG structure is not built around a privileged axis as for CEBG structures, therefore each feed would be surrounded by a crystal with the same characteristics, allowing the design of multiple feed antennas as those presented in Section 3.4.

Dielectric EBG corner reflector antennas: the second class of EBG antennas is based on a corner reflector realised with a 2-D EBG crystal made of dielectric rods arranged according to a square (SEBG) or triangular geometry. The EBG corner reflector (at bandgap frequencies) re-directs the excited fields toward the corner aperture in a similar fashion to metal corner reflector, achieving directive radiation patterns in that privileged direction.

The bandgap behaviour of the these structures has been characterised by computing the electromagnetic band structures of the crystals. The same limitation discussed above would apply, ie an infinite structure is assumed when computing the eigen-values of the unit cell; nevertheless the predicted results are in a good agreement with measurements.

The corner aperture angle α of these structures is limited by the geometry of the deployed crystal, ie it can only be an integer multiple of the angle included between the lattice vectors, ie $n \cdot \frac{\pi}{3}$ and $m \cdot \frac{\pi}{2}$ respectively for TEBG and SEBG crystals. We focused our attention on corner angles $\alpha < \pi$: we therefore considered the cases $n = 1,2$ for the TEBG crystal, corner aperture of respectively 60° and 120°, and the case $m = 1$ for the SEBG crystal, corner aperture of 90°.

It was demonstrated that EBG dielectric corner reflectors, at bandgap frequencies, are basically equivalent to metal corner reflectors of similar dimensions in terms of achieved gain and radiation patterns. The electric field magnitude and phase distribution within the corner was also found very similar.

5.1 Antennas structure review

For both classes of antennas, 2-D EBG crystals and a monopole feed have been used in order to minimise the complexity of the structure: the monopole excites fields with a vertical polarization which can be easily manipulated by an EBG structure made with a 2-D lattice of dielectric rods alligned to the electric field polarization; moreover, the monopole feed is easy to excite with a coaxial cable termination mounted on a horizontal ground plane which also offers mechanical support to the EBG structure.

The dielectric rods are kept in place by a plastic mask directly placed on the ground plane; the plastic mask has been included in all simulations although the influence on antennas performance was found practically null.

The finite size ground plane used to realize prototypes has an impact on the radiated fields: the direction of maximum gain (at bandgap frequencies) is not achieved at 0° elevation, ie $\theta = 90°$, but at an inclination angle $60° \leq \theta \leq 90°$. All simulations were run using an infinite ground plane in order to minimize the required computational effort, nonetheless the provided results were quite accurate once the ground plane influence was taken into account.

Simulations results could be also interpreted as if the electric wall symmetry introduced by the infinite ground plane was replaced by a symmetrical structure; the simulated structure is therefore equivalent to a double size structure, in terms of rods length, excited by a dipole rather than a monopole. Such a structure would present the advantage of symmetric radiation patterns on the E-plane but the realization of a prototype would be less straightforward compared to the monopole version. Moreover, a different method to hold dielectric rods in place would be needed; a possible realization could be made using a printed dipole on a low profile and low dielectric permittivity substrate (in order to minimize the interaction with the excited fields) fitted together with a single or multiple plastic masks to hold the dielectric rods together.

5.2 Geometrical parameter influence on antennas performance

An extensive geometrical parametric study, based on both simulations and measurements and focused on the geometrical parameters not related to the EBG crystal, was undertaken on the presented antennas. Multilayer CEBG and TEBG antennas were found with similar dependencies on geometrical parameters, in particular:

- the number of layers N_L has a small influence on antennas impedance matching; increasing N_L improves gain and FTBR although the difference between 2 and 3 layers is minimal suggesting 2 layers as an optimal compromise in terms of performances, geometrical dimensions and the required number of dielectric rods. The TEBG antenna shown reasonable performances even with a single layer, ie N_L=1, suggesting this configuration as a good solution if costs must be kept minimum.
- rods length h has a major impact on impedance matching and radiation patterns are usually improved by increasing rods length; it was therefore suggested that h could be set in order to optimise the achieved bandwidth and radiative performance.

Corner EBG antennas dependencies on geometrical parameters can be summarised as follow:

- rods length h has a similar impact on antennas performance as for multilayer TEBG and CEBG antennas: radiative performance and impedance matching are quite dependant on h which could be therefore used to optimise antennas performance.

- the influence of corner side length L on antennas performance was found inversely proportional to the corner angle α: 120° TEBG corner antenna performance were slightly influenced by L whilst 60° TEBG corner antenna impedance bandwidth, gain and FTBR were quite improved by increasing L.

- feed distance from the corner apex s was found the most important parameter for all EBG corner antennas: the monopole feed must be placed at the right distance s in order to achieve impedance matching and directive radiation patterns at the frequency range of interest.

A sensitivity analysis on dielectric rods position shown that the EBG crystal performance are quite robust to rods misplacement: at bandgap frequencies, antenna radiative performance were found little affected. Antennas impedence matching though, was found more sensitive to rods misplacement, leading in some cases to a substantial bandwidth reduction.

5.3 Dielectric material influence on antennas performance

We focused our attention on two dielectric materials supplied by Morgan Electroceramics: modified barium titanate (ε_r=76.5±2, $tan\delta = 0.95 \cdot 10^{-3}$) to build multilayer CEBG antennas and modified zirconium tin titanate ($\varepsilon_r = 37 \pm 1$, $tan\delta = 0.24 \cdot 10^{-3}$) to build multilayer TEBG antennas and EBG corner reflector antennas.

These materials have been chosen because they provided the best overall results in terms of impedance matching and radiative performance when used in the simulations of the basic prototypes (ceramic rods availability and cost have been also taken into consideration). Simulations though, shown that other dielectric materials (we focused our attention on ceramic materials available from Morgan Electroceramics [81], i.e. $\varepsilon_r =$ 9.8, 20, 30, 37, 43, 76.5, 88) could be used to fabricate the EBG structure and achieve good radiative performance although the realised impedance matching of the simulated basic prototype was found worse (a different or modified feed could be used to improve the impedance matching though).

The chosen dielectric material would also influence the maximum achievable operational bandwidth: in fact, regardless the realised impedance matching, the antenna would present realiable directive radiation patterns only at frequencies within the EBG structure bandgap. Therefore, the limiting factor is represented by the EBG structure bandgap(s) position and extension. Lattice geometrical properties also influence bandgaps position and extension; as a rule of thumb, in order to achieve a wide single bandgap, the ratio r/a must be ≤ 0.15 (where r is the rods radius and a is the lattice constant), figure 2.20, figure 3.3 and figure 4.4. For values of $r/a \geq 0.15$, multiple bandgaps may appear and they could be used to design multiband antennas as briefly demonstrated in Section 2.4.

In Section 3.3.5 the effects of the dielectric loss tangent on the TEBG antenna performances have been briefly analysed showing a very little impact at bandgap frequencies even for a $tan\delta$ 100 times higher then the nominal value. It was also suggested that the results could be interpreted as if the antenna (appropriately scaled in terms of geometrical dimensions and without considering all the other loss mechanisms) was operating at higher frequencies; results are therefore encouraging for low loss and high frequency applications of the presented EBG dielectric antennas. These assumptions are in good agreement with the measurements presented in [83], where the loss tangent of zirconium tin titanate ceramics was found with a nearly linear positive dependence on frequency.

5.4 Summary of advantages and disadvantages

The main advantages of the presented antennas can be summarised as follow:

- simple antenna structures easily extendable to dipole configurations;
- small number of dielectric rods required;
- small overall dimensions (typical dimensions for single feed antennas are $2\lambda_0 \times 1.3\lambda_0 \times 0.6\lambda_0$);
- EBG structures are based on simple 2-D crystals;
- low-loss ceramics can guarantee higher efficiency at high frequencies compared to metal structures. This is of particular interest for EBG corner antennas which present the same gain and very similar radiation patterns to metallic corner reflector antennas of similar dimensions;
- the EBG structures might be micromachined or integrated in LTCC (Low Temperature Co-fired Ceramic) technology although the realisation of "dielectric rods" could be problematic. Dielectric veins could be used to keep dielectric rods aligned during the fabrication process; veins would obviously have a disruptive influence on antennas performance which might be minimised by placing them on alternating symmetry axis;
- non-resonating structures: antennas present a larger operational bandwidth, $\geq 30\%$ compared to resonating structures (eg EBG superstrates placed above a ground plane with a feed in between) , usually $1-6\%$;
- multiple feed structures can be easily implemented from basic single feed antennas: the intrinsic symmetry of triangular and square lattices can be exploited by superimposing multiple single feed antennas rotated according to the lattices axis of symmetry;

- multiple feed antennas present very similar performance to their single feed counterparts, with the additional capability of rotating the radiation patterns of discrete angular steps by means of exciting the correspondent monopole feed.

The main disadvantages are:

- ceramic materials can be quite expensive compared to metallic structures;
- 2-D crystals based on dielectric rods have less mechanical rigidity compared to 3-D crystals, therefore they would require some form of support to keep dielectric rods in place;
- these antennas work only for linear polarization. Adding horizontal polarization capabilities would require a 3-D crystal and a different excitation;
- up to 10dB lower gain compared to EBG antennas based on resonating structures;

5.5 Future work

Future work could be focused on improving the performances of the presented antennas in terms of:

- impedance bandwidth: an optimised feed could be designed to achieve a wider impedance bandwidth, ideally covering the whole EBG structure bandgap, in order to maximize the operational frequency range;
- design, construction and testing of prototypes in "dipole configuration" to assess the feasibility of these structures;
- beam-scanning: the analysis and synthesys of multiple feed EBG structures with continuous beam scanning capabilities would be an interesting route to pursue in order to overcome the present limitations of fixed discrete angular steps.

Another interesting topic to consider for future work development is the realisation of linear arrays by vertically stacking multiple single feed EBG antennas with dipole configuration. Each dielectric rod could be realised in a single long piece or by stacking several shorter pieces in order to reduce mechanical fragility. Several linear arrays could be then placed side by side to realise a planar array. Multiple feed EBG antennas could be also used to realise linear arrays in a similar fashion, with the further capability of rotating radiation patterns of discrete angular steps.

As already mentioned, one of the main advantages of these structures is the low-loss characteristic of the dielectric materials used to build the EBG crystal. Such advantage is very interesting for high frequencies applications at which, for example, the EBG

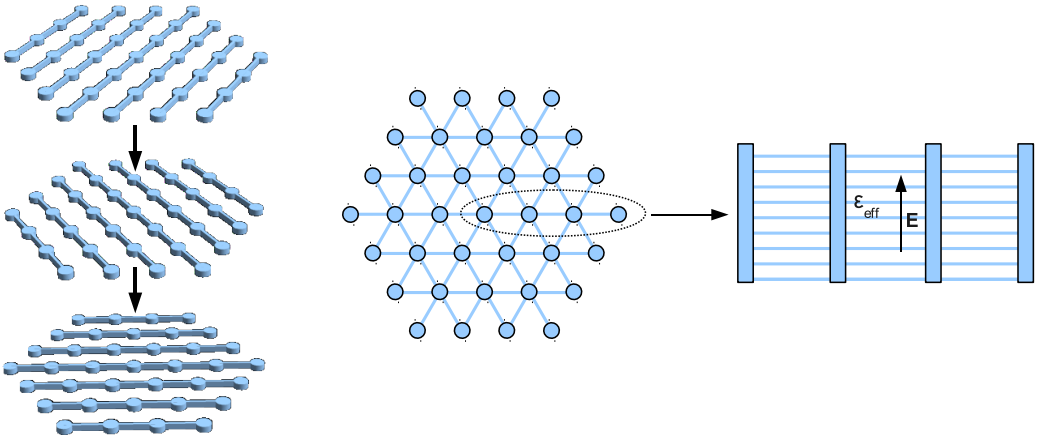

Figure 5.1: *Dielectric rods realised with connected veins.*

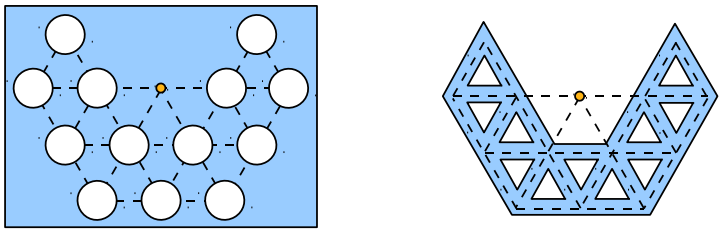

Figure 5.2: *"Dual" EBG structure for TE polarization realised with drilled holes in a dielectric block (left) or dielectric veins (right).*

structures might be manufactured and integrated in LTCC technologies [1]. Dielectric rods could be realised using veins to connect the rods sections. Veins could be placed on alternating symmetry axis in order to minimize their influence on the EBG crystal performance, figure 5.1; the electric field would be mainly perpendicular to the veins and therefore they would present a very low effective dielectric permittivity ε_{eff}. This realization would obviously require a high degree of precision although the intrinsic robustness of the analysed EBG crystals to rods misplacement would play a positive role when assessing the impact of manufacturing tolerances, LTCC tape shrinkage, etc.

Alternatively, a "dual" structure could be realised by drilling holes in a dielectric block or using dielectric veins connected according to a triangular or square geometry, figure 5.2. These structures would present a TE bandgap and therefore a different excitation would be also required: a current loop could be used (rather than a monopole/dipole) in order to excite a strong magnetic field aligned to the EBG crystal holes axis. In figure 5.3 the electromagnetic band structure for TE modes of a triangular lattice of holes and a triangular lattice of veins are shown. These structures would be also easier to manufacture compared to a lattice of dielectric rods.

Three-dimensional crystals, such as a woodpile structure, could be also used, rather than two-dimensional crystals, to design antennas with dual-polarization capabilities. An

[1] A grateful mention is due to Yves Lacrotte for his input on LTCC technologies.

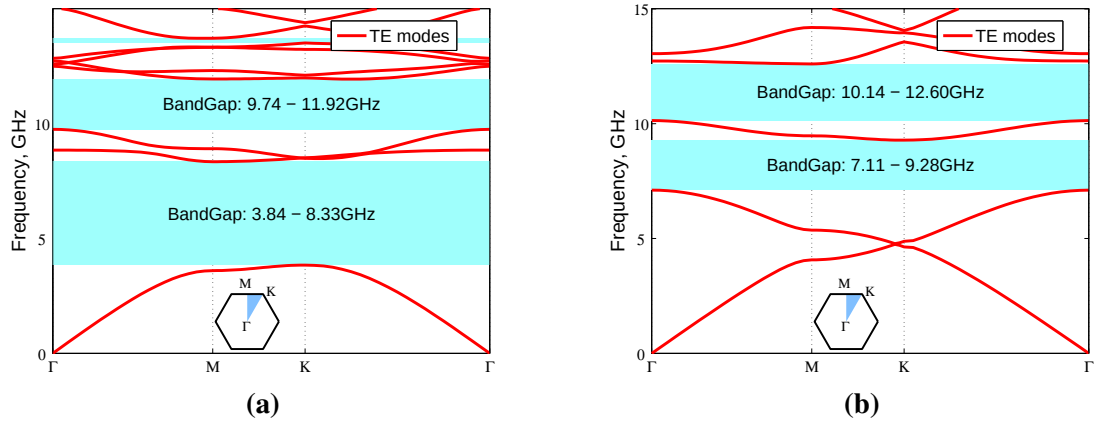

Figure 5.3: *Electromagnetic band structure for the TE modes of a two-dimensional triangular lattice of: a) holes of radius r=1.5mm drilled in a dielectric block with ε_r=37, lattice constant a=13mm; b) dielectric veins of width w=2.6mm, ε_r=37 and lattice constant a=13mm.*

alternative feeding mechanism would required to excite both polarizations: a cross dipoles configuration might be used, with both dipoles printed on a low profile and low losses substrate to minimize the impact on antenna performances.

Appendix A – The Finite-Difference Time-Domain algorithm

A.1 Introduction

The Finite-Difference Time-Domain (FDTD) technique has been widely used to solve electromagnetic problems since its first formulation made by Yee [88]. In this appendix the main characteristics of the FDTD algorithm and the main features of the in-house developed FDTD solver are presented. The FDTD solver has been coded in Matlab to take advantage of the grapich user interface as well as debug and plotting capabilities; electric and magnetic field update equations as well as near-to-far-fields transformation have been coded in C though in order to decrease the computational time.

A.2 The FDTD Algorithm

The FDTD algorithm is based on the discretization in time and space of Maxwell's equations [88–90]:

Faraday's Law:

$$\frac{\partial \mathbf{B}}{\partial t} = -\nabla \times \mathbf{E} - \mathbf{J}_m \tag{A.1}$$

$$\frac{\partial}{\partial t}\iint_S \mathbf{B}\cdot d\hat{S} = -\oint_C \mathbf{E}\cdot d\hat{l} - \iint_S \mathbf{J}_m \cdot d\hat{S} \tag{A.2}$$

Ampere's Law:

$$\frac{\partial \mathbf{D}}{\partial t} = \nabla \times \mathbf{H} - \mathbf{J}_e \tag{A.3}$$

$$\frac{\partial}{\partial t}\iint_S \mathbf{D}\cdot d\hat{S} = \oint_C \mathbf{H}\cdot d\hat{l} - \iint_S \mathbf{J}_e \cdot d\hat{S} \tag{A.4}$$

Gauss's Law for the electric field:

$$\nabla \cdot \mathbf{D} = 0 \tag{A.5}$$

$$\oiint_S \mathbf{D}\cdot d\hat{S} = 0 \tag{A.6}$$

Gauss's Law for the Magnetic field:

$$\nabla \cdot \mathbf{B} = 0 \tag{A.7}$$

$$\oiint_S \mathbf{B}\cdot d\hat{S} = 0 \tag{A.8}$$

Assuming linear, isotropic and non-dispersive materials, we can add the following constitutive equations:

$$\mathbf{B} = \mu\mathbf{H} \tag{A.9}$$

$$\mathbf{D} = \varepsilon\mathbf{E} \tag{A.10}$$

Materials with electric and magnetic losses are taken in account defining equivalent magnetic and electric currents:

$$\mathbf{J}_m = \tilde{\sigma}\mathbf{H} \tag{A.11}$$

$$\mathbf{J}_e = \sigma\mathbf{E} \tag{A.12}$$

If we substitute the relations (A.9)-(A.12) in (A.1) and (A.3), we obtain:

$$\frac{\partial \mathbf{H}}{\partial t} = -\frac{1}{\mu}\nabla \times \mathbf{E} - \frac{\tilde{\sigma}}{\mu}\mathbf{H} \tag{A.13}$$

$$\frac{\partial \mathbf{E}}{\partial t} = \frac{1}{\varepsilon}\nabla \times \mathbf{H} - \frac{\sigma}{\varepsilon}\mathbf{E} \tag{A.14}$$

which can be expanded into a system of six coupled scalar equations equivalent to Maxwell's curl equations in the three-dimensional rectangular coordinate system (x, y, z):

$$\frac{\partial H_x}{\partial t} = \frac{1}{\mu} \cdot \left(\frac{\partial E_y}{\partial z} - \frac{\partial E_z}{\partial y} - \tilde{\sigma}H_x\right) \tag{A.15}$$

$$\frac{\partial H_y}{\partial t} = \frac{1}{\mu} \cdot \left(\frac{\partial E_z}{\partial x} - \frac{\partial E_x}{\partial z} - \tilde{\sigma}H_y\right) \tag{A.16}$$

$$\frac{\partial H_z}{\partial t} = \frac{1}{\mu} \cdot \left(\frac{\partial E_x}{\partial y} - \frac{\partial E_y}{\partial x} - \tilde{\sigma}H_z\right) \tag{A.17}$$

$$\frac{\partial E_x}{\partial t} = \frac{1}{\varepsilon} \cdot \left(\frac{\partial H_z}{\partial y} - \frac{\partial H_y}{\partial z} - \sigma E_x\right) \tag{A.18}$$

$$\frac{\partial E_y}{\partial t} = \frac{1}{\varepsilon} \cdot \left(\frac{\partial H_x}{\partial z} - \frac{\partial H_z}{\partial x} - \sigma E_y\right) \tag{A.19}$$

$$\frac{\partial E_z}{\partial t} = \frac{1}{\varepsilon} \cdot \left(\frac{\partial H_y}{\partial x} - \frac{\partial H_x}{\partial y} - \sigma E_z\right) \tag{A.20}$$

This system of six coupled partial differential equations forms the basis of the FDTD numerical algorithm.

The algorithm assumes the space organized as a discrete, uniform rectangular lattice in which a point is denoted as:

$$(i, j, k) = (i\Delta x, j\Delta y, k\Delta z) \tag{A.21}$$

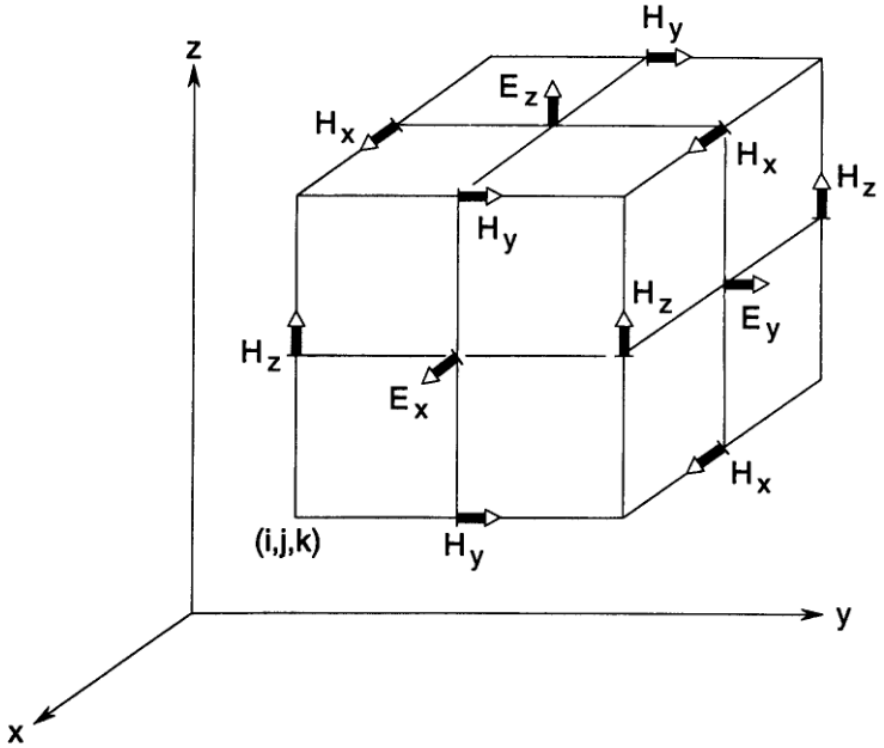

Figure A.1: *Position of the electric and magnetic field vector components about a cubic unit cell of the Yee space lattice [88].*

where Δx, Δy, Δz are the spacial increment steps in the corresponding coordinate direction and i, j and k are integer indexes. A function of the discrete space and discrete in time is denoted as:

$$u(i\Delta x, j\Delta y, k\Delta z, n\Delta t) \;=\; u^n_{i,j,k} \tag{A.22}$$

where Δt is the discrete time step indexed by the integer n. The discretization in space of Maxwell's curl equation is based on the expression of space derivatives using centered finite-differences, which yields to a second order accuracy approximation:

$$\frac{\partial u}{\partial x}(i\Delta x, j\Delta y, k\Delta z, n\Delta t) \;=\; \frac{u^n_{i+1/2,j,k} \;-\; u^n_{i-1/2,j,k}}{\Delta x} \;+\; O[(\Delta x)^2] \tag{A.23}$$

The equations are then solved for both magnetic and electric fields which, in FDTD basic formulation, are centered on a space grid as the one showed in figure A.1, hence each electric/magnetic field component is surrounded by four circulating magnetic/electric components. These configuration implicitly enforce Gauss Law relations, therefore the Yee mesh is divergence-free with respect to its electric and magnetic fields, which means the absence of free electric and magnetic charges in the modelled source-free space.

The discretization in time of Maxwell's curl equation is based on the expression of time derivatives using centered finite-differences as well, which yields again to a second

order accuracy approximation:

$$\frac{\partial u}{\partial t}(i\Delta x, j\Delta y, k\Delta z, n\Delta t) \;=\; \frac{u_{i,j,k}^{n+1/2} \;-\; u_{i,j,k}^{n-1/2}}{\Delta t} \;+\; O[(\Delta t)^2] \tag{A.24}$$

Electric and magnetic fields components are centered in time using a leapfrog arrangement: basically each time step is divided in two sub-steps: in the first sub-step electric fields components are updated using the magnetic field components calculated in the previous time step; then in the second sub-step, magnetic fields components are updated using electric fields components calculated in the previous sub-step. This process continue iteratively until the last time step. The leapfrog arrangement implies that electric field components are computed only at time $n\Delta t$, while magnetic field components only at time $(n+1/2)\Delta t$.

Using the above considerations and notations, we can now express Maxwell's equations using the FDTD approximation, omitting mathematical derivation, as:

$$\begin{aligned} m \;&=\; MEDIA_{H_x}|_{\,i,j,k} \\ H_x|_{\,i,j,k}^{\,n+1/2} \;&=\; D_a(m) H_x|_{\,i,j,k}^{\,n-1/2} \;+\; D_b(m) \;\cdot\; \begin{bmatrix} (E_y|_{\,i,j,k+1/2}^{\,n} \;-\; E_y|_{\,i,j,k-1/2}^{\,n}) \;- \\ (E_z|_{\,i,j+1/2,k}^{\,n} \;-\; E_z|_{\,i,j-1/2,k}^{\,n}) \end{bmatrix} \end{aligned} \tag{A.25}$$

$$\begin{aligned} m \;&=\; MEDIA_{E_x}|_{\,i,j,k} \\ E_x|_{\,i,j,k}^{\,n+1} \;&=\; C_a(m) E_x|_{\,i,j,k}^{\,n} \;+\; C_b(m) \;\cdot\; \begin{bmatrix} (H_z|_{\,i,j+1/2,k}^{\,n+1/2} \;-\; H_z|_{\,i,j-1/2,k}^{\,n+1/2}) \;- \\ (H_y|_{\,i,j,k+1/2}^{\,n+1/2} \;-\; H_y|_{\,i,j,k-1/2}^{\,n+1/2}) \end{bmatrix} \end{aligned} \tag{A.26}$$

where:

$$D_a(m) \;=\; \left(\frac{1 - \frac{\tilde{\sigma}(m)\Delta t}{2\mu(m)}}{1 + \frac{\tilde{\sigma}(m)\Delta t}{2\mu(m)}} \right) \tag{A.27}$$

$$D_b(m) \;=\; \frac{\left(\frac{\Delta t}{\mu(m)\Delta} \right)}{\left(1 + \frac{\sigma(m)\Delta t}{2\mu(m)} \right)} \tag{A.28}$$

$$C_a(m) \;=\; \left(\frac{1 - \frac{\sigma(m)\Delta t}{2\varepsilon(m)}}{1 + \frac{\sigma(m)\Delta t}{2\varepsilon(m)}} \right) \tag{A.29}$$

$$C_b(m) \;=\; \frac{\left(\frac{\Delta t}{\varepsilon(m)\Delta} \right)}{\left(1 + \frac{\sigma(m)\Delta t}{2\varepsilon(m)} \right)} \tag{A.30}$$

Only E_x and H_x have been shown, but similar expressions are derived for the other components. Coefficients (A.27)-(A.30) are point-wise constant, therefore they can be

calculated and stored before the time-stepping begins. The index m is used to address the electrical properties of the specific material when M different materials are present in the computational domain.

Once all the coefficients are computed, the algorithm is ready to start. The last parameter that need to be carefully chosen is the time step increment Δt. It can be mathematically proved that, in order to be stable, the algorithm time step increments, for a uniform cubic lattice, has to respect the constraint:

$$\Delta t \leqslant \frac{1}{v_{max}\sqrt{\frac{1}{(\Delta x)^2}+\frac{1}{(\Delta y)^2}+\frac{1}{(\Delta z)^2}}} = \frac{1}{v_{max}\sqrt{\frac{1}{\Delta^2}+\frac{1}{\Delta^2}+\frac{1}{\Delta^2}}} = \\ = \frac{1}{v_{max}\sqrt{\frac{3}{\Delta^2}}} = \frac{\Delta}{v_{max}\sqrt{3}} \tag{A.31}$$

where Δ is the spacial step and v_{max} is the maximum light speed in the modelled media. This constraint is known as the "Courant limit". It can also be shown that numerical dispersion is minimized (but not eliminated) by operating at the Courant limit, therefore FDTD codes should run as close as possible to the Courant limit.

Reduction to 2D and 1D: assuming that field excitation and modelled geometry have no variation along one or two coordinate directions, the presented 3D algorithm can be easily reduced respectively to 2D and 1D implementations. All the above computational considerations are still valid, with the exception of Courant limit, which for uniform lattice of n dimensions can be shown to be:

$$\Delta t \leqslant = \frac{\Delta}{v_{max}\sqrt{n}} \tag{A.32}$$

A.3 Absorbing Boundary Conditions

The last issue which is needed to be taken in account is the computational domain boundaries. Many geometries of interest are defined in open regions where the spatial domain of the computed field is unbounded in one or more coordinate directions. It's clearly impossible to define an infinite computational domain. Hence the computational domain must be chosen big enough to contain the structure of interest and appropriate boundary conditions (Absorbing Boundary Conditions - ABCs) must be applied on the outer perimeter of the domain in order to simulate its extension to infinity. The reason that computational domain needs proper ABCs is that if we just truncate the lattice we are "physically" assuming fields equal to zero out of the boundary, which might not be the real physical configuration of the implemented problem. Many different ABCs can be found in literature, each of them with different characteristics and suitable applications, nonetheless the concept behind is always the same: truncating the space lattice to computational

feasible dimension and minimizing the numerical error introduced by such truncation. Therefore, ABCs are fundamental for the correct truncation of the space lattice: they have to guarantee minimal reflection (zero in theory) of the impinging wave for any angle of incidence. The implemented ABCs are the Uniaxial Perfectly Matched Layer (UPML) ABCs [89, 91, 92].

It can be shown that given a plane wave incident on a half-space with an interface in a $w = constant$ plane and composed of a uniaxial medium with the permittivity and permeability tensors:

$$\bar{\bar{\varepsilon}}_2 = \varepsilon_1 \bar{\bar{s}} \tag{A.33}$$

$$\bar{\bar{\mu}}_2 = \mu_1 \bar{\bar{s}} \tag{A.34}$$

$$\bar{\bar{s}} = \begin{bmatrix} s_w^{-1} & 0 & 0 \\ 0 & s_w & 0 \\ 0 & 0 & s_w \end{bmatrix} \tag{A.35}$$

the plane wave is purely transmitted in the uniaxial medium independently of the angle of incidence, polarization and frequency. Extending this approach to a generalized three-dimensional formulation, inside the UPML region, Maxwell's curl equations can be written as:

$$\nabla \times \breve{\mathbf{H}} = j\omega\varepsilon \bar{\bar{s}}\, \breve{\mathbf{E}} \tag{A.36}$$

$$\nabla \times \breve{\mathbf{E}} = -j\omega\mu \bar{\bar{s}}\, \breve{\mathbf{H}} \tag{A.37}$$

where S is the diagonal tensor defined as:

$$\bar{\bar{s}} = \begin{bmatrix} s_x^{-1} & 0 & 0 \\ 0 & s_x & 0 \\ 0 & 0 & s_x \end{bmatrix} \begin{bmatrix} s_y & 0 & 0 \\ 0 & s_y^{-1} & 0 \\ 0 & 0 & s_y \end{bmatrix} \begin{bmatrix} s_z & 0 & 0 \\ 0 & s_z & 0 \\ 0 & 0 & s_z^{-1} \end{bmatrix} = \begin{bmatrix} s_x^{-1} s_y s_z & 0 & 0 \\ 0 & s_x s_y^{-1} s_z & 0 \\ 0 & 0 & s_x s_y s_z^{-1} \end{bmatrix} \tag{A.38}$$

with

$$s_x = k_x + \frac{\sigma_x}{j\omega\varepsilon}; \qquad s_y = k_y + \frac{\sigma_y}{j\omega\varepsilon}; \qquad s_z = k_z + \frac{\sigma_z}{j\omega\varepsilon} \tag{A.39}$$

We can divide the computational domain in different regions, figure A.2, according to the different values assigned to k_w and σ_w in each particular region:

- Lossless isotropic interior region: in this region the tensor S is equal to the unity tensor, ie $\sigma_w = 0$ and $k_w = 1$;
- UPML absorbers in the Outer-Boundary planes: in the w outer-boundary plane,

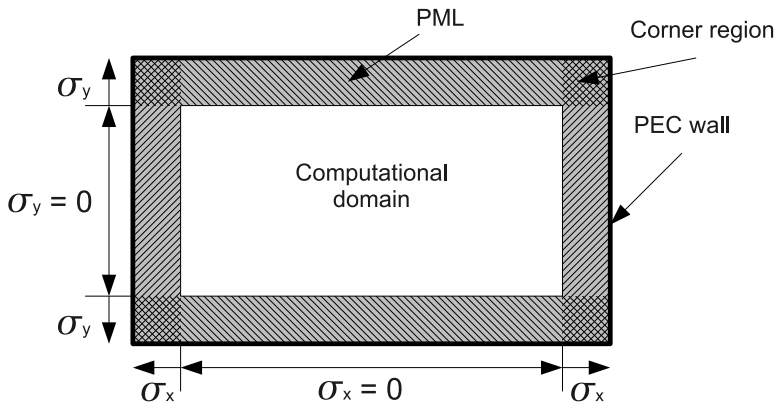

Figure A.2: *Computational domain division in UPML regions.*

only σ_w is not equals to zero. All k_w are equal to 1;

- UPML absorbers in the Dihedral Corners: in the $w-t$ dihedral corner, σt and σ_w are not zero and all k_w are equal to 1;
- UPML absorbers in the Trihedral Corners: in these regions all σ_w are not zeros and all k_w are equal to 1;
- PEC wall: the computational domain is assumed to be surrounded by PEC walls.

The reflection error introduced by a PML of thickness d for a given angle of incidence θ is:

$$R(\theta) \;=\; e^{-2\sigma_w \eta d \cos(\theta)} \tag{A.40}$$

where η and θ are respectively the PML's characteristic wave impedance and conductivity. The error is maximum for an angle of incidence $\theta = 90$ degrees. To reduce the error on a given thickness, conductivity needs to be properly set because a too large value of σ_w will introduce spurious reflection in the free space region whilst a too small value would not be effective. A good solution is grading σ_w from zero at the interface $w = 0$, to its maximum value at $w = d$. The introduced error is then:

$$R(\theta) \;=\; e^{-2\sigma_w \eta \cos(\theta) \int_0^d \sigma_w dw} \tag{A.41}$$

The conductivity grading usually follows a polynomial profile:

$$\sigma_w(w) \;=\; (w/d)^m \sigma_{w,\,Max} \tag{A.42}$$

$$k_w(w) \;=\; 1 + (k_{w,\,Max} - 1) \cdot (w/d)^m \tag{A.43}$$

The reflection error can be calculated substituting (A.42) in (A.41), which yields to:

$$R(\theta) \;=\; e^{-2\sigma_{w,\,Max}\eta d\cos(\theta)/(m+1)} \tag{A.44}$$

Given a thickness d and a maximum error $R(0)$, we can calculate the optimal $\sigma_{w,\,Max}$ as :

$$\sigma_{w,\,Max} \;=\; -\frac{(m+1)\ln[R(0)]}{2\eta d} \tag{A.45}$$

Even when using graded profile, the error cannot be completely eliminated. In fact increasing too much the conductivity will introduce anyway spurious reflections, while increasing the thickness increases the computational effort. The recommended value for the exponent is $3 < m < 4$ (in this implementation, 4 has been used), while for a PML region of 10 cells thickness the optimal $\sigma_{w,\,opt}$ for a typical error $R(0) \;=\; e^{-16}$ is:

$$\sigma_{w,\,opt} \;=\; -\frac{(m+1)\cdot(-16)}{2\eta d} \;=\; \frac{8(m+1)}{\eta(n\Delta)} \;=\; \frac{0.8(m+1)}{\eta\Delta} \tag{A.46}$$

Using the above considerations and notations and omitting mathematical derivation, UPML Finite-Difference expressions can be derived (only shown for E_x):

$$D_x|^{n+1}_{i+1/2,j,k} \;=\; C_1(j)\;\cdot\; D_x|^{n}_{i+1/2,j,k} \;+\; C_2(j)\;\cdot \left(\frac{H_z|^{\,n+1/2}_{\,i+1/2,j+1/2,k} \;-\; H_z|^{\,n+1/2}_{\,i+1/2,j-1/2,k}}{\Delta y} \;-\; \frac{H_y|^{\,n+1/2}_{\,i+1/2,j,k+1/2} \;-\; H_y|^{\,n+1/2}_{\,i+1/2,j,k-1/2}}{\Delta z}\right) \tag{A.47}$$

$$E_x|^{\,n+1}_{\,i+1/2,j,k} \;= C_3(k)\;\cdot\; E_x|^{\,n}_{\,i+1/2,j,k} \;+\; C_4(k)\;\cdot \Big[C_5(i)\;\cdot\; D_x|^{\,n+1}_{\,i+1/2,j,k} \;-\; C_6(i)\;\cdot\; D_x|^{\,n}_{\,i+1/2,j,k}\Big] \tag{A.48}$$

where:

$$C_1(j) = \frac{2\varepsilon k_y(j) - \sigma_y(j)\Delta t}{2\varepsilon k_y(j) + \sigma_y(j)\Delta t} \tag{A.49}$$

$$C_2(j) = \frac{2\varepsilon \Delta t}{2\varepsilon k_y(j) + \sigma_y(j)\Delta t} \tag{A.50}$$

$$C_3(k) = \frac{2\varepsilon k_z(k) - \sigma_z(k)\Delta t}{2\varepsilon k_z(k) + \sigma_z(k)\Delta t} \tag{A.51}$$

$$C_4(k) = \frac{1}{[2\varepsilon k_z(k) + \sigma_z(k)\Delta t]\varepsilon} \tag{A.52}$$

$$C_5(i) = 2\varepsilon k_x(i) + \sigma_x(i)\Delta t \tag{A.53}$$

$$C_6(i) = 2\varepsilon k_x(i) - \sigma_x(i)\Delta t \tag{A.54}$$

The price to pay for UPML implementation is that two update equations have to be computed for each fields components, whilst in the FDTD standard formulation only one is needed. This implies doubling the computational effort and computational time. This is true in the PML regions, but in the working space, standard FDTD update equations can be used. Using this approach the PML computational effort is very small compared to the working volume's.

A.4 Near to far fields transformation

Near to far fields transformation is implemented using the equivalence principle and following the procedure presented in [74]. Symmetries can be used when to halve the computational domain using PMC or PEC symmetry planes for example when an infinite ground plane is assumed to be present. Electric and magnetic equivalent surface currents are calculated using electric and magnetic fields tangential to a fictitious rectangular surface surrounding the structure of interest (shown in figure A.3):

$$\mathbf{J}_s = \hat{n} \times \mathbf{H} = \hat{n} \times (\hat{a}_x H_x + \hat{a}_y H_y + \hat{a}_z H_z) \tag{A.55}$$

$$\mathbf{M}_s = -\hat{n} \times \mathbf{E} = -\hat{n} \times (\hat{a}_x E_x + \hat{a}_y E_y + \hat{a}_z E_z) \tag{A.56}$$

The field components used in the above expressions are intended to be in the frequency domain, therefore the time domain fields components need to be transformed by DFT to frequency domain, shown for the H_x component:

$$H_x(\omega_i) = \frac{1}{N_t} \sum_{n=1}^{N_t} H_x(n\Delta t) e^{-jn\Delta t\,\omega_i} \tag{A.57}$$

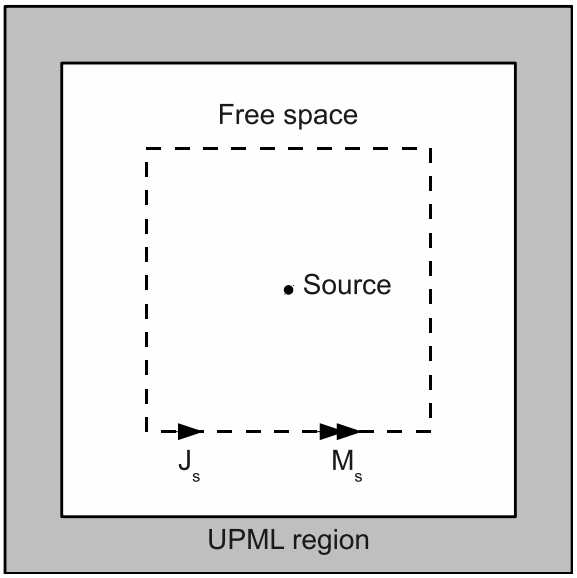

Figure A.3: *Fictitious surface on which equivalent sources are computed.*

This can be easily done on-the-fly introducing a very small computational overhead; in fact, given a ω_i set of frequencies at which the near to far field transformation is needed, the on-the-fly DFT is computed at each time step n for each ω_i as:

$$H_x(\omega_i) \;=\; H_x(\omega_i) \;+\; H_x(n\Delta t)e^{-jn\Delta t\,\omega_i} \tag{A.58}$$

at the end of the time-stepping, H_x needs to be normalized, i.e. divided by the number of time steps N_t.

Once all the frequency domain field components are ready, the equivalent sources can be calculated using (A.55) and (A.56). The far fields, with respect to figure A.4, are then computed using the vector potentials equations:

$$E_\theta \;=\; -\frac{jke^{-jkr}}{4\pi r}(L_\phi \;+\; \eta N_\theta) \tag{A.59}$$

$$E_\phi \;=\; \frac{jke^{-jkr}}{4\pi r}(L_\theta \;-\; \eta N_\phi) \tag{A.60}$$

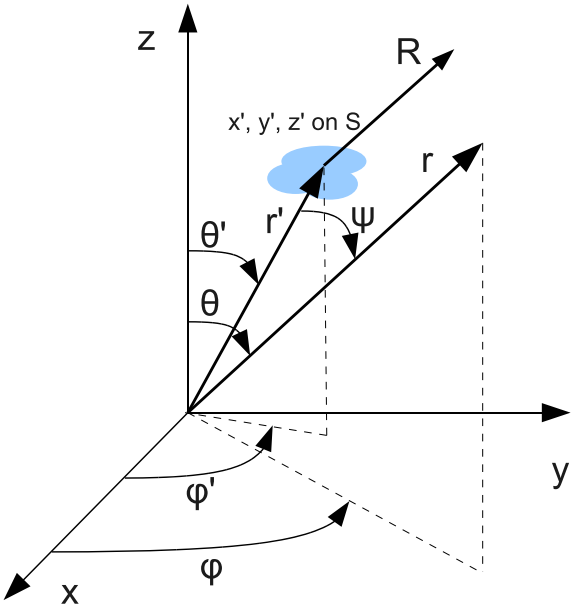

Figure A.4: *Coordinate system for near to far field transformation [74].*

with:

$$N_\theta = \iint_S [J_x \cos\theta\cos\phi + J_y \cos\theta\sin\phi - J_z \sin\theta] e^{jkr'\cos\psi} ds' \tag{A.61}$$

$$N_\phi = \iint_S [-J_x \sin\phi + J_y \cos\phi] e^{jkr'\cos\psi} ds' \tag{A.62}$$

$$L_\theta = \iint_S [M_x \cos\theta\cos\phi + M_y \cos\theta\sin\phi - M_z \sin\theta] e^{jkr'\cos\psi} ds' \tag{A.63}$$

$$L_\phi = \iint_S [-M_x \sin\phi + M_y \cos\phi] e^{jkr'\cos\psi} ds' \tag{A.64}$$

where ψ is the angle between the vectors r and r' as shown in figure A.4. The integrals in (A.61)-(A.64) are numerically computed using summations.

The antenna directivity D is then calculated using:

$$D(\theta,\phi) = 4\pi \frac{U(\theta,\phi)}{P_{rad}} \tag{A.65}$$

where radiation intensity U and radiated power P_{rad} are given by:

$$U(\theta,\phi) = \frac{1}{2\eta}(|E_\theta|^2 + |E_\phi|^2) \tag{A.66}$$

$$P_{rad} = \oiint_\Omega U(\theta,\phi) d\Omega = \int_0^{2\pi}\int_0^{\pi} U(\theta,\phi)\sin\theta d\theta d\phi \tag{A.67}$$

Appendix B – The Plane-Wave Eigensolver

B.1 Introduction

In this appendix the algorithm of the planewave eigen-solver used to compute the photonic band structure of the triangular and square lattices shown in Chapter 3 and Chapter 4 is presented along with general concepts on photonic crystals. Since the EBG crystals we used are only made of dielectric materials, we followed the approach used for photonic crystals in [2] and [93].

B.2 Dielectric function and the reciprocal space

The dielectric permittivity spatial distribution of an infinite periodic structure can be expressed by the periodic function:

$$\varepsilon(\mathbf{r}) = \varepsilon(\mathbf{r}+\mathbf{R}) \tag{B.1}$$

where $\mathbf{r}$ is a 3-D vector in the coordinate space and $\mathbf{R}$ is the set of lattice vectors. The dielectric function can be Fourier-expanded in the wave vector domain:

$$\varepsilon(\mathbf{r}) = \int g(\mathbf{k}) \cdot e^{j\cdot\mathbf{k}\cdot\mathbf{r}} d\mathbf{k} \tag{B.2}$$

We can substitute (B.1) in (B.2):

$$\varepsilon(\mathbf{r+R}) = \int g(\mathbf{k}) \cdot e^{j\cdot\mathbf{k}\cdot\mathbf{r}} \cdot e^{j\cdot\mathbf{k}\cdot\mathbf{R}} d\mathbf{k} = \varepsilon(\mathbf{r}) = \int g(\mathbf{k}) \cdot e^{j\cdot\mathbf{k}\cdot\mathbf{r}} d\mathbf{k} \tag{B.3}$$

Equation (B.3) is true when $g(\mathbf{k}) = 0$ or $e^{(j\cdot\mathbf{k}\cdot\mathbf{R})} = 1$, ie $g(\mathbf{k}) = 0$ everywhere except for those values of $\mathbf{k}$ which satisfy the condition $e^{(j\cdot\mathbf{k}\cdot\mathbf{R})} = 1$ for any lattice vector $\mathbf{R}$. The wave vectors $\mathbf{k}$ which satisfy the condition $\mathbf{G}\cdot\mathbf{R} = n2\pi$, where n is an integer, are called reciprocal lattice vectors $\mathbf{G}$ and they form their own periodic lattice. The dielectric function expansion can be then expressed as:

$$\varepsilon(\mathbf{r}) = \sum_{\mathbf{G}} g_{\mathbf{G}} \cdot e^{j\cdot\mathbf{G}\cdot\mathbf{r}} \tag{B.4}$$

where $g_{\mathbf{G}}$ are the coeeficients of the corrisponding plane waves.

The reciprocal lattice vectors $\mathbf{G}$ can be calculated imposing the condition $\mathbf{G}\cdot\mathbf{R} = n2\pi$ when $\mathbf{R}$ and $\mathbf{G}$ are expressed in terms of their primitive vectors:

$$\mathbf{R} = l\mathbf{a}_1 + m\mathbf{a}_2 + n\mathbf{a}_3$$

$$\mathbf{G} = l'\mathbf{b}_1 + m'\mathbf{b}_2 + n'\mathbf{b}_3 \tag{B.5}$$

where $\mathbf{a}_i$ and $\mathbf{b}_i$ are respectively the primitive vectors of $\mathbf{R}$ and $\mathbf{G}$, leading to:

$$\mathbf{G}\cdot\mathbf{R} = (l\mathbf{a}_1 + m\mathbf{a}_2 + n\mathbf{a}_3)(l'\mathbf{b}_1 + m'\mathbf{b}_2 + n'\mathbf{b}_3) = n2\pi \tag{B.6}$$

The above can be easily satisfied if we construct the $\mathbf{b}_i$ according to:

$$\mathbf{a}_i \cdot \mathbf{b}_j = 2\pi\delta_{ij} \tag{B.7}$$

with $\delta_{ij} = 1$ when $i = j$ and $\delta_{ij} = 0$ when $i \neq j$, leading to:

$$\begin{aligned}
\mathbf{b}_1 &= 2\pi\frac{\mathbf{a}_2 \times \mathbf{a}_3}{\mathbf{a}_1 \cdot (\mathbf{a}_2 \times \mathbf{a}_3)} \\
\mathbf{b}_2 &= 2\pi\frac{\mathbf{a}_3 \times \mathbf{a}_1}{\mathbf{a}_1 \cdot (\mathbf{a}_2 \times \mathbf{a}_3)} \\
\mathbf{b}_3 &= 2\pi\frac{\mathbf{a}_1 \times \mathbf{a}_2}{\mathbf{a}_1 \cdot (\mathbf{a}_2 \times \mathbf{a}_3)}
\end{aligned} \tag{B.8}$$

The lattice vectors of the 2-D triangular and square lattices analysed in Chapter 3 and Chapter 4, figure B.1, respectively are:

Triangular lattice

$$\begin{aligned}
\mathbf{a}_{1T} &= \frac{a_T}{2}\left(\hat{\mathbf{x}}\sqrt{3} + \hat{\mathbf{y}}\right) \\
\mathbf{a}_{2T} &= \frac{a_T}{2}\left(\hat{\mathbf{x}}\sqrt{3} - \hat{\mathbf{y}}\right)
\end{aligned} \tag{B.9}$$

Square lattice

$$\begin{aligned}
\mathbf{a}_{1S} &= a_S\hat{\mathbf{x}} \\
\mathbf{a}_{2S} &= a_S\hat{\mathbf{y}}
\end{aligned} \tag{B.10}$$

where a_T and a_S are respectively the triangular and square lattice constants and $\hat{\mathbf{x}}$ and $\hat{\mathbf{y}}$ being the cartesian unit vectors. Using (B.8) with the primitive vector $\mathbf{a}_3$ of an arbitrary length (there is no variation along the z direction), we can calculate the primitive

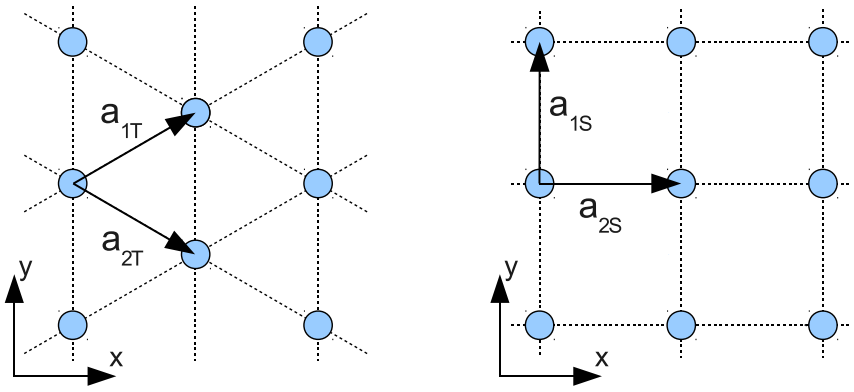

Figure B.1: *2-D crystals: a) triangular lattice of dielectric rods; b) square lattice of dielectric rods.*

reciprocal vectors for the triangular and square reciprocal lattices:

Reciprocal triangular lattice

$$\mathbf{b}_{1T} = 2\pi\frac{\mathbf{a}_{2T}\times\hat{\mathbf{z}}}{\mathbf{a}_{1T}\cdot(\mathbf{a}_{2T}\times\hat{\mathbf{z}})} = 2\pi\frac{\frac{a_T}{2}\left(\hat{\mathbf{x}}\sqrt{3}-\hat{\mathbf{y}}\right)\times\hat{\mathbf{z}}}{\frac{a_T}{2}\left(\hat{\mathbf{x}}\sqrt{3}+\hat{\mathbf{y}}\right)\cdot\left(\frac{a_T}{2}\left(\hat{\mathbf{x}}\sqrt{3}-\hat{\mathbf{y}}\right)\times\hat{\mathbf{z}}\right)} = \\ = \frac{2\pi}{a_T}\left(\hat{\mathbf{x}}\frac{\sqrt{3}}{3}+\hat{\mathbf{y}}\right)$$

$$\mathbf{b}_{2T} = 2\pi\frac{\hat{\mathbf{z}}\times\mathbf{a}_{1T}}{\mathbf{a}_{1T}\cdot(\mathbf{a}_{2T}\times\hat{\mathbf{z}})} = 2\pi\frac{\hat{\mathbf{z}}\times\frac{a_T}{2}\left(\hat{\mathbf{x}}\sqrt{3}+\hat{\mathbf{y}}\right)}{\frac{a_T}{2}\left(\hat{\mathbf{x}}\sqrt{3}+\hat{\mathbf{y}}\right)\cdot\left(\frac{a_T}{2}\left(\hat{\mathbf{x}}\sqrt{3}-\hat{\mathbf{y}}\right)\times\hat{\mathbf{z}}\right)} = \\ = \frac{2\pi}{a_T}\left(\hat{\mathbf{x}}\frac{\sqrt{3}}{3}-\hat{\mathbf{y}}\right)$$

Reciprocal square lattice

$$\mathbf{b}_{1S} = 2\pi\frac{\mathbf{a}_{2S}\times\hat{\mathbf{z}}}{\mathbf{a}_{1S}\cdot(\mathbf{a}_{2S}\times\hat{\mathbf{z}})} = 2\pi\frac{a_S\hat{\mathbf{y}}\times\hat{\mathbf{z}}}{a_S\hat{\mathbf{x}}\cdot(a_S\hat{\mathbf{y}}\times\hat{\mathbf{z}})} = 2\pi\frac{a_S\hat{\mathbf{x}}}{a_S\hat{\mathbf{x}}\cdot a_S\hat{\mathbf{x}}} = \frac{2\pi}{a_S}\hat{\mathbf{x}}$$

$$\mathbf{b}_{2S} = 2\pi\frac{\hat{\mathbf{z}}\times\mathbf{a}_{1S}}{\mathbf{a}_{1S}\cdot(\mathbf{a}_{2S}\times\hat{\mathbf{z}})} = 2\pi\frac{\hat{\mathbf{z}}\times a_S\hat{\mathbf{x}}}{a_S\hat{\mathbf{x}}\cdot(a_S\hat{\mathbf{y}}\times\hat{\mathbf{z}})} = 2\pi\frac{a_S\hat{\mathbf{y}}}{a_S\hat{\mathbf{x}}\cdot a_S\hat{\mathbf{x}}} = \frac{2\pi}{a_S}\hat{\mathbf{y}} \qquad \text{(B.11)}$$

Therefore, the reciprocal triangular and square lattices are triangular and square lattices themselves, figure B.2, with spacing:

$$b_T = \frac{4\pi}{a_T\sqrt{3}}$$
$$b_S = \frac{2\pi}{a_S} \qquad \text{(B.12)}$$

Given the periodicity of the reciprocal lattice, we need to consider only the wave

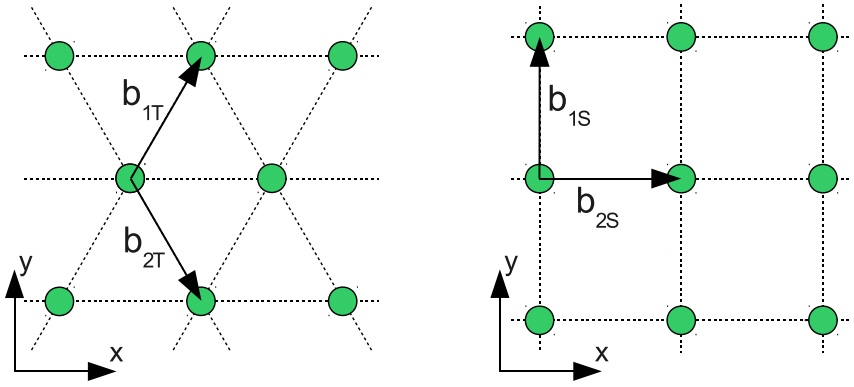

(a) **(b)**

Figure B.2: *Reciprocal lattices of: a) 2-D triangular lattice of dielectric rods; b) 2-D square lattice of dielectric rods.*

vectors $\mathbf{k}$ within the region of space in which we cannot get from one part of the volume to another by adding any $\mathbf{G}$: adding $\mathbf{G}$ to $\mathbf{k}$ would in fact lead to $j \cdot \mathbf{k} \cdot \mathbf{R} + j \cdot \mathbf{G} \cdot \mathbf{R}$, but $\mathbf{G} \cdot \mathbf{R} = n2\pi$, therefore we are considering the same physical mode. This region of space is called the (first) Brillouin zone. The region to consider can be further reduced by taking into account the lattice intrinsic symmetry, leading to the "irreducible Brillouin zone". Both the Brillouin zone and the irreducibile Brillouin zone of the triangular and square reciprocal lattices are shown in figure B.3.

The minima and maxima of a given band almost always occur at zones edges and often at corners: therefore, we just need to consider the set of wave vectors along the contour of the irreducible Brillouin zone in order to fully characterize the photonic band structure of the crystal. Photonic band structure is usually computed starting from the centre of the Brillouin zone Γ, then moving along the edges toward all the other vertex and finally closing the contour or "k-path" by returning to Γ; irreducible zone vertex are designated with Greek letters by convention.

With reference to figure B.3 and equation (B.12), the k-path for a triangular lattice is $\Gamma \rightarrow M \rightarrow K \rightarrow \Gamma$, where the vertex points Γ, M and K respectively correspond to $\mathbf{k} = 0$, $\mathbf{k} = \frac{b_T}{2}\hat{\mathbf{y}}$ and $\mathbf{k} = \frac{b_T\sqrt{3}}{6}\hat{\mathbf{x}} + \frac{b_T}{2}\hat{\mathbf{y}}$; the k-path for a square lattice is $\Gamma \rightarrow X \rightarrow M \rightarrow \Gamma$, where the vertex points Γ, X and M respectively correspond to $\mathbf{k} = 0$, $\mathbf{k} = \frac{b_S}{2}\hat{\mathbf{y}}$ and $\mathbf{k} = \frac{b_S}{2}\hat{\mathbf{x}} + \frac{b_S}{2}\hat{\mathbf{y}}$.

B.3 Photonic crystal master equation

Maxwell curl equations:

$$\nabla \times \mathbf{E}(\mathbf{r}) - j\omega\mu_0\mathbf{H}(\mathbf{r}) = 0$$

$$\nabla \times \mathbf{H}(\mathbf{r}) + j\omega\varepsilon(\mathbf{r})\mathbf{E}(\mathbf{r}) = 0 \qquad \text{(B.13)}$$

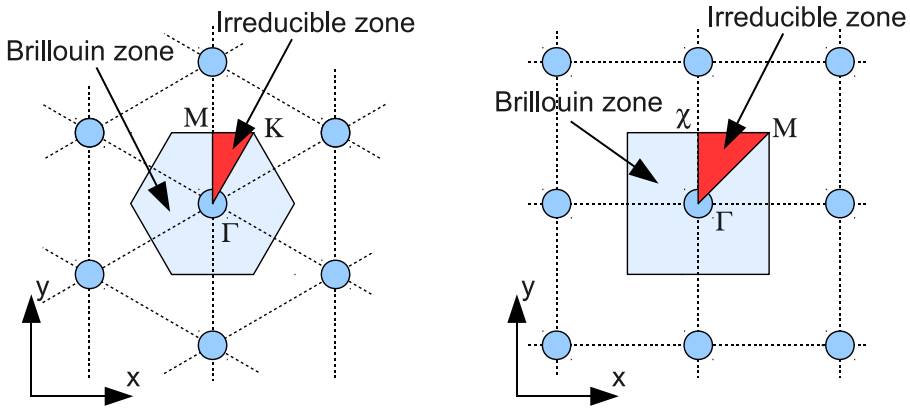

(a) **(b)**

Figure B.3: *Brillouin and irreducibile Brillouin zone of the reciprocal lattices of: a) 2-D triangular lattice of dielectric rods; b) 2-D square lattice of dielectric rods.*

can be manipulated leading to the Helmholtz equations:

$$\frac{1}{\varepsilon(\mathbf{r})}\nabla\times\{\nabla\times\mathbf{E}(\mathbf{r})\} = \frac{\omega^2}{c^2}\mathbf{E}(\mathbf{r}) \tag{B.14}$$

$$\nabla\times\left\{\frac{1}{\varepsilon(\mathbf{r})}\nabla\times\mathbf{H}(\mathbf{r})\right\} = \frac{\omega^2}{c^2}\mathbf{H}(\mathbf{r}) \tag{B.15}$$

Since the dielectric function is periodic, the electric field and magnetic field spatial distribution are also periodic and can be represented in the form of Bloch functions:

$$\mathbf{E}(\mathbf{r}) = \mathbf{E}_{\mathbf{k}n}(\mathbf{r})\cdot e^{j\cdot\mathbf{k}\cdot\mathbf{r}} \tag{B.16}$$

$$\mathbf{H}(\mathbf{r}) = \mathbf{H}_{\mathbf{k}n}(\mathbf{r})\cdot e^{j\cdot\mathbf{k}\cdot\mathbf{r}} \tag{B.17}$$

Bloch functions are plane waves multiplied by a periodic function with the same periodicity of the lattice:

$$\mathbf{E}_{\mathbf{k}n}(\mathbf{r}+\mathbf{R}) = \mathbf{E}_{\mathbf{k}n}(\mathbf{r}) \tag{B.18}$$

$$\mathbf{H}_{\mathbf{k}n}(\mathbf{r}+\mathbf{R}) = \mathbf{H}_{\mathbf{k}n}(\mathbf{r}) \tag{B.19}$$

Wave functions can be represented in the wave vectors space using the Fourier expansion:

$$\mathbf{E}_{\mathbf{k}n}(\mathbf{r}) = \sum_{\mathbf{G}}\mathbf{E}'_{\mathbf{k}n}(\mathbf{G})\,e^{(j(\mathbf{k}+\mathbf{G})\cdot\mathbf{r})} \tag{B.20}$$

$$\mathbf{H}_{\mathbf{k}n}(\mathbf{r}) = \sum_{\mathbf{G}}\mathbf{H}'_{\mathbf{k}n}(\mathbf{G})\,e^{(j(\mathbf{k}+\mathbf{G})\cdot\mathbf{r})} \tag{B.21}$$

where $\mathbf{G}$ is the reciprocal lattice vector, $\mathbf{E}'_{\mathbf{k}n}(\mathbf{G})$ and $\mathbf{H}'_{\mathbf{k}n}(\mathbf{G})$ are the wave functions in the wave vectors domain. The inverted dielectric function is also periodic and can be expanded as

$$\frac{1}{\varepsilon(\mathbf{r})} = \sum_G \chi(\mathbf{G}) \cdot e^{(j\mathbf{G}\cdot\mathbf{r})} \tag{B.22}$$

$\chi($**G** are the Fourier expansion coefficients given by:

$$\chi\mathbf{G} = \frac{1}{V_0}\int_{V_0} \frac{1}{\varepsilon(\mathbf{r})}\, e^{(-j\mathbf{G}\cdot\mathbf{r})}\mathrm{d}\mathbf{r} \tag{B.23}$$

where V_0 is the unit cell volume.

Substituting (B.20)-(B.22) in (B.14)-(B.15) and performing some simplifications (for details see [], Chapter 4):

$$-\sum_G \chi\left(\mathbf{G}-\mathbf{G}'\right)(\mathbf{k}+\mathbf{G}') \times \{(\mathbf{k}+\mathbf{G}')\times\mathbf{E}_{\mathbf{k}n}(\mathbf{G}')\} = \frac{(\omega^E_{\mathbf{k}n})^2}{c^2}\mathbf{E}_{\mathbf{k}n}(\mathbf{G}) \tag{B.24}$$

$$-\sum_G \chi\left(\mathbf{G}-\mathbf{G}'\right)(\mathbf{k}+\mathbf{G}') \times \{(\mathbf{k}+\mathbf{G}')\times\mathbf{H}_{\mathbf{k}n}(\mathbf{G}')\} = \frac{(\omega^H_{\mathbf{k}n})^2}{c^2}\mathbf{H}_{\mathbf{k}n}(\mathbf{G}) \tag{B.25}$$

Equations (B.24) and (B.25) are Equations B10 B11 are called "Master Equations" for three-dimensional photonic crystals and their solutions are the eigen-states of the crystal. The matrix differential operator is used to compose a matrix which eigen-values are computed for different wave vectors and they represent the band structure of the crystal.

B.3.1 Master equations for 2-D crystals

Electromagnetic waves propagating through a 2-D crystal can be decomposed in TM and TE polarizations:

$$\begin{aligned}
TM)\quad & \frac{\partial E_y}{\partial x} - \frac{\partial E_x}{\partial y} = -\frac{1}{c}\frac{\partial B_z}{\partial t} \\
& \frac{\partial H_z}{\partial y} = \frac{1}{c}\frac{\partial D_x}{\partial t} \\
& \frac{\partial H_z}{\partial x} = -\frac{1}{c}\frac{\partial D_y}{\partial t}
\end{aligned} \tag{B.26}$$

$$\begin{aligned}
TE)\quad & \frac{\partial H_y}{\partial x} - \frac{\partial H_x}{\partial y} = \frac{1}{c}\frac{\partial D_z}{\partial t} \\
& \frac{\partial E_z}{\partial y} = -\frac{1}{c}\frac{\partial B_x}{\partial t} \\
& \frac{\partial E_z}{\partial x} = \frac{1}{c}\frac{\partial B_y}{\partial t}
\end{aligned} \tag{B.27}$$

The Helmholtz equations for the TM and TE polarization can be respectively derived as:

$$TM) \quad -\left\{\frac{\partial}{\partial x}\frac{1}{\varepsilon(\mathbf{r}_\parallel)}\frac{\partial}{\partial x}+\frac{\partial}{\partial y}\frac{1}{\varepsilon(\mathbf{r}_\parallel)}\frac{\partial}{\partial y}\right\}H_z(\mathbf{r}_\parallel) = \frac{\omega^2}{c^2}H_z(\mathbf{r}_\parallel) \tag{B.28}$$

$$TE) \quad -\frac{1}{\varepsilon(\mathbf{r}_\parallel)}\left\{\frac{\partial^2}{\partial x^2}+\frac{\partial^2}{\partial y^2}\right\}E_z(\mathbf{r}_\parallel) = \frac{\omega^2}{c^2}E_z(\mathbf{r}_\parallel) \tag{B.29}$$

where $\mathbf{r}_\parallel$ is the 2-D coordinate vector (lying on the same plane of the photonic crystal). The electric field and magnetic field spatial distribution are periodic and, with analogy to the 3-D case, can be represented in the form of Bloch functions. The periodic wave functions and the inversed dielectric function can be expanded using Fourier series over the reciprocal lattice vectors $\mathbf{G}_\parallel$ leading to the "2-D Master equations"

$$TM) \quad \sum_{\mathbf{G}_\parallel}\chi\left(\mathbf{G}_\parallel-\mathbf{G}'_\parallel\right)\left|\mathbf{k}_\parallel+\mathbf{G}'_\parallel\right|^2\mathbf{E}_{z,\mathbf{k}_\parallel n}(\mathbf{G}'_\parallel) = \frac{(\omega^E_{\mathbf{k}n})^2}{c^2}\mathbf{E}_{z,\mathbf{k}_\parallel n}(\mathbf{G}_\parallel) \tag{B.30}$$

$$TE) \quad \sum_{\mathbf{G}_\parallel}\chi\left(\mathbf{G}_\parallel-\mathbf{G}'_\parallel\right)\left(\mathbf{k}_\parallel+\mathbf{G}_\parallel\right)\left(\mathbf{k}_\parallel+\mathbf{G}'_\parallel\right)\mathbf{H}_{z,\mathbf{k}_\parallel n}(\mathbf{G}'_\parallel) = \frac{(\omega^H_{\mathbf{k}n})^2}{c^2}\mathbf{H}_{z,\mathbf{k}_\parallel n}(\mathbf{G}_\parallel) \tag{B.31}$$

with

$$\chi\left(\mathbf{G}_\parallel\right) = \frac{1}{A_0}\int_{A_0}\frac{1}{\varepsilon(\mathbf{r}_\parallel)}e^{(-j\mathbf{G}_\parallel\cdot\mathbf{r}_\parallel)}\mathrm{d}\mathbf{r}_\parallel \tag{B.32}$$

The matrix differential operators, as for the 3-D case, are then used to compose a matrix which eigen-values are computed for different wave vectors and they represent the band structure of the 2-D crystal.

B.4 Plane-wave eigensolver algorithm

The plane-wave eigensolver algorithm is based on the following steps:

1. The unit cell is discretized in a $N_x \times N_y \times N_z$ mesh and the Fourier expansion of the inversed dielectric function is computed as

$$\begin{aligned}\chi(\mathbf{G}) &= \frac{1}{V_0}\int_{V_0}\frac{1}{\varepsilon(\mathbf{r})}e^{(-j\mathbf{G}\cdot\mathbf{r})}\mathrm{d}\mathbf{r} = \\ &= \frac{1}{a\cdot b\cdot c}\iiint\frac{1}{\varepsilon(x,y,z)}e^{(j(G_x x+G_y y+G_z z))}\,\mathrm{d}x\,\mathrm{d}y\,\mathrm{d}z = \\ &= \frac{1}{a\cdot b\cdot c}\sum_{i=0}^{N_x}\sum_{j=0}^{N_y}\sum_{k=0}^{N_z}\frac{1}{\varepsilon(x_i,y_j,z_k)}e^{(j(G_x x_i+G_y y_j+G_z z_k))}\cdot\Delta x_i\cdot\Delta y_j\cdot\Delta z_k\end{aligned} \tag{B.33}$$

with $i = 1,2,...,N_x$ $j = 1,2,...,N_y$ $k = 1,2,...,N_z$ and Δ_x, Δ_y and Δ_z being respectively the spatial step along the x, y and z direction. For the 2-D case the Fourier expansion of the inversed dielectric function is computed on a $N_x \times N_y$ mesh:

$$\begin{aligned}
\chi\left(\mathbf{G}_{\parallel}\right) &= \frac{1}{A_0}\int_{A_0}\frac{1}{\varepsilon(\mathbf{r}_{\parallel})}\, e^{(-j\mathbf{G}_{\parallel}\cdot\mathbf{r}_{\parallel})}\mathrm{d}\mathbf{r}_{\parallel} = \\
&= \frac{1}{a\cdot b}\iint\frac{1}{\varepsilon(x,y)}\, e^{(j(G_x x+G_y y))}\,\mathrm{d}x\,\mathrm{d}y = \\
&= \frac{1}{a\cdot b}\sum_{i=0}^{N_x}\sum_{j=0}^{N_y}\frac{1}{\varepsilon(x_i,y_j)}\, e^{(j(G_x x_i+G_y y_j))}\cdot\Delta x_i\cdot\Delta y_j
\end{aligned} \tag{B.34}$$

with $i = 1,2,...,N_x$ $j = 1,2,...,N_y$ and Δ_x and Δ_y being respectively the spatial step along the x and y direction. For an arbitrary dielectric function, the Fourier expansion coefficients of (B.23) or (B.32) must be numerically evaluated using respectively (B.33) or (B.34) but there might be analytical solutions for standard crystals such as dielectric spheres or dielectric rods placed in a uniform medium.

2. A set of wave vectors along the irreducible zone contour is defined, including the extrema and a certain number of points in between. The more points the higher resolution in the vector space; the number of eigen-values problems to solve increases linearly with the dimension of the wave vectors set.

3. The reciprocal lattice vectors set is defined using $2N_G + 1$ plane waves with $N_G = 1,2,3...$, leading to a set with $(2NG+1)^n$ elements, where n is the crystal dimensionality. Increasing the number of waves increases the accuracy of which the dielectric function is synthesized but the dimension of the matrix differential operator is exponentially increased. Qualitatively good results can be obtained with a relative small number of plane waves though.

4. The Fourier expansion coefficients of the dielectric function are computed using the reciprocal lattice vectors set defined in the previous step.

5. The eigen-values of the matrix differential operator (B.24)-(B.25) or (B.30)-(B.31) are computed for each wave vector and used to deline the photonic band structure of the crystal.

Appendix C – Antenna measurements setup

All the measurements presented in this work were undertaken in the Microwave Lab of Heriot-Watt University. In figure C.1 is depicted the antenna measurement setup, it consists of:

- a 5 sides shielded anechoic chamber;
- a vector network analyser (VNA) HP8510B;
- a vertical linear polarized source horn antenna connected to the VNA's port 1;
- an azimuthal positioner with analogue controller;
- the antenna under test (AUT) connected to port 2;
- a standard gain X-band horn antenna (STD) of known gain G_{STD} (not shown in the picture).

The gain transfer method [94] has been used to measure the AUT gain radiation patterns on the azimuthal and on the elevation plane (by rotating both source antenna and AUT of 90°):

- the source antenna was placed on a tripod and connected to VNA's port 1.
- The standard horn antenna was connected to VNA's port 2 and placed on the azimuthal positioner at a distance R big enough to ensure far fields region condition: this distance must be greater than the greatest sum of the individual far field distances for the pairs $Source-AUT$ and $Source-STD$:

$$R \geq max(R_S + R_{STD}, R_S + R_{AUT}) \tag{C.1}$$

  where R_S, R_{AUT} and R_{STD} are respectively the source antenna, the AUT and the standard gain horn antenna far field region distances.
- Far field condition was verified with the "6dB rule", ie doubling the distance between the antennas should decrease the received power level by 6dB.
- an $S_{12}|_{STD}$ reference measurement was taken making sure the antennas were properly aligned in terms of maximum received power and polarization.
- The standard antenna was then replaced by the AUT on the azimuthal positioner and connected to the VNA's port 2 making sure as before that antennas were properly aligned.
- The $S_{12}(\phi)|_{AUT}$ as a function of the angle ϕ was recorded.

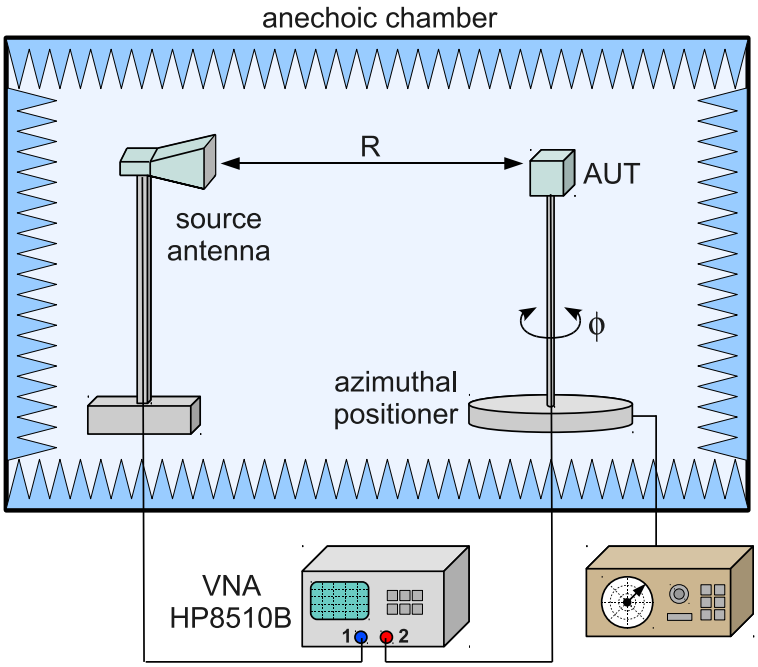

Figure C.1: *Antenna measurements setup.*

- The AUT gain G_{AUT} was finally computed using the standard horn gain G_{STD} and the $S_{12}|_{STD}$ reference measurement:

$$G_{AUT}(\phi) = G_{STD} + [S_{12}(\phi)|_{AUT} - S_{12}|_{STD}] \tag{C.2}$$

References

[1] E. Yablonovitch, "Inhibited spontaneous emission in solid-state physics and electronics," *Physical review letters*, vol. 58, pp. 2059–2062, May 1987. PMID: 10034639.

[2] J. Joannopoulos, S. Johnson, J. Winn, and R. Meade, *Photonic Crystals: Molding the Flow of Light (Second Edition)*. Princeton University Press, Feb. 2008.

[3] F. Yang and Y. Rahmat-Samii, *Electromagnetic Band Gap Structures in Antenna Engineering*. The Cambridge RF and Microwave Engineering Series, Cambridge University Press, 2008.

[4] D. Sievenpiper, L. Zhang, R. Broas, N. Alexopolous, and E. Yablonovitch, "High-impedance electromagnetic surfaces with a forbidden frequency band," *Microwave Theory and Techniques, IEEE Transactions on*, vol. 47, no. 11, pp. 2059–2074, 1999.

[5] D. Sievenpiper, L. Zhang, and E. Yablonovitch, "High-impedance electromagnetic ground planes," in *Microwave Symposium Digest, 1999 IEEE MTT-S International*, vol. 4, pp. 1529–1532 vol.4, 1999.

[6] F. Yang, K. Ma, Y. Qian, and T. Itoh, "A uniplanar compact photonic-bandgap (UC-PBG) structure and its applications for microwave circuit," *Microwave Theory and Techniques, IEEE Transactions on*, vol. 47, no. 8, pp. 1509–1514, 1999.

[7] M. Thevenot, C. Cheype, A. Reineix, and B. Jecko, "Directive photonic-bandgap antennas," *Microwave Theory and Techniques, IEEE Transactions on*, vol. 47, no. 11, pp. 2115–2122, 1999.

[8] M. S. D. M. Thèvenot, "Design of a new photonic cover to increase antenna directivity," *Microwave and Optical Technology Letters*, vol. 22, no. 2, pp. 136–139, 1999.

[9] C. Cheype, C. Serier, M. Thevenot, T. Monediere, A. Reineix, and B. Jecko, "An electromagnetic bandgap resonator antenna," *Antennas and Propagation, IEEE Transactions on*, vol. 50, no. 9, pp. 1285–1290, 2002.

[10] Y. J. Lee, J. Yeo, R. Mittra, and W. S. Park, "Application of electromagnetic bandgap (EBG) superstrates with controllable defects for a class of patch antennas as spatial angular filters," *Antennas and Propagation, IEEE Transactions on*, vol. 53, no. 1, pp. 224–235, 2005.

[11] A. Kanso, R. Chantalat, M. Thevenot, T. Monediere, and B. Jecko, "Dual band dielectric EBG resonator antenna," in *Antennas and Propagation, 2009. EuCAP 2009. 3rd European Conference on*, pp. 3240–3243, 2009.

[12] A. Weily, A. Weily, K. Esselle, K. Esselle, B. Sanders, and T. Bird, "Woodpile EBG resonator antenna with double slot feed," in *Antennas and Propagation Society International Symposium, 2004. IEEE*, vol. 2, pp. 1139–1142 Vol.2, 2004.

[13] A. Weily, A. Weily, L. Horvath, L. Horvath, K. Esselle, B. Sanders, and T. Bird, "A planar resonator antenna based on a woodpile EBG material," *Antennas and Propagation, IEEE Transactions on*, vol. 53, no. 1, pp. 216–223, 2005.

[14] Y. Lee, Y. Zhao, Y. Hao, and C. Parini, "A free-formed EBG resonator antenna at millimeter wave frequencies," in *Antennas and Propagation, 2006. EuCAP 2006. First European Conference on*, pp. 1–4, 2006.

[15] Y. Lee, Y. Lee, X. Lu, X. Lu, Y. Hao, S. Yang, R. Ubic, J. Evans, and C. Parini, "Directive millimetre-wave antenna based on freeformed woodpile EBG structure," *Electronics Letters*, vol. 43, no. 4, pp. 195–196, 2007.

[16] Y. Lee, Y. Lee, Y. Hao, Y. Hao, and C. G. Parini, "Low profile high directivity millimetrewave antenna using freeformed metamaterial," in *Infrared and Millimeter Waves, 2007 and the 2007 15th International Conference on Terahertz Electronics. IRMMW-THz. Joint 32nd International Conference on*, pp. 943–944, 2007.

[17] Y. Lee, X. Lu, Y. Hao, S. Yang, J. Evans, and C. Parini, "Directive millimetrewave antennas using freeformed ceramic metamaterials in planar and cylindrical forms," in *Antennas and Propagation Society International Symposium, 2008. AP-S 2008. IEEE*, pp. 1–4, 2008.

[18] K. Lugo, R. Gomez, Y. Lee, N. Farahat, R. Mittra, and Y. Hao, "FDTD analysis of an antenna covered by a dielectric woodpile EBG superstrate," in *Antennas and Propagation Society International Symposium, 2008. AP-S 2008. IEEE*, pp. 1–4, 2008.

[19] F. Frezza, L. Pajewski, E. Piuzzi, C. Ponti, and G. Schettini, "Design and fabrication of a 3D-EBG superstrate for patch antennas," in *Microwave Conference, 2009. EuMC 2009. European*, pp. 1496–1499, 2009.

[20] A. Feresidis and J. Vardaxoglou, "High gain planar antenna using optimised partially reflective surfaces," *Microwaves, Antennas and Propagation, IEE Proceedings -*, vol. 148, no. 6, pp. 345–350, 2001.

[21] A. Feresidis, G. Goussetis, S. Wang, and J. Vardaxoglou, "Artificial magnetic conductor surfaces and their application to low-profile high-gain planar antennas," *Antennas and Propagation, IEEE Transactions on*, vol. 53, no. 1, pp. 209–215, 2005.

[22] N. Guerin, S. Enoch, G. Tayeb, P. Sabouroux, P. Vincent, and H. Legay, "A metallic Fabry-Perot directive antenna," *IEEE Transactions on Antennas and Propagation*, vol. 54, no. 1, pp. 220–224, 2006.

[23] R. Chantalat, L. Moustafa, M. Thevenot, T. Monediere, and B. Jecko, "Low profile EBG resonator antennas," *International Journal of Antennas and Propagation*, vol. 2009, pp. 1–7, 2009.

[24] L. Moustafa and B. Jecko, "Design of a wideband highly directive EBG antenna using Double-Layer frequency selective surfaces and multifeed technique for application in the Ku-Band," *Antennas and Wireless Propagation Letters, IEEE*, vol. 9, pp. 342–346, 2010.

[25] J. Ju, D. Kim, W. Lee, and J. Choi, "Design method of a Circularly-Polarized antenna using Fabry-Pérot cavity structure," *ETRI Journal*, vol. 33, no. 2, pp. 163–168, 2011.

[26] L. Moustafa and B. Jecko, "EBG structure with wide defect band for broadband cavity antenna applications," *Antennas and Wireless Propagation Letters, IEEE*, vol. 7, pp. 693–696, 2008.

[27] L. Moustafa, M. Thevenot, T. Monediere, and B. Jecko, "Design method of EBG material with wide defect band," in *Antennas and Propagation, 2009. EuCAP 2009. 3rd European Conference on*, pp. 3235–3239, 2009.

[28] G. Palikaras, A. Feresidis, and J. Vardaxoglou, "Cylindrical electromagnetic bandgap structures for directive base station antennas," *Antennas and Wireless Propagation Letters, IEEE*, vol. 3, pp. 87–89, 2004.

[29] G. Palikaras, A. Feresidis, and J. Vardaxoglou, "Cylindrical electromagnetic band gap structures for base station antennas," in *Antennas and Propagation Society International Symposium, 2004. IEEE*, vol. 2, pp. 1163–1166 Vol.2, 2004.

[30] G. Palikaras, A. Feresidis, and Y. Vardaxoglou, "Design of cylindrical Omni-Directional patch antenna with superimposed EBG surfaces," in *Antennas and Propagation Conference, 2007. LAPC 2007. Loughborough*, pp. 297–300, 2007.

[31] G. K. Palikaras, A. P. Feresidis, and Y. C. Vardaxoglou, "Radiation characteristics of cylindrical microstrip patch antennas using metallic EBG surfaces as superstrates," in *Antennas and Propagation International Symposium, 2007 IEEE*, pp. 1321–1324, 2007.

[32] H. Chreim, E. Pointereau, B. Jecko, and P. Dufrane, "Omnidirectional electromagnetic band gap antenna for base station applications," *Antennas and Wireless Propagation Letters, IEEE*, vol. 6, pp. 499–502, 2007.

[33] E. Pointereau, E. Pointereau, H. Chreim, H. Chreim, B. Jecko, and P. Dufrane, "Omnidirectional cylindrical electromagnetic bandgap antenna with dual polarization," *Antennas and Wireless Propagation Letters, IEEE*, vol. 6, pp. 450–453, 2007.

[34] Y. Lee, X. Lu, Y. Hao, S. Yang, C. Parini, and J. Evans, "Cylindrical EBG antenna for short range gigabit wireless communications at millimetre-wave bands," *Electronics Letters*, vol. 45, no. 3, pp. 136–138, 2009.

[35] Y. Lee, Y. Hao, and C. Parini, "High-gain omni-directional antenna using a freeformed cylindrical cavity for high data-rate short range communications at millimetre-wave bands," in *Antennas and Propagation, 2009. EuCAP 2009. 3rd European Conference on*, pp. 2828–2831, 2009.

[36] Y. Lee, X. Lu, Y. Hao, S. Yang, J. Evans, and C. Parini, "Narrow-beam azimuthally omni-directional millimetre-wave antenna using freeformed cylindrical woodpile cavity," *Microwaves, Antennas & Propagation, IET*, vol. 4, no. 10, pp. 1491–1499, 2010.

[37] E. Ozbay, B. Temelkuran, and M. Bayindir, "Microwave applications of photonic crystals," *Progress In Electromagnetics Research*, vol. 41, pp. 185–209, 2003.

[38] A. Weily, A. Weily, K. Esselle, K. Esselle, B. Sanders, and T. Bird, "A woodpile EBG sectoral horn antenna," in *Antennas and Propagation Society International Symposium, 2005 IEEE*, vol. 4B, pp. 323–326 vol. 4B, 2005.

[39] A. Weily, A. Weily, K. Esselle, K. Esselle, T. Bird, and B. Sanders, "Linear array of woodpile EBG sectoral horn antennas," *Antennas and Propagation, IEEE Transactions on*, vol. 54, no. 8, pp. 2263–2274, 2006.

[40] H. Caglayan, I. Bulu, and E. Ozbay, "Highly directional enhanced radiation from sources embedded inside three-dimensional photonic crystals," *Optics Express*, vol. 13, no. 19, pp. 7645–7652, 2005.

[41] B. Temelkuran, M. Bayindir, E. Ozbay, R. Biswas, M. M. Sigalas, G. Tuttle, and K. M. Ho, "Photonic crystal-based resonant antenna with a very high directivity," *Journal of Applied Physics*, vol. 87, pp. 603–605, Jan. 2000.

[42] I. Khromova, I. Ederra, R. Gonzalo, and B. P. de Hon, "Symmetrical pyramidal horn antennas based on EBG structures," *Progress In Electromagnetics Research B*, vol. 29, pp. 1–22, 2011.

[43] H. Boutayeb, T. Denidni, A. Sebak, and L. Talbi, "Design of elliptical electromagnetic bandgap structures for directive antennas," *Antennas and Wireless Propagation Letters, IEEE*, vol. 4, pp. 93–96, 2005.

[44] H. Boutayeb, T. Denidni, A. Sebak, and L. Talbi, "Metallic EBG structures for directive antennas using rectangular, cylindrical and elliptical shapes," in *Antennas and Propagation Society International Symposium, 2005 IEEE*, vol. 1A, pp. 762–765 Vol. 1A, 2005.

[45] H. Boutayeb, T. Denidni, K. Mahdjoubi, A. Tarot, A. Sebak, and L. Talbi, "Analysis and design of a cylindrical EBG-based directive antenna," *Antennas and Propagation, IEEE Transactions on*, vol. 54, no. 1, pp. 211–219, 2006.

[46] M. P. Kesler, J. G. Maloney, B. L. Shirley, and G. S. Smith, "Antenna design with the use of photonic band-gap materials as all-dielectric planar reflectors," *Microwave and Optical Technology Letters*, vol. 11, no. 4, pp. 169–174, 1996.

[47] G. S. Smith, M. P. Kesler, and J. G. Maloney, "Dipole antennas used with all-dielectric, woodpile photonic-bandgap reflectors: Gain, field patterns, and input impedance," *Microwave and Optical Technology Letters*, vol. 21, no. 3, pp. 191–196, 1999.

[48] F. Yang and Y. Rahmat-Samii, "Curl antennas over electromagnetic band-gap surface: a low profiled design for CP applications," in *Antennas and Propagation Society International Symposium, 2001. IEEE*, vol. 3, pp. 372–375 vol.3, 2001.

[49] F. Yang and Y. Rahmat-Samii, "Reflection phase characterizations of the EBG ground plane for low profile wire antenna applications," *Antennas and Propagation, IEEE Transactions on*, vol. 51, no. 10, pp. 2691–2703, 2003.

[50] Z. Li, G. Wang, and Y. Cao, "A Low-Profile equiangular spiral antenna using a novel EBG ground plane," in *Antennas, Propagation & EM Theory, 2006. ISAPE '06. 7th International Symposium on*, pp. 1–3, 2006.

[51] R. Langley, "Antennas combined with high impedance bandgap surfaces," in *Antennas and Propagation, 2009. EuCAP 2009. 3rd European Conference on*, pp. 2602–2606, 2009.

[52] V. V. Yem and T. T. Phuong, "Ultra-wide band low-profile spiral antennas using an EBG ground plane," in *Advanced Technologies for Communications (ATC), 2010 International Conference on*, pp. 89–94, 2010.

[53] N. A. Abbasi and R. Langley, "A small quad-band automotive antenna," in *Antennas and Propagation (EuCAP), 2010 Proceedings of the Fourth European Conference on*, pp. 1–5, 2010.

[54] R. Coccioli, F. Yang, K. Ma, and T. Itoh, "Aperture-coupled patch antenna on UC-PBG substrate," *Microwave Theory and Techniques, IEEE Transactions on*, vol. 47, no. 11, pp. 2123–2130, 1999.

[55] F. Yang, C. Kee, and Y. Rahmat-Samii, "Step-like structure and EBG structure to improve the performance of patch antennas on high dielectric substrate," in *Antennas and Propagation Society International Symposium, 2001. IEEE*, vol. 2, pp. 482–485 vol.2, 2001.

[56] S. Sharma and L. Shafai, "Enhanced performance of an aperture-coupled rectangular microstrip antenna on a simplified unipolar compact photonic band gap (UC-PBG) structure," in *Antennas and Propagation Society International Symposium, 2001. IEEE*, vol. 2, pp. 498–501 vol.2, 2001.

[57] M. Rahman and M. Stuchly, "Wideband microstrip patch antenna with planar PBG structure," in *Antennas and Propagation Society International Symposium, 2001. IEEE*, vol. 2, pp. 486–489 vol.2, 2001.

[58] N. Llombart, A. Neto, G. Gerini, and P. D. Maagt, "Planar circularly symmetric EBG structures design and analysis," in *Microwave Conference, 2004. 34th European*, vol. 1, pp. 451–454, 2004.

[59] N. Llombart, A. Neto, G. Gerini, and P. de Maagt, "Planar circularly symmetric EBG structures for reducing surface waves in printed antennas," *Antennas and Propagation, IEEE Transactions on*, vol. 53, no. 10, pp. 3210–3218, 2005.

[60] Y. Coulibaly, H. Boutayeb, T. Denidni, and L. Talbi, "Gain enhancement of a dielectric resonator antenna using a cylindrical electromagnetic crystal substrate," in *Antennas and Propagation Society International Symposium, 2007 IEEE*, pp. 1325–1328, 2007.

[61] H. Boutayeb and T. Denidni, "Gain enhancement of a microstrip patch antenna using a cylindrical electromagnetic crystal substrate," *Antennas and Propagation, IEEE Transactions on*, vol. 55, no. 11, pp. 3140–3145, 2007.

[62] P. Kovacs, "High gain microstrip antenna using planar circularly symmetric EBG structures," in *Radioelektronika, 2007. 17th International Conference*, pp. 1–5, 2007.

[63] D. Qu, L. Shafai, and A. Foroozesh, "Improving microstrip patch antenna performance using EBG substrates," *Microwaves, Antennas and Propagation, IEE Proceedings* -, vol. 153, no. 6, pp. 558–563, 2006.

[64] L. Inclan-Sanchez, J. Vazquez-Roy, and E. Rajo-Iglesias, "Gain enhancement of a multilayer microstrip patch antenna by means of a truncated planar periodic structure," in *Antennas and Propagation, 2009. EuCAP 2009. 3rd European Conference on*, pp. 3206–3209, 2009.

[65] E. R. Brown, C. D. Parker, and E. Yablonovitch, "Radiation properties of a planar antenna on a photonic-crystal substrate," *Journal of the Optical Society of America B*, vol. 10, no. 2, p. 404, 1993.

[66] R. Gonzalo, P. D. Maagt, and M. Sorolla, "Enhanced patch-antenna performance by suppressing surface waves using photonic-bandgap substrates," *Microwave Theory and Techniques, IEEE Transactions on*, vol. 47, no. 11, pp. 2131–2138, 1999.

[67] J. Colburn and Y. Rahmat-Samii, "Patch antennas on externally perforated high dielectric constant substrates," *Antennas and Propagation, IEEE Transactions on*, vol. 47, no. 12, pp. 1785–1794, 1999.

[68] J. Iriarte, I. Ederra, and R. Gonzalo, "Design and characterisation of a high efficiency ceramic ebg patch antenna," *Microwaves, Antennas & Propagation, IET*, vol. 4, no. 8, pp. 1056–1062, 2010.

[69] H. Chreim, E. Pointereau, and B. Jecko, "4x90 degrees sectorial metallic EBG antenna for high gain omnidirectional coverage," in *Antennas and Propagation, 2007. EuCAP 2007. The Second European Conference on*, pp. 1–6, 2007.

[70] H. Chreim, M. Hajj, E. Arnaud, B. Jecko, C. Dall'omo, and P. Dufrane, "Multibeam antenna for telecommunications networks using cylindrical EBG structure," *Antennas and Wireless Propagation Letters, IEEE*, vol. PP, no. 99, p. 1, 2009.

[71] H. Chreim, B. Jecko, C. Dall'omo, and P. Dufrane, "Cylindrical EBG multibeam antenna for telecommunication networks," in *Antennas and Propagation, 2009. EuCAP 2009. 3rd European Conference on*, pp. 3810–3812, 2009.

[72] D. Serhal, M. Hajj, R. Chantalat, J. Drouet, and B. Jecko, "Multifed sectoral EBG antenna for WiMAX applications," *Antennas and Wireless Propagation Letters, IEEE*, vol. 8, pp. 620–623, 2009.

[73] D. Serhal, M. Hajj, and B. Jecko, "High gain sectoral metallic EBG antenna," in *Antennas and Propagation, 2009. EuCAP 2009. 3rd European Conference on*, pp. 3196–3199, 2009.

[74] C. A. Balanis, *Antenna Theory: Analysis and Design, 2nd Edition*. Wiley, 2 ed., May 1996.

[75] F. Yang and Y. Rahmat-Samii, "Microstrip antennas integrated with electromagnetic band-gap (EBG) structures: a low mutual coupling design for array applications," *Antennas and Propagation, IEEE Transactions on*, vol. 51, no. 10, pp. 2936–2946, 2003.

[76] L. Yang, Z. Feng, F. Chen, and M. Fan, "A novel compact electromagnetic band-gap (EBG) structure and its application in microstrip antenna arrays," in *Microwave*

Symposium Digest, 2004 IEEE MTT-S International, vol. 3, pp. 1635–1638 Vol.3, 2004.

[77] N. Llombart, A. Neto, G. Gerini, and P. D. Maagt, "Planar circularly symmetric EBG's to improve the isolation of array elements," in *Antennas and Propagation Society International Symposium, 2005 IEEE*, vol. 2A, pp. 582–585 vol. 2A, 2005.

[78] Y. Yao, X. Wang, and Z. Feng, "A novel dual-band compact electromagnetic bandgap (EBG) structure and its application in multi-antennas," in *Antennas and Propagation Society International Symposium 2006, IEEE*, pp. 1943–1946, 2006.

[79] E. Rajo-Iglesias, O. Quevedo-Teruel, and L. Inclan-Sanchez, "Mutual coupling reduction in patch antenna arrays by using a planar EBG structure and a multilayer dielectric substrate," *Antennas and Propagation, IEEE Transactions on*, vol. 56, no. 6, pp. 1648–1655, 2008.

[80] H. F. Shaban, H. A. Elmikaty, and A. A. Shaalan, "Study the effects of electromagnetic band-gap (ebg) substrate on two patch microstrip antenna," *Progress In Electromagnetics Research B*, vol. 10, pp. 55–74, 2008.

[81] "Dielectric materials." http://www.morganelectroceramics.com/materials/dielectric/.

[82] K. S. Cole and R. H. Cole, "Dispersion and absorption in dielectrics i. alternating current characteristics," *The Journal of Chemical Physics*, vol. 9, no. 4, p. 341, 1941.

[83] P. Bolivar, M. Brucherseifer, J. Rivas, R. Gonzalo, I. Ederra, A. Reynolds, M. Holker, and P. de Maagt, "Measurement of the dielectric constant and loss tangent of high dielectric-constant materials at terahertz frequencies," *Microwave Theory and Techniques, IEEE Transactions on*, vol. 51, no. 4, pp. 1062–1066, 2003.

[84] J. Kraus, *Antennas*. New York: McGraw-Hill, 2nd ed. ed., 1988.

[85] J. Kraus, "The Corner-Reflector antenna," *Proceedings of the IRE*, vol. 28, no. 11, pp. 513–519, 1940.

[86] E. Harris, "An experimental investigation of the corner-reflector antenna," *Proceedings of the IRE*, vol. 41, no. 5, pp. 645–651, 1953.

[87] H. Cottony and A. Wilson, "Gains of finite-size corner-reflector antennas," *Antennas and Propagation, IRE Transactions on*, vol. 6, no. 4, pp. 366–369, 1958.

[88] K. Yee, "Numerical solution of inital boundary value problems involving maxwell's equations in isotropic media," *Antennas and Propagation, IEEE Transactions on*, vol. 14, pp. 302–307, May 1966.

[89] A. Taflove, *Advances in Computational Electromagnetics - The Finite-Difference Time- Domain Method*. Artech House, 1998.

[90] K. S. Kunz and R. J. Luebbers, *The Finite Difference Time Domain Method for Electromagnetics*. CRC, 1993.

[91] S. Gedney, "An anisotropic perfectly matched layer-absorbing medium for the truncation of FDTD lattices," *Antennas and Propagation, IEEE Transactions on*, vol. 44, pp. 1630–1639, Dec. 1996.

[92] Z. Sacks, Z. Sacks, D. Kingsland, D. Kingsland, R. Lee, and J. Lee, "A perfectly matched anisotropic absorber for use as an absorbing boundary condition," *Antennas and Propagation, IEEE Transactions on*, vol. 43, no. 12, pp. 1460–1463, 1995.

[93] I. A. Sukhoivanov and I. V. Guryev, *Photonic Crystals: Physics and Practical Modeling*. Springer, Oct. 2009.

[94] "IEEE standard test procedures for antennas," 1979.